Vortex Structures in the Wakes of Two- and Three-Dimensional Bodies

James Venning

A thesis submitted to Monash University in fulfilment of
the requirements for the degree of

Doctor of Philosophy

Statement of originality

This thesis contains no material which has been accepted for the award of any other degree or diploma at any university or equivalent institution and, to the best of my knowledge and belief, this thesis contains no material previously published or written by another person, except where due reference is made in the text of the thesis.

JAVenning

James Venning

April 8, 2016

COPYRIGHT NOTICES

ABSTRACT

This thesis reports on an experimental study into the flow structure of two different bluff bodies: an inclined flat plate with a quasi-two-dimensional wake and the Ahmed body with a highly three-dimensional wake. Each wake is measured using particle image velocimetry with high spatial and temporal resolution. Time-average results are presented showing the effect of angle-of-attack and Reynolds number on the flow around the flat plate. Results showing the formation of large scale von Kármán vortices from the merging of smaller shear layer vortices is presented and the ratio of these frequencies is quantified.

The nature of the major wake structures of the Ahmed body is presented and the strength of each structure is quantified through measuring the circulation. An analysis of the circulation variation with downstream location reveals the tilting of vorticity and the subsequent merging of structures. The dynamics of the vortex motion is illustrated using two-dimensional space-time plots revealing large, periodic motions in the wake.

The influence of the longitudinal structures on the wake is investigated by systematically varying the lateral spacing of the c-pillars. By increasing the rear-slant aspect ratio, the induced downwash between the two longitudinal structures is reduced. The critical aspect ratio between reattaching and completely separated flow is presented. The effect of aspect ratio on the dynamics of these structures is shown to be minimal.

ACKNOWLEDGEMENTS

I must start these acknowledgements with my academic supervisors, who have been an enormous help over these years. Each of them possess a different skill-set that has been vital to me getting this finished: Mark with your understanding and writing tips, David Burton with your practical intuition, David Lo Jacono with your coding and post-processing, and John with all-of-the-above but also your big-picture guidance. You have been an example of professionalism and it has been an absolute pleasure to be your student.

My colleagues at Monash have been great fun and a real assistance. The discussions at lunch with Justin, Joseph, Marty and Pauline were both enlightening and enjoyable. Jisheng, Tim, James, Nathan, Mick, plus our Swedish friends Patrick and Simon, all helped along the way and were a pleasure to befriend. Most thanks must be for Andraś, who taught me everything. I'll also remember fondly the table tennis and Sichuan dinners. Thanks to Nat de Rose, Andrew Smith and Michael Terkeley for building all my models. Thank you Bev, Nicole, and Helen for keeping MIGR off my back.

Thanks to my parents for putting up with me, and for letting me live in their house. Thanks to Dad for his constant asking if I've *"finished that P-H-blummin'-D yet."* Most particular thanks to Elizabeth and Charlotte for showing me there are much more important things to life than fluid mechanics!

To the glory of God alone.

NOMENCLATURE

Acronyms

CCD	Charge-coupled device
FFT	Fast Fourier transform
FOV	Field of view
HWA	Hot wire anemometry
LDV	Laser Doppler velocimetry
PIV	Particle image velocimetry
POD	Proper orthogonal decomposition
RMS	Root mean square
ROI	Region of interest
SNR	Signal to noise ratio
STD	Standard deviation
TR-PIV	Time-resolved particle image velocimetry

Greek symbols

α	Angle of attack	$\circ$
Γ	Circulation	m^2s^{-1}
κ	Curvature	
μ	Dynamic viscosity	kg/ms
ω	Vorticity	$1/s$
ρ	Density	kg/m^3s

Non-dimensional numbers

C_D	Drag coefficient
Re	Reynolds number
St	Strouhal number

Roman symbols

B	Bias error	
c	Plate chord length	m
f	Frequency	Hz
H	Ahmed body height	m
I	Turbulence intensity	
k	Wave number	
L	Ahmed body length	m
M	POD spatial mode	
P	Precision error	
t	Time	s
U	Velocity	m/s
u	Streamwise velocity	m/s
v	Transverse velocity	m/s
W	Ahmed body width	m
w	Vertical velocity	m/s
x	Streamwise direction	
y	Transverse direction	
z	Vertical direction	

Subscripts

∞	Freestream
FA	Frontal area
i	Imaginary component
K	von Kármán
r	Real component
SL	Shear layer

CONTENTS

LIST OF FIGURES

List of Tables

Chapter 1

Introduction

The study of fluid mechanics traces its routes back to the Ancient Greeks, who studied buoyancy forces and hydraulic machinery. Now, the field is recognised as complex and diverse. One of the many areas studied within this discipline is that of wakes, which are regions of flow immediately downstream of a body. For a streamlined body, the fluid usually stays well attached over the whole body. However, when the viscous effects cause the flow velocity to fall to zero, the flow leaves the surface of the body. These are the characteristics of bluff bodies and separated flows.

Flow separation is of great importance in fluid dynamics because it usually causes the drag to increase. Separated flows are also generally characterised by the presence of large vortices, which are regions of locally rotating flow. These vortices are energy rich and result in increased mixing in the wake.

Lord Kelvin's theorem implies that for an incompressible fluid all vorticity in the wake must be generated at the body's surface. For a two-dimensional bluff body, vorticity builds up into large-scale vortices, which are then alternately shed downstream. Such structures are generally named von Kármán vortices after Theodore von Kármán, although Henri Bénard actually described them a few years earlier. The periodic shedding of these vortices is of practical importance due to the extra structural loading placed on the body and the influence of these vortices on downstream objects.

For a three-dimensional bluff body, the flow complexity increases significantly. One of the modes of advecting vorticity downstream can still be through von Kármán vortex analogues, but the transport of vorticity can also occur through large-scale three-dimensional structures, such as trailing streamwise vortices. Figure 1.1 shows dye visualisation over a Concorde displaying this type of vortical structure. These structures have low pressure cores, which may be helpful in the case of a delta-wing or even an insect wing to produce more lift, or may be unhelpful in the case of a ground vehicle by producing more drag.

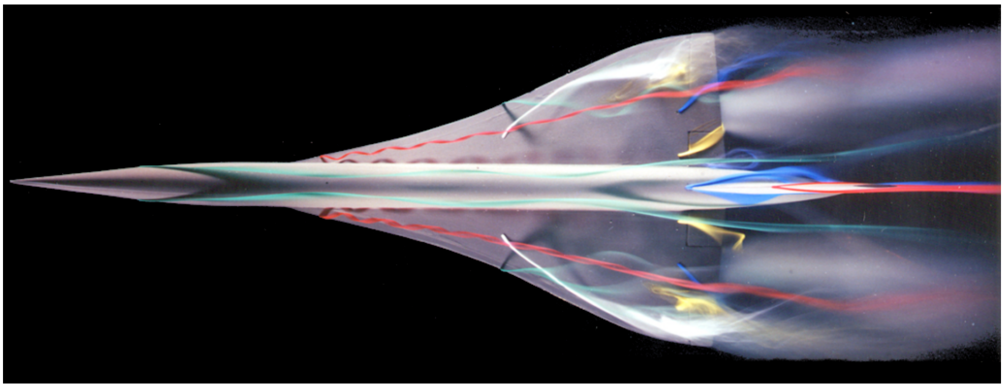

Figure 1.1: Three-dimensional vortical structures over the wings of a scale-model Concorde. The three-dimensionality and turbulent nature of the wake is evident. Photo: H Werle, from Delery (2001)

This thesis studies the separated wakes of both two- and three-dimensional bodies. The choice of bodies for this study allowed the investigation of both fundamental and practical fluid dynamics. The first body is a two-dimensional flat plate. The most canonical body in regards to separated flows is the circular cylinder, and the wake is well researched. Moving to a flat plate removes the cylinder's curvature, and the associated variability in the separation points. The absence of rotational symmetry also adds another degree of freedom in the alignment of the plate with the flow. The wakes of sharp-edged bodies in general have received much less attention than that of the circular cylinder.

The second body used in this study is the Ahmed body, which is a generalised car shape widely used in aerodynamics. The body produces a wake with similar large-scale features to the wake of a real car, without the introduction of details that are specific to any particular vehicle. This body has been well-studied for the last thirty years, with advances made using both experimental and numerical methods.

One way of altering the wake of a bluff body is by varying the aspect ratio, i.e., the ratio of a body's characteristic width to its height. Research into finite wings, flows over steps and cylinder wakes have all shown that the aspect ratio can have strong effects on the large structures in the wake. Generally, reducing the aspect ratio causes the flow to be more three-dimensional increasing the influence of the end effects on wake development. While these effects are documented for some bodies, an in-depth study of the influence of this parameter has not been conducted for the Ahmed body.

This experimental study furthers our understanding of separated flows in several ways. Detailed wake measurements are provided for the flat plate across a wide range of Reynolds numbers and angles of incidence, and for the Ahmed body for various aspect ratios. Both the spatial and temporal resolution of these measurements were fine to provide high quality data in the near wake, allowing both the time-averaged fields and wake dynamics to be investigated. The evolution of the shear-layer vortices is demonstrated showing their role in the formation of von Kármán vortices.

The influence of the side vortices on the flow of the three-dimensional Ahmed body is presented. The geometry is systematically varied to move the longitudinal structures away from each other and the effect on the flow is measured through velocity and force measurements. The dynamics of the flow is illustrated showing the dominant modes and quantifying the dominant wake frequencies.

CHAPTER 2

A REVIEW OF THE LITERATURE

2.1 Introduction

This chapter introduces the relevant literature to the issues studied in this thesis. Particular mention is given to places in the literature that need further work, some of which is covered in this thesis. The review is split into two sections, the first dealing with three-dimensional flow separations - especially that related to ground vehicles. The generation of structures in the wakes of such bodies and the resultant effects on the aerodynamic forces are explored. The idea of generalizing a body to simplify aerodynamic investigations is presented, with a detailed review given of studies into the wake of one particular reference model, the Ahmed body. The macro structures in the wake are all defined and the effects of various geometric changes on these structures is presented. Previous investigations into the wake dynamics are summarised showing the disagreement amongst researchers regarding the nature of the fluctuations in the wake of that model.

The second part of this review investigates quasi-two-dimensional separations. The wakes of bodies with fixed separation points, i.e. a flat plate normal to the flow, is discussed before breaking the wake symmetry by introducing an angle-of-attack. It is shown that one of the key features are shear layer vortices produced behind the sharp edges. The generation of these vortices and their formation into von Kármán vortices are shown to be well-studied in cylinders and spheres, but that the formation of these in the wake of sharp-edged bodies has not been investigated to date.

2.2 Three-dimensional separations

2.2.1 The wake of ground vehicles

Automobiles are usually designed with focus given to features such as the cabin requirements, engines, safety standards, aesthetics and regulations regarding size; often with these concerns given higher priority than the aerodynamic performance. As such, vehicle aerodynamicists must usually work around the other constraints on the design. The aerodynamic considerations also vary depending on the intended application, for example, the aerodynamics of transport vans and race cars are different. Although there are large differences in ground vehicle aerodynamics, there are some common features. Firstly, all cars are bluff bodies in close ground proximity. Being bluff the drag on the car is usually dominated by pressure losses in the wake region, as opposed to skin friction losses. The fact that the body is in close proximity to the ground is shown to have a significant effect on the aerodynamics (Klemperer, 1922), see figure 2.1. Klemperer found that the drag of a streamlined shape increased by a factor of two when placed in ground proximity due to the breaking of symmetry with eventual separation on the upper surface. Secondly, the flow is complex: it is three-dimensional, comprises of turbulent boundary layers and wakes (figure 2.2), and often it is dominated by large separated regions containing longitudinal vortices.

The major goals of vehicle aerodynamics are four-fold. Firstly, and usually of prime importance, is the reduction of aerodynamic drag. This is usually driven by environmental or economic reasons due to the fuel consumption reductions that can be gained. While the amount of fuel savings from drag reductions vary between vehicles, for a mid-sized car the gain in fuel economy compared to the drag reduction is approximately 14% for urban driving and 46% for highway driving (Hucho, 1998) (that is, if the drag on the vehicle was reduced by 10%, the fuel consumption would drop by 4.6% when driving on the highway). Besides lower fuel consumption, low drag also results in better acceleration and an increase in the vehicle's top speed. The aerodynamic drag is discussed further in section 2.2.1.1.

Secondly, noise reduction. As vehicle speeds increase, the relative importance of aerodynamic noise is more significant than that of the other sources such as the engine, drive train and tires. Significant improvements in those areas have also made aerodynamic noise more noticeable in passenger cars, driving further development in this area. Acoustic wind tunnels with low ambient noise are used to investigate this issue.

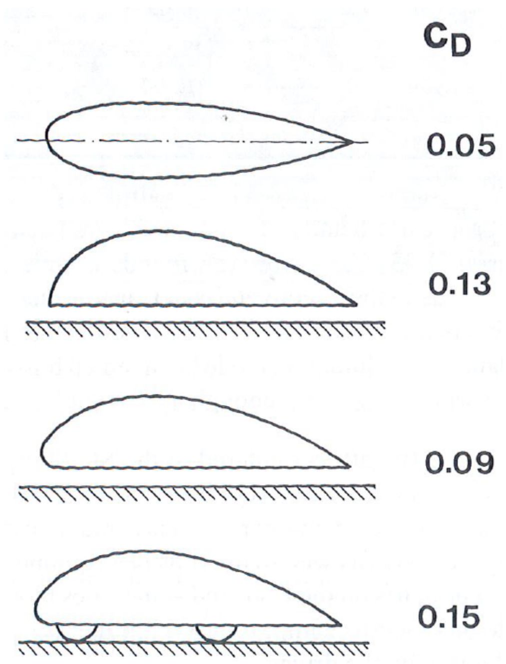

Figure 2.1: The effect of ground clearance on a streamlined body. The drag coefficient increases when the is placed near the ground plane due to separation off the top surface. A half body near the ground plane will have reduced drag when the sharp front edge is rounded, reducing separation. The addition of wheels increases the drag. Hucho (1998) after Klemperer (1922).

Figure 2.2: Turbulent flow inside the near wake of a car. Photo: Opel from Tropea *et al.* (2007).

Thirdly, lift reduction. Generally, a vehicle will produce lift due to the accelerated flow between the body and the ground surface. For an average consumer car, this is not necessarily a problem. For a race car, however, negative lift (down-force) is essential for cornering performance, as the side force generated by the tires increases with down-force.

Fourthly, stability. The flow around a vehicle is usually asymmetric. Side forces and fluctuating wind loads cause forces and moments which affect the vehicle's stability. These are more significant at high speeds and can noticeably affect the drivability of a vehicle and in some cases can be a safety concern. Additional concerns for vehicle aerodynamicists are the forces on body parts, soiling patterns, particulate deposit, and the interior flow systems.

The wake of ground vehicles is highly complex - it is three dimensional, contains steep pressure gradients, and both open and closed regions of separated flow. Body appendages such as mirrors and door handles, etc. cause closed regions of separated flow. The major separation, though, occurs at the truncated trailing edge of the roof (figure 2.3), leading to a large wake with low pressure. This separation is almost inevitable as the body length required to keep the flow attached is impractical except for extreme cases (such as land speed record attempts). This is considered a quasi-two-dimensional separation, but three-dimensional separations are also common. When the flow rolls over the slanted surfaces of a vehicle, conical vortices are formed. These occur primarily at the A and C pillars of a vehicle. They are energetic and can extend far behind the car (Bearman *et al.*, 1989).

2.2.1.1 Aerodynamic drag

For a car at highway speeds, the aerodynamic drag typically accounts for approximately 75% of the total resistance (Hucho, 1998). Given its importance, the reduction of drag is the main focus of vehicle aerodynamicists.

Drag is a function of four variables:

$$D = \frac{1}{2}\rho {U_\infty}^2 C_D A \tag{2.1}$$

1. ρ - the density of the fluid, is essentially constant for all vehicles, or at least is unchangeable by the engineer
2. U_∞ - the relative velocity of the vehicle to the air. This varies across different driving conditions.

(a) Smoke introduction upstream.

(b) Smoke introduced into the separated region.

Figure 2.3: Separation at trailing edge of the roof of a passenger vehicle. Photo from Volkswagen.

3. C_D - the drag coefficient. This is essentially a function of the shape of the body. Other factors such as the surface finish also play a minor role.

4. A - the frontal area, which is set by the size of the vehicle and usually out of the control of the aerodynamicist.

The only variable in equation 2.1 that can be altered by an aerodynamic engineer is the drag coefficient, and hence the importance of that number.

Aerodynamicists have improved car design, which has experienced a significant drop in drag. The reduction is due to several factors. Firstly, at the turn of the twentieth century, shapes were adapted from other disciplines such as ship-building and airplane manufacturing. These borrowed applications were usually unsuccessful given the differences in vehicle aerodynamics, and the lack of a real need for low drag coefficients in the early days when vehicles were slow, but the C_D still reduced when compared to the early box-like designs.

After the first world war the application of streamlining to vehicles improved as fluid mechanists applied their knowledge to the field. Tear-drop shaped vehicles were produced and drag coefficients of one-third that of contemporaries were realised (Hucho, 1998).

Thirdly, in the 1970s and 1980s (figure 2.4), detail optimisation became a popular tool. The methodology involves incrementally changing a design parameter (for example a radius on a corner) and measuring the drag on the entire car as a function of that radius. This technique, though time consuming, allowed for the optimisation of the entire car. Bearing in mind the other constraints on production vehicle design, it is no surprise that experimental vehicles have been manufactured with drag coefficients of half that of the present day production vehicle.

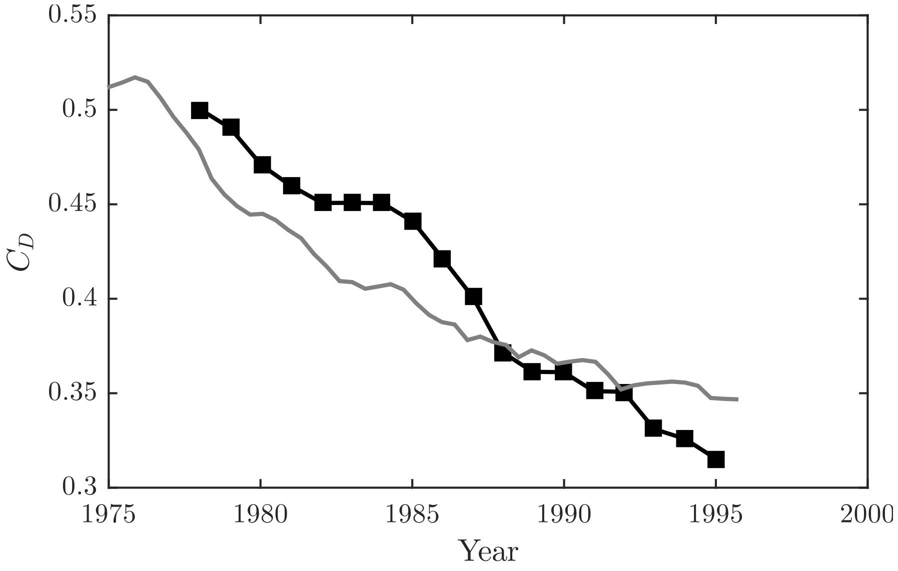

FIGURE 2.4: Drag coefficient of Chrysler (black) and sales-weighted drag coefficient of Ford series (gray) automobiles. Improvements in car design have resulted in a steady decrease in the drag coefficient of cars. Data reproduced from Hucho (1998).

The momentum equation can be written in a way that expresses the drag as three integrals (Onorato & Costelli, 1984):

$$C_D A = \int_S (1 - C_{P_{total}})\, dS - \int_S \left(1 - \frac{u}{U_\infty}\right)^2 dS + \int_S \left[\left(\frac{v}{U_\infty}\right)^2 + \left(\frac{w}{U_\infty}\right)^2\right] dS \qquad (2.2)$$

The drag can then be associated to these three parts. Firstly, the drop in stagnation pressure across the volume. Secondly, the streamwise velocity defect, and thirdly, the vortex drag. The vortex drag is substantial in vehicle aerodynamics due to the presence of longitudinal vortices. Onorato & Costelli (1984) performed wake traverses and found the local contribution to drag is highest in the presence of these vortices. The vortices exert a low pressure on the base of the vehicle due to the high axial flow through their cores.

2.2.2 The wake of Ahmed models

Given the great variety in shapes of ground vehicles, a simplified body is needed for the sake of consistent testing. If real car shapes, as opposed to simplified bodies were used, the results from any given experiment would be suitable only for the particular make and model tested, i.e., there would be no generality. During the second half of the twentieth century, several generalised aerodynamic shapes were created. These were designed to produce the bulk of the flow features of a real car, without being specific to any one model. One downside of such testing is that details such as mirrors, or even wheels, are often left out even though they have a major influence on the aerodynamics. For the study of the large, macro structures in the wake, however, these generalised bodies are suitable.

The oil crisis of the 1970s provided impetus for improving the aerodynamic analysis of vehicles. Drag reduction became a high priority and systematic investigations into the aerodynamic effects of vehicle geometry were researched in earnest. Janssen & Hucho (1974) were the earliest vehicle aerodynamicists to find a critical geometry in this field. They experimented on varying the rear slant angle of a hatch-back automobile and measured the resultant drag. They found that between 28° and 32° (relative to the horizontal) the separation point shifted from the rear of the roof to the rear of the vehicle (figure 2.5). When the flow separates fully, the drag was noted to be a minimum, which is counter to what is expected from aircraft aerodynamics where separation is avoided.

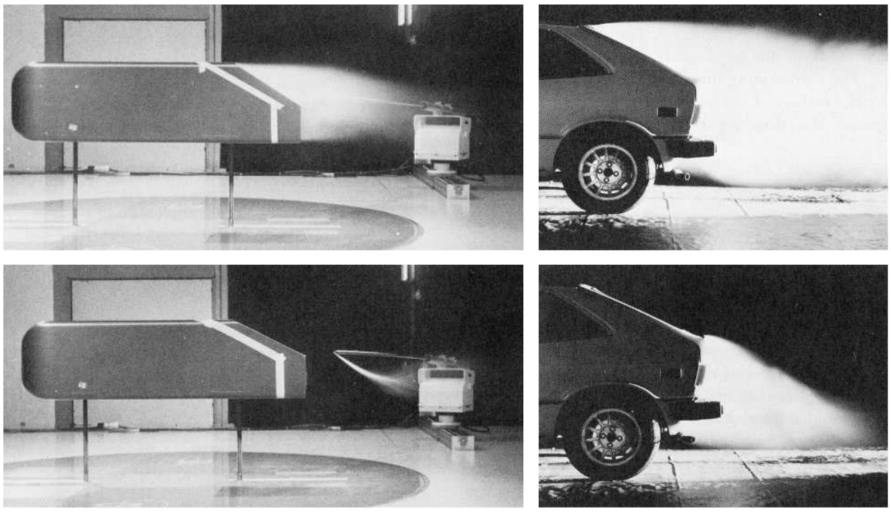

Figure 2.5: Simplified body (left, Morel (1978*b*)) and full scale vehicle (right, Hucho (1998)) in fully separated (top) and reattaching (bottom) flow states. After Pagliarella (2009).

Morel (1978*b*) continued this analysis and proposed that two distinct regimes existed. At high slant angles, the wake was quasi-axisymmetric and closed. Below the critical angle, he suggested the flow separates over the slant edges into two large vortices, noting their similarity to delta-wing flows (figure 2.25).

They suggest that the cause of the counter-intuitive observation regarding separated flows with decreased drag is that when the flow is completely separated the wake is relatively uniform (with low pressure), but when the flow is attached and three-dimensional, energy rich vortices cause low pressures at some points on the rear surface. These hypotheses were tested by wind tunnel experiments, confirming the existence of two strong vortices at angles below 27.5°. They measured pressure coefficients as low as -2 near the edge of the body, explaining the high drag in the partially-attached case.

The Ahmed body (Ahmed *et al.*, 1984) followed several years later, modifying the Morel body to match the sizes of vehicles at Volkswagen. This body has a rounded front end, a width-to-height aspect ratio of 1.35, and a slant at the rear end in a similar manner to a fastback vehicle (figure 3.7). This body has become the standard shape for simplified aerodynamic experiments.

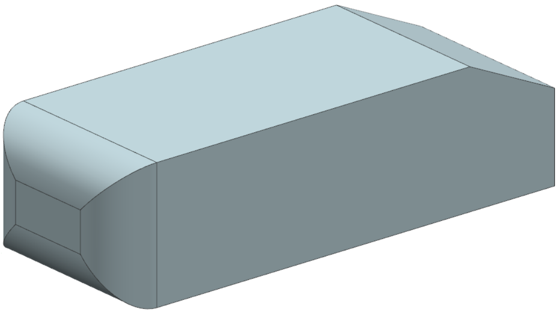

Figure 2.6: The Ahmed model as described in Ahmed *et al.* (1984). The body has length $1044mm$, width $389mm$ and height $288mm$. The rounded front end has radius of $100mm$ and the slant at the rear end is $222mm$ long regardless of the slant angle. Pictured is the 25° case.

2.2.2.1 The main flow structures

The initial work by Ahmed *et al.* (1984) identified three major structures in the wake (figure 2.7):

1. The A recirculation region that is formed as the flow separates at the top of the vertical back surface of the model
2. The B recirculation region that is formed due to the separation at the base of the model
3. The c-pillar vortices that form as the vorticity in the side boundary layers roll up over the slant edges

The largest structure in the wake are the c-pillar vortices. These vortices are so-named due to their formation at the third pillar, or “c-pillar”, of a sedan-type vehicle. The vortices are formed

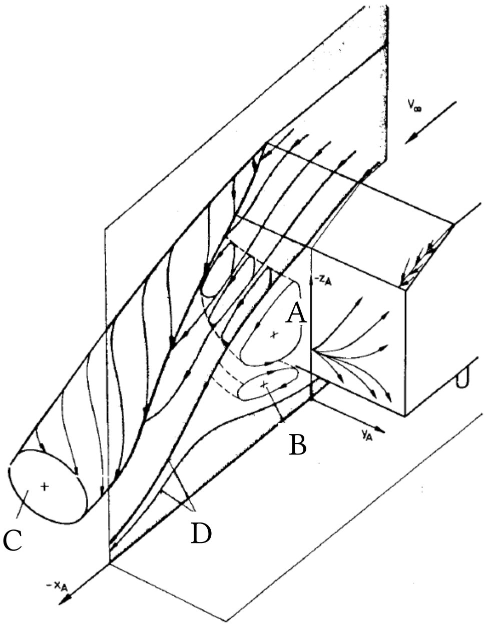

Figure 2.7: Structures in the wake of the Ahmed body after Ahmed *et al.* (1984).

from vorticity that is generated along the sides of the body. When this boundary layer reaches the angled slant it rolls up into two longitudinal vortices. The vortices are counter rotating, inducing a large downwash between them. These have been visualised in many experiments, for example, Vino *et al.* (2005) uses smoke visualisation to identify them (figure 2.8).

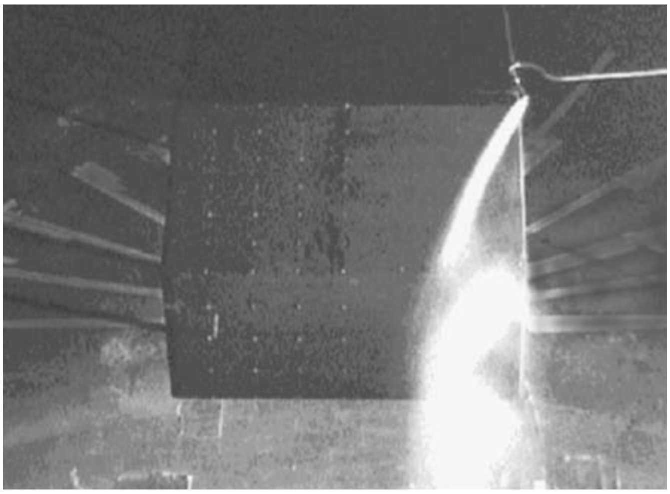

Figure 2.8: Smoke visualisation highlighting the c-pillar vortex in the wake of an Ahmed body. After Vino *et al.* (2005).

Spohn & Gilliéron (2002) present flow visualisation results to show the formation of the vortical structures in the near wake. The c-pillar vortices are shown to form with an adjacent counter-rotating vortex inside separation region E (note that this is separate to the secondary-vortex below and outboard of the c-pillar vortex). They suggest that the separation zone is more complex than that suggested in Ahmed *et al.* (1984), particularly noting the existence of attachment zone N_1 (figure 2.10) and a pair of foci in region E. Krajnović & Davidson (2005*b*) extends the near-wake work with the suggestion that there are in fact three pairs of longitudinal vortices, adding a pair rotating the same way as the c-pillar vortices and located further inboard than the secondary vortex.

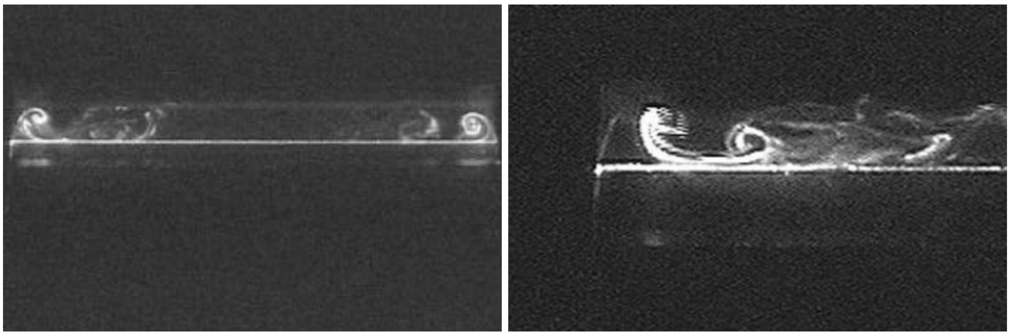

FIGURE 2.9: Flow visualisation showing the roll-up of the c-pillar vortex (top) and the counter-rotating vortex inside separation bubble E (over the slant). After Spohn & Gilliéron (2002).

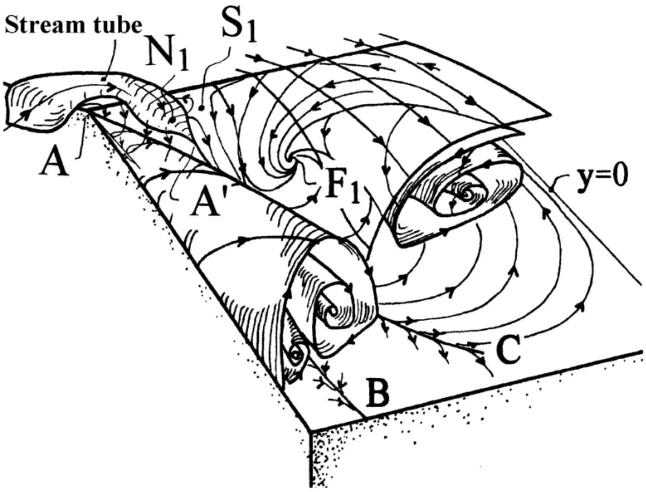

FIGURE 2.10: Proposed topology of the separation zone. After Spohn & Gilliéron (2002).

While much attention is rightly given to the c-pillar vortices, the nature of the A and B recirculation regions is debated in the literature. Some studies (e.g., Beaudoin & Aider, 2008; Beaudoin *et al.*, 2004; Joseph *et al.*, 2011; Drouin *et al.*, 2002; Wang *et al.*, 2013; Zhang *et al.*, 2015) interpret these regions as a torus (figure 2.11), similar to the toroidal wake of a cube or a square-backed Ahmed model (Gilliéron & Kourta, 2009; Grandemange *et al.*, 2013) as in figure 2.12, while others interpret them as two horseshoe vortices (e.g., Ahmed *et al.*, 1984; Gant, 2002). Krajnović & Davidson (2005*b*) state both that the vortex cores form a “ring-like vortex” and that they are two horse-shoe vortices with A tilting downstream and B tilting vertically (figure 2.13). Either way they reject the proposal of Ahmed *et al.* (1984) that these two vortices are situated above each other with trailing legs.

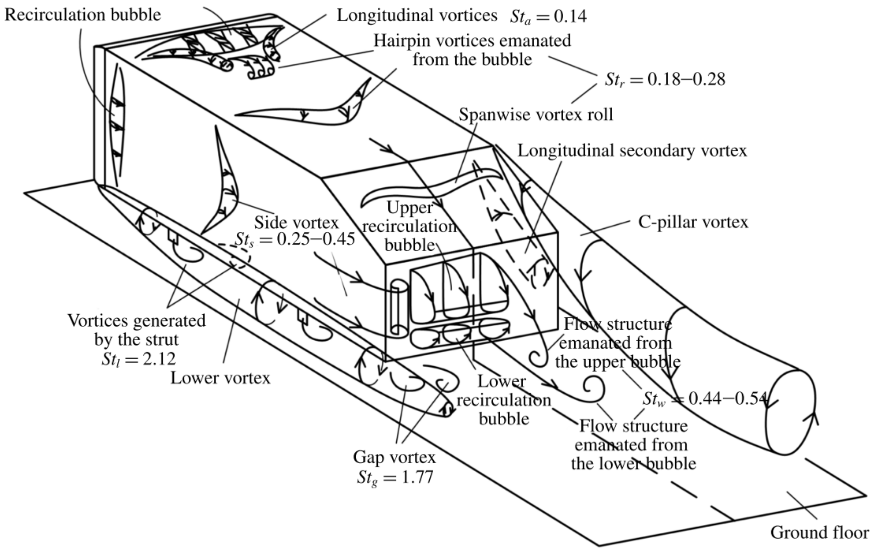

Figure 2.11: Schematic from Zhang *et al.* (2015) describing the macro structures and shedding frequencies around an Ahmed model.

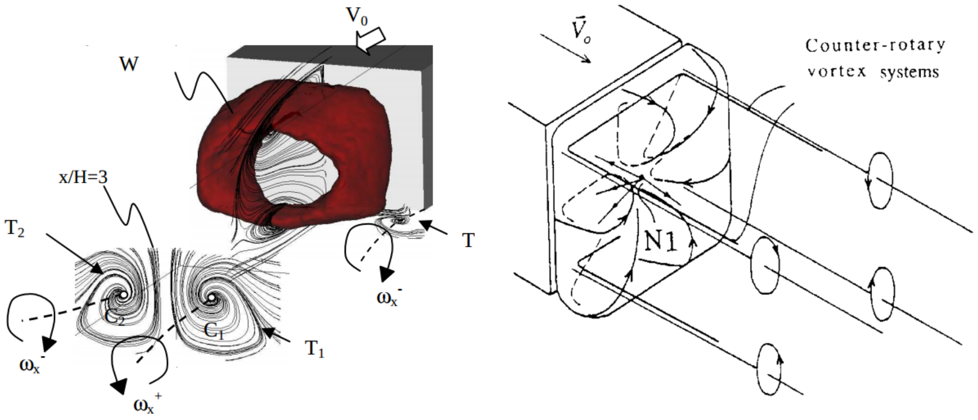

Figure 2.12: (a) Wake of the square-back bluff body showing the recirculation toroid W, the longitudinal vortices T_1 and T_2, and the corner vortices T. (b) Schematic of wake. From Rouméas *et al.* (2009) and Gilliéron *et al.* (1999) respectively.

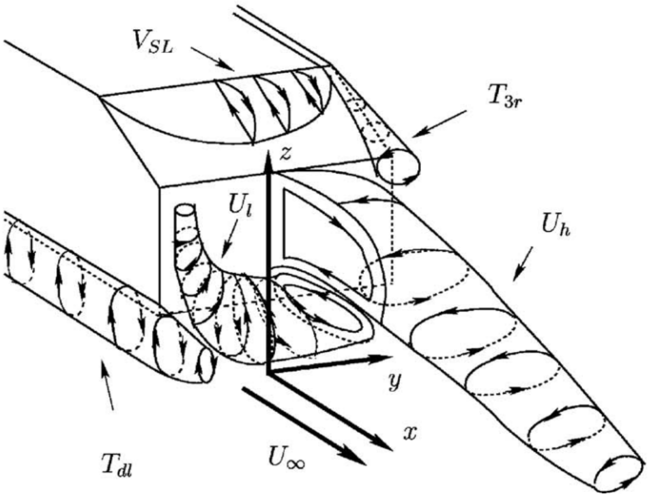

FIGURE 2.13: Schematic from Krajnović & Davidson (2005*b*) showing the A vortex tilting downstream into a longitudinal structure, while the B vortex tilts upwards along the sides of the model.

2.2.2.2 The effect of slant angle

The wake has been shown to be dependent on the slant angle. It is agreed (eg. Ahmed *et al.*, 1984; Sims-Williams & Dominy, 1998; Bayraktar *et al.*, 2001; Spohn & Gilliéron, 2002; Lienhart & Becker, 2003; Vino *et al.*, 2005) that there are three fundamental regimes (figure 2.14):

1. $\boldsymbol{\alpha \leq 12^\circ}$: In this regime, the flow remains attached over the slant angle so separation occurs across the entire vertical base of the model. The flow is essentially two-dimensional, resulting in low drag.

2. $\boldsymbol{12^\circ \leq \alpha \leq 30^\circ}$: In this regime, separation occurs at the start of the slant. The flow reattaches before the slant ends, and then separates again at the vertical base. The flow also separates over the slant angle, causing the formation of the c-pillar vortices. This results in a three-dimensional flow, and high drag that increases with slant angle (figure 2.15). This increase is due to the strengthening of the trailing vortices which exert low pressure behind the body. These reach maximum strength at 30°. The induced downwash between the vortices aids the reattachment of the flow. The drag also increases because the size of the separated region over the slant becomes larger as the angle is increased.

3. $\boldsymbol{\alpha \geq 30^\circ}$: Past 30°, the flow remains separated over the slant region (figure 2.16). Whilst the c-pillar vortices still exist, they are much weaker, and the flow is more two-dimensional. The drag force drops in this regime. Vino *et al.* (2005) showed that in this regime the separated region above the slant and the A vortex combine.

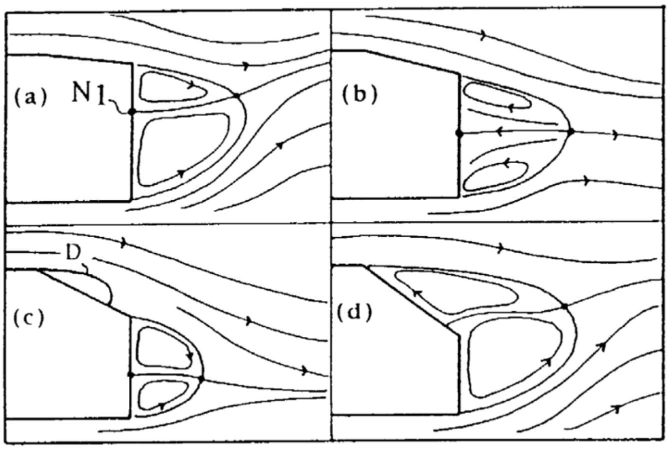

Figure 2.14: The various regimes according to the slant angle of the Ahmed model. After Gilliéron *et al.* (1999). The first two images correspond to $\alpha \leq 12°$; c) is $12° \leq \alpha \leq 30°$; and d) is $\alpha \geq 30°$.

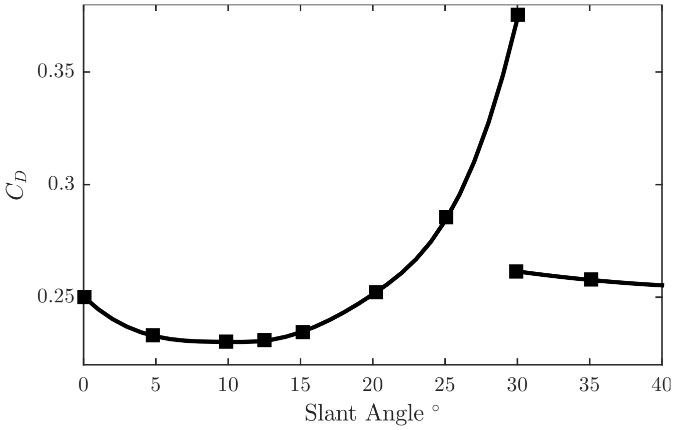

Figure 2.15: The effect of the slant angle on the drag coefficient of the Ahmed body. Data from Ahmed *et al.* (1984).

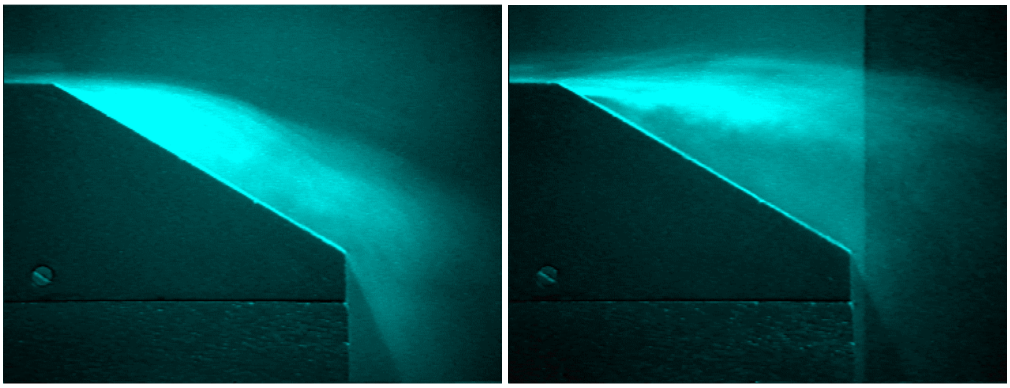

Figure 2.16: Flow visualisation from Sims-Williams & Dominy (1998) showing the two flow conditions at a slant angle of 30°. The flow was switched between the two cases by using a plate to guide the flow into the separated state, where it would remain for several minutes.

2.2.2.3 Effect of Reynolds number

Low-speed water tunnels allow for more detailed wake measurements to be made than are possible in high-speed wind tunnels. Some downsides to water tunnel testing are that the scale is generally limited to smaller models and the speed is lower than that attainable in wind tunnels. These two factors combine to lower the maximum Reynolds number attainable by roughly two orders of magnitude, even when accounting for the water's kinematic viscosity being a tenth that of air.

One concern that is raised is the validity of low-speed water tunnel testing given its low Reynolds number. This question must be investigated for each situation. Generally, the Reynolds number problem manifests itself on radiused corners. At low Reynolds numbers, the flow separates at the radius, which can cause an increase in drag. As the Reynolds number increases, the flow reattaches onto the radius, reducing the drag. With a further increase in the Reynolds number, the separation is eventually removed.

For the case of the Ahmed body, there are, except at the front end, sharp edges at all separation points. This aids in Reynolds number insensitivity as the separation points should not vary with Reynolds number. Spohn & Gilliéron (2002) use flow visualisation at a Reynolds number of 3×10^4 to show that the wake structures are similar to studies at $Re \sim \mathcal{O}10^6$.

Vino *et al.* (2005) showed that there were some effects on the aerodynamics with Reynolds number. It was shown that there was a small (15%) decrease in the drag coefficient between a Reynolds number of 0.76×10^6 and 2.5×10^6, where the drag is a minimum, before rising again. The Reynolds number range tested in that study was up to 2.83×10^6. They showed that the Reynolds number effects were not due to boundary layer transition by tripping the flow for all Reynolds numbers and noting that there was no significant difference in the results, showing there to be a turbulent boundary layer for all Reynolds numbers. They decline to comment on the reasons for the drag increase above 2.5×10^6.

2.2.2.4 Aspect ratio effects

Morel (1978*a*) hypothesised that the aspect ratio of the slanted surface might be quite important as it "establishes the relative proximity of the two edge vortices which drive the fluid mechanics" of the second (reattaching) regime. He also suggests, though, that the aspect ratio effect is mainly due to the c-pillar vortices influencing less of the base area as the aspect ratio increases.

Since then, however, the aspect ratio has not received much attention. Johnson *et al.* (2004) performed numerical simulations at a Reynolds number of 2.86×10^6 investigating the effect of aspect ratio on the drag of the Ahmed model. They found that the drag coefficient was roughly constant for all bodies with narrower aspect ratios than 1.8, but wider bodies experienced a lower drag. They suggest that the effect of increasing aspect ratio beyond the critical value is the same as increasing the slant angle beyond 30°. They also noted that the strength of the c-pillar vortices was independent of aspect ratio (at least for a slant angle of 22°).

Okada *et al.* (2005), however, in experimental results suggested that the c-pillar vortices were weaker when the aspect ratio of the rear slant was increased from 1.75 to 2.19. They proposed that the downwash created between the two vortices was not sufficient to promote reattachment when the aspect ratio is above a critical value.

Williams *et al.* (1999) from Ford Motor Co. experimentally investigated the effect of frontal aspect ratio on rounded rectangular boxes to simulate van configurations. They found that an increase in aspect ratio caused a linear drop in the drag coefficient. Whilst this flow would also have trailing vortices, their relative dominance of them would be minor compared to fast-back models with slanted trailing edges.

In recent work, Corallo *et al.* (2015) numerically studied the effects of the aspect ratio on the lift and drag. They found that a critical aspect ratio exists for body widths at least 10% narrower than the standard model. For bodies wider than this, a 15% drop in drag and an almost complete removal of lift occurred. They attributed this to the change in separation regimes at the rear end. They also noted an increase in drag coefficient with aspect ratio, either side of the critical point, explaining that it is due to the non-linear scaling of frontal area near the stagnation point with body width.

2.2.3 Wake dynamics

As shown, a large quantity of literature, both in experimental and computational, has been produced on the effect that slant angle has on the wake and hence the body forces. The majority of these studies are focused on the time-averaged wake, which is helpful to an extent, but can be deceptive because the time-averaged flow can hide flow features or produce unphysical results as in figure 2.17 (Gilhome, 2002; Dallman & Schewe, 1987). Therefore, studying the instantaneous flow is important in understanding the physical mechanisms at play.

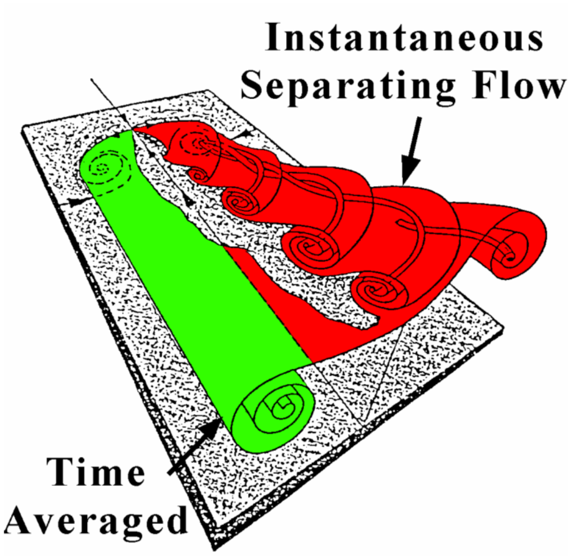

Figure 2.17: The deception of using time-averaged results when analysing a wake. Green represents the time-averaged flow and red is the instantaneous flow. After Gilhome (2002) and Dallman & Schewe (1987).

Many papers have studied the dynamics of various parts of the wake of Ahmed models. These are summarised in table 2.1 where the reported Strouhal number has been converted to use the same length scale for comparison between papers. It is noted that there is a surprising spread in the data between papers. For example, when considering the Strouhal number of the shear layer, numbers from 0.08 up to 22.72 are reported.

Table 2.1: Previous studies on wake dynamics. The Strouhal and Reynolds numbers use the square-root of the frontal area as the length scale.

Study	Technique	Reynolds number	α_S	Structure	Strouhal
Vino *et al.* (2005)	Surface pressure	$5.5 - 7.7 \times 10^5$	30°	Base	0.39
Krajnović & Davidson (2005*a*)	LES	2.32×10^5	25°	Slant	0.174 & 0.302
Minguez *et al.* (2008)	LES	8.98×10^5	25°	Front separation	0.174
				Slant	0.314
				Behind base	0.488
Thacker *et al.* (2010)	Hot-wire & PIV	7.05×10^5	25°	Slant	0.22
Thacker *et al.* (2013)	Hot-wire, surface pressure, & PIV	7.05×10^5	25°	Near slant	0.227
				Above slant	1.30
				Shear layer	22.72 & 5.16
Joseph *et al.* (2012)	Wake pressure	4.48×10^5	25°	Shear layer	0.356
		6.73×10^5			0.499
		$4.48 - 6.73 \times 10^5$		Near wake	0.535
Joseph *et al.* (2013)					4.27
Mcnally *et al.* (2012)	Surface pressure	3.42×10^5	25°	Base	0.404
Tunay *et al.* (2014)	PIV	1.74×10^4	25°	Wake velocity	0.36
			30°		0.256 & 0.209
			35°		0.256 & 0.093
Volpe *et al.* (2014)	Pressure & PIV	6.02×10^5	0°	Shear layer	0.08
				Base sides	0.136
Zhang *et al.* (2014)	Hot-wire	6.59×10^4	25°	Front separation	0.196 & 0.140
				c-pillar	0.265
				A & B shedding	0.442

Some notable features from this literature review are included below. The studies cited here were chosen as they are well regarded in other literature and they provide some physical explanations for the variations they see. Both Berger *et al.* (1990) (for a sphere) and Duell & George (1999) (behind a square-backed bluff body) noticed a pumping of the base pressure region at low frequency. They suggest this is due to the pairing of shear layer vortices which they observed at the sides of the body. For a fastback style vehicle, however, the side-shedding is suppressed, as would be this mechanism.

Regarding the hatch-back shape, Sims-Williams *et al.* (2001) studied the wake, finding unsteadiness to be much less coherent than in two-dimensional cases. They commented that Strouhal numbers were inconsistent between two testing tunnels. at Strouhal numbers of 0.119 and 0.32. They related this to anti-symmetric oscillation in the strength of the c-pillar vortices and a symmetric strength oscillation of the rear-pillar vortices respectively. They proposed that the shedding from the underbody interacted with the downwash of the c-pillar vortices to produce these fluctuations.

Lienhart & Pêgo (2012) found a distinct spectral peak corresponding to a Strouhal number of approximately $\mathrm{St} = 0.51$, higher than that found by Sims-Williams *et al.*. They concluded that this feature was due to the periodic shedding of vortices emanating from upstream, however, an attempt to identify the structures associated with this frequency was not made.

Vino *et al.* (2005) shows alternate shedding of A and B structures at $\mathrm{St} = 0.39$ analogously to von Kármán vortex shedding behind other bluff bodies. They base this reasoning on the fact that pressure probes on the vertical base contain the same frequency but 180° out of phase.

Thacker *et al.* (2010) used PIV to analyse the flow over the backlight using the Proper Orthogonal Decomposition (POD). This study is relevant as it is one of the few that use observations over a whole field at once (as opposed to wake traverses with velocity probes) to explain the dynamics. They show that the first mode of the POD is associated with a flapping of the slant recirculation region. This is explained as not vortex shedding due to there being no correlation between the first two modes. This analysis reveals that the recirculation region is not always attached (figure 2.18), but rather flaps at $\mathrm{St} = 0.22$.

The purpose of this review into the dynamics was to show that there is not yet a coherent picture of how the macro structures vary in time. Whilst specific papers are able to extract single points of information, there is no consistency between them. The work of Thacker *et al.* begins to show a more suitable way to analyse the wake, beginning with planar PIV fields and investigating the dynamics in the whole vector field.

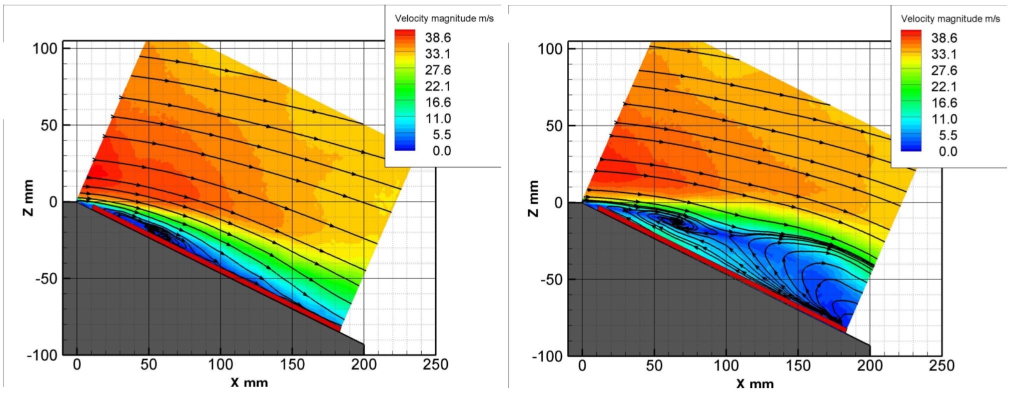

FIGURE 2.18: Conditionally averaged PIV frames based on the coefficient of the POD first mode. The reattachment is shown to be intermittent and this region flaps at a frequency of St $= 0.22$. From Thacker *et al.* (2010).

2.2.3.1 Bistability

In recent work, Grandemange *et al.* (2013) found that the wake behind the square-back Ahmed model exhibits evidence of a lateral bistability. While this exact phenomenon is not expected in the Ahmed body wake due to the strong c-pillar vortices, it is noteworthy due to the fact that bluff bodies (this bistability is also noticed in double backward-facing steps (Herry *et al.*, 2011)) tend to prefer an asymmetrical wake. This feature is addressed in section 6.4 and hence a brief review is given here.

They present data showing the recirculation region shifts between two preferred asymmetric positions, which, over a long time-scale produce a symmetric wake in the time-averaged sense. This was shown to occur only above a critical ground clearance of 0.07. Figure 2.19 shows that there is a preferred vertical (z) position of the momentum barycentre, but two different horizontal (y) positions.

Volpe *et al.* (2015) reported the same bistability and using PIV results. Figure 2.20 (a) shows the long-time canonical average, showing asymmetry because one mode exists for more instances than the other. The average of the two phases, shown in figure 2.20 (d), shows a much more symmetric wake.

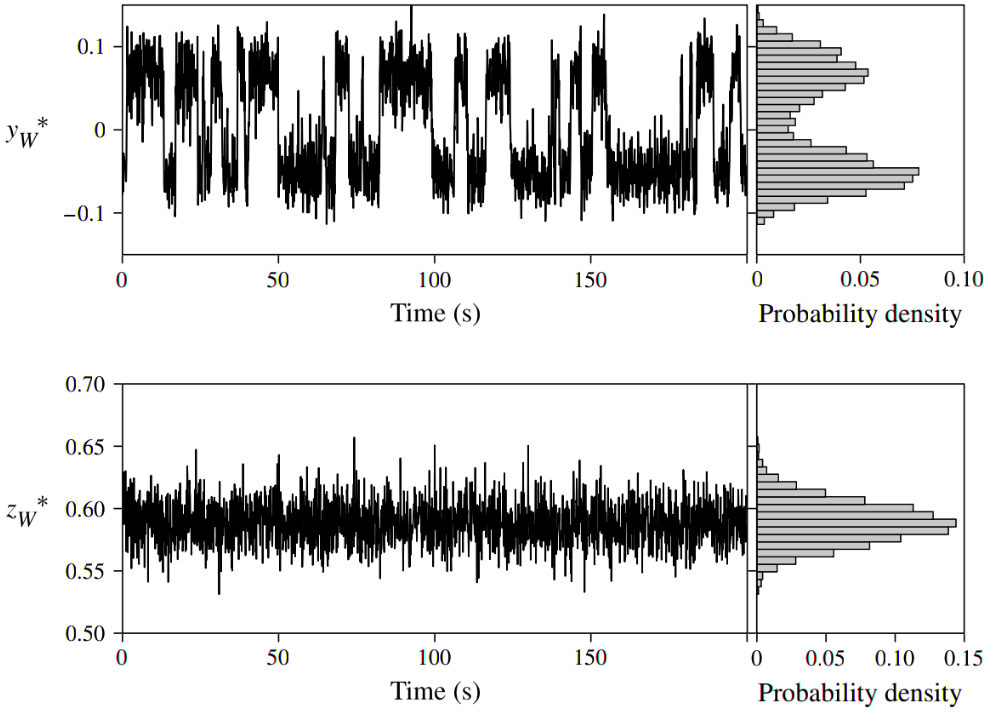

FIGURE 2.19: Time evolution of the barycentre of momentum deficit in the y-direction (a) and the z-direction (b) with associated probability distributions. Grandemange *et al.* (2013).

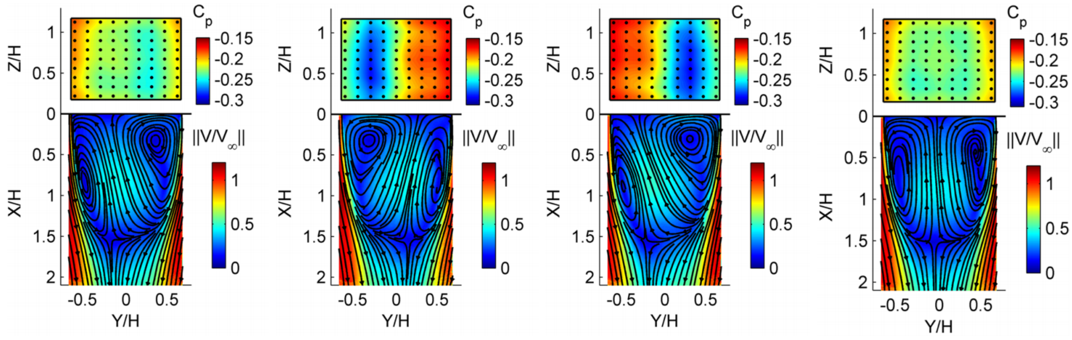

(a) Canonical average

(b) Conditional average, phase L

(c) Conditional average, phase R

(d) Average of L and R

FIGURE 2.20: (top) Pressure on the back surface of the square-back Ahmed model. (bottom) Velocity field at the mid-height plane. Volpe *et al.* (2015)

2.2.4 Analogous Flows

2.2.4.1 Backward facing step

An analogous flow to that over the roof of a vehicle before a sharp angle is that of a backward facing step. The boundary layer on the top surface separates at the step location before reattaching at some point downstream. This location varies due to the flapping of the shear layer (Rajasekaran, 2011). Between the recirculating flow in the separation bubble and the freestream flow above, a strong shear is present. This can produces shear layer vortice, which merge into coherent structures. These widen the shear layer and are eventually shed downstream after reattachment.

The flow is shown to be a function of the step aspect ratio. For an infinite width step, the wake is two-dimensional, but with finite span, the wake becomes three-dimensional due to the vortices developing from the sides of the step. de Brederode & Bradshaw (1972) found that the flow remained two-dimensional for aspect ratios larger than 10. For low aspect-ratio flows, the reattachment length onto the ground plane is reduced (Lim *et al.*, 1990) as flow from over the step sides impinges onto the ground plane.

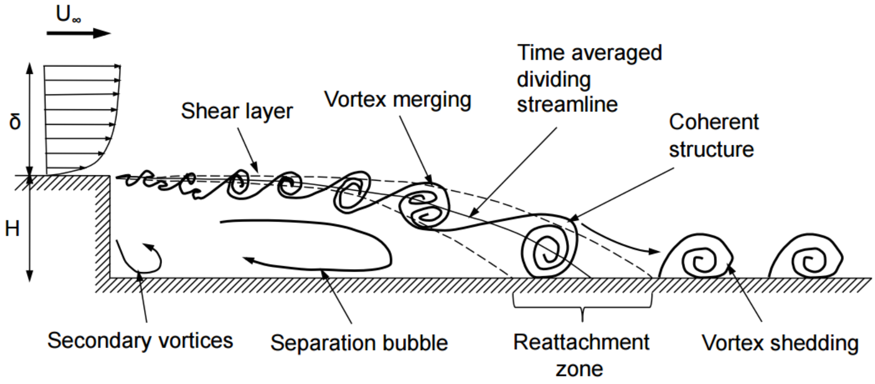

FIGURE 2.21: Key features of flow over a backward facing step. Rajasekaran (2011).

2.2.4.2 Finite wings and plates

A wing produces lift because the pressure above the wing is lower than that below the wing. One byproduct of this is that the air under the wing tends to curl around the ends of the wing (figure 2.22), driven by the pressure imbalance. These vortices induce a downwash between them, leading to an effective reduction in the angle-of-attack of the wing, hence reducing the lift. This change in angle-of-attack also tilts the lift vector downstream, effectively increasing the drag. This component of drag is referred to as induced drag.

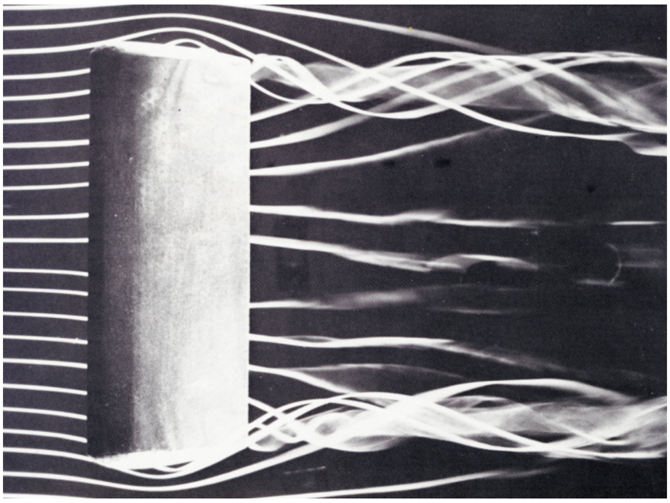

FIGURE 2.22: Smoke visualisation of the three-dimensional effects of finite aspect ratio wings. The wing-tip vortices are shown. Van Dyke (1982).

One of the effects of reducing aspect ratio is that the end effects become more important in the overall wake. Huang *et al.* (2015)[1] showed that even for a stalled trapezoidal plate, increasing the taper angle (and hence strengthening the vortices) caused the flow to reattach. Additionally, they showed that increasing the aspect ratio can cause a steady, attached flow to become separated and turbulent (figure 2.23).

(a) $\Lambda = 20^\circ$, AR = 2 (b) $\Lambda = 30^\circ$, AR = 2 (c) $\Lambda = 20^\circ$, AR = 4

FIGURE 2.23: Wake behind trapezoidal plates at varying taper angles and aspect ratios. All plates are inclined at 30°. Huang *et al.* (2015).

Taira & Colonius (2009) showed that at low Reynolds number ($Re = 300$), the flow over a two dimensional plate is steady for angles-of-attack less than 15°, becoming periodic for angles higher than that. As the aspect ratio dropped, the flow was shown to be steady for much higher angles, even up to 30° at aspect ratio 1.

---

[1] This study was undertaken by the author, though is not included in this thesis.

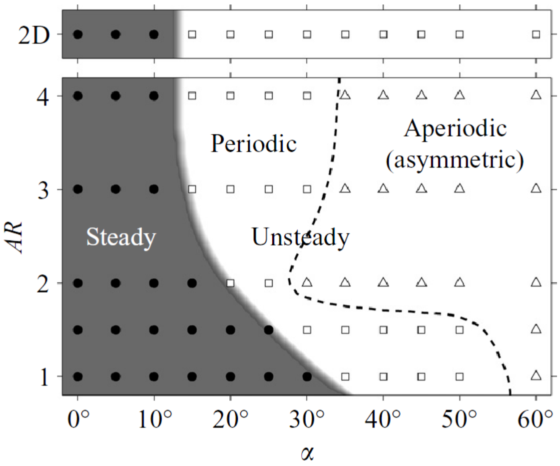

Figure 2.24: Parameter map showing the combined effect of aspect ratio and angle-of-attack on the wake dynamics of a rectangular plate. Low aspect ratios are shown to stabilise the flow even at high angles-of-attack. Taira & Colonius (2009).

2.2.4.3 Delta wing

Vortices are essential for the operation of delta wings. They are again formed by the pressure difference between the under wing (high pressure) and above (low pressure). As the flow is drawn over the swept leading edges, they curl over into strong vortices. Below these primary vortices exist secondary vortices. The pressure in the cores of the vortices is low, aiding the lift generation by such a wing, and allowing the stall angle to increase (35° for a 60° swept delta wing Lawford (1964)).

After stall, the vortices on a delta wing breakdown, or burst (Werle, 1973; Peckham & Atkinson, 1957; Elle, 1958) When the vortex does breakdown, the lift of the wing decreases and the flow becomes unstable, buffeting the wing Anderson (2007).

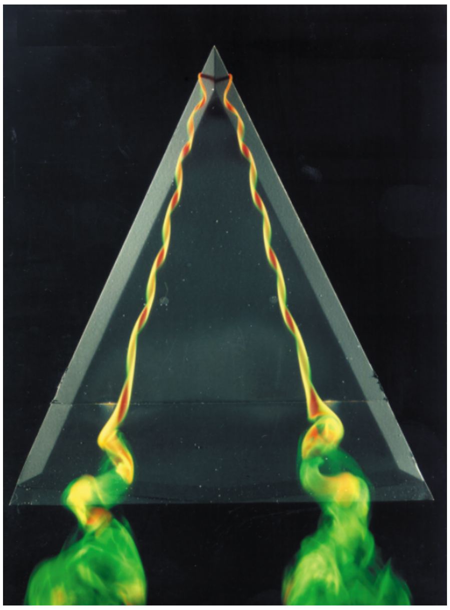

FIGURE 2.25: Leading edge vortex breakdown over a delta wing. Delery (2011).

2.3 Quasi-two-dimensional separations

Two-dimensional separations are much better understood than three-dimensional ones. When a boundary layer developing along a surface under an adverse pressure gradient (pressure increasing in the streamwise direction) develops to the point where the velocity gradient reaches zero, the flow separates from the surface (figure 2.26). This reversed boundary layer causes the primary flow to separate from the surface to form recirculating flow (reversed flow under the shear layer). This separated region must eventually close, either on the body surface itself or downstream in the wake. The first case is usually referred to as a separation bubble. Often such flows exhibit turbulent structures (figure 2.27).

2.3.1 The wake of circular cylinders

The canonical body in the study of bluff body fluid dynamics is the circular cylinder. Before the survey of literature in this area begins, two important concepts must be introduced. One of the most significant early works in understanding the wake of this body was that presented by von Karman & Rubach (1912), analyzing the stability of the vortex street in the wake of the cylinder. The vortices in such wakes are named von Kármán vortices in his honour.

The Strouhal number, named after Vincenc Strouhal, who investigated wires singing in the wind and noted that the frequency was linearly dependent on the wind velocity. His dimensional analysis led to the description of the Strouhal number:

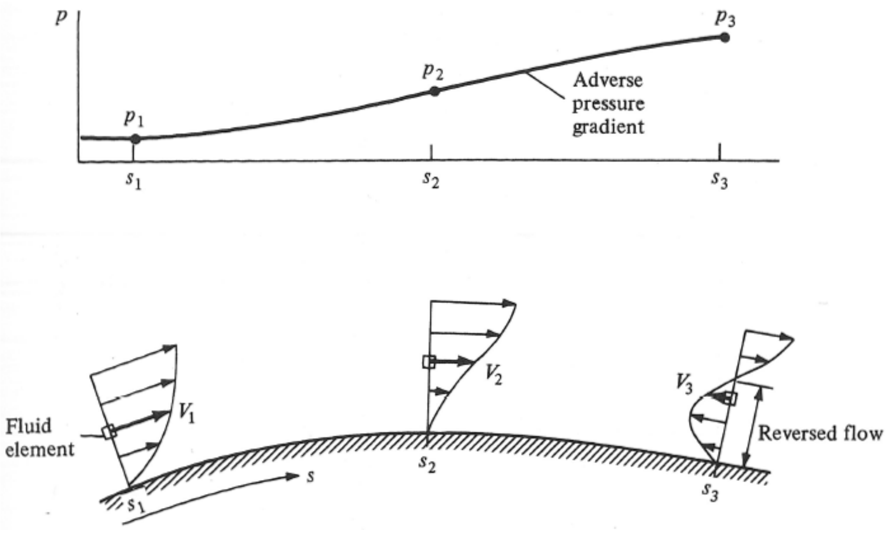

Figure 2.26: Separated flow induced by an adverse pressure gradient. Flow separation occurs somewhere between points 2 and 3. From Anderson (2007).

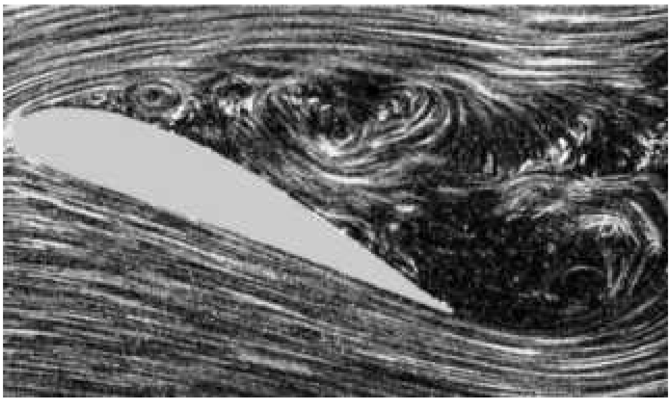

Figure 2.27: Streaklines past a stalled airfoil showing separation of the flow away from the body and the formation of large eddies in the wake. Photo courtesy Jagannath.

$$St = \frac{f \times L}{U_\infty} \tag{2.3}$$

The wake of the circular cylinder has been seen to contain three major transitions (plus numerous more at higher Reynolds number) moving the flow through regimes of creeping, separated, shedding, and three-dimensional shedding. The details are taken from the review article by Williamson (1996). The transitions progress through Reynolds number as described by equation 2.4:

$$Re = \frac{\rho \times D \times U_\infty}{\mu} \tag{2.4}$$

Whilst these particular transitions are of low relevance to this research, they are presented here as they reveal key details of the wake and its formation, and some of the ideas here are developed further below.

Creeping flow $Re < 5$

At these Reynolds numbers there is no separation on the cylinder and the flow is steady.

Laminar steady regime $5 < Re < 49$

Separation occurs close to $Re = 5$ with two steady, symmetric vortices form in the wake. The length of these recirculation regions grows with increasing Reynolds number (Taneda, 1956; Gerrard, 1978; Dennis & Chang, 1970) and the base pressure drops (Thom, 1933).

Laminar vortex shedding $49 < Re < 194$

Above a Reynolds number of 49, the wake instability (a manifestation of the Hopf bifurcation) causes the wake to oscillate as vortices are shed periodically from alternate sides. Gerrard (1966) suggests that the periodic shedding stems from the interaction between the two shear layers. The vortices grow independently (being fed by the corresponding shear layer) until one of them can draw the opposite shear layer across the wake. As this vorticity is oppositely signed, it cuts off the original vortex from the shear layer. This free vortex now moves downstream with the freestream velocity. The shear layer that cut off the free vortex now grows to be the dominant vortex, and the whole procedure is symmetrically repeated.

The shedding is two-dimensional in the sense that it does not vary in the axial direction. There is still a time-averaged recirculation region and the base pressure drops.

Three-dimensional wake transition $190 < Re$

Here the wake undergoes a transition into a three-dimensional turbulent wake. Grant (1958) attributed this to counter-rotating streamwise vortices. Wu *et al.* (1994) showed that these vortices are superimposed on the vortex sheet, wrapping around the Strouhal vortices.

2.3.2 The shear layer

In his famous paper, Reynolds (1883) described an experiment where two fluids of different density were placed in a tube. When the tube was inclined, a shear between the two layers was generated. When the shear was high enough, waves formed between the two fluids. As the shear increased, the waves eventually curled over and formed fully turbulent mixing.

What Reynolds was observing here is the Kelvin-Helmholtz instability manifesting itself through the creation of shear layer vortices, which are much smaller than the von Kármán vortices. It has since been shown that these shear layer vortices form only above a certain Reynolds number which ranges from 1000-3000 depending on the study in question (Wu *et al.*, 1996) - this suggests that the onset Reynolds number could be a function of the background noise in the test facility.

Winant & Browand (1974) studied the pairing of shear layer vortices in a mixing layer. They noted the development started with a small wave formed by the initial instability (either from external forcing or background noise). These waves grow into discrete vortices as they travel downstream. These vortices interact by rolling around each other and eventually pair (also Grinstein *et al.* (1995)). Because the pairing is driven by small variations in the strength or spacing of the vortices, the pairing of such vortices does not always occur at the same location, nor do all vortices pair. By forcing the initial instability at a constant frequency (rather than the variable background noise), the row of shear layer vortices are more evenly spaced, resulting in a decrease of pairing and a delay to the onset of a fully turbulent wake.

Grinstein *et al.* (1995) investigated the shear layer formation in a jet, where a shear layer must arise due to the velocity difference between the natural flow and the jet. As these vortices move downstream and react with each other, the vorticity is spread, and the core of the jet disappears. Contrary to the findings of Winant & Browand (1974), Grinstein *et al.* found that the vortices merge with each other at fixed locations of $2D$ and $4D$.

Ho & Huang (1982) and Huang & Ho (1990) perturbed a shear flow at a range of frequencies. They noted that the shear layer vortices quantized (figure 2.29), that is, an integer number of vortices merge, according to which subharmonic of the fundamental frequency is used in the forcing. In Ho & Huang (1982), they describe ‘collective interaction’, where a large (ten or more) number of shear layer vortices coalesce. They found that this was only the case when forcing the mixing layer at high levels.

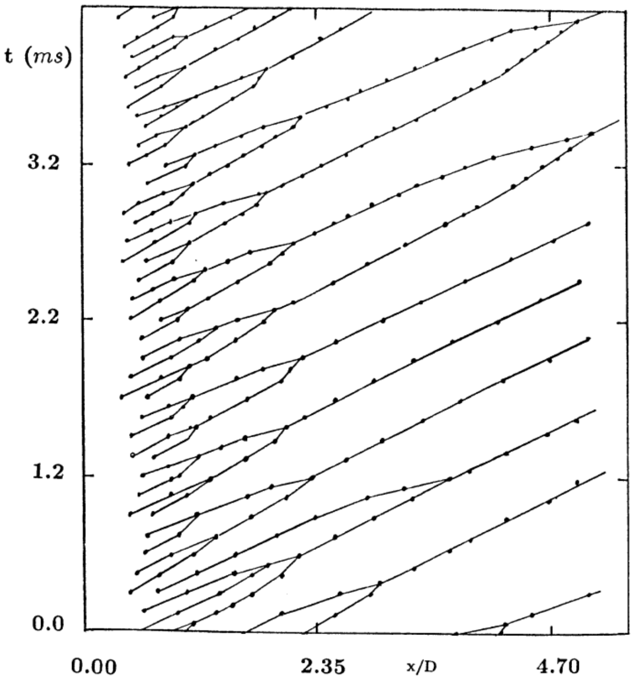

Figure 2.28: Vortex history for Kelvin-Helmholtz vortices from a jet. (after Grinstein *et al.* (1995)).

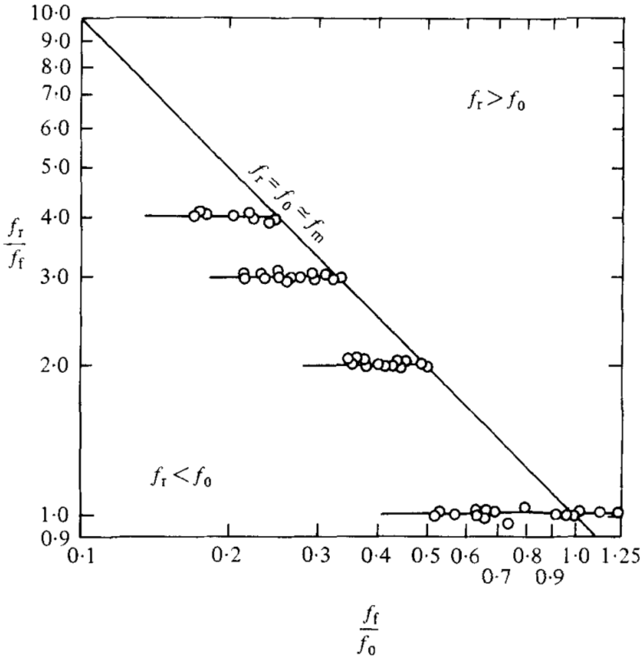

Figure 2.29: Data from Ho & Huang (1982) showing the mode diagram of a plane mixing layer. The ordinate is the ratio of the response frequency to the forcing frequency, and the abscissa is the ratio between the forcing frequency and the most amplified frequency.

They explain that the superposition of the forcing frequency $M \times f_0$ onto the fundamental frequency f_o causes a lateral spacing of the M shear layer vortices per fundamental cycle. Since the vortices are in a shear layer, there is a velocity gradient, slowing down the shear layer vortex that is furthest downstream, and speeding up that vortex which is closest. When the vortex cores are aligned, merging results from mutual induction.

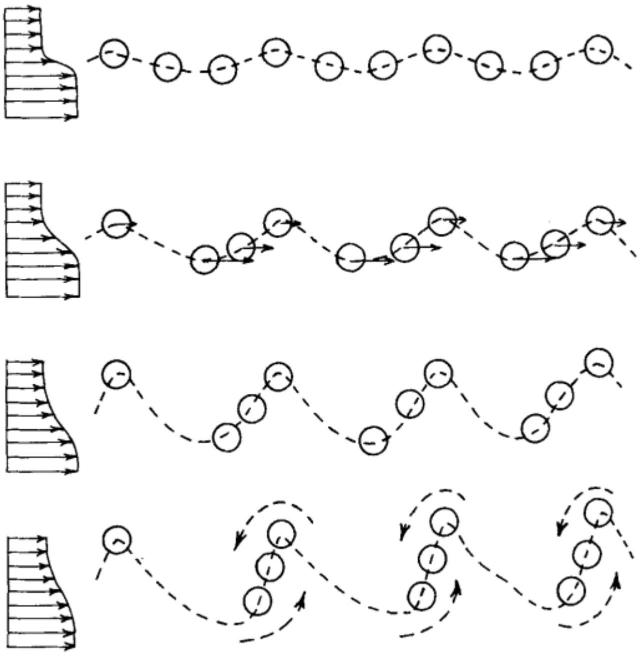

Figure 2.30: Schematic of subharmonic vortex merging (after Ho & Huang (1982)).

2.3.3 von Kármán vortex formation

In the wakes of bluff bodies, the shear layer vortices are observable only in the near wake, but their vorticity is advected downstream through the von Kármán vortices. The shedding of von Kármán vortices results from the interactions of the two separated shear layers (Gerrard, 1966). The nature of this formation has been well studied with respect to the circular cylinder, though with some aspects there is no real consensus on the issue.

Regarding the quantification of how the vorticity from the shear layer is moved downstream through the von Kármán vortices, several studies are outlined below, mostly for the circular cylinder case. A linear stability analysis on a perturbed shear-layer, as performed by Michalke (1965), suggests that the shear layer oscillation frequency should scale with the ratio of the freestream velocity to the momentum thickness of the layer.

Bloor (1964) used hot-wire anemometry to study the shear layer instability behind a circular cylinder and the frequency of vortices compared to the von Kármán. She found that the ratio

f_{SL}/f_K went with Reynolds number proportionally to $Re^{0.5}$, justifying this relationship with a dimensional argument. The frequency of the shear layer 'waves' was found to be proportional to $U_\infty^{\frac{3}{2}}$. Since f_{SL} is proportional to a characteristic velocity (U_∞) divided by a length (δ_1, the boundary-layer thickness at the point of separation). Since, in a laminar boundary layer, $\delta \propto \frac{l\nu}{U_\infty}^{\frac{1}{2}}$, $\delta_1 \propto \frac{l_1\nu}{U_\infty}^{\frac{1}{2}}$ with l_1 being the distance from the forward stagnation point to the separation point on the cylinder, which in turn is proportional to the cylinder diameter. Thus,

$$\delta_1 \propto \frac{D\nu}{U_\infty}^{\frac{1}{2}} \tag{2.5}$$

and

$$f_{SL} \propto \frac{U_\infty^{\frac{3}{2}}}{D\nu}. \tag{2.6}$$

The von Kármán Strouhal number, $\mathrm{St} = f_K D/U_\infty$, has been found to be roughly constant at 0.2 across the Reynolds number range used by Bloor. Hence, she could conclude that

$$\frac{f_{SL}}{f_K} \propto \frac{U_\infty^{\frac{3}{2}}}{(D\nu)^{\frac{1}{2}}}\frac{D}{U_\infty} = Re^{\frac{1}{2}}. \tag{2.7}$$

Wei & Smith (1986) used both hydrogen-bubble flow-visualisation and hot-wire anemometry to investigate these instabilities and their frequency. Both sets of experiments point to a more appropriate exponent of 0.87, discounting the results of Bloor due to the limited data points (three) used in the analysis and the dimensional argument claiming that the characteristic length for a free shear layer should not be the boundary layer thickness. They also observed a three-dimensional transition shortly after their formation, suggesting this to be the mechanism towards turbulence in the von Kármán vortices at Reynolds numbers higher than 260[2].

Kourta *et al.* (1987), however, agreed with the 0.5 exponent of Bloor. Whilst acknowledging the differences with the work of Wei & Smith, they did not go into details as to why their work should be accepted.

Prasad & Williamson (1997) argued against this finding by reanalysing the data from a series of papers and added their own hot-wire data to show that overall the fit went with:

$$\frac{f_{SL}}{f_K} = 0.0235 \times Re^{0.67} \tag{2.8}$$

---

[2] This was argued against by Wu *et al.* (1996).

explaining that the exponent should be larger than 0.5 due to the assumption made by Bloor that is only approximately correct since the Strouhal number gradually decreases with Reynolds number.

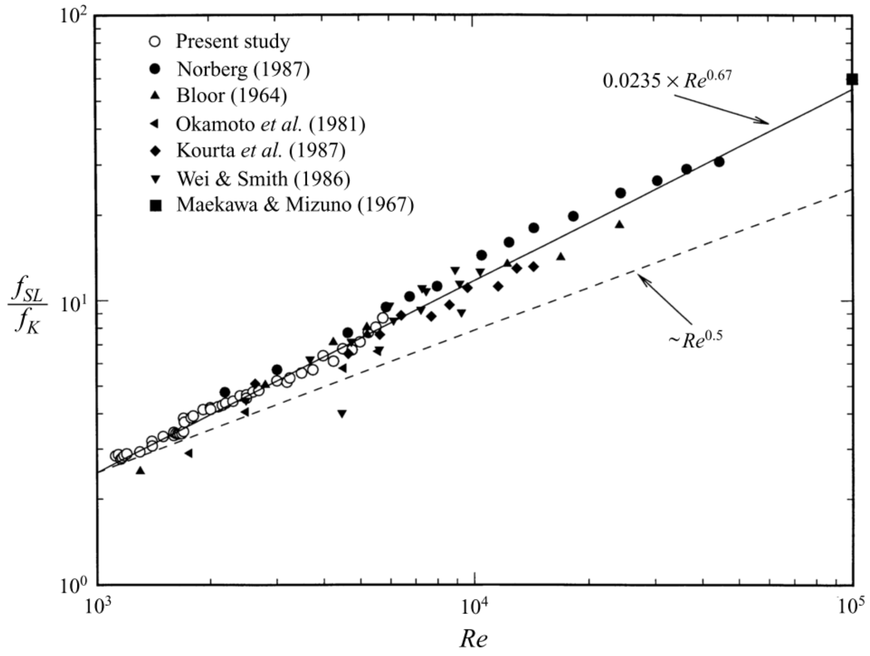

FIGURE 2.31: Data from Prasad & Williamson (1997) showing variation of the shear layer to von Kármán frequency of a circular cylinder as a function of Reynolds number.

Thompson & Hourigan (2005) suggested that a global fit across Reynolds number is not suited, showing that piecewise functions fitted with exponents close to 0.5 match the data well across a range of Reynolds numbers. They explain that the fundamental physics are varying across Reynolds number so it is reasonable to expect the frequency ratio to vary also.

The studies encountered in this literature review all use a similar method for ascertaining the shear layer frequency: a hot wire (or other) probe is placed at a particular location downstream of the plate, and a time series is acquired. A typical spectrum is reproduced in figure 2.32 showing clear peaks at the von Kármán frequency and its harmonics. The shear layer frequency, however, is taken as the maximum point of a broadband peak (this peak is also described in the paper as one of the sharper peaks they analysed). This peak is broadband due to the variation of shear layer frequency in time and in space. The frequency varies with space due to vortex merging and the expansion of the shear layer with downstream position. The shear layer generates much smaller (and higher frequency) vortices than each measurement technique can capture. It is only as these vortices merge with downstream position and become larger (and lower frequency) that they are measurable. Hence, when a probe is placed at a single point in the shear layer, the frequency information may not represent the entire dynamics of the shear layer.

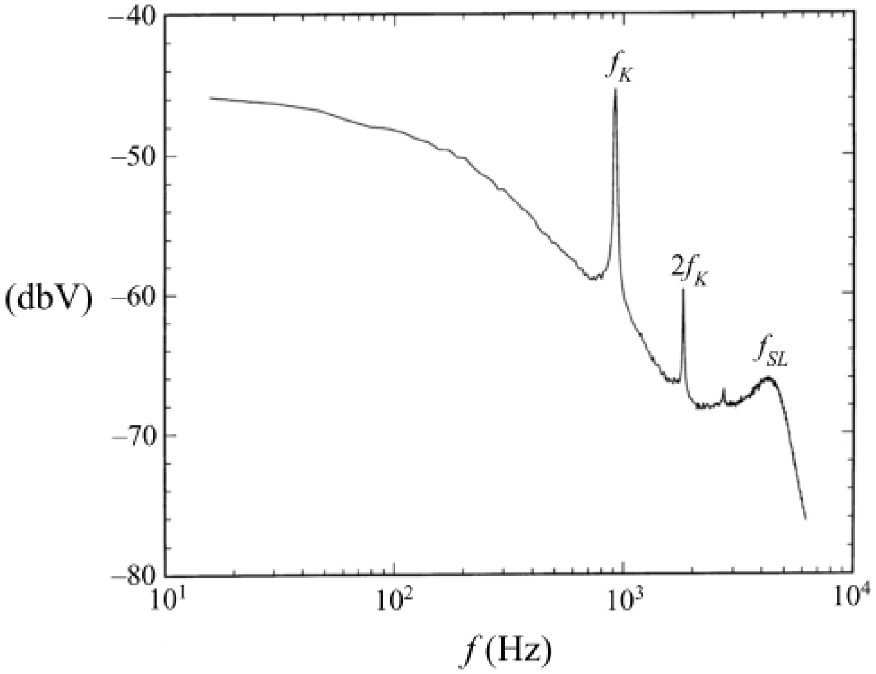

Figure 2.32: Data from Prasad & Williamson (1997) showing frequencies in the wake of a circular cylinder displaying sharp peaks at the von Kármán frequency and harmonics, but a broadband peak at the shear layer.

2.3.4 Shear layers in other wakes

Nakamura *et al.* (1991) studied plates parallel to the flow for plates at a range of chord-to-thickness ratios. They found that the shedding frequency went in integral multiples of 0.6 (figure 2.33. They interpreted this as a requirement to spatially fit an integer number of shear layer vortices along the chord.

For the case of a square cylinder, Minguez *et al.* (2011) found a shear layer to von Kármán ratio of 46 (experimental) or 25 (computational) at $Re = 21400$. The disparity between these numbers suggest there is a limitation in one, or both, of the techniques used in the study. Even so, both these numbers are higher than that proposed by Prasad & Williamson for the circular cylinder.

Data from Sakamoto & Haniu (1990) compiled information from several studies for the wake of spheres and found it to be in good agreement with Prasad & Williamson. There have been no studies other than Minguez *et al.* (2011) on sharp-edged geometries where this instability has been studied in depth.

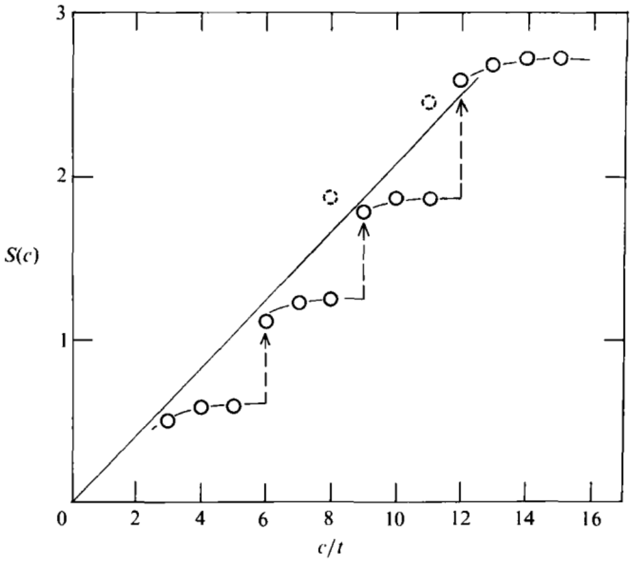

Figure 2.33: Strouhal number against chord-to-thickness ratio of a flat plate mounted in-line with the flow (after Nakamura *et al.* (1991)).

Table 2.2: Previous studies on flat plate wakes. L and W denote the recirculation length and the wake width respectively.

Authors	Method	*Re*	*St*	*L*	*W*
Dennis *et al.* (1993)	Experimental	5-20	0.1 - 15		
Saha (2007)	Numerical	30 - 175	0.1665		
Najjar & Balachandar (1998)	Numerical	250	0.1613	2.35	0.8
Narasimhamurthy & Andersson (2009)	Numerical	750	0.168	1.96	0.7
Najjar & Vanka (1995*a*)	Numerical	1000	~0.143	2.55	
Lisoski (1993)	Towing Tank	1000s	0.148		
Kiya & Matsumura (2006)	Wind Tunnel	23000	0.146		
Bradbury (1976)	Wind Tunnel	26400		1.92	
Leder (1991)	PIV	28000		2.5	0.82
Fage & Johansen (1927)	Wind Tunnel	32000 - 180000	0.146	NA	NA

2.3.5 Wakes of bodies with fixed separation points

For extremely blunt bodies, like a flat plate normal to the flow, separation occurs at the sharp edges regardless of the nature of the boundary layer flow (Munson *et al.*, 1990). There have been numerous studies, both experimental and numerical, on the wake of such a plate (summarised in table 2.2).

Perhaps the earliest research into this problem was by Fage & Johansen (1927) who placed full-width plates across their wind tunnel. Besides confirming the existence of the vortex shedding mechanism for this geometry, they showed that it could be measured with a hot-wire even

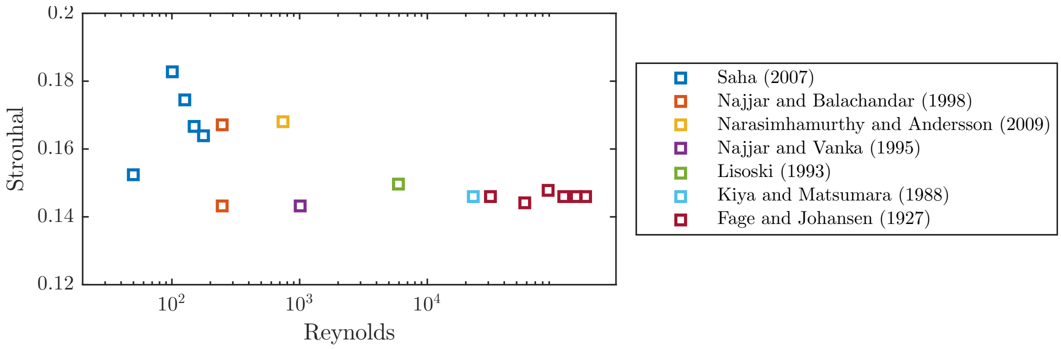

Figure 2.34: The effect of Reynolds number on the shedding Strouhal number of flat plates. Data is a compilation of the papers in table 2.2.

outside the vortex street where the fluctuations are more steady. Across a Reynolds number range of 32000 to 180000, they found that the shedding frequency was a linear function of velocity (i.e., the Strouhal number did not depend on the Reynolds number).

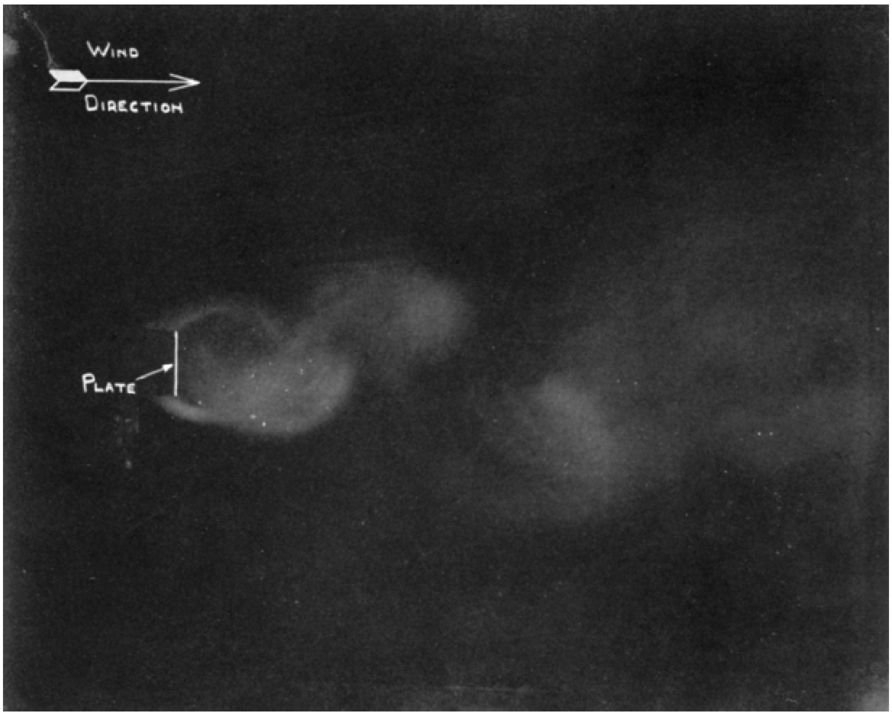

Figure 2.35: Fage & Johansen (1927) smoke visualisation showing the vortex street behind a normal flat plate.

Saha (2007) showed that the wake was not entirely independent of Reynolds number effects. They studied the far-wake at low Reynolds numbers (less than 175) numerically. The initially unsteady far-wake at Re = 35 is stabilised between 75 and 140, before being unstable again with large scale unsteadiness oscillating at a lower frequency than the near-wake (figure 2.36 (c)). These Reynolds number transitions in the far-wake are shown to not influence the drag coefficient or near-wake Strouhal number.

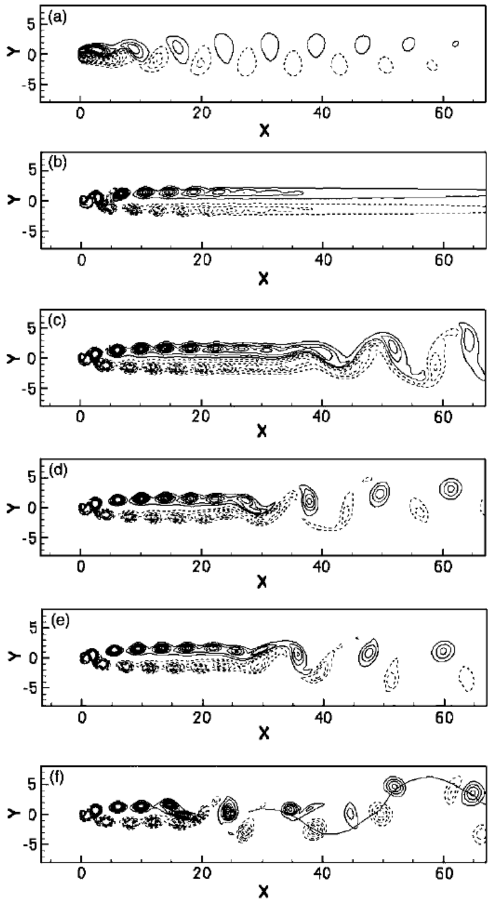

Figure 2.36: Instantaneous spanwise vorticity contours showing the effect of Reynolds number on the far wake. (a) $Re = 35$; (b) $Re = 100$; (c) $Re = 145$; (d) $Re = 150$; (e) $Re = 150$; (f) $Re = 175$. From Saha (2007).

Lisoski (1993) looked at the effect of aspect ratio on the vortex shedding of the plate. They found that for an aspect ratio of 6 there were long periods of no shedding. To ensure constant shedding an aspect ratio of at least 10 was necessary.

2.3.5.1 Low frequency unsteadiness

Some experimental (Lisoski, 1993) and numerical (Joshi *et al.*, 1994; Najjar & Vanka, 1995*b*) studies found evidence of low frequency undulations in the wake. It was seen across a wide range of Reynolds numbers from 250 to 250000. This low-frequency is roughly one-tenth of the shedding frequency, and manifests itself in the drag signal. This was confirmed by a low Reynolds number (250) study by Najjar & Balachandar (1998) who found the flow switched between a high and low drag case. The recirculation region switch between 1.70 and 3.13 respectively (width of 0.72 and 0.92). They also noted that the shear layer vortices roll up close to the plate in the H regime, are more compact, and are coherent. They suggest that the low frequency is due to an interaction between the shedding frequencies in H and L.

2.3.6 Breaking symmetry with inclination angle

The symmetry of the shedding wake can be broken by the introduction of an inclination angle to the plate. Fage & Johansen (1927) also varied angle of attack and found that it was fairly constant when non-dimensionalised to the projected chord. Knisely (1990) showed that this was only true for thin plates (thickness-to-chord ratios less than 0.1), as an increase in thickness starts to introduce Reynolds number effects.

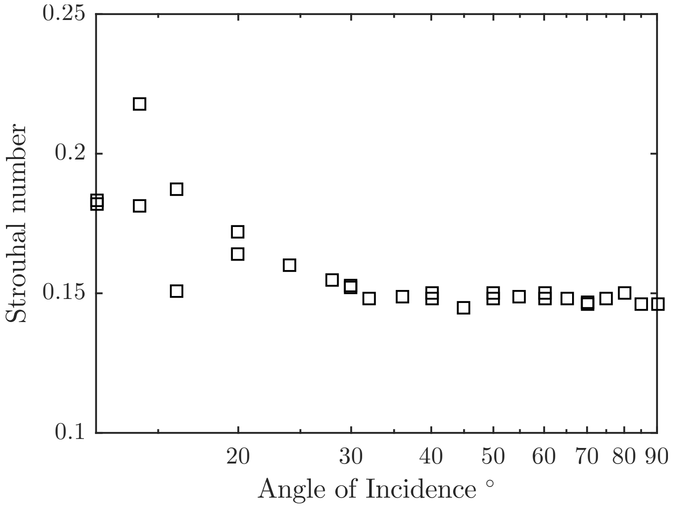

FIGURE 2.37: Strouhal number variation with angle of incidence for a two-dimensional flat plate for $Re > 30000$. Reproduced with data from Fage & Johansen (1927).

2.4 Literature summary and research questions

This literature review gives the key background information relating to ground vehicle aerodynamics. It focuses on the nature of the two- and three-dimensional separations and their analogous (and more canonical) flows in the wakes of circular cylinder and flat plates. Several research questions arise from this review:

1. There are still several questions arising from the study of the near-wake of the Ahmed body. The formation and nature of some of the key structures are yet to be identified, most notably the A and B vortices. High resolution data fields are required for such investigations.

   What is the nature of the A and B vortices - are they formed in a torus behind the base or are they stacked above each other trailing free legs?

2. The disagreement in the literature about the cause of variations in the wake can be answered with temporally-resolved wake maps and the use of tools such as the POD to

reveal more details on the dynamics.

How do the macro structures in the wake vary in time?

3. Whilst it has been studied to some extent on other shapes (eg. airfoils, plates, etc.), the effect of separating the longitudinal vortices from each other has not been studied for the Ahmed body.

   What effect does separating the c-pillars, and hence the longitudinal vortices, have on the wake of the Ahmed body?

4. Regarding the two-dimensional separations, the von Kármán street formation from the shear layers has been well documented for the circular cylinder, but no details could be found regarding the same process for sharp edged geometries.

   How do the shear layers form into von Kármán vortices for a flat plate with sharp edges?

Chapter 3

Experimental Methods

3.1 Introduction

This chapter introduces the facilities and experimental methods used throughout the study. Section 3.2 introduces the water channel and quantifies the flow quality, as well as describing the sub-channel used to achieve low-Reynolds number flows. Section 3.3 describes the plate geometries and Ahmed bodies used. Section 3.4 discusses the data acquisition methods including the PIV system and force measurement. The final section, section 3.5, discusses the post-processing of the acquired velocity fields, including techniques for characterising the frequencies in the flow, as well as methods for determining the bounds of a vortex and the circulation contained therein. Section 3.6 discusses some of the uncertainty analysis involved in the experiments.

3.2 Flow system

Experiments were conducted in the free-surface, recirculating water channel in the FLAIR (Fluids Laboratory for Aeronautical and Industrial Research) laboratory at Monash University (figure 3.1). The flow is driven by a mixed-flow pump that is controlled by sending serial signals through an RS-435 protocol. This was done using a LabView program. The outlet from the pump leads to an upstream settling tank, where the flow is conditioned by a pressure plate, a honeycomb, and a fine-mesh. These devices condition the flow by straightening it and through the introduction of small-scale turbulence, which breaks down the large-scale structures. A three-dimensional contraction (area ratio 5.1) accelerates the flow prior to the test section. The test section is $4m$ long, $800mm$ deep, and $600mm$ wide. It is manufactured from glass to allow optical measurements. The free-stream velocity was controllable from 0.048 to $0.456ms^{-1}$.

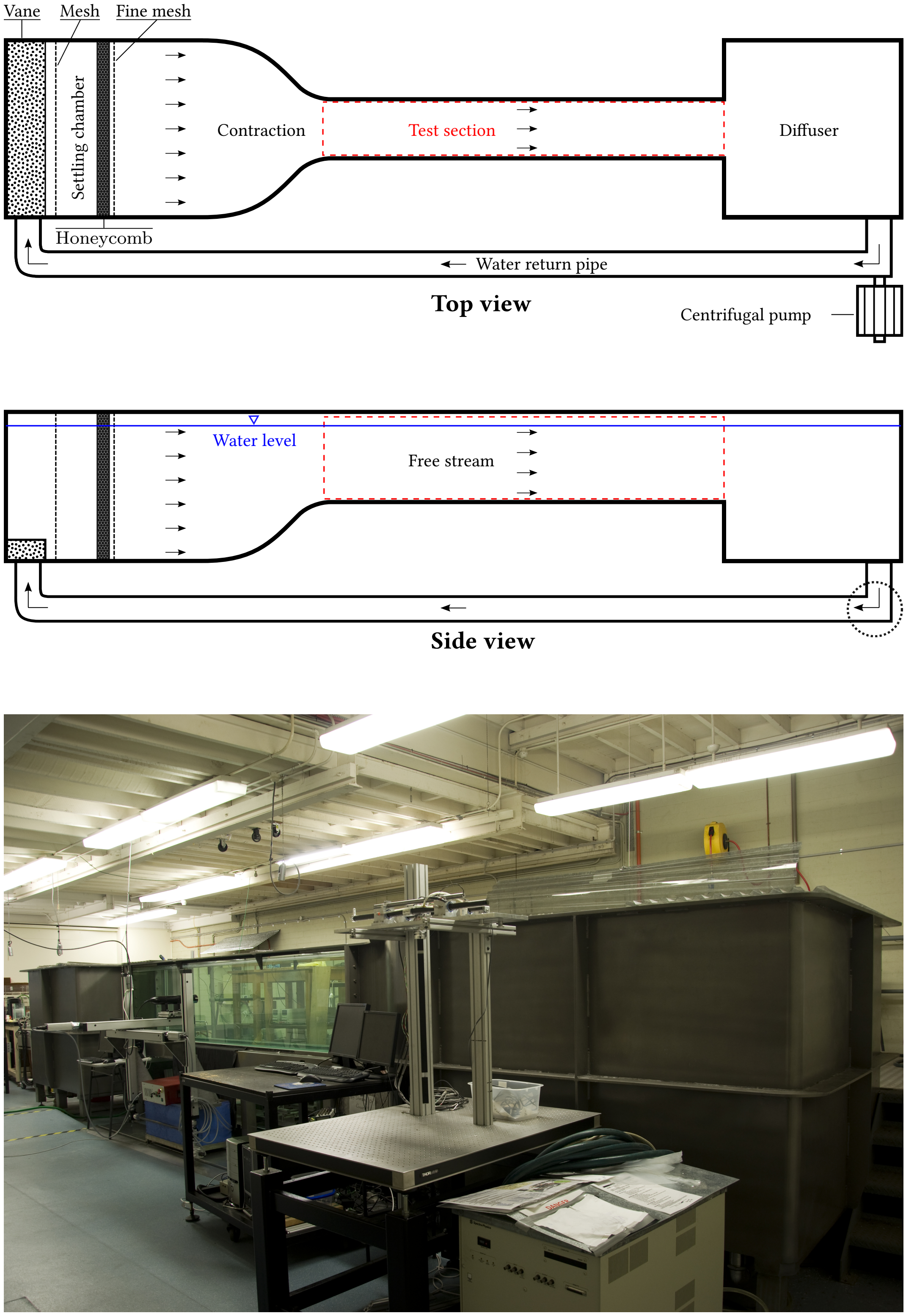

Figure 3.1: Schematic views and a photograph of the water channel facilities (courtesy J. Zhao).

The flow quality in the channel was quantified using LDV (Laser Doppler Velocimetry). LDV is an accurate, non-intrusive optical technique for the measurement of the point-wise velocity of tracer particles in a fluid. The scattered light from two laser beams are collected and the frequency shift due to the doppler effect can be calculated. This frequency shift is directly proportional to the particle velocity. The results (figure 3.2) show that, for a free-stream velocity of 0.365ms^{-1}, the in-flow conditions were a turbulence intensity (I_u) of less than 0.5%, and non-uniformity of $\pm$ 1% across the usable test section.

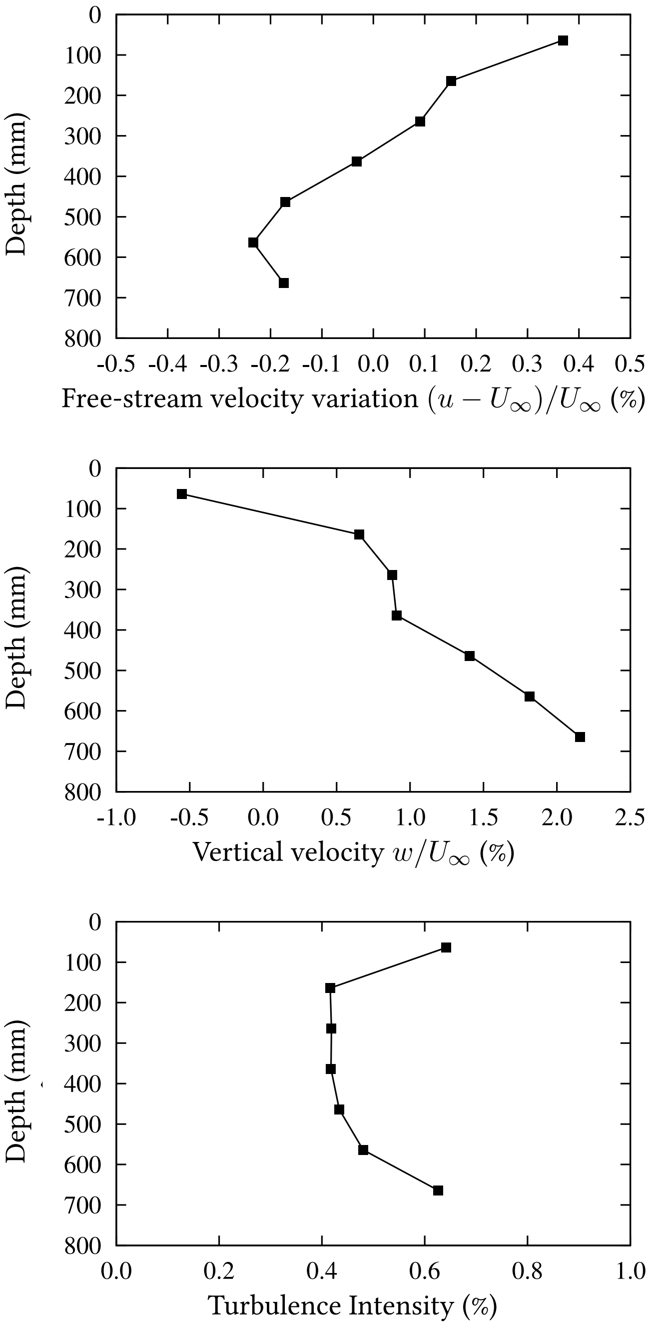

FIGURE 3.2: In-flow conditions in the FLAIR water channel, measured by two-component LDA system with free-stream velocity $U_\infty = 0.365ms^{-1}$.

3.2.1 Sub-channel

To achieve low Reynolds numbers whilst maintaining low turbulence intensity and non-uniformity, the sub-channel described by Radi *et al.* (2014) was utilised. It is a 'u'-shaped bucket that sits in the middle of the water channel with a variably porous plate at the trailing end. This porosity results in a pressure increase within the bucket, causing low velocity flow inside the bucket, and higher velocity flow outside the bucket. The porosity of the trailing plate varies this pressure change, and therefore the velocity reduction.

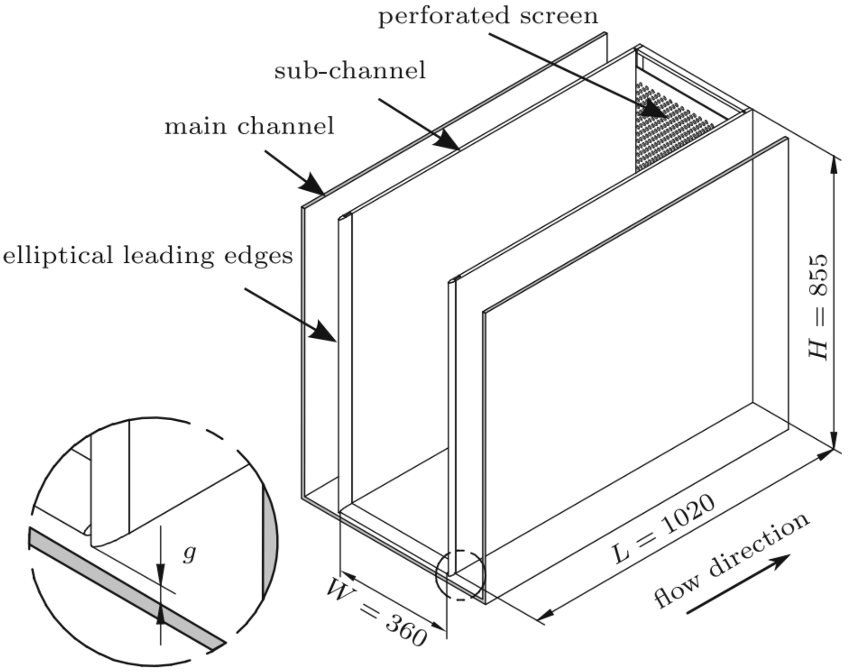

Figure 3.3: Geometry of the sub-channel flow velocity reduction device. Radi *et al.* (2014)

The streamwise velocity field was measured for a series of pump frequencies between 6 and 13 Hz, and porosity values of 0.041, 0.154 and 0.390. The stream-wise velocity and turbulence levels are reported in figure 3.4. The velocity is shown to be linear with pump frequency, with lower porosities causing greater reductions in the flow velocity. The turbulence levels are generally less than 1%, except at very low velocities (where the turbulence is still less than 2%).

For the experiments involving the normal flat plate and quantifying the frequencies as a function of Reynolds number, a large Reynolds range was required. Thus, the sub-channel was used with three different porosity settings. The pump frequency was kept between 6 and 13 Hz when the sub-channel was used. An overlap of three data points was maintained between each data set. Figure 3.5 has the Reynolds number range and pump settings used.

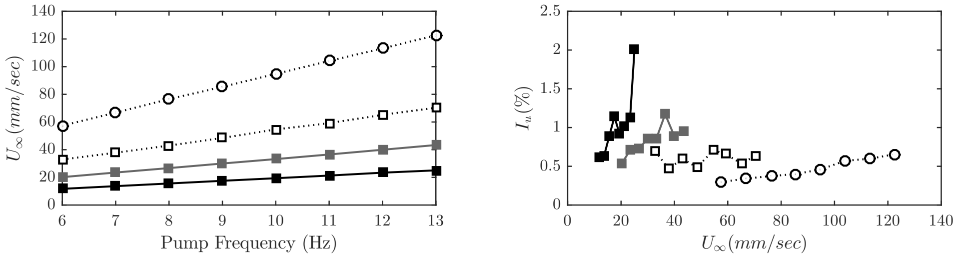

Figure 3.4: Streamwise velocity and turbulence measurements in the sub-channel for various pump frequencies and porosity levels. Black filled squares are 4.1% porosity, gray squares are 15.4% porosity, open squares are 39% porosity, and open circles are 100% porosity.

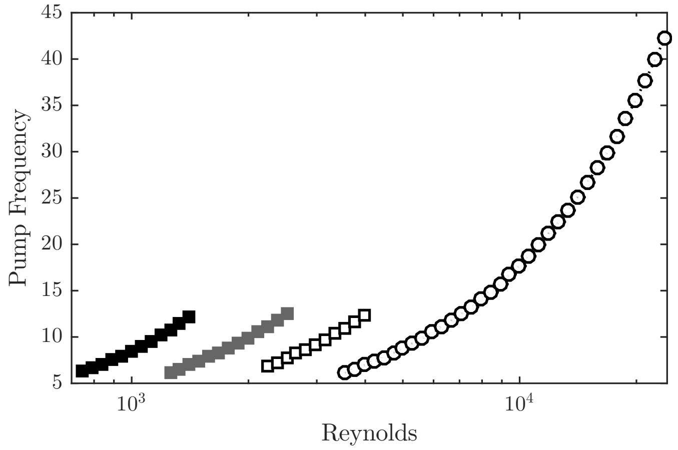

Figure 3.5: Reynolds number range and pump settings used in the normal flat plate experiments. Black filled squares are 4.1% porosity, gray squares are 15.4% porosity, open squares are 39% porosity, and open circles are 100% porosity.

The acquisition parameters were chosen to capture both the von Kármán phenomena and the shear layer vortex cycles at high temporal resolution. The sampling frequency was thus set to twenty times the estimated shear layer frequency - that is, twenty PIV frames were acquired per shear layer cycle. The number of von Kármán cycles captured varies with Reynolds number, from 48 periods at the low Reynolds numbers, to 10 at the higher end. These settings reduce the accuracy of time-averaged measurements and long time-scale measurements such as the Strouhal number, but the interesting phenomena in this study were in the development of the shear layer, so priority was given to that time- and length-scale. Table 3.1 shows the experimental settings for each run conducted in this part of the study.

Table 3.1: Experimental parameters for the Reynolds sweep for the normal, two-dimensional flat plate. Note that $\Delta t = 0$ indicates cinematic capturing.

Run	Re	U_∞ mm/s	Pump	Δt (ms)	Acquisition rate (Hz)	Acquisition time (s)	Porosity
01	748	12.5	6.26	95.8	2.2	1445	4.1%
02	793	13.2	6.66	90.1	2.4	1313	4.1%
03	840	14.0	7.07	84.8	2.6	1192	4.1%
04	889	14.9	7.52	79.8	2.9	1083	4.1%
05	942	15.7	7.98	75.1	3.2	984	4.1%
06	998	16.7	8.48	70.7	3.5	894	4.1%
07	1057	17.7	9.01	66.6	3.9	812	4.1%
08	1120	18.7	9.56	62.7	4.3	737	4.1%
09	1186	19.8	10.15	59.1	4.7	670	4.1%
10	1256	21.0	10.78	55.7	5.2	608	4.1%
11	1331	22.2	11.44	52.5	5.7	553	4.1%
12	1410	23.5	12.14	49.4	6.3	502	4.1%
13	1256	21.0	6.22	57.9	6.3	500	15.4%
14	1331	22.2	6.59	54.6	6.9	457	15.4%
15	1410	23.5	6.99	51.5	7.6	414	15.4%
16	1493	24.9	7.41	48.6	8.4	375	15.4%
17	1582	26.4	7.86	45.8	9.2	342	15.4%
18	1675	28.0	8.33	43.2	10.1	312	15.4%
19	1775	29.6	8.83	40.8	11.2	281	15.4%
20	1880	31.4	9.35	38.5	12.3	256	15.4%
21	1991	33.3	9.91	36.3	13.5	233	15.4%
22	2109	35.2	10.51	34.3	14.9	211	15.4%
23	2234	37.3	11.14	32.3	16.4	192	15.4%
24	2367	39.5	11.80	30.5	18.1	174	15.4%
25	2507	41.9	12.51	28.8	19.9	158	15.4%
26	2234	37.3	6.89	34.9	13.5	233	39.0%
27	2367	39.5	7.29	32.9	14.9	211	39.0%
28	2507	41.9	7.73	31.1	16.4	192	39.0%
29	2655	44.3	8.19	29.3	18.1	174	39.0%
30	2813	47.0	8.67	27.7	19.9	158	39.0%
31	2979	49.8	9.19	26.1	21.9	144	39.0%
32	3156	52.7	9.74	24.7	24.1	131	39.0%
33	3343	55.8	10.31	23.3	26.5	119	39.0%
34	3541	59.1	10.93	22.0	29.2	108	39.0%
35	3751	62.6	11.58	20.7	32.2	98	39.0%
36	3973	66.4	12.26	19.6	35.4	89	39.0%

Continued on next page

Table 3.1 – *Continued from previous page*

Run	Re	U_∞ (mm/s)	Pump	Δt (ms)	Acquisition rate (Hz)	Acquisition time (s)	Porosity
37	3541	59.1	6.17	19.4	29.2	108	100%
38	3751	62.6	6.55	18.3	32.2	98	100%
39	3973	66.3	6.95	17.3	35.4	89	100%
40	4209	70.2	7.37	16.3	39.0	81	100%
41	4458	74.4	7.82	15.4	42.9	73	100%
42	4722	78.8	8.29	14.5	47.2	67	100%
43	5002	83.5	8.79	13.6	52.0	61	100%
44	5298	88.4	9.33	12.9	57.3	55	100%
45	5612	93.7	9.89	12.1	63.0	50	100%
46	5945	99.2	10.49	11.4	69.4	45	100%
47	6297	105.1	11.12	10.8	76.4	41	100%
48	6670	111.3	11.79	10.2	84.1	37	100%
49	7065	117.9	12.50	9.6	92.6	34	100%
50	7484	124.9	13.25	0.0	101.9	62	100%
51	7927	132.3	14.05	0.0	112.2	56	100%
52	8397	140.2	14.89	0.0	123.6	51	100%
53	8895	148.5	15.78	0.0	136.0	46	100%
54	9422	157.3	16.73	0.0	149.8	42	100%
55	9980	166.6	17.73	0.0	164.9	38	100%
56	10571	176.5	18.80	0.0	181.5	35	100%
57	11198	187.0	19.92	0.0	199.8	32	100%
58	11861	198.0	21.11	0.0	220.0	29	100%
59	12564	209.8	22.37	0.0	242.2	26	100%
60	13309	222.2	23.71	0.0	266.6	24	100%
61	14097	235.4	25.13	0.0	293.5	21	100%
62	14932	249.3	26.63	0.0	323.1	19	100%
63	15817	264.1	28.22	0.0	355.7	18	100%
64	16754	279.8	29.90	0.0	391.6	16	100%
65	17747	296.3	31.68	0.0	431.1	15	100%
66	18799	313.9	33.57	0.0	474.6	13	100%
67	19913	332.5	35.57	0.0	522.5	12	100%
68	21093	352.2	37.69	0.0	575.3	11	100%
69	22342	373.1	39.93	0.0	633.3	10	100%
70	23666	395.2	42.31	0.0	697.2	9	100%

3.3 Models

3.3.1 Plates

Plates were manufactured out of 316 stainless steel to avoid corrosion and surface deformation over time in the water channel. The plates were manufactured to the specifications given in table 3.2. They were made with $3mm$ thick plate and the edges were bevelled to 15° in order

Table 3.2: Plate geometries.

	2D
Inclination angles	50 – 90
Reynolds number	750 – 24000
Chord	60mm
Span	750mm
AR	12.5

to minimize the effects of thickness that were seen by Lisoski (1993) for example; the use of sharp edges stabilises the separation points. The two-dimensional plate was held by a spigot at the bottom of the sub-channel, and a stepper motor at the top (figure 3.6). The stepper motor allowed the quick, accurate, and automated change of incidence angle. The motor was controlled via a Parker Hannifin 6K motion controller.

3.3.2 Ahmed models

Ahmed bodies (figure 3.7) with a slant angle of 25° were used, which, according to Ahmed *et al.* (1984), should produce wakes in the high-drag regime far from the critical angle of 30°. The models were scaled down to 25% of the original size proposed by Ahmed *et al.* (1984) to reduce blockage effects (blockage was less than 2%). The resulting size for the standard width (AM10) model was 261mm long × 97mm wide × 72mm high. The models were manufactured out of Acetal using a CNC-mill. This manufacturing method was chosen as it resulted in smooth bodies with no gaps, joins, or bolt-heads to disrupt the flow.

Eight bodies were manufactured with varying widths between 60% and 130% of the standard model (see 6.1 for details). The height and length of the models were kept constant, resulting in a varying aspect ratio. The aspect ratio was defined as the aspect ratio of the slant area, that is, AR $= W/L_S$, following Morel (1978*a*).

The characteristic length used for Reynolds number calculations was the square root of the frontal area. Even though traditionally the length of the model is used for vehicle aerodynamic applications, a more fluid dynamic approach would suggest the square-root of the frontal area is a more appropriate length, especially given the fact that the body is in ground effect. That said, section 2.2.2.3 shows that Reynolds number has little effect on the Ahmed wake once the flow over the rear slant has attached.

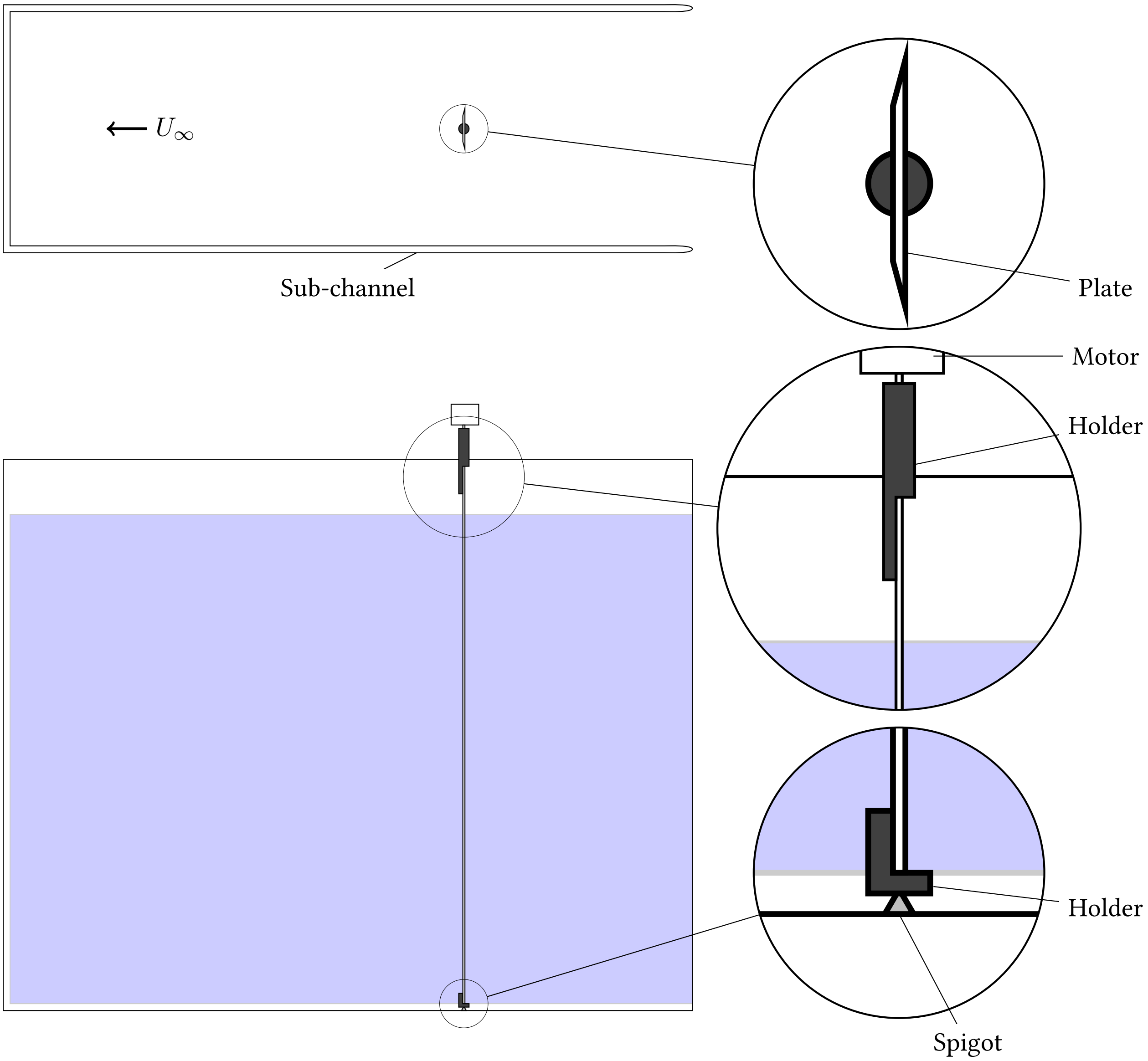

Figure 3.6: Mounting of the two-dimensional plate in the sub-channel. Note that the zoomed in sections on the right hand side of the figure are not at a common scale.

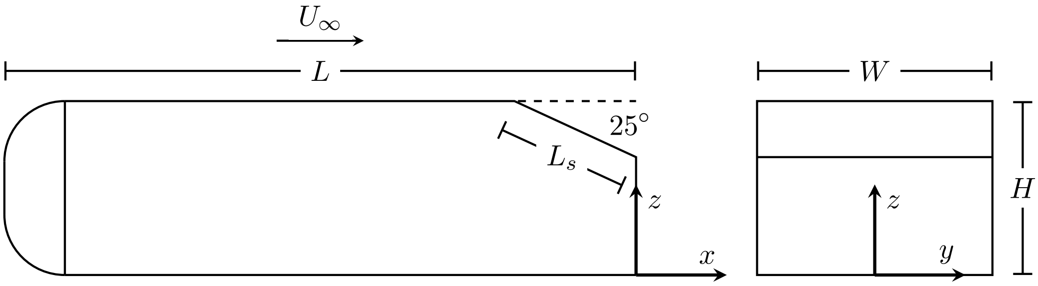

Figure 3.7: Ahmed body geometry and axis reference. The standard (AM10) aspect ratio is shown. Dimensions: $L = 261mm$, $L_S = 55.5mm$, $W = 97mm$, and $H = 72mm$. Coordinate system origin is located at the centre of the base at the rear of the Ahmed model.

3.3.3 Ground plane

A flat plate was used to simulate the ground plane during the Ahmed body experiments. The plate extended $4.2H$ upstream of the leading edge of the model and had a 4:1 elliptical leading edge. The boundary layer was measured using high magnification PIV at eight downstream locations from the ground plane leading edge. The boundary layer was analysed with no Ahmed body in the water channel. At each location, 600 image pairs were obtained, with a magnification factor of $11.02px/mm$ and $\Delta t = 2.6ms$. Images were cross-correlated with a $32 \times 32px$ interrogation window shifted by $8px$ in each direction (75% overlap).

Theoretically, the Blasius equation provides the expected boundary layer growth with local Reynolds number as:

$$\delta = \frac{5x}{\sqrt{Re_x}} \tag{3.1}$$

The displacement thickness is the distance by which the ground plane would have to be moved towards the fluid in order to maintain the same flow rate in an inviscid fluid as occurs in the real fluid. In practical aerodynamics, this measure is of more use than the conventional boundary layer thickness.

$$\delta^* = \int_0^\infty 1 - \frac{u(y)}{U_\infty} dy \tag{3.2}$$

which has the theoretical form in a laminar flow:

$$\delta = \frac{1.72x}{\sqrt{Re_x}} \tag{3.3}$$

The boundary layer profiles at the eight locations are given in figure 3.8 (a). The ordinate in this plot is the distance from the plate in the normal direction normalised by the gap between the flat plate and the Ahmed body. Figure 3.8 (b) shows that the boundary layer growth is in quite good agreement with, though slightly higher than, the Blasius solution. Regardless, the boundary layer is much shorter than the base of the Ahmed body, which is positioned at $x/L = 1.15$.

The models were attached to the ground plane via two symmetric airfoil stilts. The stilts were manufactured out of stainless steel and had a chord of $57mm$ and thickness of $17mm$. The central stilt methodology was used to allow for the measurement of the model's drag. Symmetric airfoils were chosen as opposed to circular cylinders in order to minimise the influence of these structures in the wake.

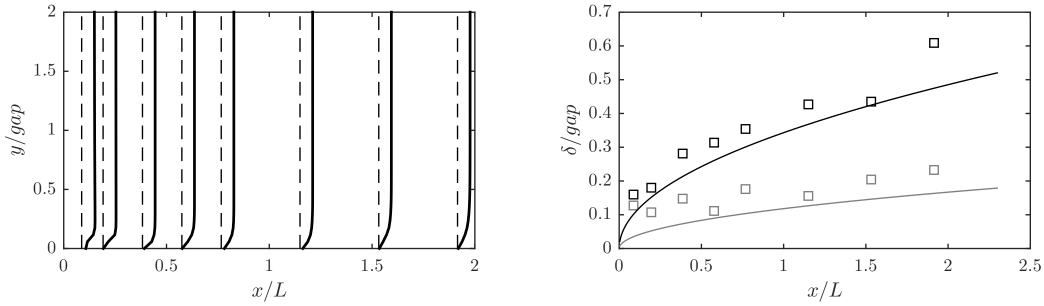

(a) Boundary layer profiles

(b) Boundary layer thickness and displacement thickness growth

Figure 3.8: Boundary layer profiles and growth with downstream position along the ground plane. Figure (b) contains both the 99% U_∞ boundary layer thickness (black) and the displacement thickness (gray). Theoretical solutions are given with solid lines.

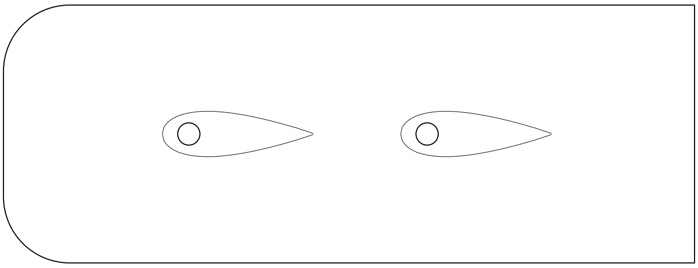

Figure 3.9: Bottom view of the Ahmed model showing the location and scale of the airfoil stilts.

3.4 Experimental measurement systems

3.4.1 DAQ

The temperature measurements and the PIV timing system were controlled through a National Instruments BNC-2110 DAQ board. The system was set up with eight analogue input channels capable of measuring $\pm 10V$ with 16-bit resolution and maximum sampling rate of 250 kHz. Two 32-bit digital counters were used to provide the timing inputs for the PIV system.

To obtain high signal quality for force measurements, it was necessary that the voltages be measured with differential readings. When measuring voltages in differential mode, each channel measures a positive signal with respect to analog ground, at the same time as measuring the negative signal with respect to the same ground. The difference between them produces a cleaner signal than can be obtained by measuring single ended, where all voltage channels are referenced against the same negative channel. To do this a National Instruments USB DAQ board was used, which allowed for the wiring of the six necessary channels in a differential mode. This reduced the electrical noise in the force signals (figure 3.10.

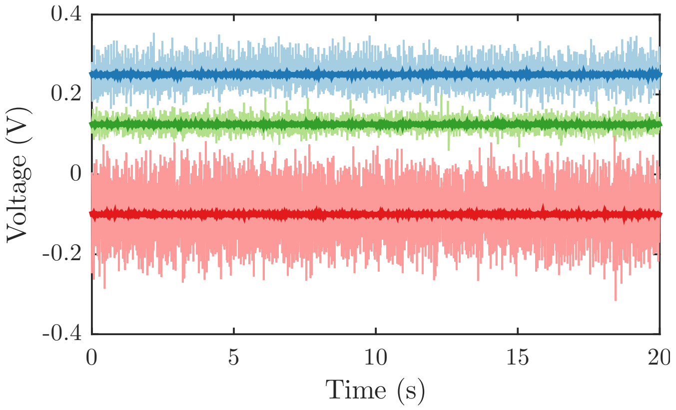

Figure 3.10: Three voltage signals measured by ATI force transducer. Darker colours indicate voltages as read using differential mode while light signals are from single-ended readings.

A LabVIEW program was developed to allow the simultaneous measurement of the analogue inputs as well as the triggering of the PIV system and control of the watter channel's pump velocity.

3.4.2 Particle Image Velocimetry

Instantaneous velocity fields were acquired using a Particle Image Velocimetry (PIV) system. PIV is a non-intrusive velocity mapping technique that uses the tracking of particles seeded in the flow and the definition of velocity as displacement divided by time. This is implemented by observing neutrally buoyant particles in the flow at two separate time-instances. The principles of PIV are well explained in the literature (eg. Raffel *et al.*, 2007; Adrian, 1991). The specific procedure for these experiments is now described.

3.4.2.1 Flow seeding

The choice of particles for seeding depends on the fluid and the magnification factor required for the experiment. The first parameter of importance with regards to the fluid is the density, which should be matched to the flow in order for the particles to follow the flow, as well as neither sinking nor floating. The second is the refractive index, which must be different to that of the fluid for the particles to be visible when illuminated. For these experiments, the fluid was always fresh water, and hence the particles chosen were Vestosint spherical particles with density 1.016 g/cm^3 and refractive index 1.52 (at 590nm).

The magnification factor of the experiment is important when determining the size of the particles. The particles should be large enough to scatter sufficient light to be captured by the camera, they should also be small enough to have a fast response time to follow the flow well. The magnification factors used in these experiments were between 9 and 40 px/mm, and the mean particle size was $56\mu m$, giving particle size on the image between half of one pixel to two pixels.

The particles must be mixed throughout the volume. Particles were mixed with water and Triton X 100, a non-ionic surfactant that aids mixing and prevents particle conglomeration. This particle mixture was then siphoned into the water channel. Sufficient particle density was verified through the mean intensity of the acquired images as well as the quality of the cross-correlations.

3.4.2.2 Illumination

The particles were illuminated using two different laser systems depending on the experiment, both produced $532nm$ radiation. The time-resolved system used a continuous laser (MML-N-$532nm$-$5W$ from Changchun New Industries, China) which created a $3mm$ diameter laser beam. The standard PIV setup involved a pair of Minilite II Continuum Nd:YAG (neodymium-doped yttrium aluminium garnet) lasers. The laser beam had energy $25mJ$, higher than the equivalent in the continuous system ($5W \times 2ms = 10mJ$), meaning brighter images were attainable using the pulsed system. The main restriction in this system is the maximum frame rate of $15Hz$, limiting this laser to experiments that were not time-resolved.

In both cases, the beam was passed through a series of optical components to direct it in the desired direction. It then passed through a series of cylindrical lenses in order to split the beam into a sheet. The focal length of the cylindrical lens was chosen based on the width of the required sheet, which was in turn a function of the magnification factor of the experiment and the desired frame size.

3.4.2.3 Camera

Two cameras were used in this investigation. When using the continuous lasers for time-resolved PIV (TR-PIV), a PCO Dimax S4 camera was used. This camera has a CMOS sensor with resolution 2016 × 2016 pixels. The maximum frame-rate at full resolution is $1279fps$, which is an equivalent Δt of $0.8ms$. At full resolution, the camera can hold 6307 images.

For the standard PIV setup, a PCO 4000 camera was used. This is a 10.7 mega-pixel sensor (4008×2672 pixels) capable of imaging at $5fps$. This camera was used when temporal resolution was not as important as spatial resolution.

The cameras were coupled with Nikkor lenses either 50mm or 105mm focal length, depending on the experimental setup and the magnification factor required. The magnification factor, the relationship between physical space and pixel space, was calculated by imaging a standard ruler placed in the middle of the laser plane. All images were saved as 8-bit bmp files.

3.4.2.4 Timing

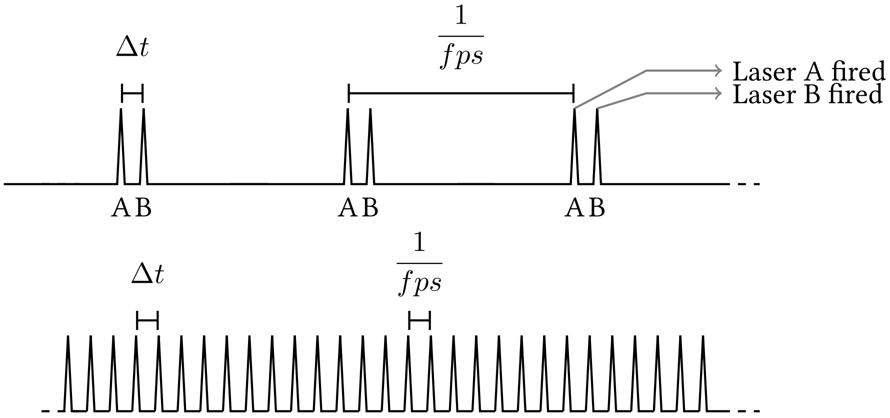

Figure 3.11: Timing systems for the two PIV setups. The standard method (top) consists of the correlation of individual A-B pairs. For time-resolved PIV, cinematic correlation is used, where each image is correlated with the image after it. The number of velocity fields realized is one less than the number of images acquired. fps is the acquisition frame rate (frames per second).

The timing of the cameras and lasers are critical for accurate velocity measurements. Here, timing was controlled via the DAQ board described in section 3.4. There are two timing setups possible, described by figure 3.11. For the standard configuration, pairs of images are acquired at a particular frame rate, with a specific Δt between pulses. The choice of the frame rate is usually limited by the camera and laser hardware. The Δt is chosen based on:

1. *the flow characteristics of interest* - there is a set range of displacements that the cross-correlation can accurately determine. The upper limit is the window size, and the lower limit is determined by the acceptable error (bearing in mind that the correlation error with sub-pixel accuracy is approximately 0.1 pixels). Due to this range, the Δt must be chosen to target the specific flow velocities that are of most interest. Due to these experiments focusing on the wakes of bodies, the slower, separated flow was given higher priority than the free-stream.

2. *the through-plane velocity component* - it is important that the majority of particles imaged in the first photograph are still present in the laser plane by the second photograph. This limits the maximum Δt to the time taken for a particle to travel through the thickness of the laser sheet. For PIV acquired where one of the components resolved is in the streamwise direction, this is normally not a concern, but for cross-stream flow, this can create problems. By limiting the Δt, one reduces the amount of time the flow has to move the particles within the field of view, hence reducing the displacement of the correlation, and thus decreasing the signal-to-noise ratio of the resolved vectors. To improve this situation, it is possible to use a thicker laser sheet, or to displace the laser sheet between image realizations, allowing a larger Δt, and hence longer displacements. This method is described in Waldman & Breuer (2012) and was investigated for the current experiment but deemed to be not worthwhile. This is discussed further in section 3.4.2.7.

3. *the magnification factor* - the magnification factor influences the Δt in that higher magnification factors will result in shorter Δt. For a target pixel displacement of twelve pixels, for example, a velocity of interest of $200 mm/s$, and a magnification factor of 10 px/mm, the required Δt is:

$$\Delta t = \frac{\text{px}}{u \times \text{MF}} = \frac{12px}{200\frac{mm}{s} \times 10\frac{px}{mm}} = 0.006s \tag{3.4}$$

3.4.2.5 Cross-correlation

Validated in-house cross-correlation software (Fouras *et al.*, 2007) was used to calculate the displacement across the region of interest. The code breaks the entire field down to a 64×64 grid, using a FFT-based cross-correlation algorithm to estimate the average displacement across each window with sub-pixel accuracy. After this initial pass, the window size is reduced to 32×32 pixels, and a 75% overlap is applied.

3.4.2.6 2+1D2C PIV

The PIV methodology discussed thus far refers to a 2D2C-PIV system, that is, a two-dimensional plane measuring two components of velocity (both in-plane components). In order to observe the flow structures in the wake, 2+1D2C PIV is employed, where multiple 2D planes across the out-of-plane direction are acquired, allowing two-components of velocity to be calculated across an entire volume.

To test the reliability of measurements, data was taken behind the Ahmed body in two different 2+1D2C configurations, an xy plane translated through z (transverse planes), and an xz plane translated through y (vertical planes). The first plane acquires u and v velocity fields, and the second u and w. Since both planes calculate the u component, this can be compared across the two methods (figure 3.12).

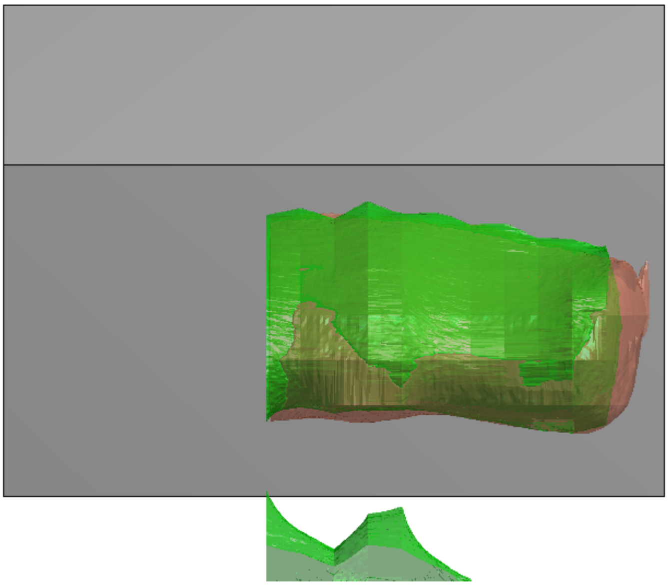

Figure 3.12: Isosurface of streamwise velocity ($u = 0$) in the wake of the Ahmed body showing the consistency of 2+1D2C PIV acquisition in two different experiments. Red data is from the vertical planes and green data is from transverse planes.

The iso-surface in figure 3.12 shows that the broad structure of the recirculating region is the same in both cases. The lower green structure is not present in the red data set as the measurement volume did not extend to that z-position. The data from each experiment was interpolated onto a common grid to allow the quantitative analysis of the differences. The mean of the difference is presented in figure 3.13 showing maximum errors of 10% close to the edge of the body.

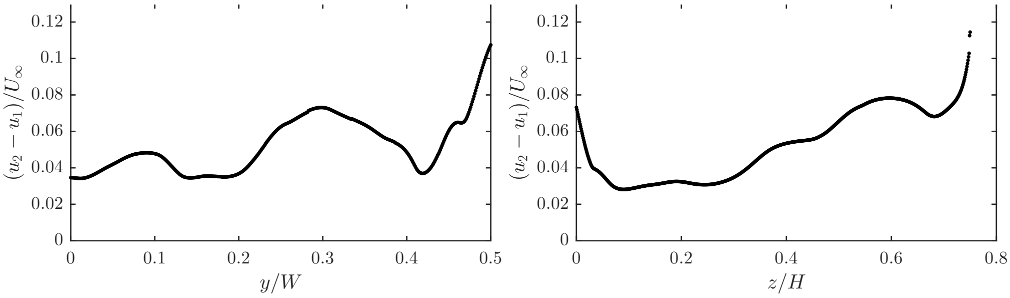

Figure 3.13: Spatial average of the absolute of the difference between the two measured u variables.

3.4.2.7 Cross-stream PIV

To acquire the cross-stream (yz) PIV planes, a glass mirror was placed at 45° to the freestream direction downstream of the Ahmed body (figure 3.14). This allowed the longitudinal structures in the wake to be measured.

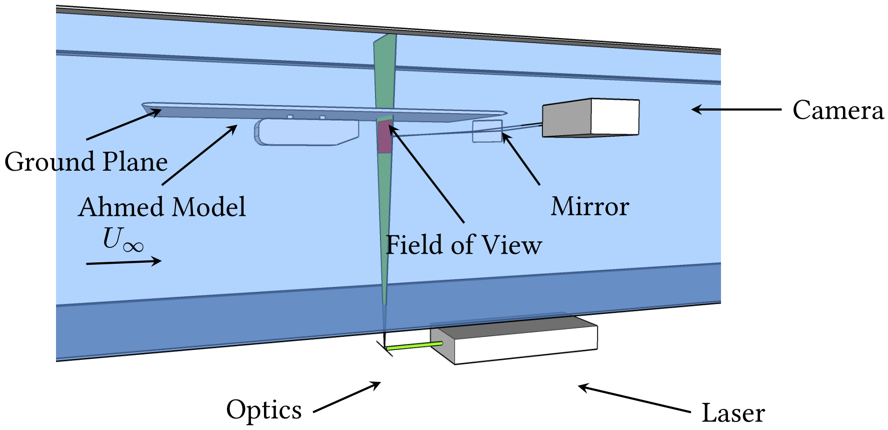

Figure 3.14: Experimental setup for the cross-stream PIV experiments in the wake of the Ahmed body.

To evaluate the effect of the mirror on the flow, two tests were performed. Firstly, PIV was used to quantify the upstream effect of the mirror on the yaw of the flow. Secondly, the velocity behind the body was compared with and without a mirror present.

Figure 3.15 shows the upstream effect of the mirror. It can be first noted that the results at both free-stream velocity settings are similar. As these represent the extremes of the velocities used in the experiments, it indicates that the flow validation is acceptable for the whole range of velocities. In both cases the divergent streamlines are parallel for $x < -150mm$. This suggests that $150mm$ downstream is a good lower limit for the mirror placement. Additionally, the contours of u show that beyond this position, the flow is within a few percent of the freestream level.

To be downstream of the trailing edge of the ground plane, and to give the required optics, the optimum position for the mirror was $420mm$ downstream of the body. Of that $420mm$, wake measurements were acquired in the first $130mm$, leaving $290mm$ downstream. Given the upstream influence of the mirror was limited to approximately $150mm$, this was deemed to be sufficiently far downstream. To confirm that the mirror was having no other effects on the flow, a streamwise (xz) plane was captured behind the Ahmed body, both with and without the downstream mirror in place. The results are shown in figure 3.16 which gives the streamwise

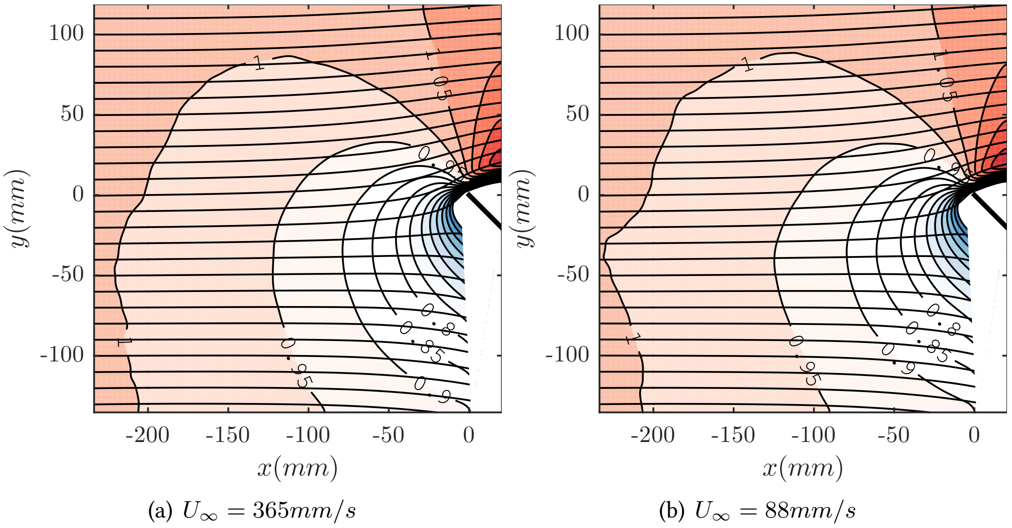

(a) $U_\infty = 365mm/s$ (b) $U_\infty = 88mm/s$

Figure 3.15: Horizontal (xy) PIV plane with a 45° mirror in the same location as it is in figure 3.14. Contours of streamwise velocity (u) overlaid with streamlines. Contour levels are at 5% increments of U_∞.

(u) and vertical (w) components of velocity. It is clear that any changes due to the mirror are lower than the measurement errors.

One of the concerns of cross-stream PIV is the high ratio of through-plane velocity to in-plane velocities. Due to the fast through-plane velocity, the time-delay Δt between the image acquisitions is limited to small values. If the Δt is too long, the particles will move out of the laser plane before they can be imaged the second time (and new particles will be illuminated that weren't in the first image). This limits the Δt to low values and creates a compromise: if the Δt is low, the in-plane displacements are low, reducing the signal-to-noise ratio; if the Δt is high, the displacements are higher, but the correlation errors are also higher.

In order to alleviate these problems, there are several approaches. Waldman & Breuer (2012) suggests displacing the illumination plane between the images for correlation. This allows a higher Δt without losing particles. For the flow considered by Waldman & Breuer (2012), trailing vortices behind a wing, this method worked well in improving the correlations. For the Ahmed flow, however, the axial flow is less uniform across the acquisition plane, meaning the benefits of this method also would be non-uniform. Additionally, and more importantly, the Ahmed wake contains large regions of recirculating flow, where the flow is moving upstream. If the laser plane were moved downstream between image A and B, no correlation would be possible.

A second method for reducing the errors is to have a thicker laser plane, illuminating a volume rather than a quasi-plane. This works a similar way to offsetting the laser plane, without the

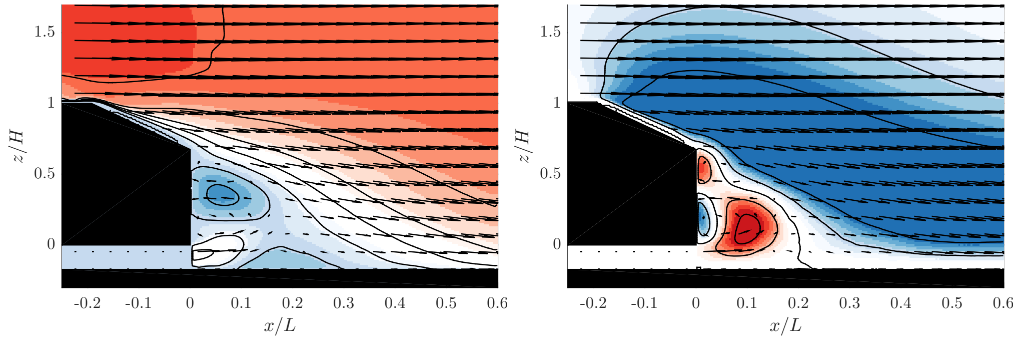

(a) No mirror, u (b) No mirror, w

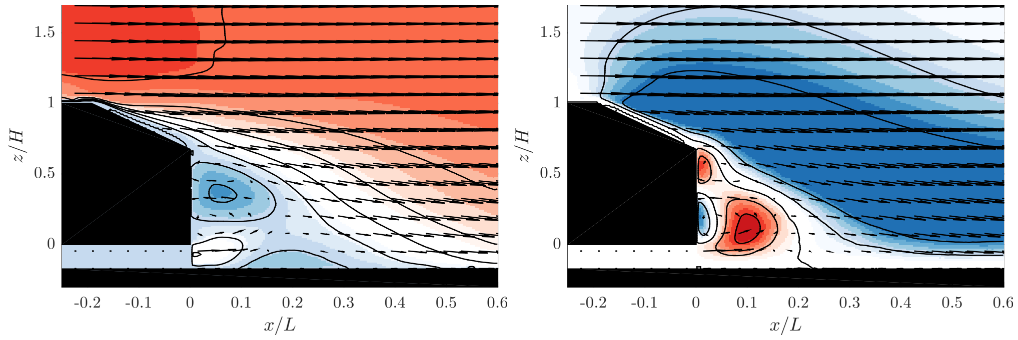

(c) With mirror, u (d) With mirror, w

Figure 3.16: The effect of a downstream mirror on flow in the symmetry plane behind a standard width Ahmed body. Filled contours are the velocity field (left is streamwise (u), right is vertical (w), overlaid with velocity vectors. Contour levels are constant between the top row (no mirror) and the bottom (with mirror).

problem of recirculating flow. Given that a laser plane thickness of $3mm$, which is already higher than for other similar setups, returned high quality correlations, the $3mm$ laser plane was chosen.

3.4.3 Force measurement

Force measurements in aerodynamic experiments are broadly in two categories, those with the balance inside the model (*internal balances*), and those with the balance outside the model (*external balances*). Some of the advantages of the internal balance are that it will only measure forces on the body without measuring the force of the sting, and that the moments are reduced. One of the disadvantages is that the balance must be small enough to fit into the body, and if the cavity is exposed to water, must be water-proof.

The forces on the Ahmed models were measured using an off-the-shelf force balance. The ATI Mini-40 force balance measures all six components of force and torque (F_x, F_y, F_z, M_x, M_y, and M_z). The sensor utilises silicon strain gauges which provide high signal-to-noise ratios. It is rated to IP-68 water-proofing, meaning it is protected from long-term immersion up to $4m$ depth, making it suitable as an internal balance in the water channel.

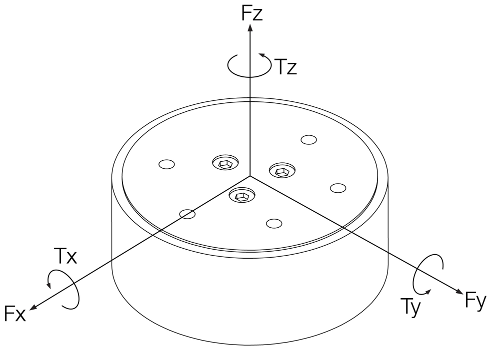

Figure 3.17: ATI force balance and coordinate system for forces and moments.

Each Ahmed body was hollowed out to provide a cavity for the internal balance. The balance was placed approximately at the centre-of-mass, calculated using a CAD model of the bodies. Figure 3.18 shows how the balance was assembled. Everything above the ATI (red) is static (fixed to the channel walls), and everything below is fixed only through the ATI balance, to allow for the force measurement of the body, and solely the body. A $1mm$ gap is between the upper lid (orange) and the Ahmed body.

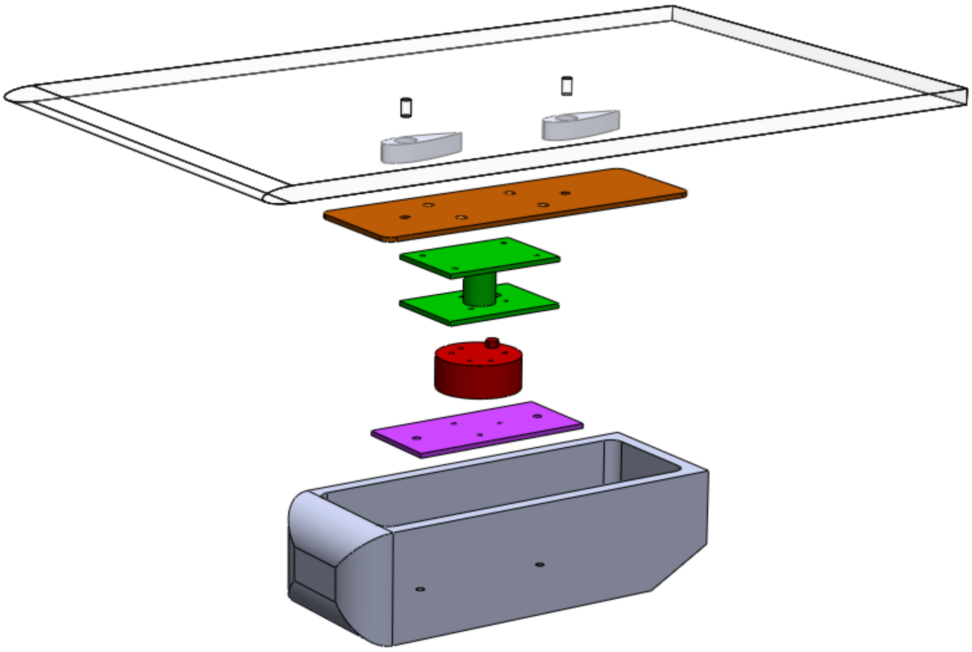

Figure 3.18: Assembly drawing for force measurement with the Ahmed body. The lower mounting plate (pink), ATI force balance (red), and upper mounting plate (green) remain as one piece. These are bolted to the base of the Ahmed model. The lid (orange) is then attached to the top of the upper mounting plate. Bolts pass through the ground plane, through the airfoil sheaths, and into the lid.

The DAQ system measured six voltages from the ATI sensor. These were converted to engineering units through the following equation:

$$A \times V = F \tag{3.5}$$

Where A is the decoupling matrix, V are the voltages, and F are the decoupled loads. For the six-component ATI balance, these values were:

$$\begin{bmatrix} 0.07425 & 0.03208 & -0.04432 & 3.15488 & 0.05079 & -3.13738 \\ -0.10618 & -3.76175 & 0.05082 & 1.84494 & -0.03609 & 1.75355 \\ 5.11041 & -0.07232 & 5.25602 & 0.04929 & 5.33130 & -0.12227 \\ -0.00238 & -0.04015 & 0.07408 & 0.01911 & -0.07755 & 0.02184 \\ -0.08326 & 0.00239 & 0.04390 & -0.03414 & 0.04446 & 0.03177 \\ -0.00026 & -0.04552 & -0.00100 & -0.04461 & 0.00113 & -0.04447 \end{bmatrix} \times \begin{bmatrix} V_1 \\ V_2 \\ V_3 \\ V_4 \\ V_5 \\ V_6 \end{bmatrix} = \begin{bmatrix} F_x \\ F_y \\ F_z \\ M_x \\ M_y \\ M_z \end{bmatrix} \tag{3.6}$$

To ensure the decoupling matrix was correct, a static, linear force calibration was performed. The ATI balance was mounted to a level, fixed plate and various masses were attached to the balance. For each mass, an accurate weight measurement was taken, and then it was applied to the balance. To check for hysteresis, measurements were taken when both loading and unloading the forces. The results (figure 3.19 shows linear results, no hysteresis, and a 1:1 relationship between the measured and applied forces.

The force balance was validated by measuring the body forces acting on a static circular cylinder across a range of Reynolds numbers. The data is in figure 3.20 showing stable measurements that fit well with literature. The data matches better with other experiments in the same facility, even though these were with a different force measurement system. This indicates that the differences are due more to the water channel than errors in the force measurement.

3.4.4 Temperature measurement

The temperature of the water was measured using a resistive temperature detector connected to the data acquisition system. The temperature was logged to calculate the Reynolds number for each experiment.

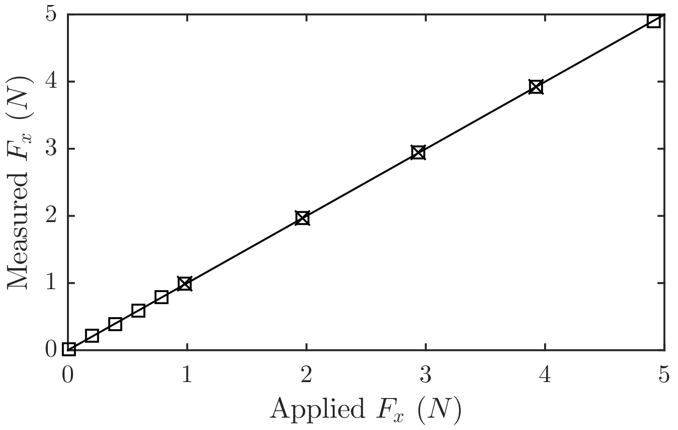

(a) Forces applied in x direction.

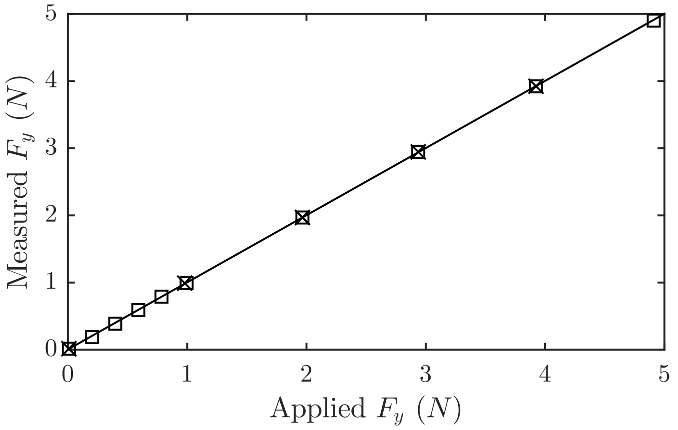

(b) Forces applied in y direction.

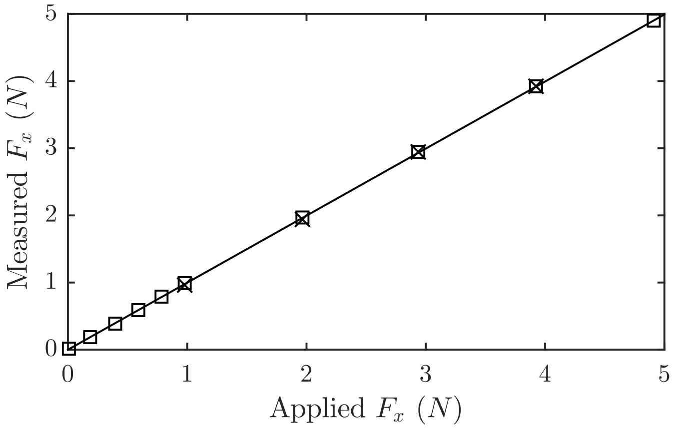

(c) Forces applied in z direction.

FIGURE 3.19: Linear calibration results for ATI force balance measuring static known masses. Hysteresis is checked by loading (squares) and unloading (crosses). The gradients (and 95% confidence bounds) of the linear fits for F_x, F_y, and F_z respectively are: 0.9992 (0.9987, 0.9998), 0.9996 (0.9991, 1), and 0.9983 (0.9971, 0.9994).

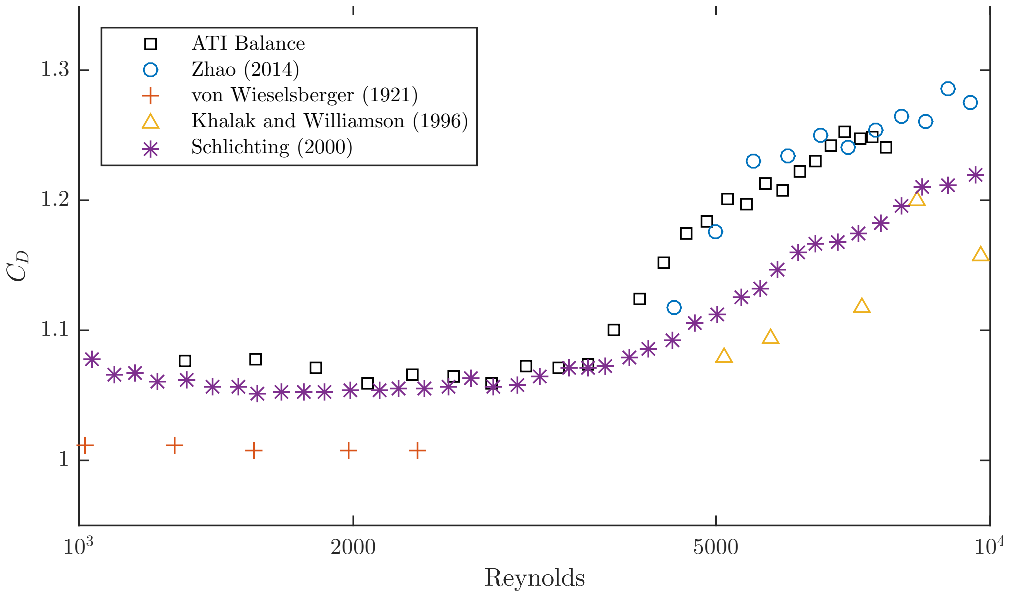

Figure 3.20: Drag of a circular cylinder as a function of Reynolds number. Data from Zhao *et al.* (2014) was acquired with the same setup as validated in the paper though the data is from personal communication. Data from the ATI force balance matches well with previous experiments in the same facility but using a different force balance (Zhao *et al.*, 2014). Literature data provided from von Wieselsberger (1921), Khalak & Williamson (1996), and Schlichting (2000).

3.5 Post-processing of velocity fields

3.5.1 Spectral density estimation

The spectral density estimation tool was developed for visualising frequencies and their magnitudes throughout the spatial region in any velocity field. It is essentially an FFT being applied at each point in space, following the example of Basley *et al.* (2010). This section describes the procedure.

The estimation of the spectrum is based on a moving-window FFT over the time signal of the velocity at each point in space. The Hanning window function is applied to each subset of the time-series before applying the Fourier transform. Zero-padding is also used to smooth the output signal and aid in peak-detection.

The FFT is a powerful tool for analyzing data in time series by converting the series from the time domain to the frequency domain. It is an efficient means to calculate the Discrete Fourier Transform (DFT). The DFT converts an evenly-sampled time-series into a combination of complex sinusoids each with a coefficient related to the relative importance of that frequency in the entire spectrum. The DFT for the time series x that is N points long can be calculated by:

$$X_k = \sum_{n=0}^{N-1} x_n e^{-i2\pi k \frac{n}{N}} \qquad k = 0, \ldots, N-1. \tag{3.7}$$

Each X_k is a complex number containing the amplitude and the phase for each sinusoidal component of the time series. The frequencies start from $f = 0$ which is the time-average component and stop at the Nyquist frequency $f = f_s/2$. The frequency resolution is $\Delta f = f_s/N$. The power and phase of each frequency are given by:

$$\text{Power} = \sqrt{\text{Re}(X_k)^2 + \text{Im}(X_k)^2}/N \tag{3.8}$$

$$\phi = \text{atan2}(\text{Im}(X_k), \text{Re}(X_k)) \tag{3.9}$$

The units for the power at each frequency, for a velocity signal, is velocity root-mean-square. The phase information is relative to the start of the time-domain signal. The FFT returns a two-sided spectrum, i.e. containing positive frequencies, negative frequencies, and the time-average component. To eliminate these, every non-zero X_k value is multiplied by two and the negative half is discarded.

The spectra for all the windows from a sample data set (in this case the wake of a square plate at 60° incidence) can also be plotted, as in figure 3.21. This figure shows the variation of the powers of the frequencies with window (time). An average of all these windows is then taken to give a representation of the frequency information for the whole time series (figure 3.22). This spectrum shows five peaks: one low frequency related to the von Kármán shedding, and four peaks around a frequency of St $= 2$. To understand from where these peaks arise, an FFT is performed at every spatial point in the domain, allowing the power and phase of each frequency to be visualised across space. For example, figure 3.23 shows the power and phase information of the St $= 1.27$ frequency. From the power figure it is clear that the frequency is most dominant in the downstream region of the shear layer. It is noteworthy that the frequency is not found in the entire region of the shear layer, i.e. that the frequency varies within the shear layer. This is discussed in depth in chapter 4.

The phase information shows what regions of the flow are fluctuating in phase. A circular colour map in figure 3.24 has been designed to show the phase. Regions in the map that have the same colour are oscillating in phase with each other. Opposite colours are π out of phase, while adjacent colours are $\pi/2$ out of phase.

Since the phase information varies with time, it cannot simply be averaged as the power is (this removes the phase information). For a given frequency though, the phase of each window represents a different snapshot of the phenomena. By building these into a large matrix, and using the singular value decomposition (SVD), the zeroth mode will reveal the 'average' phase.

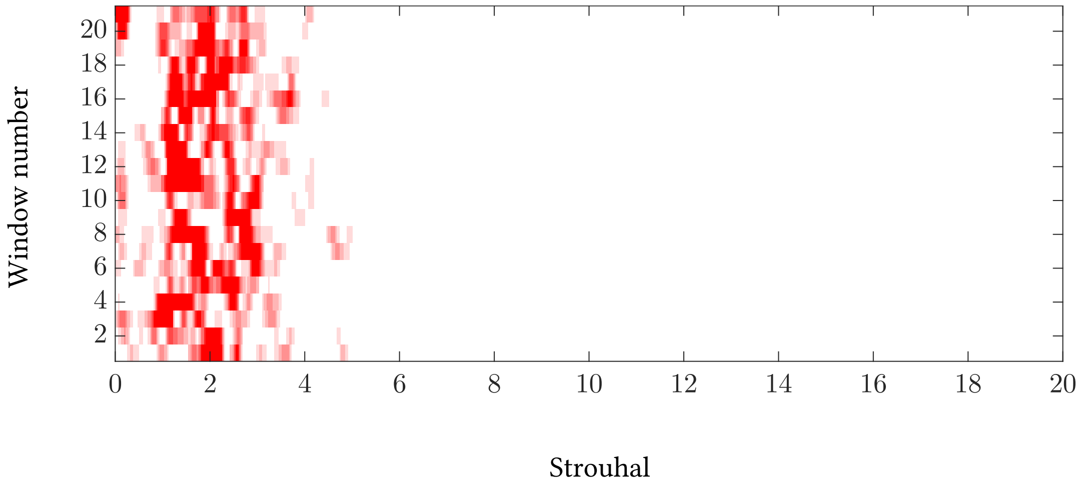

Figure 3.21: The frequency spectra from all the windows of the sample data. Darker red indicates higher power.

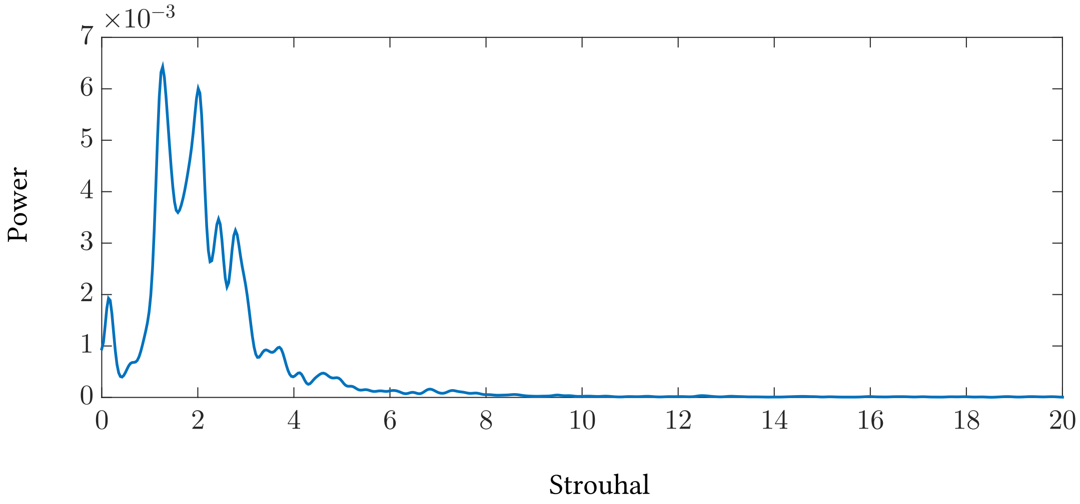

Figure 3.22: An average of all frequency spectra from the sample data.

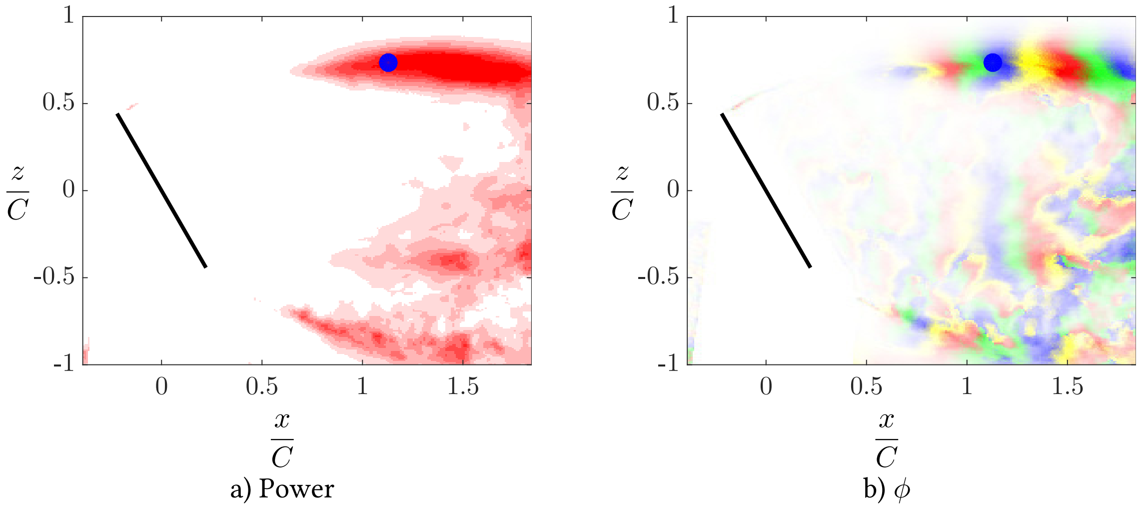

FIGURE 3.23: Power (a) and phase (b) information of the St $= 1.27$ frequency in the wake of an AR $= 1$ plate inclined at $\alpha = 60°$. In (a), red indicates power of the frequency. The blue dot represents the location of the sample data used above. In (b), phase is represented by the colour map from figure 3.24, and the transparency map is generated by the power. Flow is from left to right. Twenty-one spectra are included in the average.

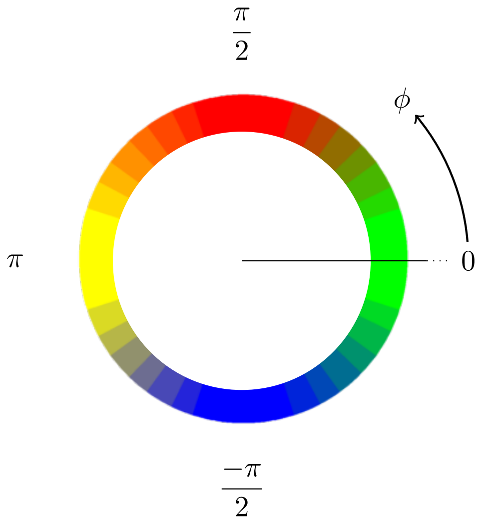

FIGURE 3.24: The colour map used for phase plots in this thesis.

3.5.2 The Γ criteria

The Γ_1 and Γ_2 criteria were described by Graftieaux (2001). Γ_2 is a Galilean invariant scalar related to the rotation of the fluid in a region of interest around each point. It is not influenced by the magnitude of velocity vectors, but rather the direction of each vector. As such, it is helpful for visualising areas of rotation, not just vorticity, which may be dominated by regions of high shear. Γ_1 is not Galilean invariant as it does not remove the local convection velocity in each interrogation region.

For a point, P, Γ_2 is defined by:

$$\Gamma_2(P) = \frac{1}{N}\sum \sin(\theta) \tag{3.10}$$

Where N is the number of points in the Γ_2 interrogation region R, and θ is the angle between the fluctuating velocity vector and a line between the origin of that vector and the point P. An illustration of these variables is given in figure 3.25. A counter-clockwise rotation is positive whilst clock-wise rotation is considered negative.

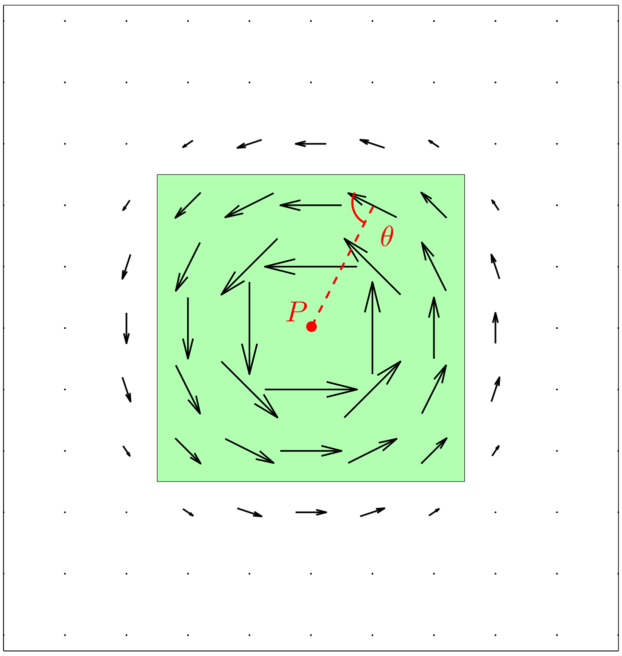

FIGURE 3.25: Γ_2 illustration for a sample vortex. Vectors represent the fluctuating (mean removed) velocity components. The interrogation region, R, is in green. The Γ_2 function is the sum of the sines of all the angles, θ, in the interrogation window. This sum is then divided by the number of points in the window, N, which is 24 in this example. Since each velocity vector in this example is perpendicular to a line from its origin to the point, P, the contribution to the Γ_2 field from each of these vectors is 1. Thus, the average across the interrogation region will also be 1.

The parameter N acts as a spatial filter: the larger it is, the more small-scale fluctuations are removed. Figure 3.26 shows how the gamma calculation varies with this interrogation region size, N. As long as the region is smaller than the vortex, the Γ_2 calculation will peak at 1, with the peak being lower than 1 if the region is larger. This gives the washed-out appearance in figure 3.27. It is therefore suggested to select the region size based on $\sqrt{2} \cdot r$ where r is the radius of the vortex.

3.5.3 Vorticity

Vorticity characterizes the rotation rate of a fluid particle. The vorticity is defined as $\omega = \nabla \times u$, that is, vorticity is the curl of the velocity field:

$$\left(\frac{\partial w}{\partial y} - \frac{\partial v}{\partial z}\right)_x + \left(\frac{\partial u}{\partial z} - \frac{\partial w}{\partial x}\right)_y + \left(\frac{\partial v}{\partial x} - \frac{\partial u}{\partial y}\right)_z \tag{3.11}$$

Because of its dependence on spatial gradients, an accurate vorticity measurement requires accurate velocity measurements with fine spatial resolution.

Vorticity is not a suitable method for characterising the location or extent of a vortex. Local vortex identification algorithms such as Q (Hunt *et al.*, 1988), λ_2 (Jeong & Hussain, 1995), Δ (Chong *et al.*, 1990), and λ_{ci} (Zhou *et al.*, 1999) all seek to identify vortex filaments from velocity fields. An excellent review of these methods is given by Chakraborty *et al.* (2005). The Q-criterion is a Galilean invariant quantity and is chosen in this study as it measures the excess rotation rate relative to the strain rate, i.e., where the local rotation dominates the shear.

3.5.3.1 Out-of-plane vorticity

Out-of-plane vorticity, ω_z can be calculated from the in-plane velocity measurements:

$$\omega_z = \frac{\partial v}{\partial x} - \frac{\partial u}{\partial y} \tag{3.12}$$

To estimate the velocity gradients, a χ^2 polynomial is fit to the velocity data, with analytical differentiation of the fields. Further details on this method can be found in Fouras & Soria (1998).

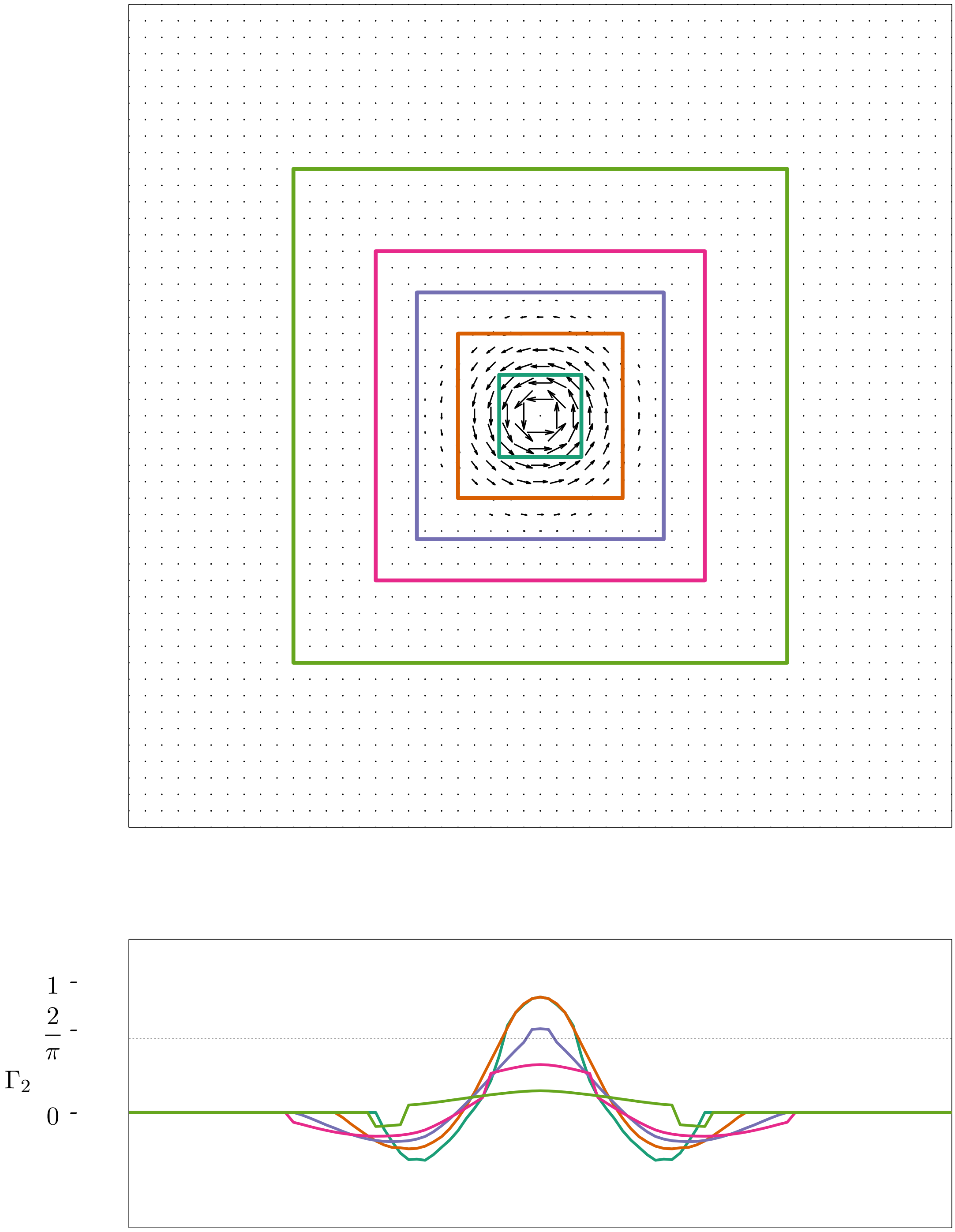

Figure 3.26: Comparison of Γ_2 calculations with changing region sizes. The various interrogation window sizes are denoted by the various colours. The Γ_2 strength as varies across the x-dimension is plotted below.

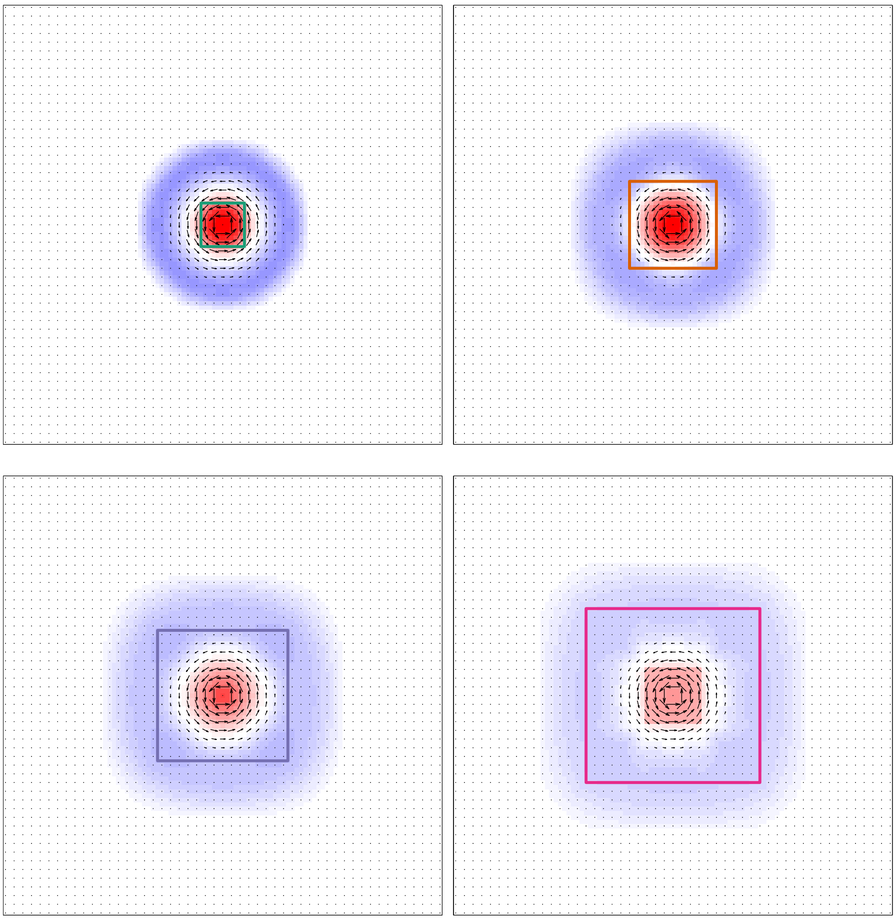

FIGURE 3.27: Γ_2 fields for the same region sizes presented in figure 3.26.

3.5.4 Circulation calculations

The circulation of a vortex can be calculated by:

$$\Gamma = \oint_C \mathbf{V} \cdot d\mathbf{l} \tag{3.13}$$

or, according to Stokes' theorem relating line integrals to surface integrals:

$$\Gamma = \iint_S \omega \cdot d\mathbf{S} \tag{3.14}$$

Theoretically, the integral in equation 3.13 should be path-independent, that is, the shape of the contour itself should not influence the integral providing it includes the vortex. However, given the PIV data is set at a discrete grid, and vorticity is diffused around the vortex, the contour chosen is in fact important.

The algorithm for integration of a velocity field ($u(x, y)$ and $v(x, y)$) around a curved contour (C) is as follows:

1. Find x and y coordinates of all points on the curve C.
2. Interpolate C onto an evenly spaced grid of N points around the curve C.
3. Interpolate u and v onto the same grid. This is performed using MATLAB's `improfile` function.
4. Calculate the angle α of each segment of C.
5. Integrate $u \times \cos\alpha - v \times \sin\alpha$ using trapezoidal quadrature function.

Figure 3.28 shows the circulation calculations for a single vortex in the wake of the Ahmed body. In the left hand image, the velocity vector field is presented, showing the strong vortical structure that is produced by the c-pillar slant. Circles with various radii all centred on the maximum vorticity are also shown. The circulation was calculated using each of these lines as the vortex bound. This is shown in figure 3.28 (b). Firstly, it can be seen that the line integral and the surface integral match well. Secondly, we see that as the circle radius increases, more of the vorticity is captured, and hence the circulation increases with radius up until a radius of $10mm$, where the circulation begins to decline. This decline is due to oppositely rotating vorticity being captured in the larger circles.

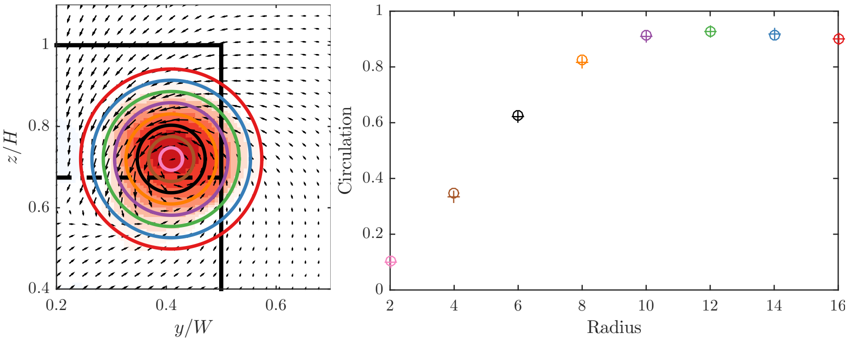

Figure 3.28: Circulation as a function of the radius used to define the contour. Circular symbols are the line integral of the velocity, plus symbols are the surface integral of the vorticity.

Rather than using a circle to define the bounds of the vortex, Graftieaux (2001) suggests the use of the Γ_2 criterion. Various contours of Γ_2 are overlaid on the plot in figure 3.29 (a). This allows a more complex vortex shape to be captured than can be found solely using a circle. The drawback with this method is that it is dependent on the level chosen (figure 3.29 (b). Graftieaux (2001) suggests that the limit of $\Gamma_2 = 2/\pi$ is suitable since, that is the lower limit beyond which the flow is locally dominated by rotation. This is the method adopted for this study.

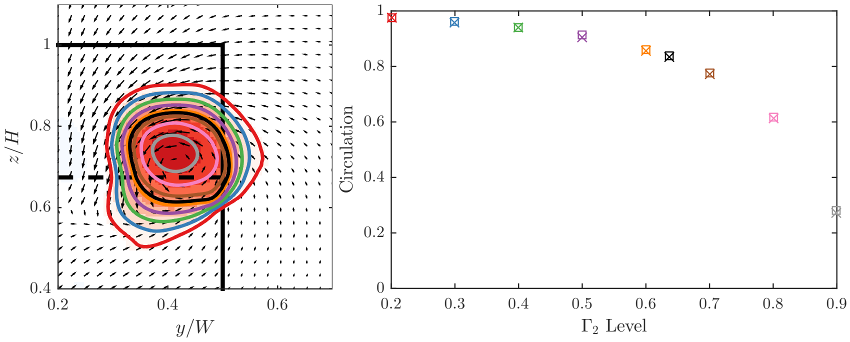

FIGURE 3.29: Circulation as a function of the Γ_2 level used to define the contour. Square symbols are the line integral of the velocity, x symbols are the surface integral of the vorticity. $\Gamma_2 = 2/\pi$ indicated by black point.

3.5.5 Proper Orthogonal Decomposition

Proper Orthogonal Decomposition (POD) is a method for identifying the structures in a flow based on the energy content of a series of modes. It is possible to rank the various motions in the flow on the kinetic energy of each mode. While the modes do not directly correspond to flow structures, the modes reveal information as to where the most energetic structures are. The method of snapshots (Sirovich, 1987) was used for the present study where the number of temporal realisations is less than the number of spatial realisations.

The velocity field in space and time $u(x,t)$ is decomposed into the temporal coefficient $a^k(t)$ of mode k and the spatial mode $\phi^k(x)$:

$$u(x,t) = \sum_{k=1}^{K} a^k(t) \cdot \phi^k(x) \tag{3.15}$$

For fluid mechanic applications, x can be viewed as a spatial coordinate, and t as the temporal coordinate. The approximation would be exact as K approaches infinity, however, the POD seeks to produce an accurate approximation using only the several most energetic modes, the methodology is as follows:

Given a set of N velocity instances:

$$\mathbf{U} = [\mathbf{u}^1 + \mathbf{u}^2 + ... + \mathbf{u}^N] \tag{3.16}$$

solve the eigenvalue problem:

$$\mathbf{C}\mathbf{A}^i = \lambda \mathbf{A}^i \tag{3.17}$$

where:

$$\mathbf{C} = \mathbf{U}^T\mathbf{U} \tag{3.18}$$

Sort the solutions according to their eigenvalues, which gives the POD modes normalized as:

$$\phi^i = \frac{\sum_{n=1}^{N} \mathbf{A}^i \mathbf{u}^n}{|| \sum_{n=1}^{N} \mathbf{A}^i \mathbf{u}^n ||} \tag{3.19}$$

The data can be reconstructed by projecting the data set on to the orthonormal modes. If all the modes are included, the instantaneous field is returned. By being selective, however, of the modes used in the reconstruction, it is possible to filter out low energy modes corresponding to small-scale structures and PIV error. Figure 3.30 shows a sequence of the same snapshots at a single point in time but with the inclusion of different numbers of modes in the reconstruction. It is clear that the instantaneous field is influenced by factors such as PIV error and turbulence which are not the major flow structures and hence are of less import in this study which focuses on the large structures themselves and their unsteadiness. Figure 3.30 (b) shows the reconstructed frame from the POD including all the modes, which is identical to the instantaneous frame. As the number of included modes decreases, the smaller structures are removed and only the large, energetic structures are left. If only the $N = 0$ mode is included, the result is the ensemble-averaged velocity field.

The spatial modes themselves reveal information about where the primary motions take place (figure 3.31). The zeroth mode is the ensemble average, indicating that the bulk of the energy is involved in the mean flow. In higher modes, the energy of the structures decrease (by definition), so the scale of motions get smaller.

Besides filtering, the POD analysis also reveals information about the turbulent flow field. It can be used to identify the major structures, as well as provide some insights into their temporal relationships. Figure 3.32 shows the energy spectra from two PIV data sets, one is the Ahmed body wake as described above. Here we see the modes are all low-energy, with a steady decline in energy with POD mode. When we consider the energy spectrum of a two-dimensional case with vortex shedding, here for example is the shedding behind the two-dimensional flat plate, we see a pair of modes early in the spectrum with high energy. In this example, over 50% of the energy is contained in the first pair of modes. From there onwards, there is again a steady decrease in the energy.

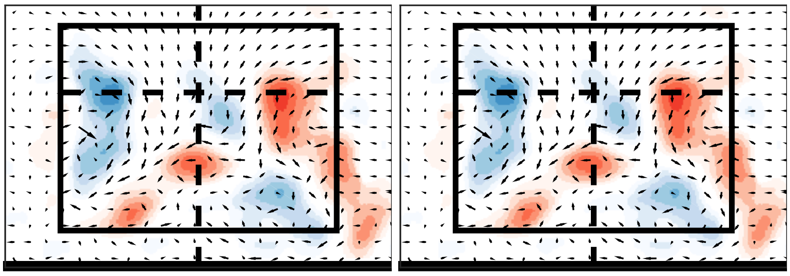

(a) Instantaneous (b) $N = 500$

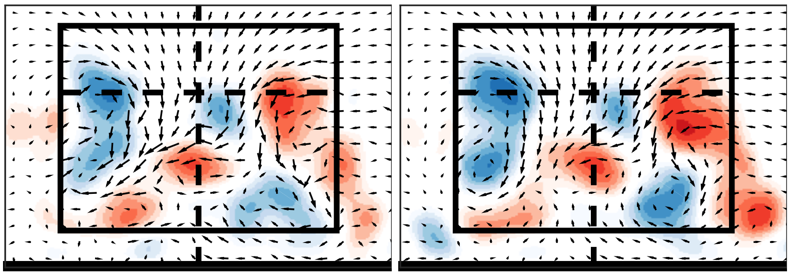

(c) $N = 100$ (d) $N = 20$

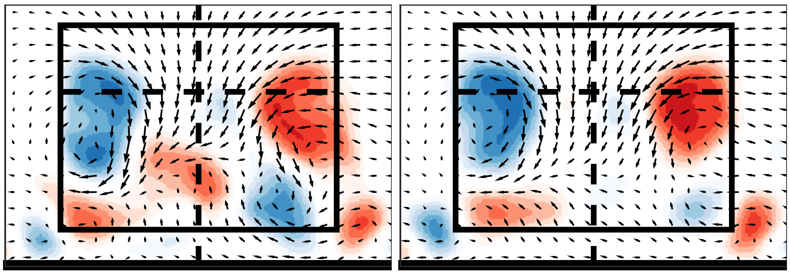

(e) $N = 10$ (f) $N = 5$

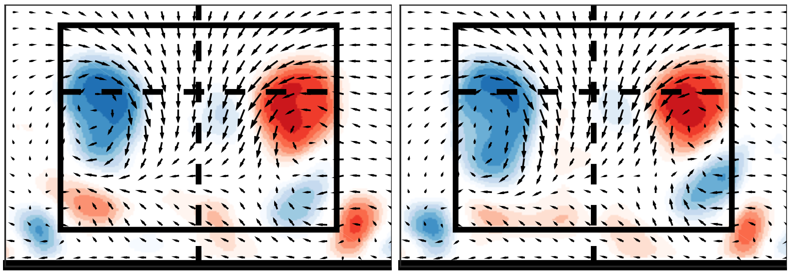

(g) $N = 3$ (h) $N = 2$

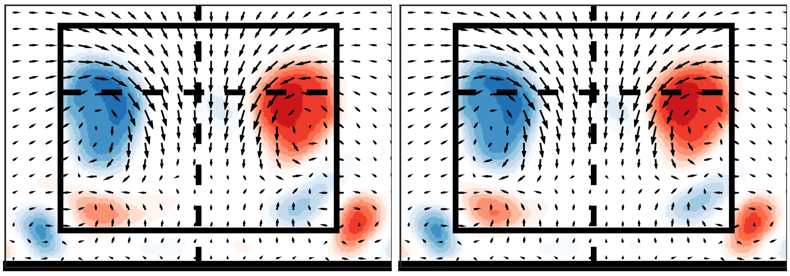

(i) $N = 1$ (j) $N = 0$

Figure 3.30: The wake of the Ahmed body shown as POD reconstructions including various numbers of POD modes.

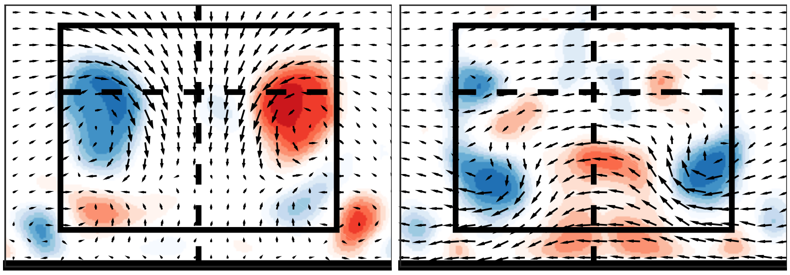

(a) $N = 0$ (b) $N = 1$

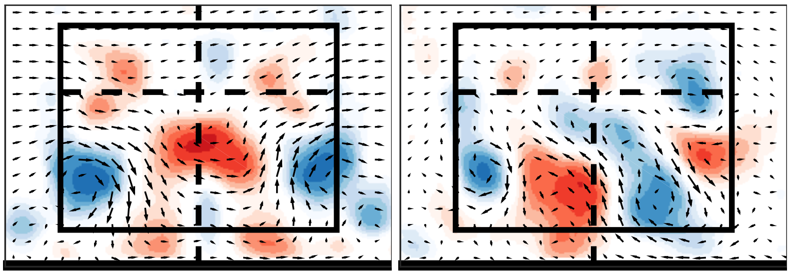

(c) $N = 2$ (d) $N = 5$

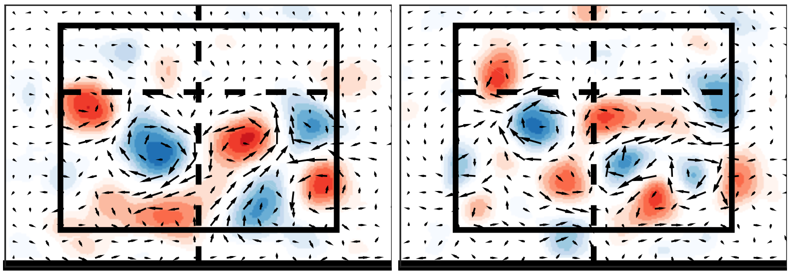

(e) $N = 10$ (f) $N = 20$

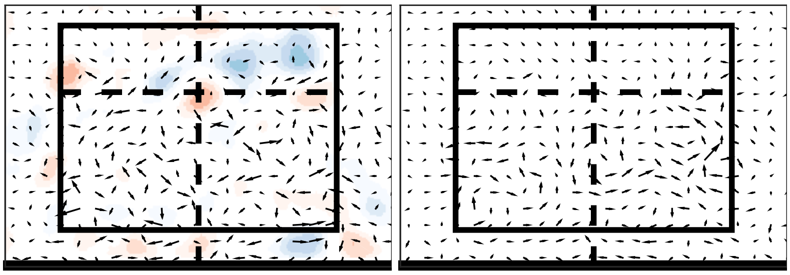

(g) $N = 100$ (h) $N = 500$

Figure 3.31: The spatial POD modes in the wake of the Ahmed body. The modes are represented by the vector field, with the filled contours representing the rotation in that field.

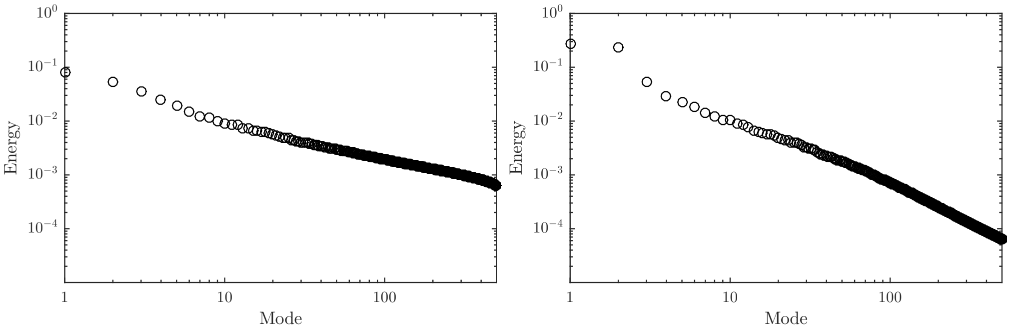

(a) Non-shedding (b) Shedding

Figure 3.32: The relative energy of each POD mode. In (a) is the turbulent wake of the Ahmed body, with no coherent shedding mechanism. In (b) is the organized vortex shedding behind a two-dimensional flat plate.

Furthermore, temporal information can be extracted from the POD, showing the relative dominance of each mode and how that varies with time. Figure 3.33 plots the eigenvectors from the POD deconstruction, that is, the temporal coefficients as they vary in time. In the non-shedding case, it is clear that the coefficients show no clear patterns or trends. Behind the flat plate, however, in figure 3.33 (b), the first two modes are periodic, and offset by a phase shift of $\pi/2$. Plotting these modes against each other, rather than time, shows the phase plot of each system (figure 3.34). In the first case, it is clear that there is no real relationship between the two modes, as evidenced by the messiness in the plot. For the shedding case, however, we can verify that the modes are oscillating at the same frequency (else there would be multiple lobes), and with the same magnitude (else the image would not be circular).

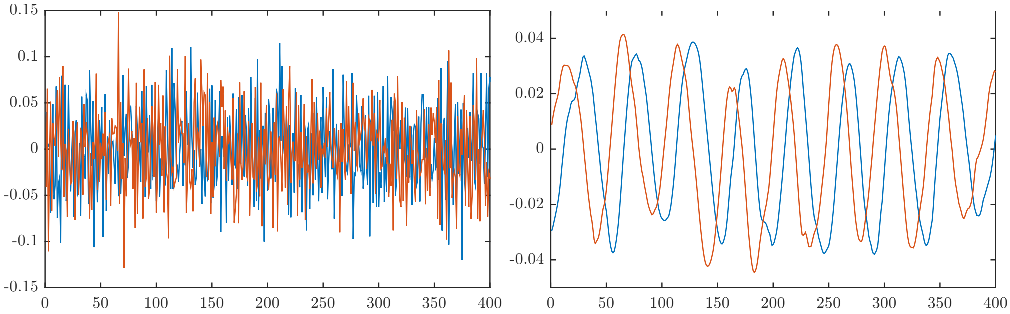

(a) Non-shedding (b) Shedding

Figure 3.33: The temporal coefficients of the first two POD modes.

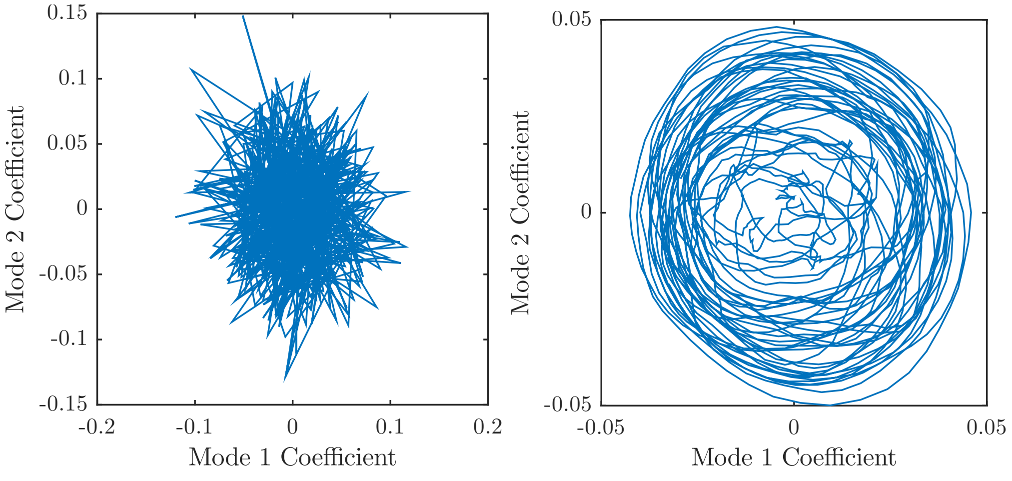

(a) Non-shedding (b) Shedding

Figure 3.34: The phase of the first two POD modes for turbulent (left) and shedding (right) cases.

3.6 Uncertainty Analysis

An uncertainty analysis was performed on the Strouhal number calculations as described by Coleman & Steele (1995), breaking down the uncertainty into the bias (B) and precision (P) errors. The contributing variables to the Strouhal number are:

$$St = \frac{fL}{U_\infty} \tag{3.20}$$

The bias limits are estimated as follows:

- B_L: 1/2 of the instrument resolution, which is $0.02mm$
- B_{U_∞}: sub-pixel accuracy of PIV measurements
- B_f: 1/2 spectral resolution from PSD measurements (varies with Re)

The precision limits are:

- P_L: $0.06mm$: twice the standard deviation of the plate chord measurements
- P_{U_∞}: twice the standard deviation of the free-stream velocity measurements

The sensitivity coefficients are derived from the partial derivative of the calculated quantity with respect to each component variable:

$$\theta_{U_\infty} = \frac{\partial St}{\partial U_\infty} = \frac{fL}{U_\infty^2} \tag{3.21}$$

Table 3.3: Sensitivity coefficients

Reynolds	θ_{U_∞}	θ_L	θ_f
790	$2.95s/m$	$13.33m^{-1}$	4.52Hz^{-1}
24000	$2.58s/m$	$0.39m^{-1}$	0.15Hz^{-1}

Table 3.4: Uncertainty analysis for Strouhal number calculations at two Reynolds numbers.

		θB	$\%B$	θP	$\%P$
$\text{Re} = 790$	L	0.000015	0.03%	0.000353	1.11%
	U_∞	0.000518	37.97%	0.003338	98.89%
	f	0.000661	62.00%	–	–
$\text{Re} = 24000$	L	0.000013	0.00%	0.000309	90.95%
	U_∞	0.000475	2.15%	0.000098	9.06%
	f	0.003209	97.85%	–	–

Table 3.5: Uncertainty results for Strouhal number calculations.

	$\text{Re} = 790$	$\text{Re} = 24000$
B_{St}	0.000840	0.003244
$\%U_{St}$	5.89%	99.01%
P_{St}	0.003357	0.000324
$\%U_{St}$	94.11%	0.99%
U_{St}	0.003460	0.003260
$\%St$	1.95%	2.10%

$$\theta_L = \frac{\partial St}{\partial L} = \frac{f}{U_\infty} \tag{3.22}$$

$$\theta_f = \frac{\partial St}{\partial f} = \frac{L}{U_\infty} \tag{3.23}$$

The uncertainty was analysed for each Reynolds number, but results are presented here for the two extremeties of the Reynolds range.

At the low end of the Reynolds range, the uncertainty primarily originates from the precision error (94%). This, in turn, is dominated by the uncertainty in U_∞(99%). The total uncertainty of the Strouhal number is less than 2%. For the same analysis at the highest Reynolds number, the uncertainty comes almost exclusively from bias errors (99%), of which 98% originates in the errors from the PSD. That said, the total uncertainty is still close to 2%.

Chapter 4

The Wake of a Flat Plate

4.1 Introduction

This chapter studies the flow around a two-dimensional flat plate. The parameters of interest are the Reynolds number and the angle-of-incidence. The two-dimensional wake is studied in both a time-averaged sense and in terms of the wake dynamics.

The chapter contains a section on experimental parameters used, outlining the plate details and the apparatus used to acquire the data. The time-averaged flow is reported to analyse the differences between the leading- and trailing-edge shear layers.

The theoretical flow dynamics behind the plate is computed using local stability analysis. These results, which predict preferred oscillation frequencies, are then compared with the experimental findings. The various frequencies in the wake are quantified and visualised, explaining the formation of von Kármán vortices from the shear-layer vorticity.

Key findings:

- the vorticity in the leading-edge shear layer is not a function of the angle-of-attack, while in the trailing-edge shear layer it is
- the ratio of circulation in the shear layers linearly depends on the angle of attack, but this is due to the increased length of the leading-edge shear layer rather than the shear gradient close to the edge
- linear stability analysis be used to calculate both the global frequency and the recirculation length

- there is a critical Reynolds number ($Re = 1500$) at which there is a minimum in the wake length and a maximum in the Strouhal number
- while this transition is at the same Reynolds number as the circular cylinder's transition at which shear-layer vortices form, the nature of the transitions is quite different
- the mechanism of von Kármán vortex formation from the free shear layer is shown to consist of an amalgamation of a variable number of shear-layer vortices
- the most common shear-layer frequency is shown to exhibit a power law relationship with the Reynolds number, through the equation $\frac{f_{SL}}{f_K} = 0.043 \times Re^{0.67}$

4.2 Measurement and Data Processing

The flat plate (section 3.3.1) was placed in the mini-channel to allow lower Reynolds numbers to be reached, consistent with the numerical predictions. The channel works by partially obstructing the flow with a pressure plate at the rear end of the mini-channel as described in section 3.2.1. This increases the flow velocity outside the mini-channel and decreases the velocity inside while keeping the inside flow uniform (Radi *et al.*, 2014).

4.2.1 PIV parameters

The continuous laser, as described in section 3.4.2.2, was used to illuminate the flow in an xy (streamwise and transverse) plane. This allowed the streamwise and transverse components of velocity to be acquired. The PCO dimax camera was used at the settings detailed in table 3.1 for the Reynolds number sweep. For the angle-of-attack study, the camera was used in two settings to focus either on the whole wake or the leading-edge shear layer. In both cases the camera was used at maximum resolution (2016×2016 pixels). The acquisition rate was $4fps$ and $8fps$ for the full wake and shear-layer studies respectively.

For the two-dimensional case two magnification factors were used to investigate the flow around the inclined plate. Figure 4.1 shows how well the two datasets overlapped. Whilst there is some variation at the edges of the window due to optical distortion, overall the fit is good.

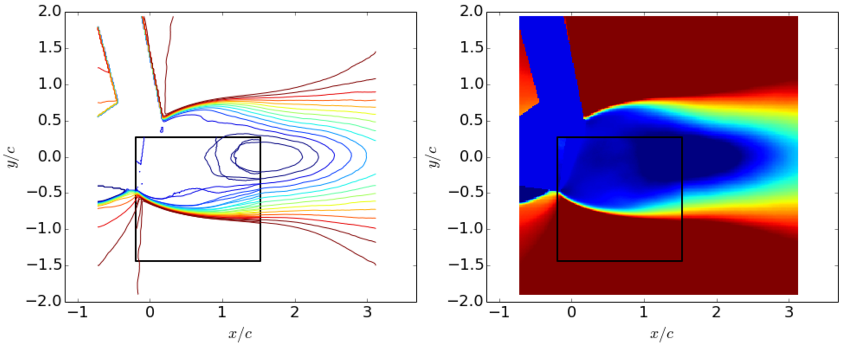

FIGURE 4.1: The time-averaged wake of a 70° plate spanning the water channel. Left shows contours of freestream velocity for the wide field of view data overlaid with data from the narrow field of view, outlined with black square. Right shows filled contours of freestream velocity.

4.3 Flow visualisation

Dye visualisation photographs can speak volumes about the physics in a fluid dynamics problem. In this case, the plate was placed in the water channel and two streams of dye were injected upstream of the plate at the same spanwise position. In the photograph in figure 4.2 the shear-layer vortices are visible in the green dye. Three clear vortices are present in the wake extending ~ 3 chord lengths downstream. At the near-edge, the vortices are already combining into a von Kármán vortex; these are shed alternately from each side.

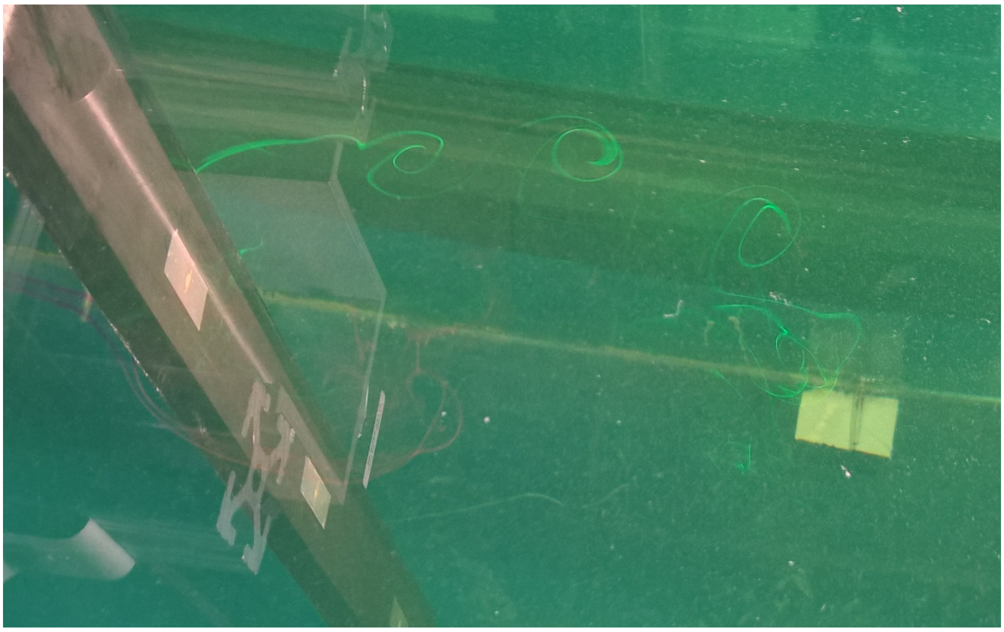

FIGURE 4.2: Dye visualisation behind the normal flat plate at $Re = 1400$.

What is not evident from the photograph but was clear in observing the visualisations was the in-phase appearance of the shear-layer vortices from each edge of the plate, that is, the shear layers were symmetric about the $y = 0$ plane (this behaviour is also evident in the PIV measurements in figure 4.19). Similarly to the findings of Gerrard (1978) for the circular cylinder, the shear-layer vortices formed parallel to the plate edge, visible as vertical 'columns' of dye moving downstream.

4.4 Time averaged results

Figure 4.3 shows the mean flow field for the flat plate, both normal to the flow and at a 60° angle-of-incidence. Several features are evident: firstly, the wake consists of two strong shear layers, as evidenced in the vorticity plots. These shear layers, and in fact the whole wake, are symmetric for the normal case. For the angled case, however, the leading-edge shear layer is longer, such that they truncate at approximately the same downstream position. This indicates where the von Kármán vortices form, since their existence results in the degradation of the shear layers in the time-averaged sense.

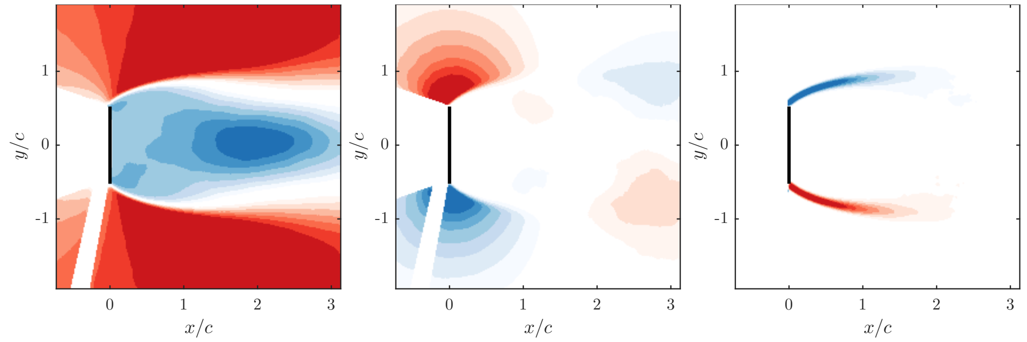

(a) Streamwise Velocity (b) Transverse Velocity (c) Spanwise Vorticity

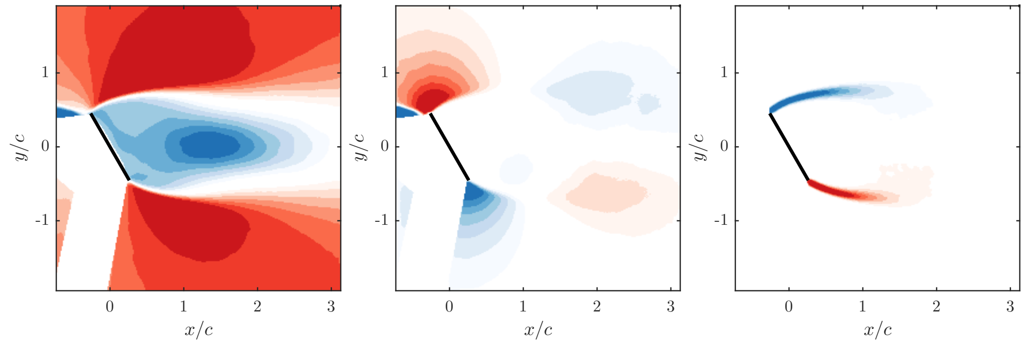

(d) Streamwise Velocity (e) Transverse Velocity (f) Spanwise Vorticity

Figure 4.3: Time-averaged flow for a two-dimensional plate at 90° (top) and 60° (bottom). The Reynolds number based on chord is 1650.

Figures 4.4 and 4.5 are given as reference for further computational work. The plots are velocity profiles across the wake for two different angles-of-attack and two different Reynolds numbers.

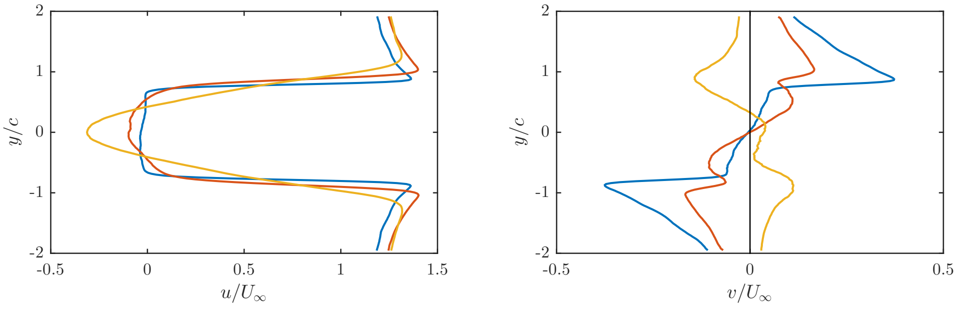

(a) $\alpha = 90^\circ$, $Re = 1650$, u profile (b) $\alpha = 90^\circ$, $Re = 1650$, v profile

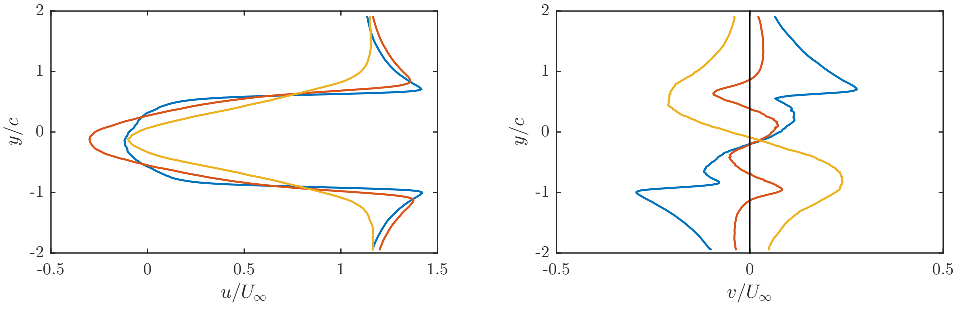

(c) $\alpha = 90^\circ$, $Re = 2240$, u profile (d) $\alpha = 90^\circ$, $Re = 2240$, v profile

Figure 4.4: Time-averaged velocity profiles for a two-dimensional plate at a Reynolds number based on chord of 1650 (top) or 2240 (bottom). The flow profiles are recorded at downstream stations of $x/c = 0.5$ (blue), $x/c = 1$ (red), and $x/c = 2$ (yellow).

The vorticity in the leading-edge shear layer is plotted as a function of downstream position in figure 4.6. The location in the shear layer was first found from the time-averaged vorticity field as the maximum magnitude of vorticity in each downstream profile. These vorticity profiles collapse with the chord, rather than projected chord. Additionally, the peak vorticity is also almost independent of the angle-of-incidence. In the trailing-edge shear layer, however, the collapse is not as good, i.e., the incidence angle has more of an influence.

Moving away from the normal orientation causes a lower peak vorticity in the trailing-edge shear layer (figure 4.7). This is expected because the projected chord is reduced. When this data is plotted as a function of projected chord, a near linear result is obtained (figure 4.8). When considering the vorticity further downstream, the result is less linear, although the vorticity still remains dependent on the angle-of-attack.

The circulation contained in these shear layers can be found by integrating the spanwise vorticity in each region. For our purposes, the region was defined (arbitrarily) as the region where the vorticity was at least 30% of the peak vorticity found in the entire plane. The results

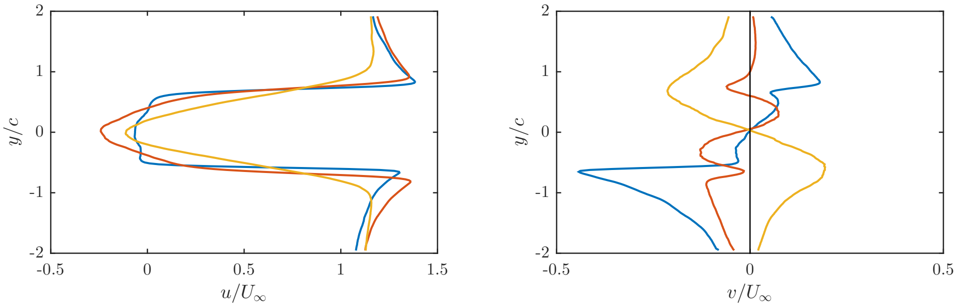

(a) $\alpha = 60^\circ$, $Re = 1650$, u profile (b) $\alpha = 60^\circ$, $Re = 1650$, v profile

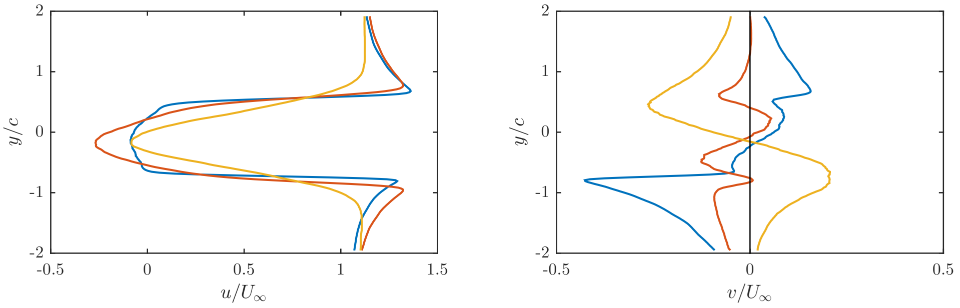

(c) $\alpha = 60^\circ$, $Re = 2240$, u profile (d) $\alpha = 60^\circ$, $Re = 2240$, v profile

Figure 4.5: Time-averaged velocity profiles for a two-dimensional plate at a Reynolds number based on chord of 1650 (top) or 2240 (bottom). The flow profiles are recorded at downstream stations of $x/c = 0.5$ (blue), $x/c = 1$ (red), and $x/c = 2$ (yellow).

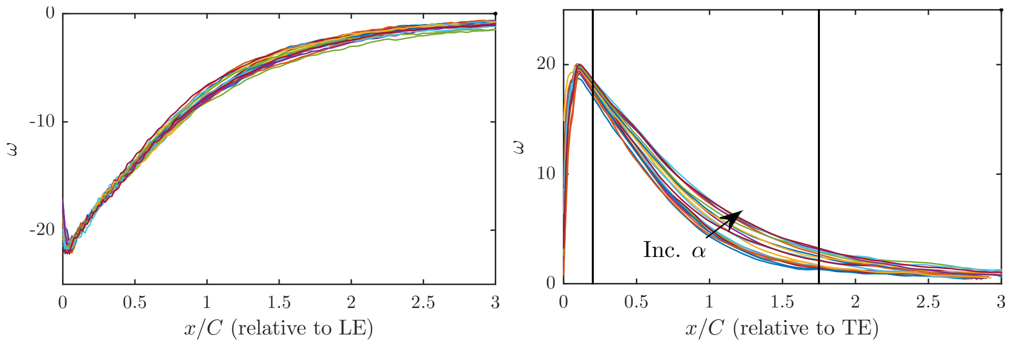

Figure 4.6: Vorticity in the leading-edge (left) and trailing-edge (right) shear layers as a function of downstream position (relative to the plate's leading and trailing-edges respectively) for multiple angles-of-attack from 50° to 90°. Vorticity is non-dimensionalised with the free-stream velocity and the chord. Vertical lines in trailing-edge plot refer to locations for figure 4.7. Arrow indicates direction of increasing incidence angle.

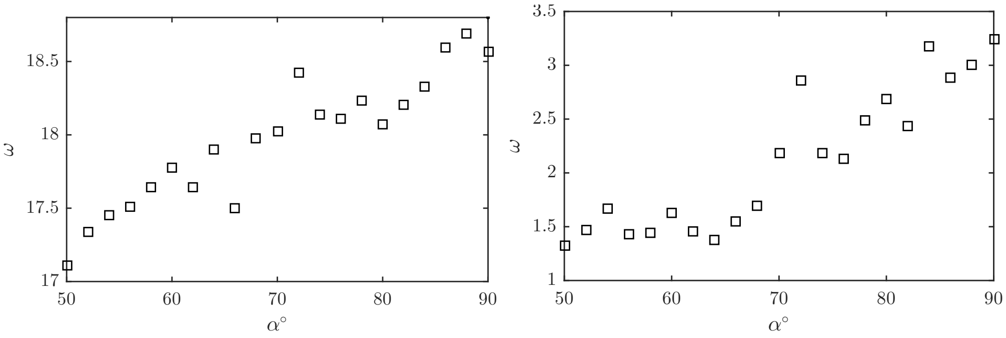

Figure 4.7: Vorticity in the trailing-edge shear layer at $x/C = 0.2$ (left) and $x/C = 1.75$ (right). These locations are marked by vertical lines in figure 4.6.

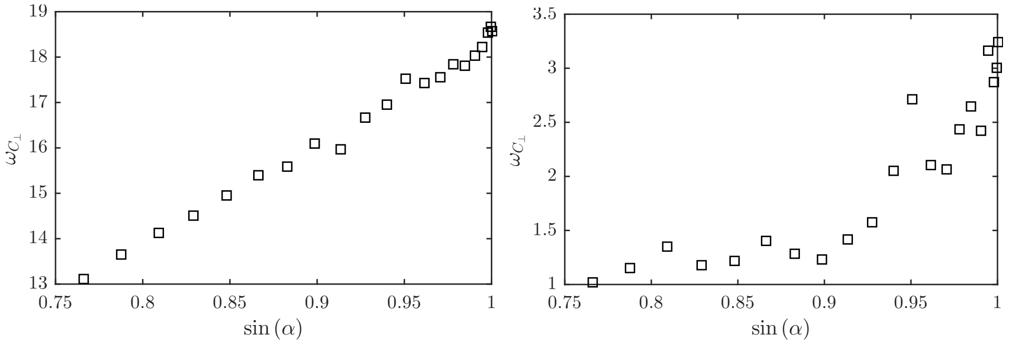

Figure 4.8: Vorticity in the trailing-edge shear layer non-dimensionalised by the projected chord as a function of the projected chord (normalised with the chord length). Downstream locations of $x/C = 0.2$ (left) and $x/C = 1.75$ (right).

(figure 4.9) show a linear trend with incidence angle. The leading- and trailing-edge shear layers have equal circulation when the plate is normal to the flow (and hence symmetric), but as the angle is lessened the leading-edge shear layer grows in relative strength.

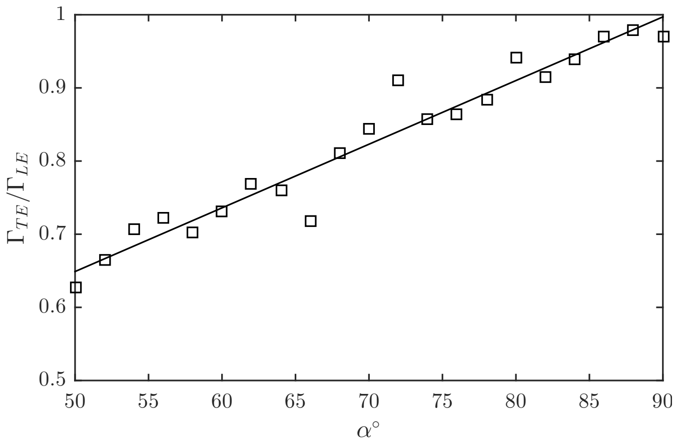

Figure 4.9: The ratio of circulation in the trailing-edge shear layer to that in the shear layer behind the leading-edge of the two-dimensional plate.

It could be thought that this is caused by the streamwise velocity gradient being different between the leading and trailing-edges. At the leading-edge, the flow must orient itself to an angle 90° plus the inclination angle, but at the trailing-edge the angle is 90° minus the inclination angle. This leads to the expectation of much stronger shear at the leading-edge compared to the trailing-edge. When the velocity profile is examined (figure 4.10), however, it is clear that there is no significant difference between the leading and trailing-edge profiles.

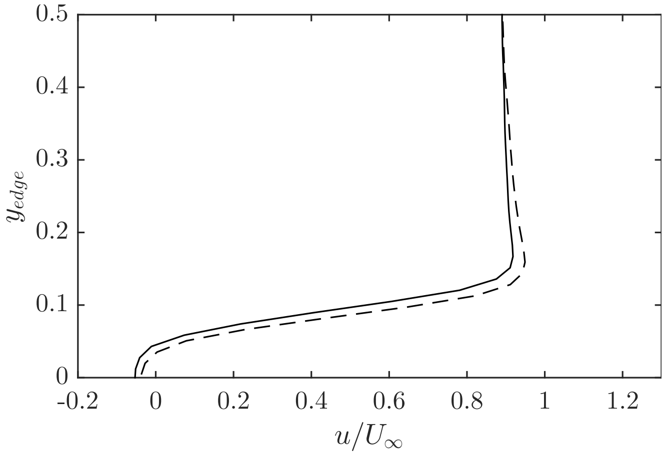

Figure 4.10: Streamwise velocity profiles $0.1c$ behind the leading (solid) and trailing (dashed) edges of the flat plate inclined at 60°. Here, y_{edge} represents the transverse distance from the edge of the plate.

In fact, when quantifying this profile using the maximum gradient of this profile, the results (figure 4.11) show that the trailing-edge profile is in fact slightly ($\sim 10\%$) steeper. It is not until downstream that a significant difference is noticed in the velocity profiles. By $1c$ downstream, the trailing-edge profile is a lot shallower (figure 4.12). The ratio between the gradients of these profiles is given in figure 4.13 as a function of angle-of-attack. Here we see a near linear trend with angle, similar to the circulation ratio of figure 4.9.

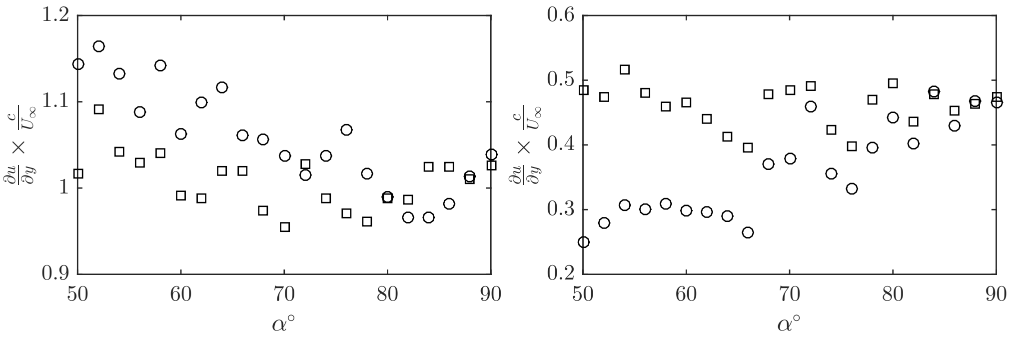

Figure 4.11: Streamwise velocity gradient from the leading-edge (squares) and trailing-edge (circles) shear layers at a point $0.1c$ downstream of the edges (left) and $1c$ downstream of the edges (right). Velocity gradient normalised by the chord length and free-stream velocity.

The circulation difference seen in figure 4.9 is due both to the increase in velocity gradient downstream and to the increased length of the leading-edge shear layer. As the angle-of-attack increases, the initiation point of the leading-edge shear layer (i.e., the leading-edge) moves

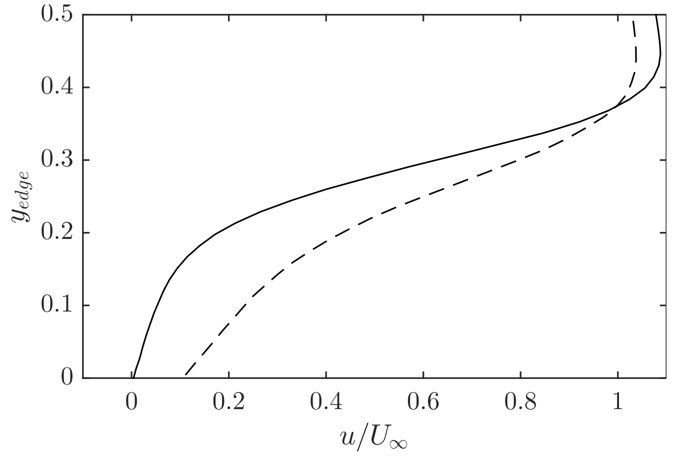

Figure 4.12: Streamwise velocity profiles $1c$ behind the leading (solid) and trailing (dashed) edges of the flat plate inclined at 60°. Here, y_{edge} represents the transverse distance from the edge of the plate.

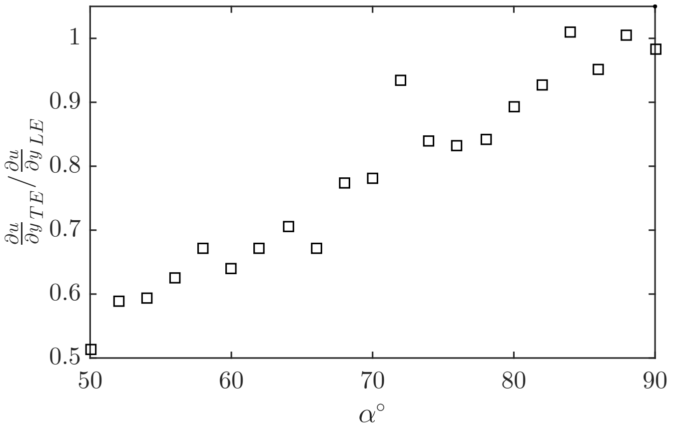

Figure 4.13: Ratio between the streamwise velocity gradient in the trailing-edge shear layer and the leading-edge shear layer at $1c$ downstream of each edge.

upstream. The downstream extent of the shear layer, however, does not move upstream as far. Similarly, the trailing-edge is shifted downstream, but the shear layer does not extend the same amount downstream, causing a difference between the two shear layer lengths (figure 4.14).

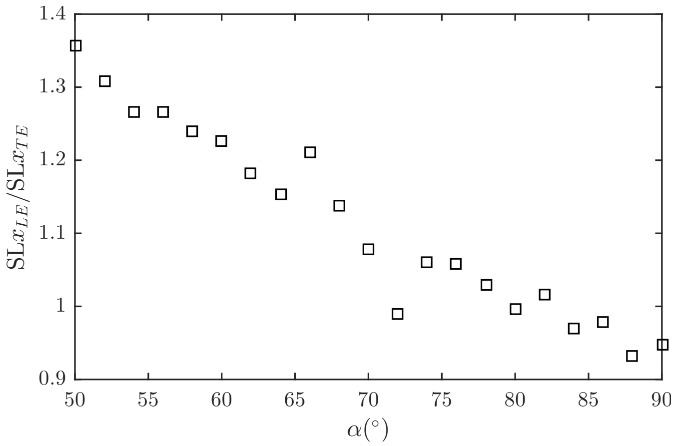

Figure 4.14: Ratio between the length of the leading-edge shear layer to the length of the trailing-edge shear layer.

4.5 Wake dynamics

4.5.1 Stability analysis

Linear stability analysis was performed following that of Monkewitz & Nguyen (1987) and based on the implementation of Leontini *et al.* (2010). This methodology relies on two assumptions, that the flow can be treated as nearly parallel, and that the time-averaged flow is a suitable choice of base flow for stability analysis. While it is expected that the flow is far from parallel, the one-dimensional stability analysis could still be used as a tool to gain an understanding of the flow and typical values for the frequencies in the wake. Regarding the second assumption, the wake is known to be already unsteady, indicating already that it may be a poor choice. The results, however, show good agreement with the measured values, and hence this tool may be used for approximate predictions. The Rayleigh stability equation, based on a velocity profile through the shear layers, is

$$\left(U(y) - \frac{\omega}{k}\right)\left(\frac{d^2\phi}{dy^2} - k^2\phi\right) - \frac{d^2U}{dy^2}\phi = 0 \tag{4.1}$$

where $U(y)$ is the flow profile, ω is the frequency of the eigenmode and k is the complex wavenumber, and ϕ is the mode shape. These variables are related through the complex wave speed ($c = \omega/k$). This equation can be solved for a particular streamwise velocity profile. The complex frequency of the most unstable eigenmode was calculated using the cusp-map method as described in Kupfer *et al.* (1987) and Schmid & Henningson (2001).

For any velocity profile, the perturbation streamfunction of each unstable mode is found as it varies across the wake. Figure 4.15 gives solutions for one such example profile. Two modes are evident: the sinuous and the varicose modes. The sinuous mode is related to the development of the von Kármán shedding and is symmetrical about the $y/c = 0$ plane. The varicose mode is anti-symmetric about the $y/c = 0$ plane (only the magnitude is shown in figure 4.15) and has maximum amplitude in the shear layers. These solutions were produced with an initial estimate of the wavenumber; in this example $k = 0.5 + 0i$.

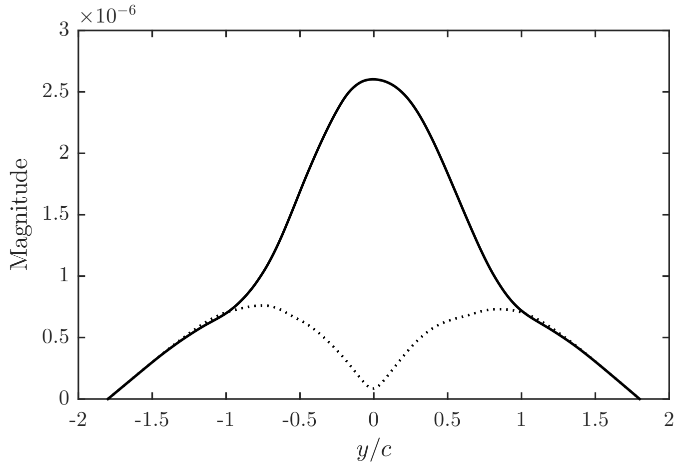

FIGURE 4.15: The magnitude of the perturbation streamfunction of the two solutions to the Rayleigh equation at a particular downstream location ($x/C = 2.87$). The sinuous mode (solid line) is symmetric and corresponds to $\omega_r = 1.0461$, $\omega_i = 0.2044$. The varicose mode (dotted line) is anti-symmetric and corresponds to $\omega_r = 0.5353$, $\omega_i = 0.1035$. The Reynolds number is 1880.

For the initial imaginary wavenumber, the contour is then tracked on the complex ω plane (figure 4.16). The imaginary component of the wavenumber is then negatively incremented, each time producing a new contour. This procedure is continued until a cusp is produced. The cusp was defined as the maximum of the curvature, κ, where the curvature is defined as four times the area of the three adjacent points divided by the product of the three lengths (i.e., the circumradius of the triangle produced by three adjacent points on the complex ω plane):

$$\begin{aligned}\kappa_j &= \frac{2 \times \left|\left((\omega_{r,j} - \omega_{r,j-1}) \times (\omega_{i,j+1} - \omega_{i,j-1}) - (\omega_{r,j+1} - \omega_{r,j-1}) \times (\omega_{i,j} - \omega_{i,j-1})\right)\right|}{\sqrt{g}} \\ g &= \left((\omega_{r,j} - \omega_{r,j-1})^2 + (\omega_{i,j} - \omega_{i,j-1})^2\right) \times \left((\omega_{r,j+1} - \omega_{r,j-1})^2 + (\omega_{i,j+1} - \omega_{i,j-1})^2\right) \\ &\quad \times \left((\omega_{r,j+1} - \omega_{r,j})^2 + (\omega_{i,j+1} - \omega_{i,j})^2\right) \qquad (4.2)\end{aligned}$$

This procedure was automated and performed for each downstream location from $x/C = 0.38$ to $x/C = 3.63$, a total of 210 profiles for each Reynolds number. The complex frequency and

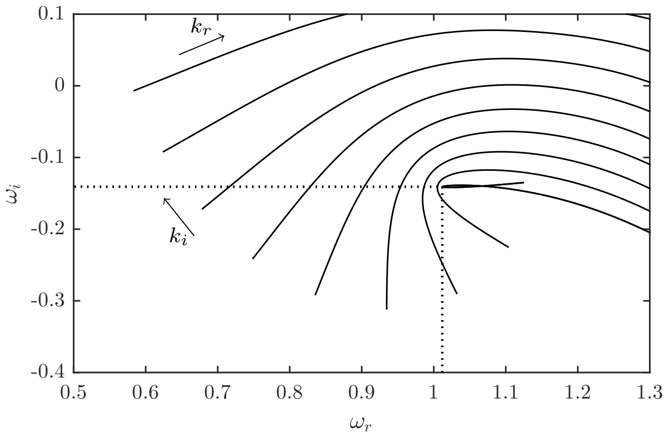

Figure 4.16: Contours of wave frequency (ω) for different imaginary components of the wavenumber for one example velocity profile. The cusp is indicated by the dotted lines and is located at $\omega_r = 1.0118$, $\omega_i = -0.1408$. The arrows indicate the direction of incrementing wavenumbers.

wavenumber can then be tracked with downstream location (figure 4.17). The real part of ω represents the frequency of the most unstable eigenmode. The imaginary part of ω is the growth rate of the perturbation growing on the base velocity profile. Where ω_i approaches zero, the mode is stationary and should give an estimation of the global frequency seen in the fully evolved flow (Koch, 1985; Monkewitz & Nguyen, 1987).

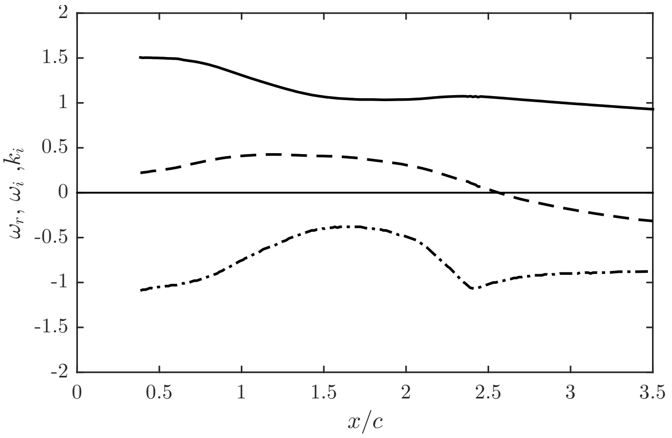

Figure 4.17: Plot of the unstable frequency (real solid, imaginary dashed) and imaginary wavenumber (dot-dashed) with downstream location in the wake of the normal flat plate at $Re = 1582$.

Figure 4.18 shows this result as a function of Reynolds number. The location of the stationary point coincides with a shortening of the wake (see Leontini *et al.*, 2010, for a circular cylinder). The experimental results confirm this. The high scatter in the data is due to the focus of this experiment being on the shear-layer structures, hence the acquisition time was shorter than necessary to have well-converged mean results, although the trend is still clear. There is a decrease in this length with Reynolds number until $Re \approx 1500$. This is presumably due to increased entrainment of the freestream flow into the wake, possibly driven by a higher degree of three-dimensionality. Above $Re = 1500$, however, there is a gradual increase in wake length. For a circular cylinder wake, this Reynolds number corresponds to the transition between the lower and intermediate subcritical regimes, where the shear-layer vortices are first formed. In this case, $Re = 1500$ is the start of a region that sees the base suction increase (Bloor, 1964; Norberg, 1994), the formation length decrease, and the drag is at a local minimum (Zdravkovich, 1997). It is clear that the cylinder transition at this same Reynolds number is not describing the same physical behaviour as seen for the plate wake due to the opposite trend in wake length as well as the evidence of shear-layer vortices well below the critical Reynolds number (figure 4.19).

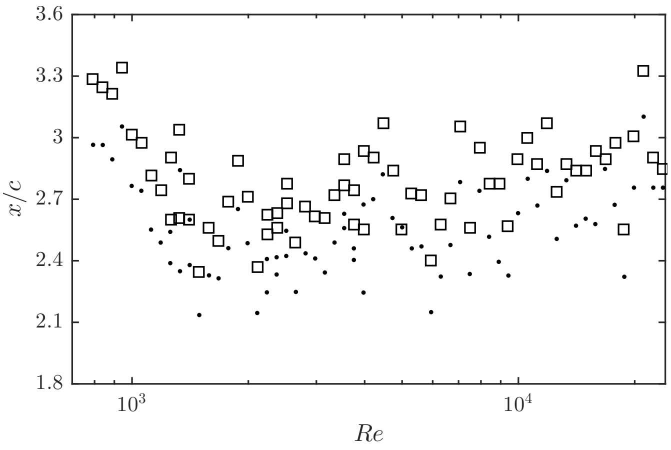

Figure 4.18: The downstream location (black squares) where the imaginary component of the unstable eigenmode approaches zero ($\omega_i = 0$) as a function of Reynolds number behind the normal flat plate. Also reported is the measured recirculation length (black dots).

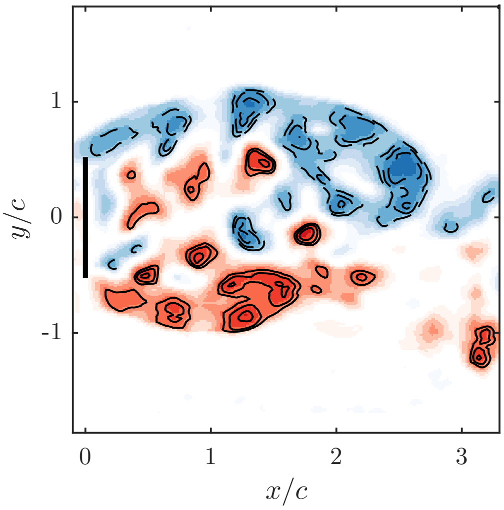

Figure 4.19: Plot of the instantaneous wake of the normal flat plate at $Re = 942$ showing the existence of shear-layer vortices.

The measured recirculation length is lower than the stationary point from the eigenmodes. Figure 4.20 shows the correlation; the offset between them is 0.3 and is invariant with Reynolds number.

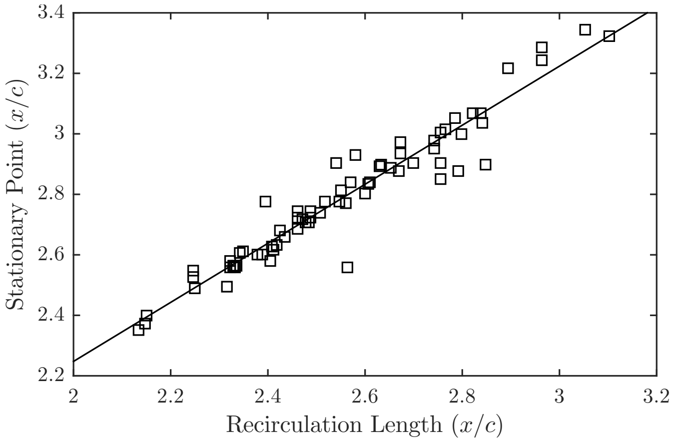

Figure 4.20: Correlation between the measured recirculation length (RL) and the location of the stationary eigenmode (SP). Linear fit is $SP = 0.976 \times RL + .295$.

The frequency of the oscillation associated with the sinuous mode, which corresponds to the von Kármán frequency, is the real component of ω. It is related to the Strouhal number through $St = \dfrac{\omega_r}{2\pi}$ due to the non-dimensionalisation of the input flow with the chord and the freestream velocity. It was calculated at each of the stationary points ($\omega_{r,\omega_i=0}$), which is an estimation of the global frequency, and is presented in figure 4.21.

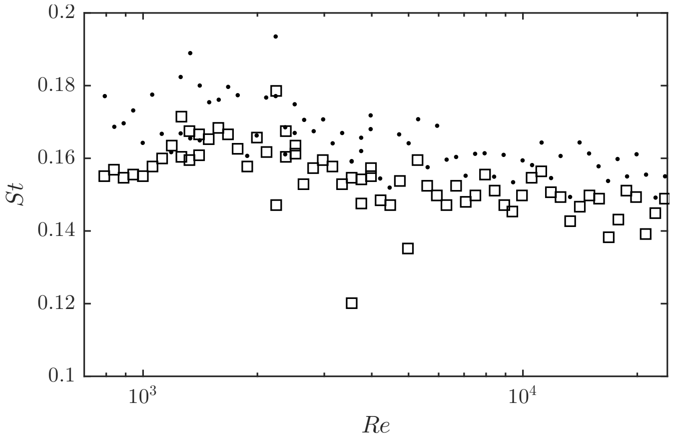

Figure 4.21: The global frequency (local frequency where the eigenmode is stationary) as a function of Reynolds number behind the normal flat plate. Measured Strouhal numbers from PIV data is given with black dots.

Similarly to figure 4.18, the correlation between the measured Strouhal number and the global frequency is good across the whole Reynolds number range. There is an offset between the two data sets meaning the estimated frequency is lower than the measured frequency. The Strouhal number is increasing until $Re \approx 1500$ and then decreases after that, the same critical Re as for the recirculation length. In the case of the Strouhal number however, the trend is the same as that seen for the circular cylinder (Norberg, 1994).

4.5.2 von Kármán shedding

Phase-averaged PIV is used to visualise the average von Kármán shedding in the wake. The data is first decomposed using POD, and the mode coefficients for the first two oscillating modes are extracted. This signal is used as the reference signal for binning the acquired PIV frames into sixteen bins. The phase of the signal was defined as $\phi = \text{atan}\left(\frac{M_1(t)}{M_2(t)}\right)$ where $M_i(t)$ is the self-normalised mode norm of the i-th POD mode. Each bin contained approximately 190 frames.

The phase-averaging (figure 4.22) reveals the well-studied von Kármán vortex shedding. The vorticity in each shear layer builds up until it is shed into the wake. This shedding alternates from each side. The common explanation for this phenomenon given by Gerrard (1966) is that the independently growing vortex becomes strong enough to kink the opposite shear layer. The induced velocity in that shear layer will then draw the shear layer into the wake, cutting off the large-scale vortex which moves downstream. While this explanation is widely accepted, the evidence supporting such a shedding mechanism is limited. This is discussed further in section 4.5.3.

The standard deviation of the streamwise velocity field peaks behind the closest of the von Kármán vortices (figure 4.23). The transverse velocity standard deviation is highest in the region between two consecutive von Kármán vortices on the same side, which indicates a high variability in the location of vortices in this region. Note that the data plotted is the standard deviation within one bin, rather than for the complete time-averaged wake.

The frequency of this von Kármán shedding can be quantified using the tool described in section 3.5.1. When considering an average frequency across the whole wake, the maximum power will be associated with the von Kármán frequency. The frequency spectrum at $\alpha = 60^\circ$ and $Re = 1430$ is shown in figure 4.24. Both the transverse and streamwise components show a single, dominant peak at $St = 0.158$. This matches up well with the literature suggesting the Strouhal number is around 0.166 for low Reynolds numbers ($Re < 1000$) and approximately 0.15 for higher Reynolds numbers. When the angle of attack is varied, the projected chord also changes, changing the frequency of the von Kármán shedding. This effect is shown in figure 4.25.

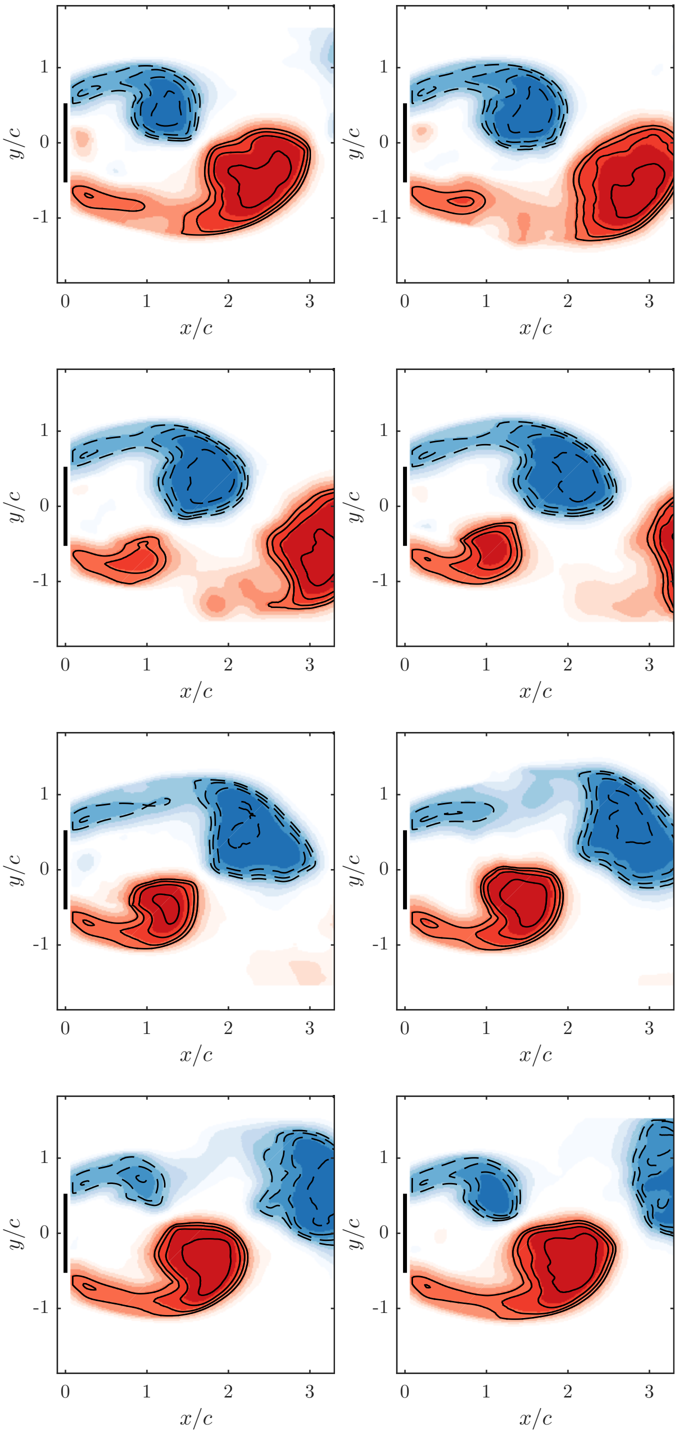

FIGURE 4.22: Phase-averaged wake of the normal flat plate showing one complete von Kármán shedding cycle for $Re = 1582$. Bins for phase averaging are $\pi/8$ wide. Filled contours are spanwise Γ_2 and are red and solid for positive rotation and blue and dashed for negative rotation.

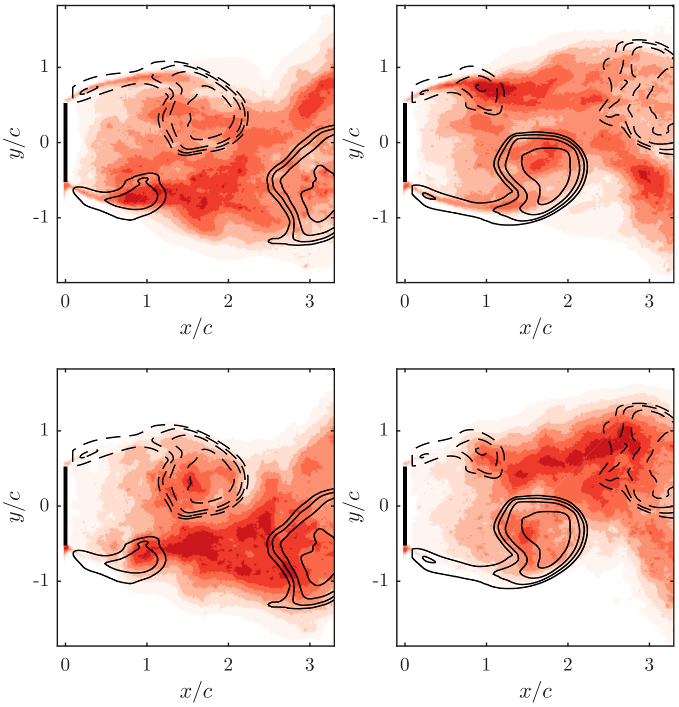

Figure 4.23: Phase-averaged wake of the normal flat plate showing two distinct phases at $Re = 1582$. Bins for phase averaging are $\pi/8$ wide. Filled contours are standard deviation of the streamwise velocity component (top) and transverse velocity component (bottom). Black contours are contours of the Γ_2 criteria and are solid for positive rotation and dashed for negative rotation.

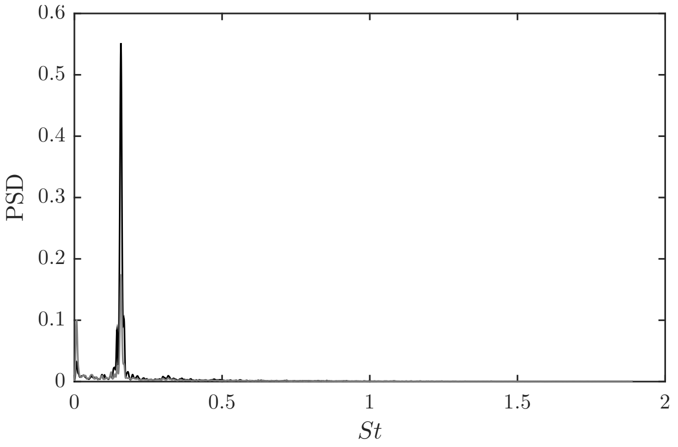

Figure 4.24: Spatial average of the power spectral density of the streamwise (grey) and transverse (black) velocity fluctuations in the wake of the two-dimensional plate at an angle of incidence of 60° and $Re = 1430$. The characteristic length for the Strouhal number is the projected chord.

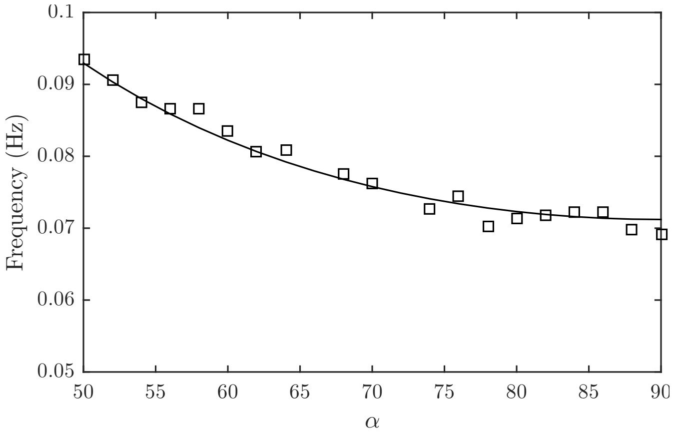

Figure 4.25: The frequency of the von Kármán shedding of the two-dimensional plate as it varies with angle of attack. Fitted line is at $St = 0.155$ based on the projected chord. Constant chord length and freestream velocity. The results are consistent with the work of Fage & Johansen (1927).

The power and phase of this frequency can be seen in figure 4.26. The streamwise fluctuations are most powerful behind the shear layer, while the most powerful transverse ones are located between the von Kármán vortices. As expected, the transverse velocity is in phase across each downstream location, with the wake lagging slightly behind the freestream flow. The streamwise fluctuations are π out-of-phase across the $y = 0$ line. Figure 4.27 extracts a line plot from figure 4.26 for clarity.

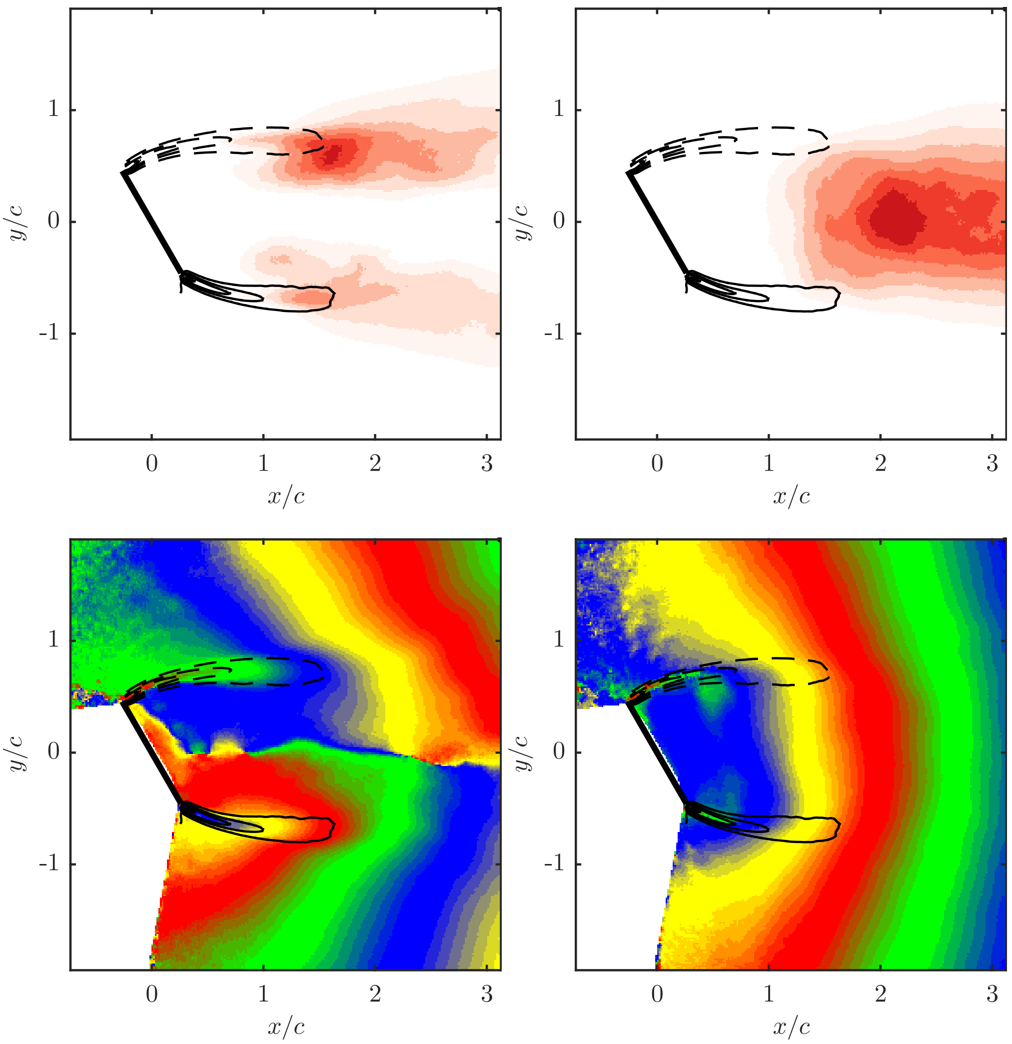

Figure 4.26: Power (top) and phase (bottom) of the streamwise (left) and transverse (right) Strouhal frequency behind the flat plate at an angle of incidence of 60° and $Re = 1430$. Contours are time-averaged spanwise vorticity measurements (negative vorticity is dashed).

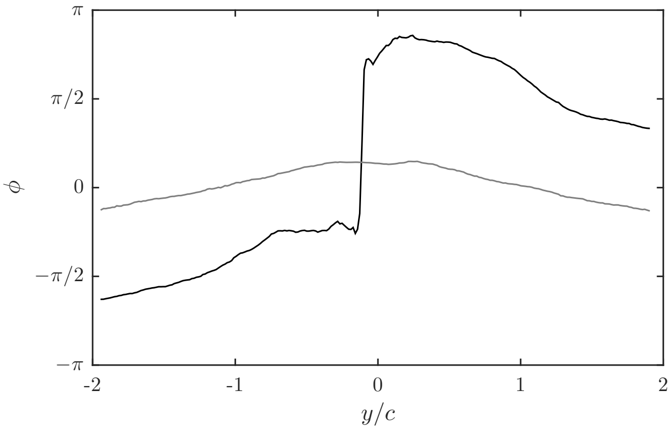

Figure 4.27: Cross-stream phase of streamwise (gray) and transverse (black) velocity fluctuations of the Strouhal frequency behind an inclined plate at $x/C = 2.5$. Plate is inclined at 60° and $Re = 1430$.

4.5.3 Shear layer shedding

To track the development of the von Kármán vortices, the shear-layer vortices are visualised by their location along a projection of the shear layer. Firstly, the shear-layer location is found for the time-averaged wake (figure 4.28) by finding the location in the shear layer with maximum magnitude of vorticity at each downstream profile.

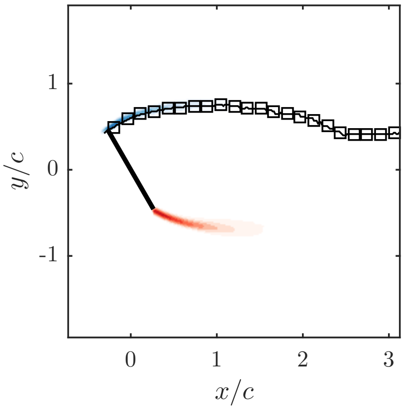

Figure 4.28: Time-averaged spanwise vorticity overlaid with the location of the shear layer (black squares) behind the flat plate inclined at 60° and Reynolds number 1430. One in 10 points are shown for clarity.

A new length x' is defined as the projected distance along this time-averaged shear layer. For any instance in time, the Γ_2 field along this line can be extracted. For a series in time, this gives a space-time diagram of the shear-layer development (figure 4.29). On the right hand side of this figure, the von Kármán shedding is evident with regular vortices advecting downstream (positive gradient). The frequency of these structures is $St = 0.157$ (figure 4.30) which is calculated through a Fourier transform at a single downstream position.

By performing this same spectral analysis at all the points in the shear layer, the frequency variation with downstream location is revealed. Figure 4.31 gives the frequency as a ratio to the von Kármán frequency. The highest detectable frequency ratio with this setup is close to 9. The peak frequency ratio drops at $x'/c = 0.5$ to 7.6 before decreasing to 5.4. This is the preferred mode until $x'/c = 2$, beyond which the von Kármán frequency dominates. These frequencies are not harmonics of a single base frequency, neither are they summations of each other, indicating that the observed vortex merging is not always a regular pairing of two shear-layer vortices.

By following the path of the shear-layer vortices in figure 4.29, it is clear that they are generated near the leading-edge at regular intervals and travel at a constant velocity downstream until

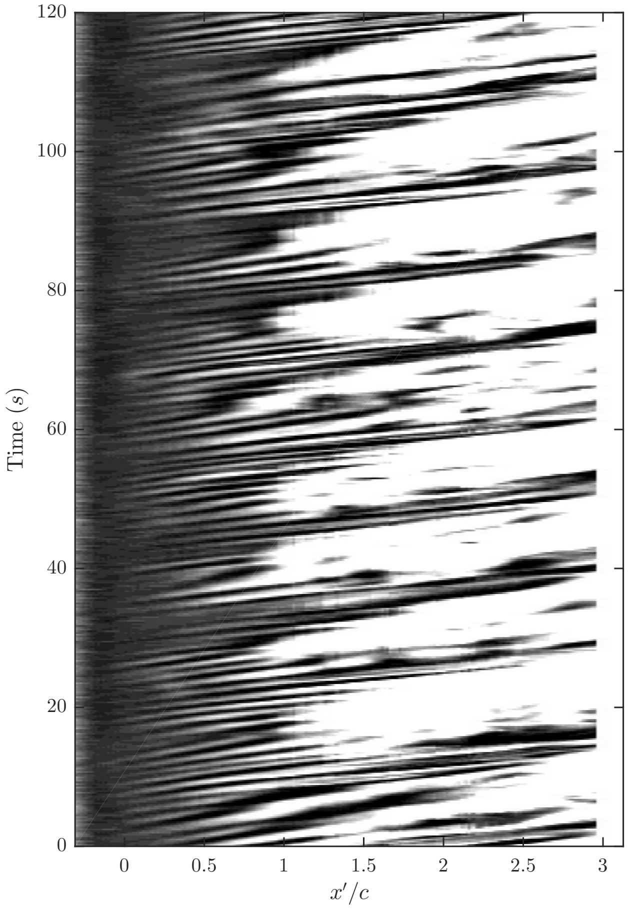

FIGURE 4.29: Space-time diagram of vortex locations in the shear layer behind the leading-edge of the flat plate inclined at 60°.

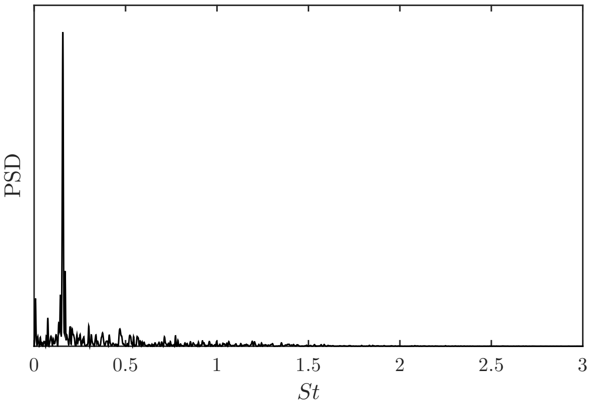

FIGURE 4.30: Power Spectral Density of the Γ_2 signal at $x'/c = 2.5$ showing a distinct peak at $St = 0.157$.

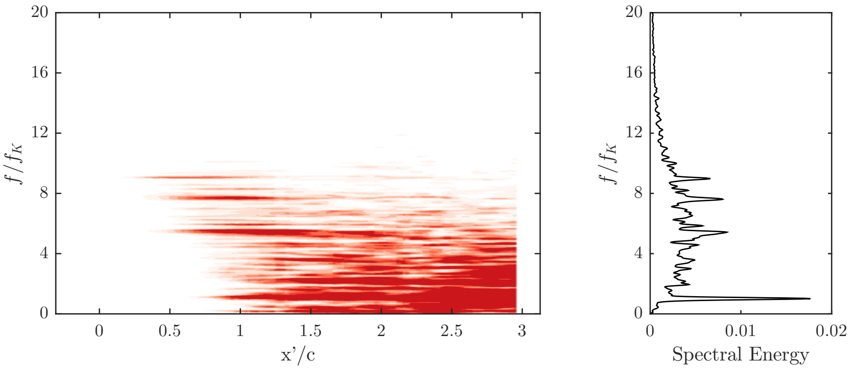

Figure 4.31: The frequency ratio (relative to the Strouhal frequency) as it varies with downstream location following the leading-edge shear layer behind the plate at 60° (left). The spatial-average of all the spectra (right).

$x'/c \approx 0.75$, where the first vortex begins to slow down (evidenced by the increase in gradient on the space-time plot. Subsequent shear-layer vortices reach the same downstream location, where they conglomerate for several shear layer cycles before merging and moving downstream as a large von Kármán vortex. This procedure is shown in the instantaneous fields in figure 4.32. This mechanism reveals similarities to the 'collective interaction' described in Ho & Huang (1982) where ten or more shear-layer vortices in a forced mixing layer were shown to coalesce, though only when high levels of forcing were introduced. For an unforced mixing layer, they report that the dominant mechanism is vortex pairing.

In the case shown in figure 4.32, seven distinct shear-layer vortices are shown to merge. Investigation of the instantaneous results show that anywhere between three and nine vortices are found per von Kármán cycle. The underlying mechanism behind this unsteadiness is uncertain. What can be seen, however, is the frequency ratio presented in figure 4.31 corresponds with this data. That is, frequency ratios as high as nine are seen, but the main peak is at 5.4.

The tracking of the path of the first (a) and last (g) vortices in this field reveal that the first vortex is drawn down into the low-speed wake where it is considerably slowed. The last vortex remains in the high-speed region which allows it to catch up with the conglomeration of shear-layer vortices as they slowly move downstream.

It seems unlikely that the positive von Kármán vortex seen at the bottom of the early frames in figure 4.32 is responsible for the initial motion of vortex a downwards into the low speed portion of the wake. This is unreasonable as the von Kármán vortex is a considerable distance from the negative shear layer. It also does not influence any other shear-layer vortices, leading

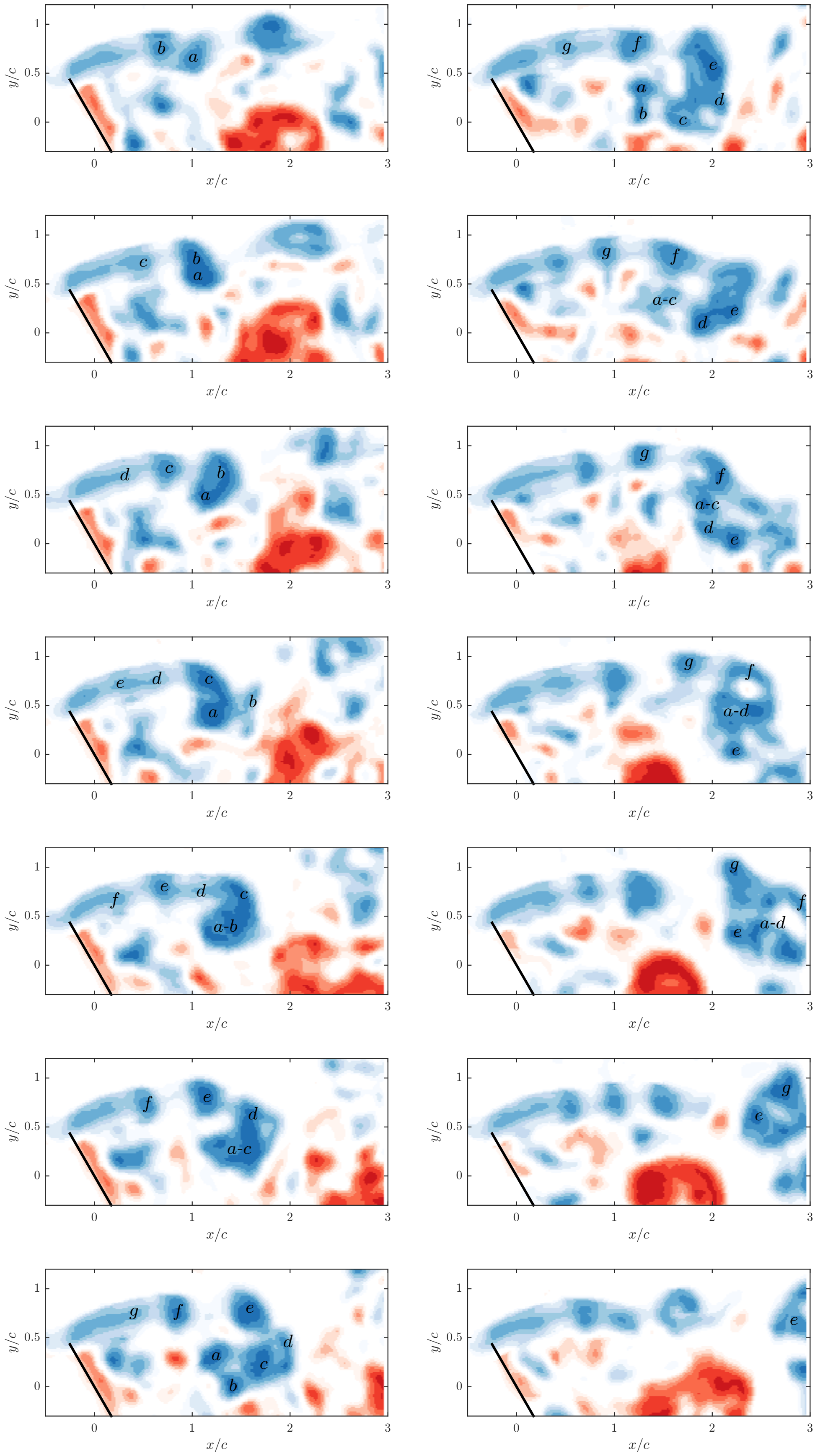

Figure 4.32: Instantaneous Γ_2 fields showing the shear-layer vortices behind the leading edge of the flat plate at 60°. Only every fourth frame is included, with time progressing down the column first.

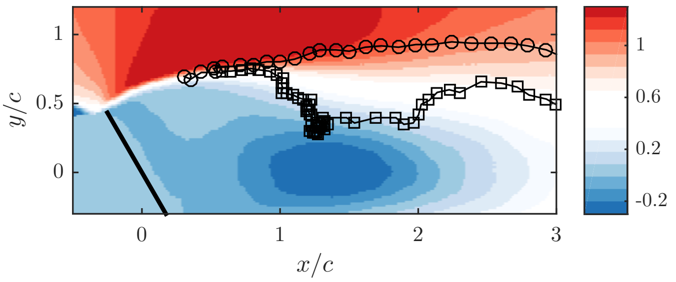

Figure 4.33: Paths of two shear-layer vortices behind the leading-edge of the inclined plate. Vortex a from figure 4.32 in squares and vortex g in circles. Filled contours are the time-averaged streamwise velocity field.

to the belief that some other mechanism causes the a vortex to drop. One contributing factor could be the induced velocity from the subsequent vortex (b) pushing a downwards. For a uniformly spaced series of equal sized vortices, the induced velocity from the previous vortex will balance the velocity from the subsequent vortex. If, however, some instability caused a separation in the shear-layer vortex series, the first vortex after some gap will be drawn into the low speed region. Once it is lower than the vortex series, it will draw subsequent vortices past it before bringing them also into the wake. The velocity profiles of a typical vortex in an instantaneous sense are given in figure 4.34.

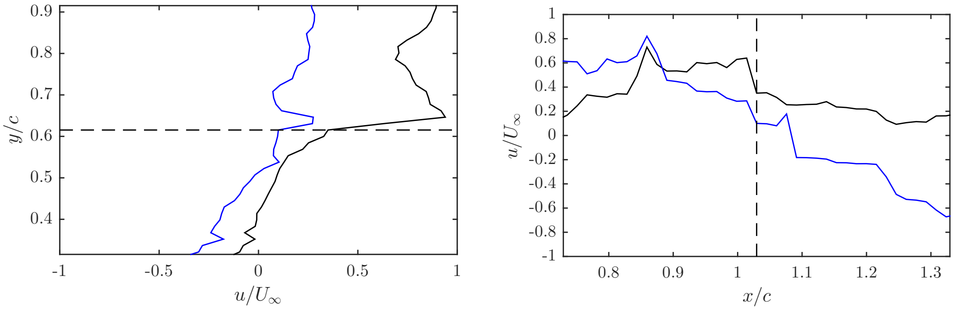

Figure 4.34: Instantaneous velocity profiles through the core of a single shear layer vortex. On the left is the vertical profile and on the right is the horizontal. Streamwise velocity is in black and vertical velocity is in blue.

The frequency information behind the trailing-edge of the plate tends to be dominated by the Strouhal number and its harmonics, even in the shear layer. For example, figure 4.35 shows the average frequency spectra across all points in the trailing-edge shear layer. It is clear that the von Kármán frequencies and the harmonics thereof are the most energetic frequencies across that region. This effect is more noticeable at the lower angles, as the difference in shear from the leading and trailing-edges becomes larger (see figure 4.9).

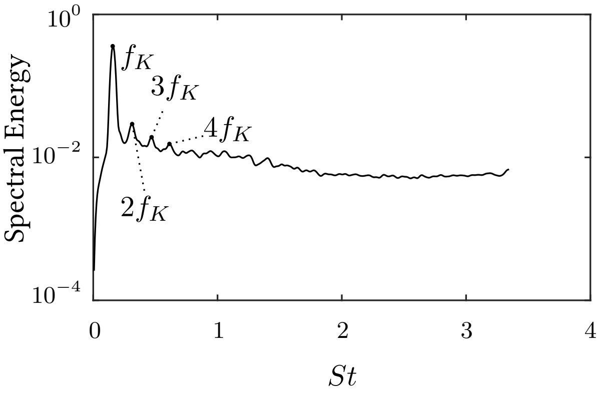

FIGURE 4.35: Spectral energy behind the trailing-edge of the flat plate at 50°.

The spectral energy of the shear-layer vortices increases in the first chord length downstream, before decreasing as the von Kármán frequency becomes more dominant. Figure 4.36 shows this relationship for two different Reynolds numbers.

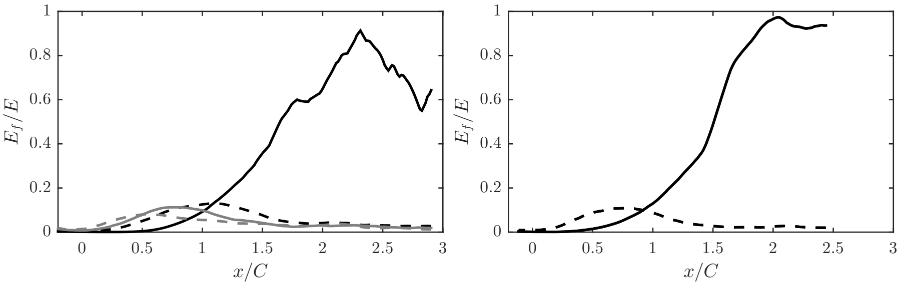

(a) Re = 1430

(b) Re = 1940

FIGURE 4.36: Relative spectral energy for key frequencies within the shear layer against downstream location. Plate is two-dimensional at angle of incidence of 60°. Left hand data contains the von Kármán frequency ($St = 0.1548$) in the black solid line, the shear-layer frequency ($St = 0.848$) in black dashes, a higher frequency f_3 ($St = 1.2019$) with the gray solid line, and the highest detectable shear-layer frequency f_4 ($St = 1.4084$) in gray dashes. Right hand data contains the von Kármán frequency ($St = 0.1574$) with solid black line and the shear-layer frequency ($St = 1.108$) in dashes.

Producing a Fourier analysis from the shear layer points (as done in figure 4.31) means how the Strouhal number varies with Reynolds number can be shown (figure 4.37). The shear-layer frequency is defined as the lowest peak in the spectrum above the von Kármán shedding frequency. There is an increase in the shear-layer shedding frequency with Reynolds number, as is expected from the work of Prasad & Williamson (1997). When the ratio between the shear-layer and von Kármán frequencies is plotted in figure 4.38, it is clear that there is a power law relationship between the ratio and the Reynolds number. This data was fitted to the equation $\frac{f_{SL}}{f_K} = \alpha \times Re^{\beta}$, with the results revealing that $\alpha = 0.043$ and $\beta = 0.67$. The value for the exponent β is in excellent agreement with Prasad & Williamson (1997), however the value for the constant α is higher by $\sim 80\%$.

Thompson & Hourigan (2005) suggest that a piece-wise fit to the circular cylinder data produces two regimes, each with an exponent of 0.5 (as Bloor (1964)). However, a similar fit to the present data would only increase the exponent (to 1.09 and 0.93 for the two Reynolds number sections), not reduce it to 0.5.

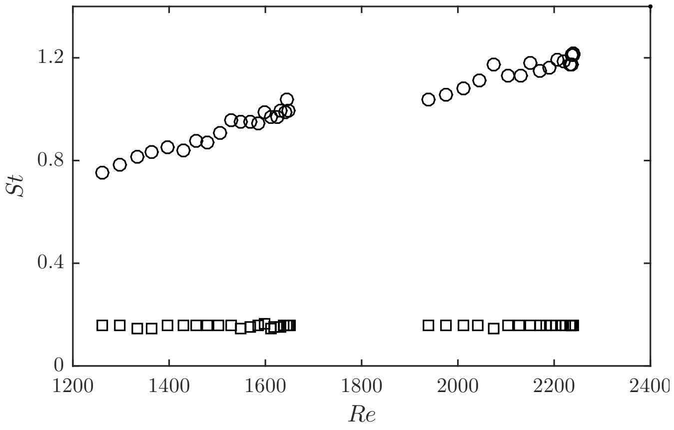

Figure 4.37: The Strouhal number of shear-layer frequency (circles) and von Kármán frequency (squares) as a function of the Reynolds number.

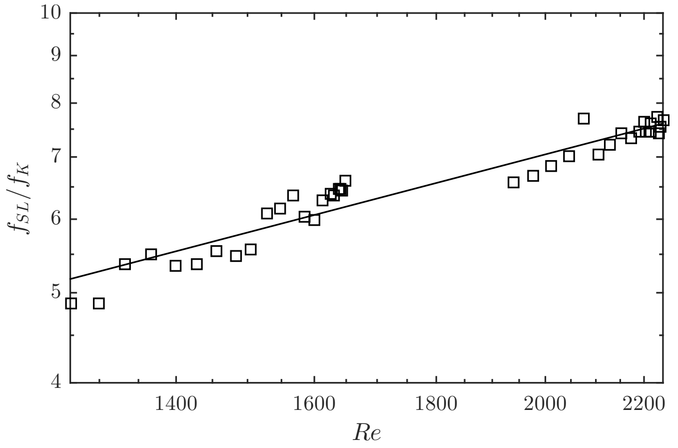

Figure 4.38: The effect of Reynolds number on the ratio of shear-layer frequency to von Kármán frequency. Black line is a power fit to the data: $f_{SL}/f_K = 0.043 \times Re^{0.67}$

4.6 Summary

This chapter has provided new information on the wake of a two-dimensional flat plate. Firstly the time-averaged flow was investigated, showing the strength of each shear layer depends on the angle-of-attack. The shear layers were found to terminate at approximately the same downstream location, resulting in a difference between the leading- and trailing-edge shear layers. This in turn led to a disparity in the circulation between the two shear layers that was a linear function with incidence angle.

Linear stability analysis was used to predict both the Strouhal frequency and the recirculation length. A transition was found to occur at a Reynolds number of ~ 1500 for the flat plate, but it was noted that this transition was not physically the same as that found for the circular cylinder at the same Reynolds number.

Finally, further light was given into the formation of von Kármán vortices and the nature of their growth and shedding downstream. PIV images showing the growth of this vortex as a conglomeration of smaller shear-layer vortices were presented, as well as the ability to track any individual shear-layer vortex through this formation. It was shown that an irregular number of shear-layer vortices form into one von Kármán vortex, though the most common number was found to be a power fit with Reynolds number according to $\frac{f_{SL}}{f_K} = 0.043 \times Re^{0.67}$. Experimental evidence supporting the theory provided by Gerrard (1966) was given for how the instability causing a streamwise displacement of the shear-layer series evolves.

CHAPTER 5

THE WAKE OF THE AHMED BODY

5.1 Introduction

This chapter provides further understanding on the wake of the Ahmed model. The problem is approached from two different perspectives. Firstly, the time-averaged wake is discussed, looking at the formation of the macro structures on the body and their evolution downstream. These large-scale structures are important since they influence the integral parameters like the body forces. Secondly, the time-varying wake is investigated to see how these structures vary in time. It is important to study instantaneous flow since these features of a wake determine key aerodynamic parameters like the stability.

The time-averaged wake of the Ahmed model is studied in three respects. Firstly, spatially-resolved velocity fields are given in the wake of the model. Secondly, due to the resolution, the circulation in the c-pillar vortex is able to be measured as the structures evolve downstream of the model. This leads to some surprising results regarding the vorticity transport between spanwise and longitudinal structures. Thirdly, the question of the nature of the recirculating A and B regions (see section 5.3.3 for an introduction regarding the importance of this question) is investigated.

Additionally, the chapter gives results regarding the dynamics of the wake. Temporally resolved velocity fields are analysed showing the motion of the vortices in the wake. A transverse pulsing of the base pressure region is shown to be the dominant mode. The spanwise flapping of the separated flow over the slant is discussed, showing that it is not a periodic phenomenon as some suggest.

Key findings:

- circulation from the recirculation region A is tilted into the streamwise direction
- this streamwise vorticity merges with the c-pillar vortex, strengthening it downstream of the body
- the boundary layer separates from the ground plane, with the separatrix causing an obstruction to the streamwise flow, hence producing a horseshoe vortex
- this horseshoe vortex merges with the c-pillar and corner vortices and circulation is constant from that point on
- the recirculation region B varies in time, alternately strengthening behind each c-pillar vortex
- this variation is the dominant temporal feature in the wake, causing the c-pillar vortex and corner vortices to oscillate
- the shedding mechanism from the separated slant region is not periodic

This chapter is based on some of the data presented in:

VENNING, J., LO JACONO, D., BURTON, D., THOMPSON, M. & SHERIDAN, J. 2015 The effect of aspect ratio on the wake of the Ahmed body. *Experiments in Fluids* **56** (6)

5.2 Measurement and Data Processing

The water channel, Ahmed models, and PIV systems have already been discussed in sections 3.2, 3.3.2, and 3.4.2 respectively. For these particular experiments, the standard width Ahmed model was used with a slant angle of 25°, which is in the high-drag regime at $\Re FA = 1.38 \times 10^6$ (Ahmed *et al.*, 1984). The Reynolds number based on the square-root of the frontal area was 3×10^4. The PIV setup is summarised in table 5.1. Velocity fields were acquired in all three orientations, at various resolutions. Different experimental parameters were necessary as each experiment targeted certain features of the wake.

Additionally, time-resolved PIV was used to be able to capture the dynamics of the wake through velocity measurements. The TR-PIV setup involved a continuous laser in conjunction with the PCO Dimax high-speed camera. The ground plane, Ahmed body, and flow conditions were the same as described above. The TR-PIV planes were:

Table 5.1: PIV acquisition parameters for the wake of the standard-width Ahmed body.

	xy	xz	yz
Camera used	PCO Dimax	PCO Dimax	PCO 4000
Number of planes	12	17	29
Plane locations	$z/H =$ $0 : 0.092 : 1.108$	$y/W =$ $-.103 : 0.051 : 0.720$	$x/L =$ $-0.2 : 0.025 : 0.5$
Image resolution	2016×2016	2016×2016	2368×1600
Field of View	$0.44L \times 1.19W$	$0.27L \times 0.96H$	$1.75W_S \times 1.6H$
Lens	105 mm	105 mm	105 mm
Magnification Factor	17.7 px/mm	29.5 px/mm	13.84 px/mm
Image pairs	1500	1500	680
Acquisition rate	10 Hz	10 Hz	2 Hz
Time-step	2 ms	2 ms	3.5 ms
Interrogation window	32×32	32×32	32×32
Overlap	75%	75%	75%
Vector field	249×249	249×249	293×197
Vector spacing	$0.005W$	$0.003W$	$0.006W$

- xy plane at $\frac{z}{H} = 0.67$
- xz planes at $\frac{y}{H} = 0$, 0.257 and 0.463
- yz planes at $\frac{x}{L} = 0.05$, 0.2 and 0.4

Images were acquired at a rate of 200Hz with no additional time-increment between the images. The images were correlated in cinematic mode with a final window size of 32×32 pixels and 75% overlap.

5.3 Time-averaged wake

5.3.1 Comparison with other studies

The present results were compared with Lienhart & Becker (2003) who provide wind-tunnel Laser Doppler Anemometer (LDA) data behind a Ahmed model at a Reynolds number of $\mathrm{Re}_{\sqrt{FA}} = 8.9 \times 10^5$, an order of magnitude higher than this study. This reference data is widely used as a test case for CFD simulations. Besides the change in Reynolds number, the other key difference in this experiment was the mounting system. While Lienhart & Becker used four cylindrical stilts mounted at the outer edges of the Ahmed body, the current experiment used two airfoil stilts in the symmetry plane. When the stilts are on the outside of the body the underbody flow is accelerated between them, while for this study the symmetry plane is in the wake of the struts, causing a slower underbody flow behind the centre of the body. This is demonstrated in figure 5.1(a) where there is a large discrepancy near $z/H = 0$. The velocity in the reference case exceeds the freestream velocity, while our experimental data shows a significant velocity reduction. It is expected that this change will weaken the B vortex whilst strengthening the corner vortices.

The other notable difference between our data and the previous LDA data of Lienhart & Becker is that the wake deficit is larger in this study. Figure 5.1(b) shows this difference in the streamwise velocity plane. This is consistent with the findings of Spohn & Gilliéron (2002) who showed that the size of separated regions tend to decrease with Reynolds number. However, despite these differences, the major streamwise structures, which are of the main interest, are consistent with Lienhart & Becker (2003), as can be seen in figure 5.2. These broad structural results also match well with numerous other papers on the topic.

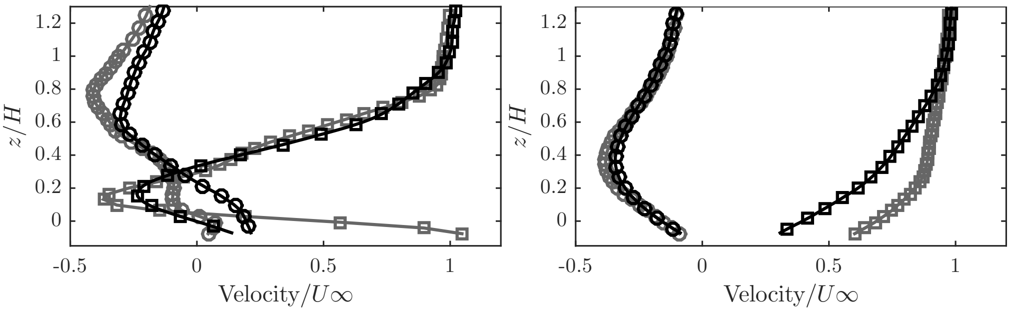

(a) $\frac{x}{L} = 0.084$ (b) $\frac{x}{L} = 0.420$

Figure 5.1: Comparison of time-averages of streamwise (squares) and vertical velocity (circles) profiles in the symmetry plane at two downstream positions in the wake of the standard-width Ahmed model. The black symbols represent the PIV data from the present study ($\mathrm{Re}_{\sqrt{FA}} = 3 \times 10^4$), only one in five points are shown for clarity. The grey symbols are LDA data from Lienhart & Becker (2003) ($\mathrm{Re}_{\sqrt{FA}} = 8.9 \times 10^5$).

5.3.2 Description of the wake

The PIV data allowed the time-mean structures in the wake to be visualized and quantified. Figure 5.3 shows a cross-stream view of the standard-width Ahmed model wake. The Γ_2 criterion (Graftieaux, 2001) was used to quantify the rotation of the flow. In figure 5.3 at $x/L = 0.1$, three structures are present on each half of the body. The positive c-pillar vortex is shown in red near the end of the slant and at the right edge of the body (with the negative vortex on the opposite side of the symmetry plane and rotating the opposite direction). This is the major structure in the wake and is formed as the boundary layer along the side of the model separates over the slant, rolling up into a longitudinal structure of which we are viewing a slice.

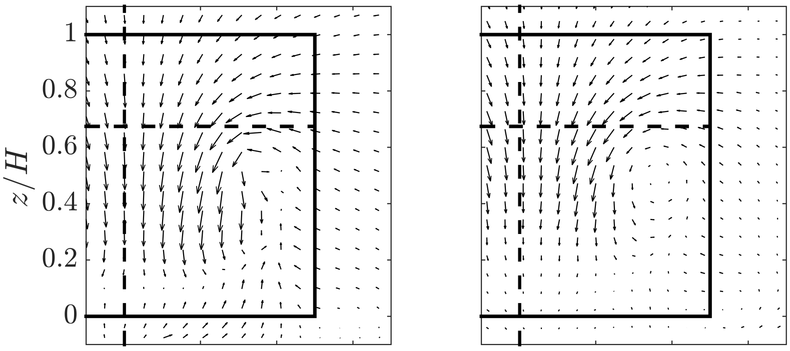

(a) LDA, $x/L = 0.192$ (b) PIV, $x/L = 0.2$

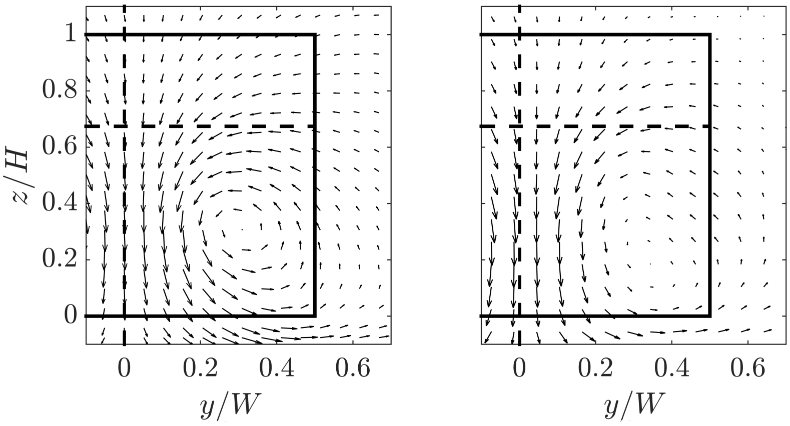

(c) LDA, $x/L = 0.479$ (d) PIV, $x/L = 0.475$

Figure 5.2: Comparison of time-averaged cross-stream (yz) velocity data represented by vectors. Left is LDA data from Lienhart & Becker (2003), right is PIV data from the present study. One in sixty-four PIV vectors shown for clarity. Free-stream velocity is towards the observer. Half of symmetry plane shown for brevity.

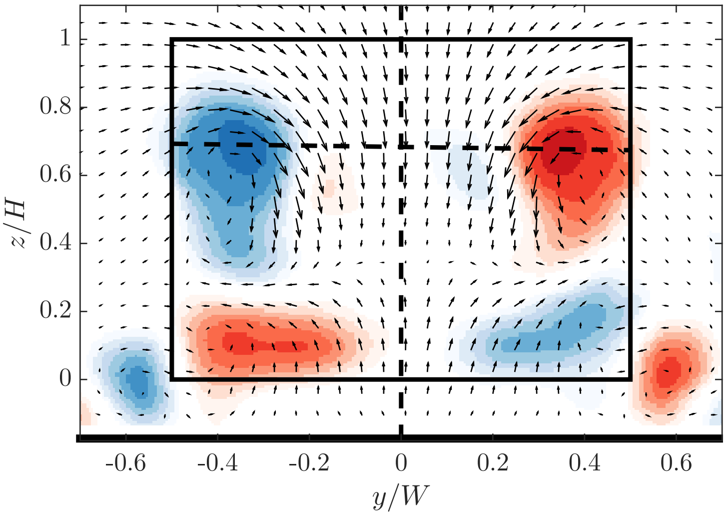

Figure 5.3: Cross-stream PIV plane behind the standard with Ahmed model at $x/L = 0.1$ showing in-plane velocity vectors overlaid with streamwise Γ_2. One in sixty-four velocity vectors are shown for clarity. The vertical black dashed line represents the symmetry plane. The solid lines represent the outline of the Ahmed body, with the dashed line the end of the slant region. Filled contours are Γ_2, with red representing positive (counter-clockwise) rotation and blue representing negative (clockwise) rotation, with levels between ± 1. Free-stream velocity is towards the observer.

Rotating the same direction as the c-pillar vortices are the corner vortices. These are formed from accelerated flow under the body rolling up over the bottom corner. The third structure evident in this plane is the blue (on right, negative rotation) structure below the c-pillar vortex. This is the streamwise element of structure B (figure 2.7), which forms as the flow separates at the bottom edge of the body. It is a predominantly spanwise structure (figure 5.5) and does not extend far downstream (figure 5.4(i)).

Figure 5.4 shows the evolution of these vortices with downstream location. Slightly further downstream at $x/L = 0.2$, figure 5.4(i) shows the persistence of the c-pillar and corner vortices, but recirculation structure B is no longer visible. By this downstream position, a new structure has emerged (structure D), which is formed as the underbody flow expands downstream of the end of the body. This causes the boundary layer on the ground plane to separate at $x/L = 0.1$, with a local separation zone resulting (see figure 5.5(a)). This separatrix forms an obstacle, which, when the spanwise vorticity that is rolling along the boundary layer approaches, tilts around into a horse-shoe vortex. As such, this structure does not extend far in the spanwise direction (notice in figure 5.5(c) that the bubble is no longer visible), but two streamwise vortices are formed. Interestingly, this vortical structure is not depicted in Ahmed's schematic of the mean flow topology, reproduced in figure 2.7, although it does appear in the study of Drouin *et al.* (2002) at a Reynolds number an order of magnitude higher than this study. Hence, this suggests that it is not generated because of the lower Reynolds number, although of course, it might be amplified by it. Zhang *et al.* (2015) has wind tunnel data at high Reynolds and with four cylindrical struts (the standard configuration), and they also show this large underbody expansion, showing that it is not simply a function of the underbody configuration.

Figures 5.4(h) and 5.4(g) show the sudden development of this structure – at $x/L = 0.15$ there is no evidence of the structure which is clear by $x/L = 0.2$. Further downstream, the associated boundary layer vortex filaments tilt away from the symmetry plane towards the corner vortex. This is consistent with a vortex in the presence of a ground plane, which has a reflected 'image' vortex on the opposite side of the ground plane with opposite rotation. The induced spanwise velocity from this image vortex pushes the D vortex away from the symmetry plane.

At $x/L = 0.3$ (figure 5.4(k)) the horseshoe vortex starts to merge with the corner vortex, and by $x/L = 0.4$ (figure 5.4(m)) the vortices have merged. The c-pillar vortex is also moving downwards, driven by the downwash from the opposite c-pillar vortex. These vortices merge with the corner and horseshoe vortices to form one large structure (figure 5.4(o)).

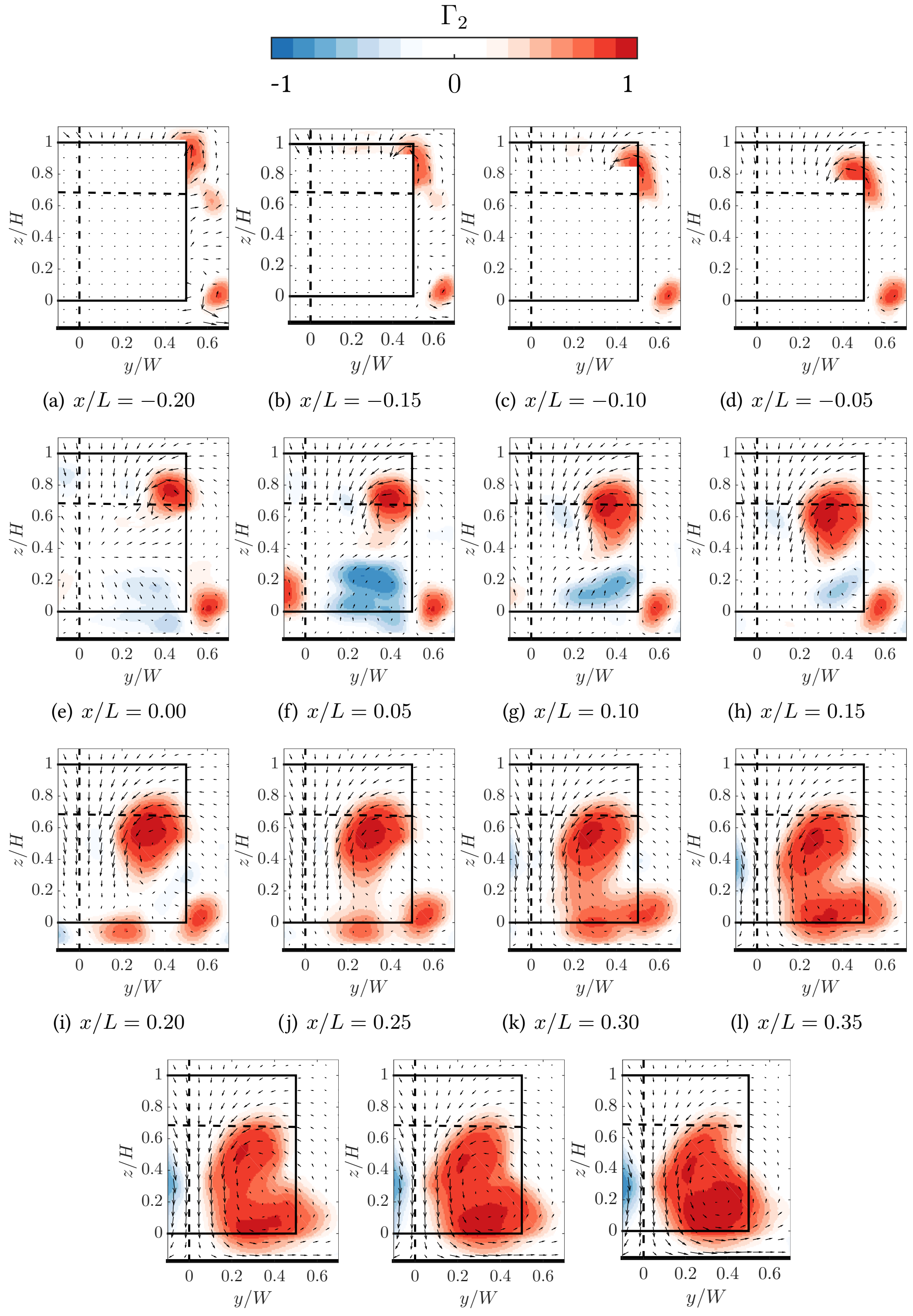

(a) $x/L = -0.20$ (b) $x/L = -0.15$ (c) $x/L = -0.10$ (d) $x/L = -0.05$

(e) $x/L = 0.00$ (f) $x/L = 0.05$ (g) $x/L = 0.10$ (h) $x/L = 0.15$

(i) $x/L = 0.20$ (j) $x/L = 0.25$ (k) $x/L = 0.30$ (l) $x/L = 0.35$

(m) $x/L = 0.40$ (n) $x/L = 0.45$ (o) $x/L = 0.50$

FIGURE 5.4: The downstream evolution of vortical structures in the wake of the standard-width Ahmed body. One half of symmetry plane and only one in one-hundred velocity vectors are shown for clarity. The vertical black dashed line represents the symmetry plane. Filled contours are Γ_2, with red representing positive (counter-clockwise) rotation and blue representing negative (clockwise) rotation, with levels between ± 1. Free-stream velocity is towards the observer.

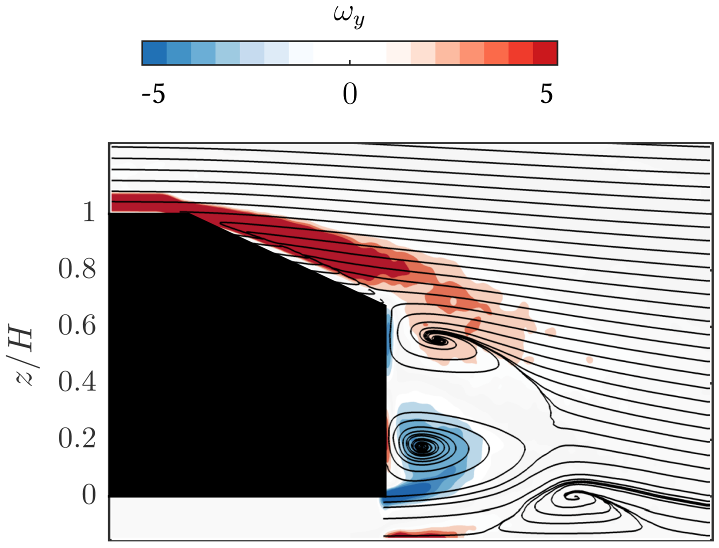

(a) $y/W = 0$

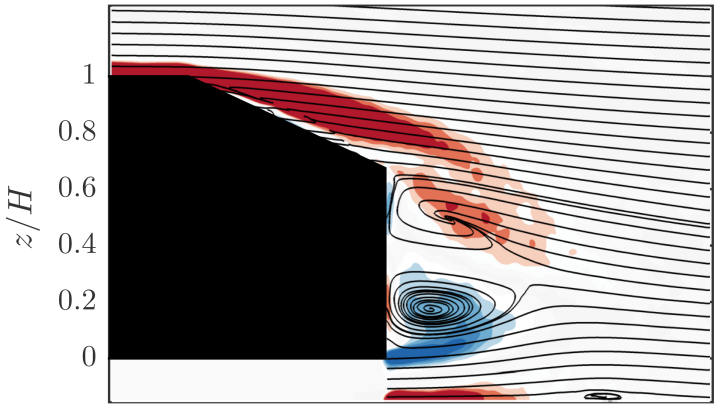

(b) $y/W = 1/6$

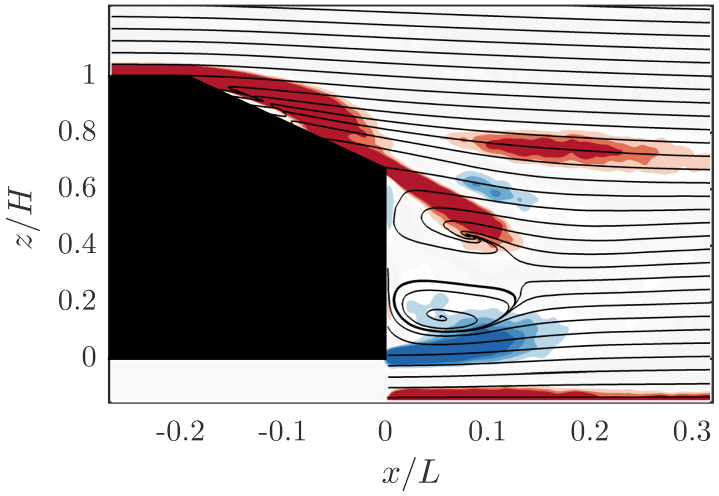

(c) $y/W = 1/3$

Figure 5.5: Spanwise vorticity and velocity streamlines in three xz planes in the time-averaged wake of the standard-width model (AM10). Positive vorticity (clockwise, red) and negative vorticity (counter-clockwise, blue), with levels between ± 5.

The spanwise structures are shown in figure 5.5. The sub-figures, which represent different spanwise planes, show streamlines based on the time-mean flow, with coloured contours of spanwise vorticity overlaid. Note that the streamlines are used to indicate the approximate local flow direction and should not be interpreted to show the trajectories of fluid particles based on the mean flow.

The streamlines indicate the recirculation regions A and B, which are generated by the flow separation at the back of the body. The separation region D, off the boundary layer, is seen in the symmetry plane (figure 5.5(a)) and a small separation is seen at $y/W = 1/6$ (figure 5.5(b)). Note that the 'banding' of positive, negative, and positive vorticity in the $y/W = 1/3$ plane is due to the plane slicing through the c-pillar vortex.

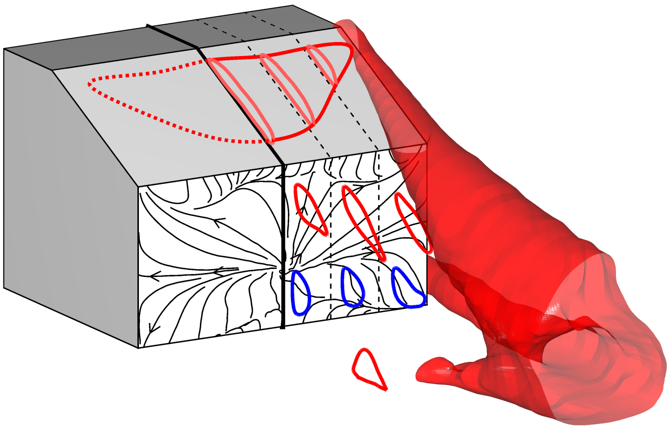

Figure 5.6: The flow topology of the standard-width (AM10) Ahmed model. Skin friction lines on the back surface are calculated from PIV data near the surface. Contour lines calculated from the spanwise Γ_2 field. The three-dimensional structure is an isosurface of Γ_2 at $2/\pi$.

The main structures in the flow contributing to the downstream wake can be seen in figure 5.6. This is a culmination of data from the cross-stream PIV planes and the streamwise planes. The separation at the top of the slant is evident, with the reattachment occurring close to the end of the slant in the middle of the body, extending less downstream for off-centre positions. The back surface has pseudo- skin-friction lines, calculated from the PIV data at the rear of the body. Three predominantly horizontal lines are on this surface, which appear between two oppositely-rotating vortices. These lines point to the existence of secondary vortices in the spanwise planes, with the three lines representing (from top to bottom) between the secondary A structure and the A structure, the A and B structures, and between the B and the secondary B vortex. It is noteworthy that there are no vertical lines present. These lines would indicate the presence of separation vortices from the sides of the body. This is further discussed in section 5.3.3.

The roll-up of the c-pillar vortex over the slant is shown, as well as the diffusing (evidenced by the expansion of the isosurface) of the vortex. The merger of the ground vortex D, the corner vortex, and the c-pillar vortex creates a large structure.

The streamwise circulation of the longitudinal vortical structures was calculated for all the downstream planes, allowing the evolution of the c-pillar vortex to be further explored. The circulation in the c-pillar vortex was determined by integrating the out-of-plane vorticity across the cross-section of the vortex. The bound was defined as where $\Gamma_2 = \pm\frac{2}{\pi}$ (Graftieaux, 2001). The vorticity was non-dimensionalised with the free-stream velocity and the square-root of the frontal area.

This data is presented in figure 5.7; several trends can be seen. Firstly, there is an increase in the circulation over the slant until $x/L = 0.1$. The growth of circulation up until $x/L = 0$, where the body ends, is explainable because the boundary layer on the side surface is rolling over the slant edge and tilting into the streamwise direction. According to Kelvin's theorem, circulation is a conserved quantity in a vortex tube; that is, in an incompressible flow vorticity originates only at the solid surfaces of the body. Since the streamwise vorticity in the c-pillar vortex is increasing even after the body ends at $x/L = 0$, this vorticity must be tilted from another plane. A plausible hypothesis is that the vorticity is fed in from the recirculation region A. While this structure is initially spanwise (figure 5.4), vortical fluid feeding along the core is tilted into the streamwise direction giving it the same sign as the corresponding c-pillar vortex; this structure is consistent with the vortex system described by Hucho (1993). While Hucho describes vortex A as having low circulation, he presents no data to support this. However, our data shows that the circulation in A has 45% as much circulation as the slant recirculation region, and B has 30%, using the Γ_2 criterion for calculating the bounds of these regions. This data, and the increase in circulation of the c-pillar vortex shows that this structure contains significant circulation. This hypothesis is investigated in detail in section 5.3.3.

From $x/L = 0.1$ to $x/L = 0.3$ the circulation remains constant. At $x/L = 0.3$, however, there is a sudden rise in the circulation. This increase occurs due to the merging of the three vortex systems: the c-pillar vortex, the corner vortex, and the horseshoe vortex. There is a slight difference (one PIV plane different) in the location of this point between the left- and right-hand vortices. This is presumably due to a slight asymmetry in the experimental setup. From $x/L = 0.375$ onwards, the circulation remains approximately constant. The streamwise circulation in each of the component vortices is given in table 5.2.

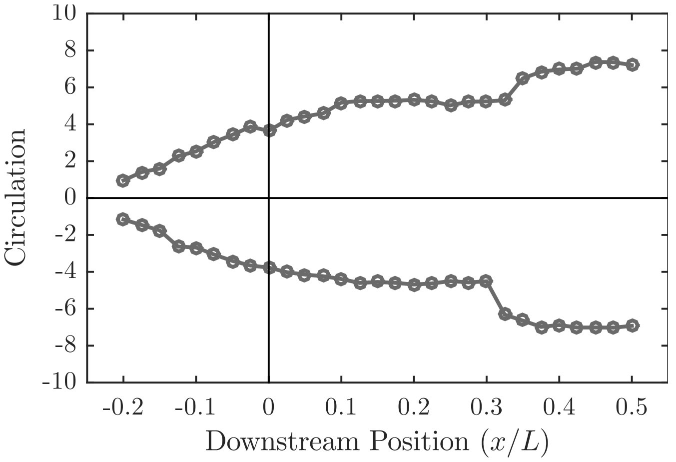

FIGURE 5.7: Time-averaged circulation (non-dimensionalised) in the c-pillar vortices as it varies with downstream location. Vertical line indicates the rear end of the Ahmed body.

Table 5.2: The circulation in each of the component vortices of figure 5.4. Gray shading represents vortex merging.

<table>
<tr><th>Plane</th><th>CPV</th><th>Corner</th><th>D</th><th>B</th></tr>
<tr><td>$x/L = 0$</td><td>3.567</td><td>0.520</td><td></td><td></td></tr>
<tr><td>$x/L = 0.1$</td><td>4.673</td><td>0.363</td><td></td><td>-0.744</td></tr>
<tr><td>$x/L = 0.2$</td><td>4.917</td><td>0.213</td><td>0.382</td><td></td></tr>
<tr><td>$x/L = 0.3$</td><td>4.818</td><td colspan="2">0.999</td><td></td></tr>
<tr><td>$x/L = 0.4$</td><td colspan="3">6.8698</td><td></td></tr>
</table>

5.3.3 The nature of the A and B recirculation regions.

Section 2.2.2.1 discusses the lack of consensus in the literature regarding the exact nature of the two spanwise vortices behind the Ahmed body. Several papers suggest they are artifacts of slicing through a single toroidal vortex, while others suggest they are two horse-shoe vortices stacked on top of each other. This section attempts to answers this question.

5.3.3.1 Flow in the spanwise planes.

Figure 5.8 shows the velocity field in the body's symmetry plane. The recirculation regions A and B are both evident. The maximum and minimum of the Γ_1 criterion are highlighted and correspond to the cores of the A and B recirculation regions respectively. If a plane further towards the edge of the body is considered (figure 5.9), the recirculation regions become much less defined. Once the plane at $y/W = 0.411$ is reached, the Γ_1 criteria no longer picks up the cores of these regions.

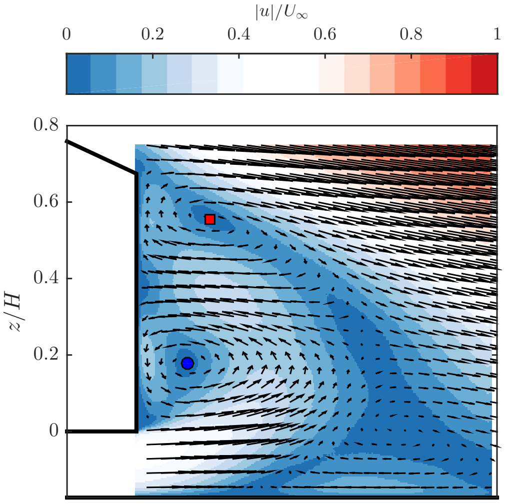

FIGURE 5.8: Flow in the symmetry plane with velocity vectors overlaid onto contours of total velocity. Only one in one hundred velocity vectors are shown for clarity. Red and blue points indicate the cores of the A and B recirculation regions respectively, found as the maximum and minimum of Γ_1 respectively.

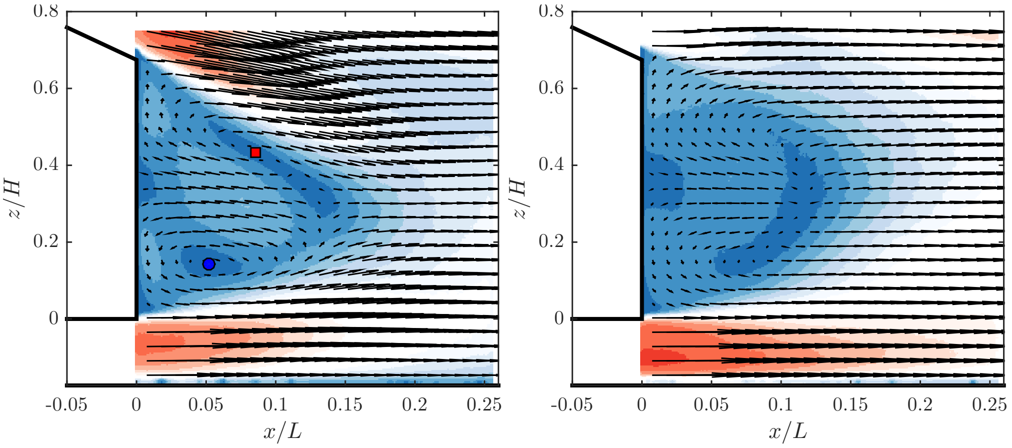

(a) $y/W = 0.308$ (b) $y/W = 0.411$

FIGURE 5.9: Flow in xz planes with velocity vectors overlaid onto contours of total velocity. Only one in one hundred velocity vectors are shown for clarity. Red and blue points indicate the core of the A and B recirculation regions respectively, found as the maximum and minimum of Γ_1 respectively.

Due to the high spatial density of the xz PIV planes the cores of the vortices can be tracked across the span. This is shown in figure 5.10. For $y/W < 0.2$, the streamwise locations of both the A and B cores increase, indicating a bend in the core. After $y/W = 0.2$, the streamwise position suddenly increases, especially of the A region, due to the bending of the region by the streamwise flow coming around the sides of the body. No data can be presented for planes beyond $y/W = 0.2$ because the region is so ill-defined that its core location cannot be determined, that is, there is no core so no core can be located.

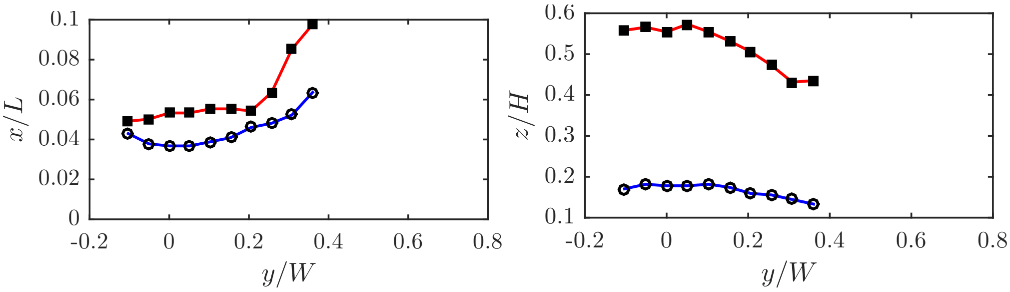

(a) Streamwise Position (b) Vertical Position

Figure 5.10: Core location of the A (red, squares) and B (blue, circles) recirculation regions against spanwise position.

It may be thought that the wake may be switching between two states, that is, sometimes the recirculation regions feed the c-pillar vortices, and sometimes they wrap around the base of the body in a toroidal manner. In order to investigate this possibility, the standard deviation of the core location is given as a function of spanwise position (figure 5.11). As there is no significant increase in the standard deviations, it seems the vortices are essentially as constant in position at the edges as they are in the symmetry plane.

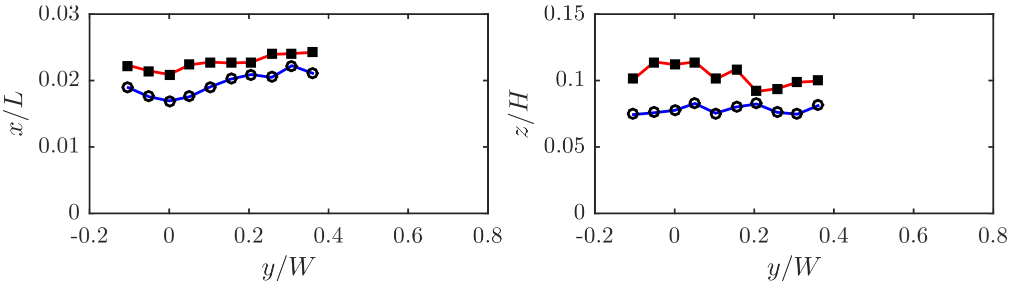

(a) Streamwise STD (b) Vertical STD

Figure 5.11: Standard deviation of the core location of A (red, squares) and B (blue, circles) recirculation regions against spanwise position.

The circulation bound in each of these regions was extracted through integration of the velocity field. Figure 5.12 shows how the circulation varies with spanwise position. The circulation in region B linearly decreases in magnitude with spanwise position, but region A has a more abrupt decrease. As the circulation is varying, and since circulation cannot be created except at the boundary of the body, some of the circulation must be tilted into another direction. This could be either the streamwise, supporting the twin-horseshoe interpretation, or the vertical direction, suggesting the vortex takes a toroidal shape.

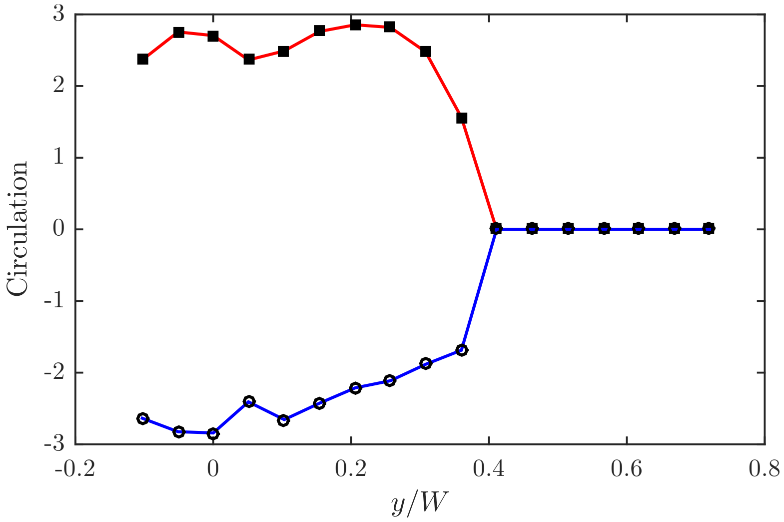

Figure 5.12: The circulation of the A (red, squares) and B (blue, circles) recirculation regions against spanwise position. Circulation is non-dimensionalised with the free-stream velocity and the square-root of the frontal area.

5.3.3.2 Transverse planes

If the recirculation regions were joined in a torus shape, one would expect to see these structures in horizontal planes taken at a range of heights. Figure 5.13 shows such a plane; clearly there is no rotation in the expected regions of the torus. For comparison, a PIV slice through the mid-height of a square-back Ahmed body is shown in figure 5.13(b), demonstrating the vertical vortices that are present within a toroidal wake. The contrast shown here is quite stark, but the only difference between the two experiments is the rear slant angle dropping to 0°.

Figure 5.14 shows isosurfaces of spanwise Γ_1, showing the core location and size of the recirculation regions across the span. At planes closer to the edge of the body, the A region tilts more into the streamwise direction than it does downwards. This is as expected if the regions were horseshoe vortices as opposed to a vortex torus or ring.

The velocity data in the two planes was reconstructed into a three-dimensional velocity field, comprising all three velocity components in a volume located behind the base. The Q-criterion (Hunt *et al.*, 1988) is used to visualise this data (figure 5.15). It is evident from this plot that the A-region merges with the c-pillar vortex, rather than tilting downwards and merging with B.

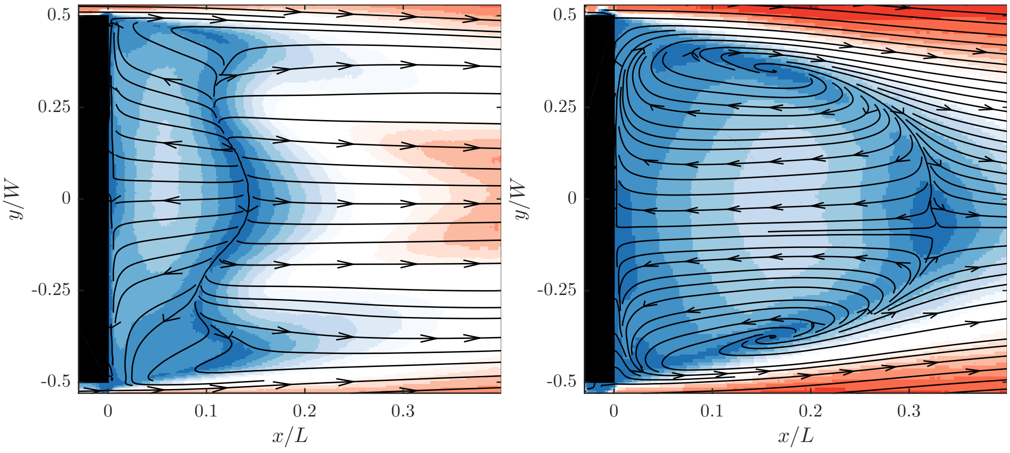

(a) 25° slant (b) Square-back

FIGURE 5.13: (a) Flow in the xy plane at $z/H = 0.369$ with velocity streamlines overlaid onto contours of total velocity. (b) Flow behind the square-back Ahmed geometry at the mid-height ($z/H = 0.5$) plane showing the vertical legs of the toroidal vortex.

Three-dimensional streamlines are presented in figure 5.16. These were generated by seed points in and around the B recirculation region, and show a cohesive picture of flow rolling up into the core of the vortex and being transported to the sides of the body. Notice that all of the streamribbons, which are seeded uniformly across the span, ultimately move downstream only at the edges of the body. This demonstrates that there is sufficient spanwise flow to move all the fluid at the centre of the body that is within the B vortex to the edges of the body. As the flow reaches the edge of the body, the shear of the free-stream velocity in the streamwise direction causes the streamlines to tilt into that direction. This is further support for the theory that the A and B vortices are in fact two horse-shoe shaped vortices above each other.

When the same procedure is followed for region A, the flow pattern is less coherent. The recirculatory nature of the flow is still evident, but the vortex is not as tight as in the B region, neither is the spanwise flow as strong. This is understandable as the B region is produced by a high shear region of practically free-stream velocity reaching the low pressure region and rolling around the bottom edge. For the A region, the flow is first separated at the top of the slant, and reattaches (in the mean flow sense) at the end of the slant, before it separates again and forms the A region.

5.3.3.3 Summary

The proposed wake structure is schematised in figure 5.18, where the cores of each major structure are indicated by solid lines. This schematic shows spanwise circulation tilting into the streamwise direction at four points. Firstly the slant recirculation region flows outwards

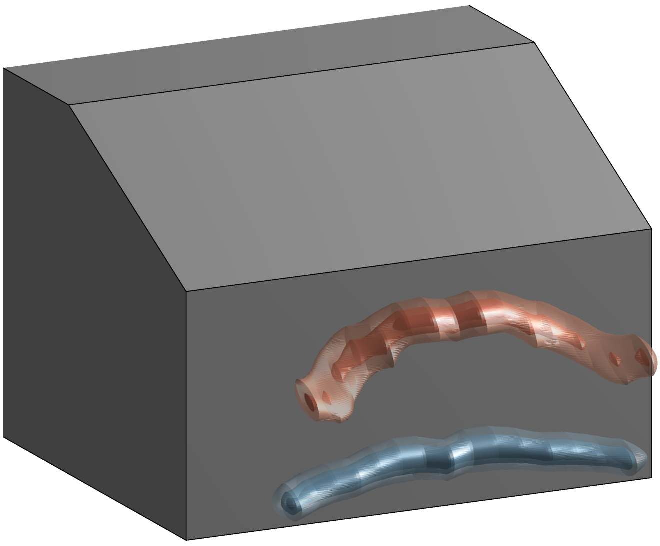

(a) Iso view

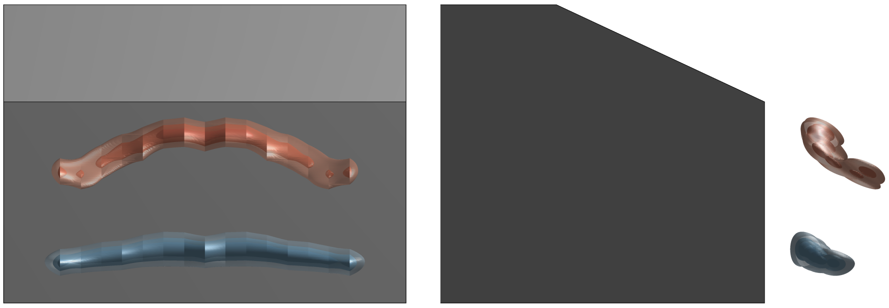

(b) Rear view

(c) Side view

Figure 5.14: Three-dimensional representations of spanwise Γ_1 criterion. Red represents positive rotation (A region), blue represents negative rotation (B region). Colours are consistent with figure 5.12.

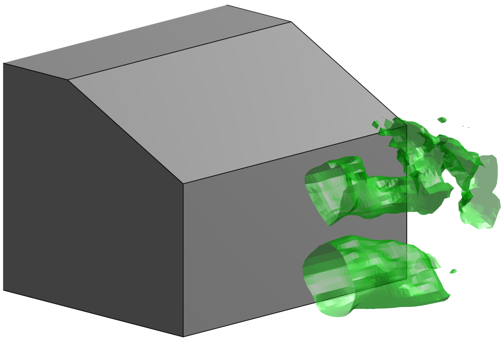

(a) Rear view

Figure 5.15: Isosurface of Q criterion after reconstructing the velocity fields from multiple two-dimensional PIV planes in both xy and xz directions.

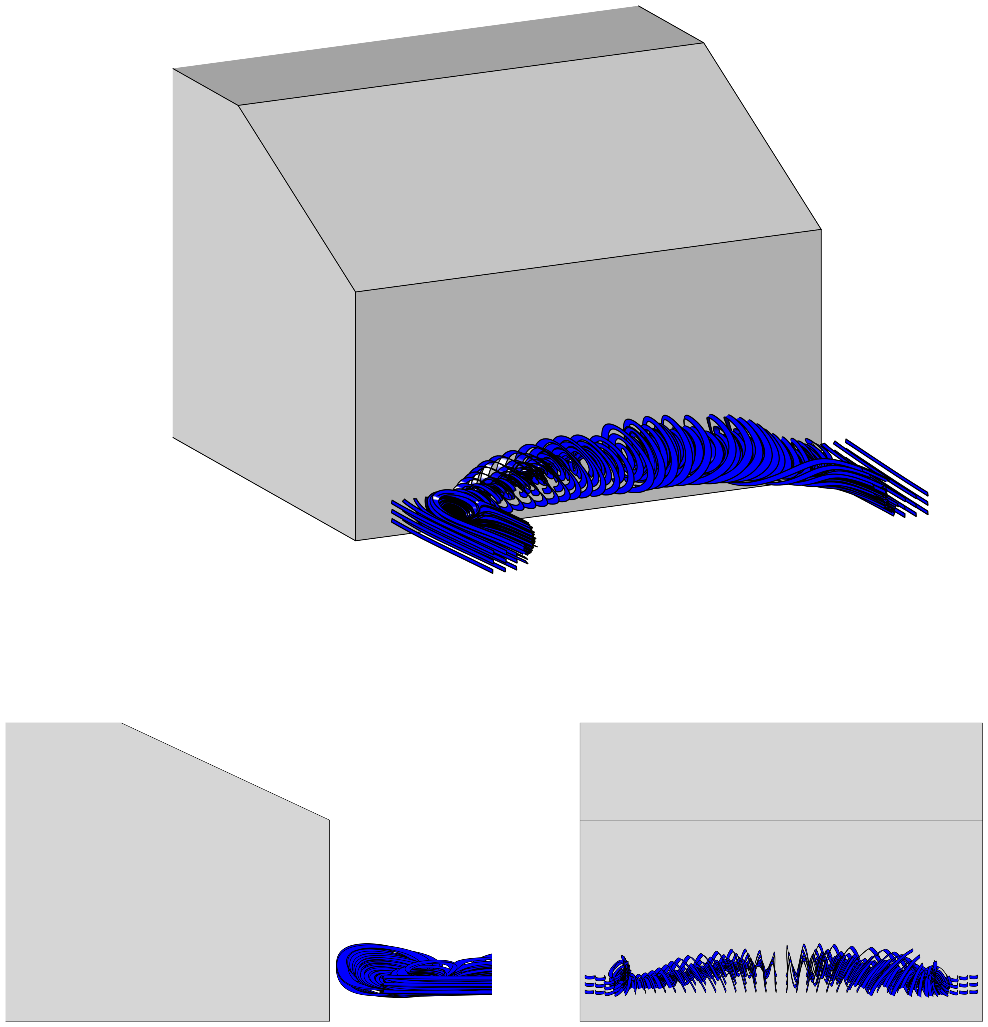

Figure 5.16: Streamribbons calculated from three-dimensional reconstruction of time-averaged velocity fields. Seed points are within the B vortex. Spanwise flow is evident until the edge of the body, where the streamribbons are tilted in the streamwise direction.

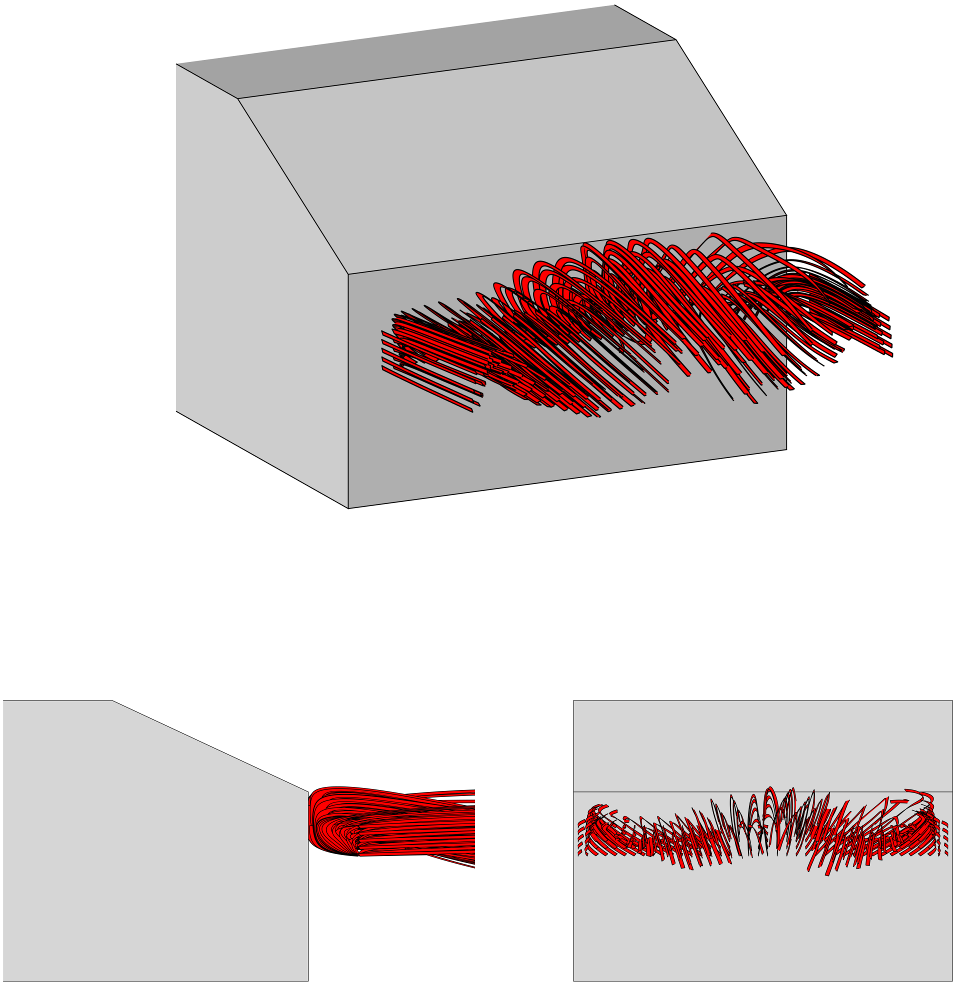

Figure 5.17: Streamribbons calculated from three-dimensional reconstruction of time-averaged velocity fields. Seed points are within the A vortex.

and into the c-pillar vortices. Next, the A and B vortices are tilted, with A joining the c-pillar vortex, and B diffusing. Finally, the boundary layer vortex hits the separatrix formed by the ground separation and tilts like a horseshoe.

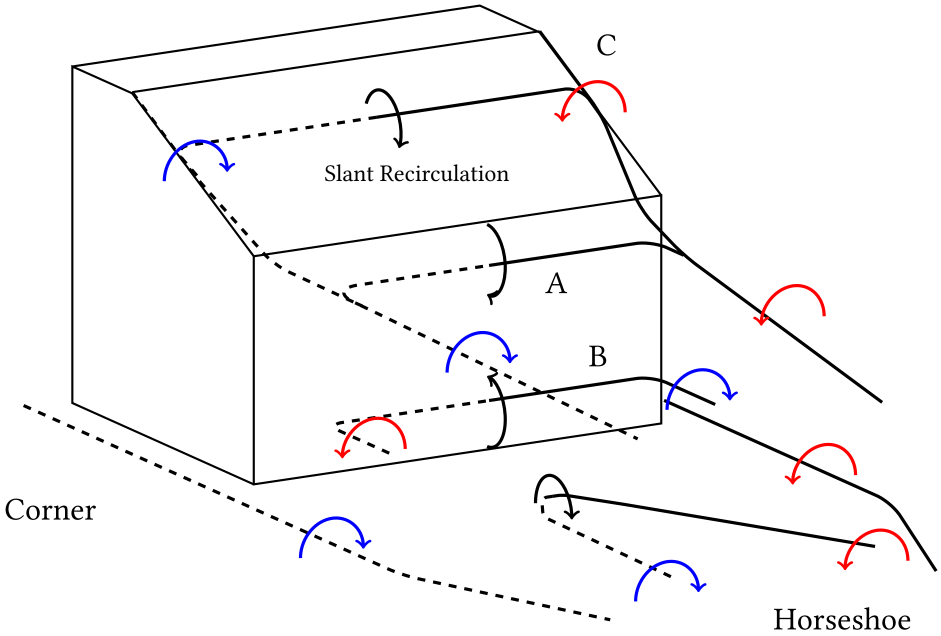

Figure 5.18: Proposed time-averaged vortex structure schematic in the wake of the standard width Ahmed body, with lines indicating location of vortex cores. The structure is dashed for $y/W < 0$ and solid for $y/W > 0$. Spanwise rotation indicated by black arrows, streamwise rotation indicated by red or blue arrows for positive or negative rotation respectively.

5.4 Wake dynamics

The standard deviations from the cross-stream PIV images are presented in figures 5.19 and 5.20 for the transverse and vertical velocity components respectively. This information reveals where the flow is more unsteady. Close to the body, the variations are most significant just above (figure 5.20(b)) and especially inside (figure 5.19(b)) the c-pillar vortex. This indicates a variation in the roll-up strength since the velocity fluctuations are strongest along the path the fluid takes in entering the vortex.

These plots show an increase in both components of standard deviation around the downstream location $x/L = 0.15$ (figures 5.19(d) and 5.20(d)). This coincides with the location where the A-vortex is joining the c-pillar. The large variations are located between the combined A- and c-pillar vortices and the B-vortex. This would suggest that there is a significant motion of the structures during this merger. This idea is developed further in section 5.4.1 below.

As the wake develops further, the variation is constrained mostly to the vortex bounds, reinforcing the fact that this longitudinal structure dominates the wake both in a time-averaged and an instantaneous sense.

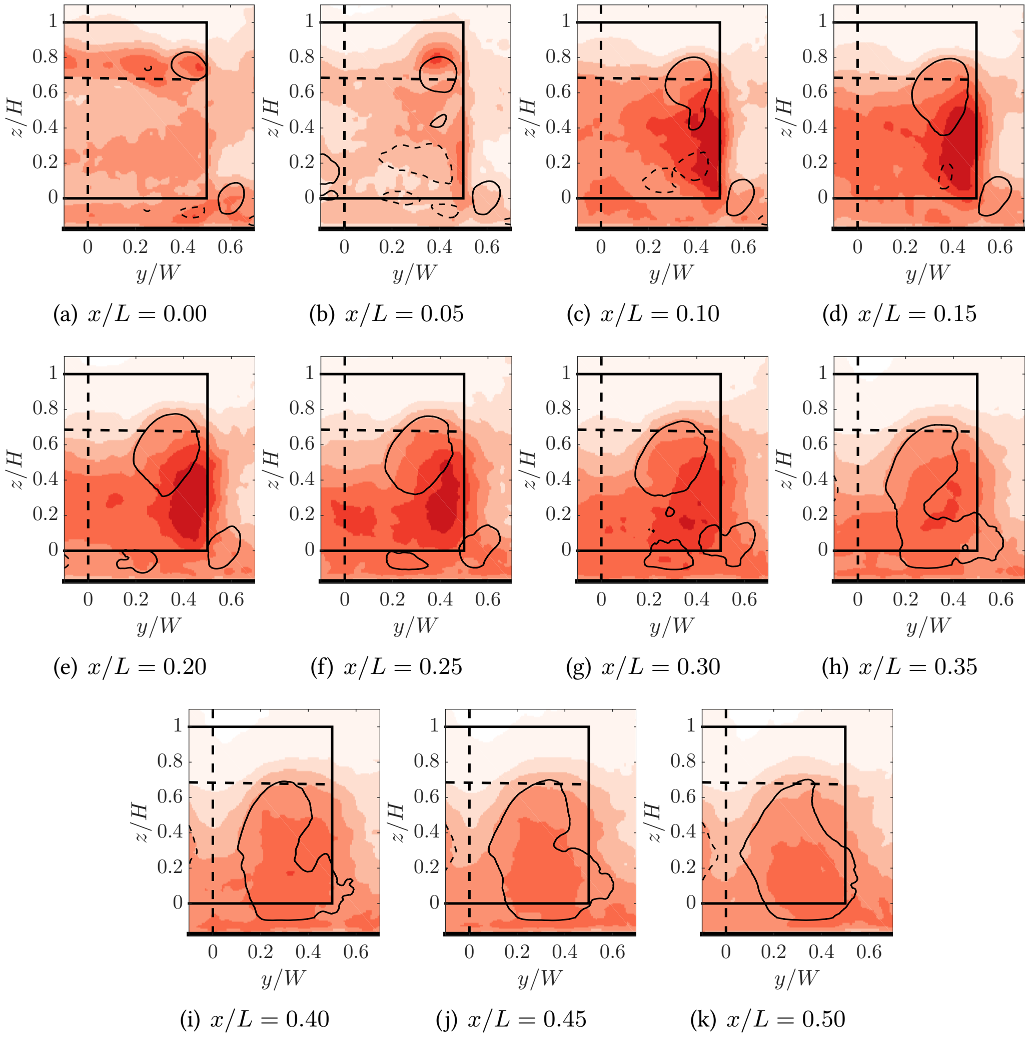

(a) $x/L = 0.00$ (b) $x/L = 0.05$ (c) $x/L = 0.10$ (d) $x/L = 0.15$

(e) $x/L = 0.20$ (f) $x/L = 0.25$ (g) $x/L = 0.30$ (h) $x/L = 0.35$

(i) $x/L = 0.40$ (j) $x/L = 0.45$ (k) $x/L = 0.50$

Figure 5.19: Standard deviation of v velocity component behind the Ahmed body. Contours of Γ_2 overlaid with solid lines for $\Gamma_2 = 2/\pi$ and dashed lines for $\Gamma_2 = -2/\pi$. Flow is toward the observer.

5.4.1 Cross-stream planes

Time-resolved PIV was used in order to visualise the dynamics of the wake structures. An FFT was performed at every spatial location across the acquisition plane. Figure 5.21 has the spatial average of all spectra in the cross-stream plane. Both the vertical and spanwise velocity fluctuations show a distinct peak at $\mathrm{St} = 0.241$. The characteristic length scale chosen for the Strouhal calculations is the body height, for reasons discussed in section 6.4.

Using the tool described in section 3.5.1, the relative strength of each frequency across the plane can be seen. Figure 5.22(a) shows that the $\mathrm{St} = 0.241$ frequency in the spanwise fluctuations is strong behind the lower corners of the model, as well behind the center of the back surface. Figure 5.22(b) shows that this frequency is strong in the vertical fluctuations just below and inside the c-pillar vortices.

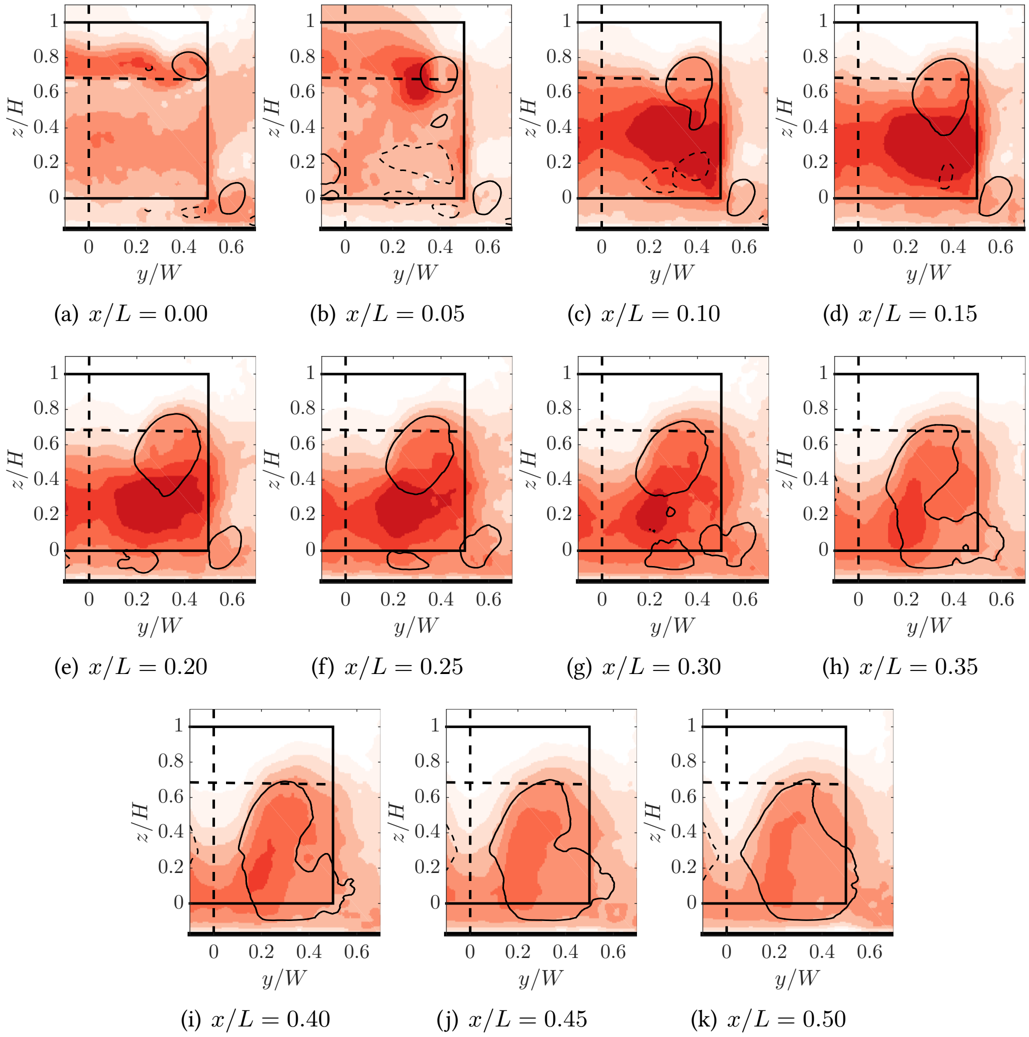

(a) $x/L = 0.00$ (b) $x/L = 0.05$ (c) $x/L = 0.10$ (d) $x/L = 0.15$

(e) $x/L = 0.20$ (f) $x/L = 0.25$ (g) $x/L = 0.30$ (h) $x/L = 0.35$

(i) $x/L = 0.40$ (j) $x/L = 0.45$ (k) $x/L = 0.50$

Figure 5.20: Standard deviation of w velocity component behind the Ahmed body. Contours of Γ_2 overlaid with solid lines for $\Gamma_2 = 2/\pi$ and dashed lines for $\Gamma_2 = -2/\pi$. Flow is toward the observer.

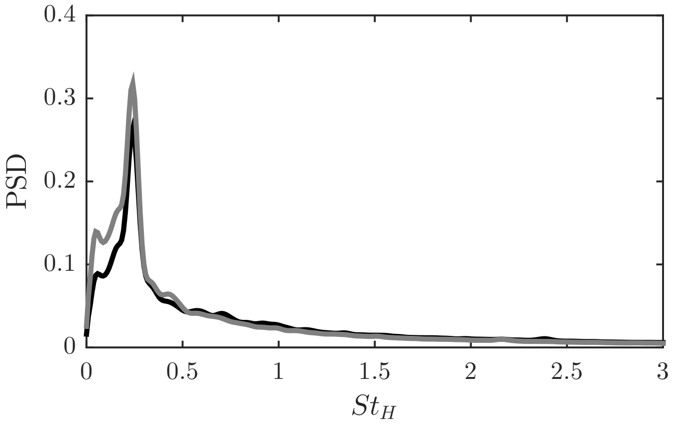

Figure 5.21: Spatial average of the Power Spectral Densities (PSD) of the velocity fluctuations in the wake behind the Ahmed body at $x/L = 0.2$. Spanwise velocity (black) and vertical velocity (gray). The dominant peak is St $= 0.241 \pm 0.0048$.

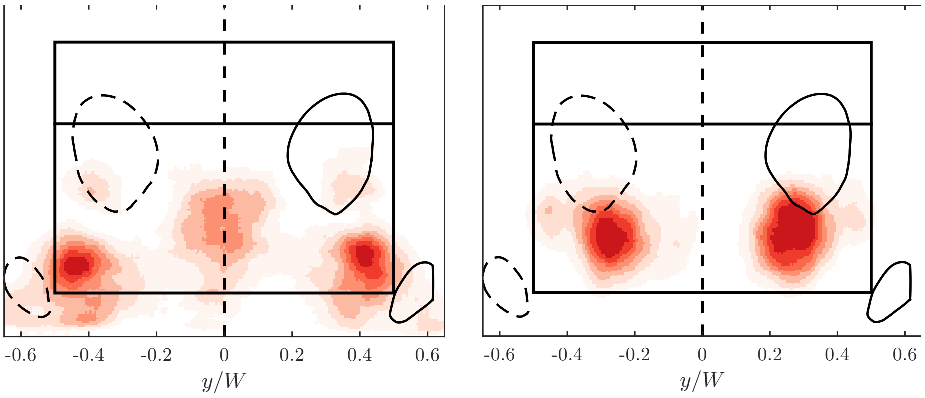

(a) Spanswise Fluctuations (b) Vertical Fluctuations

Figure 5.22: Power in the St $= 0.241$ frequency component across the cross-stream plane at $x/L = 0.2$. The time-averaged vortex bounds Γ_2=$\pm 2/\pi$ are shown with contours for reference. Positive contours represented by solid line, negative with dashed. Flow is toward the observer.

In order to understand the nature of these periodic fluctuations, subsets of the time-series in each of the regions of high power are plotted in figure 5.23. This shows the phase difference between velocity signals at opposite sides of the body. The spanwise velocity fluctuates with both sides in phase with each other, that is, at the corners, as flow is moving left (or right) on one corner, it is moving left (or right) at the other corner. On the other hand, the vertical velocity fluctuates half a wavelength out of phase, that is, upwards on one side of the body and downwards on the other.

Figure 5.24 shows that this pattern is consistent across the whole wake, with figure 5.24(a) being symmetric about the $y/W = 0$ line, and figure 5.24(b) being anti-symmetric about that line. The flow structure described by such a phase pattern is one of two structures, flapping in phase in a spanwise direction, but moving alternately in the vertical direction.

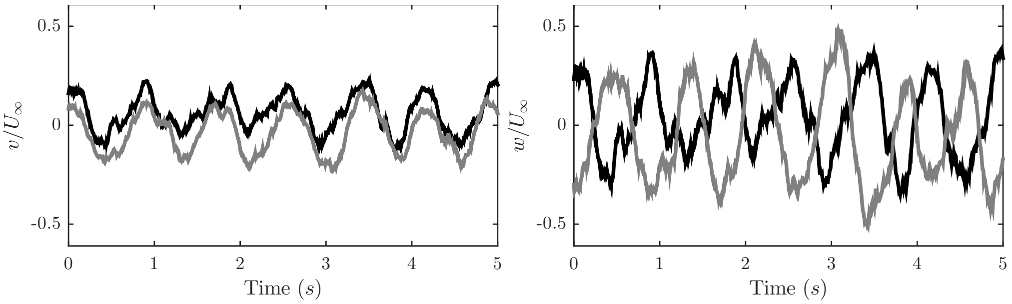

(a) Spanwise Velocity (b) Vertical Velocity

Figure 5.23: POD filtered time-series at symmetric positions downstream of the Ahmed body at $x/L = 0.2$. The points chosen represent the points of maximum power of the St $= 0.241$ frequency component (see figure 5.22). Left is spanwise velocity at $y/W = \pm 0.45$, $z/H = 0.15$. Right is vertical velocity at $y/W = \pm 0.25$, $z/H = 0.25$. Black time-series is for positive y/W positions, gray is for negative.

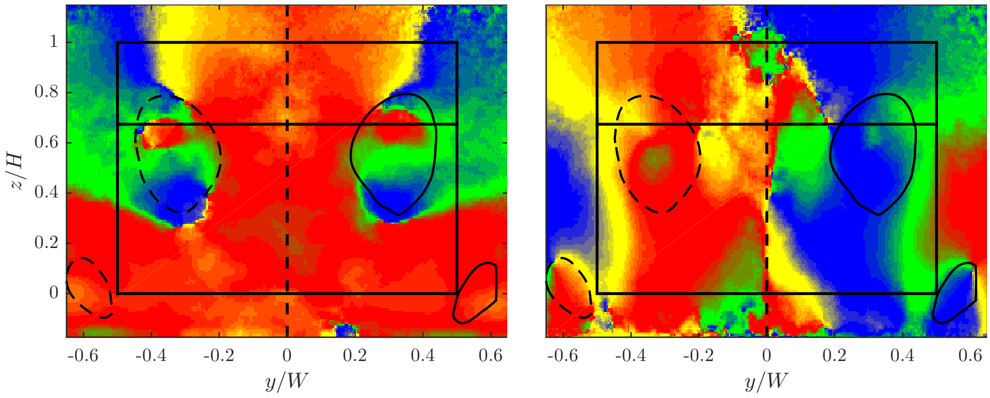

(a) Spanwise Fluctuations (b) Vertical Fluctuations

Figure 5.24: Phase of the St $= 0.241$ frequency across the cross-stream plane at $x/L = 0.2$. The time-averaged vortex bounds Γ_2=$\pm 2/\pi$ are shown with dashed lines for reference.

This data can be visualised through the use of a space-time plot. Here, the y and z axes of the plot will correspond to the y and z spatial axes, but the x axis of the plot is time. This shows how the structures vary in space through time. The data is first filtered using a POD filter as described in section 3.5.5. The reconstruction is based on the three most energetic modes, which was found to reproduce the high-energy motions of the key structures without introducing the small-scale structures and error. Figure 5.25 shows one such space-time plot, generated from PIV data at $x/L = 0.2$. Time progresses to the right of each figure, except the third, where time increases out of the page. The dominant frequency seen in the FFT analysis manifests itself in variations in the locations of the major structures. Only one element in these plots does not vary in time: the top of the c-pillar vortices remain stationary at $z/H = 0.75$. The bottom of the c-pillar vortex, on the other hand, strengthens and expands downwards. This occurs periodically (at St $= 0.241$) and when it occurs, all the following happen:

- the base of the c-pillar vortex moves outboard
- the corner vortex is shifted upwards and outboard
- the opposite c-pillar vortex is contracted to its minimum extent
- the opposite corner vortex is shifted downwards and inboard
- the streamwise element of recirculation region B is strengthened below the opposite c-pillar vortex

A longer time sequence is shown in figure 5.26. This figure shows that the oscillations described above are not dependent on the time segment selected, but are essentially constant in time.

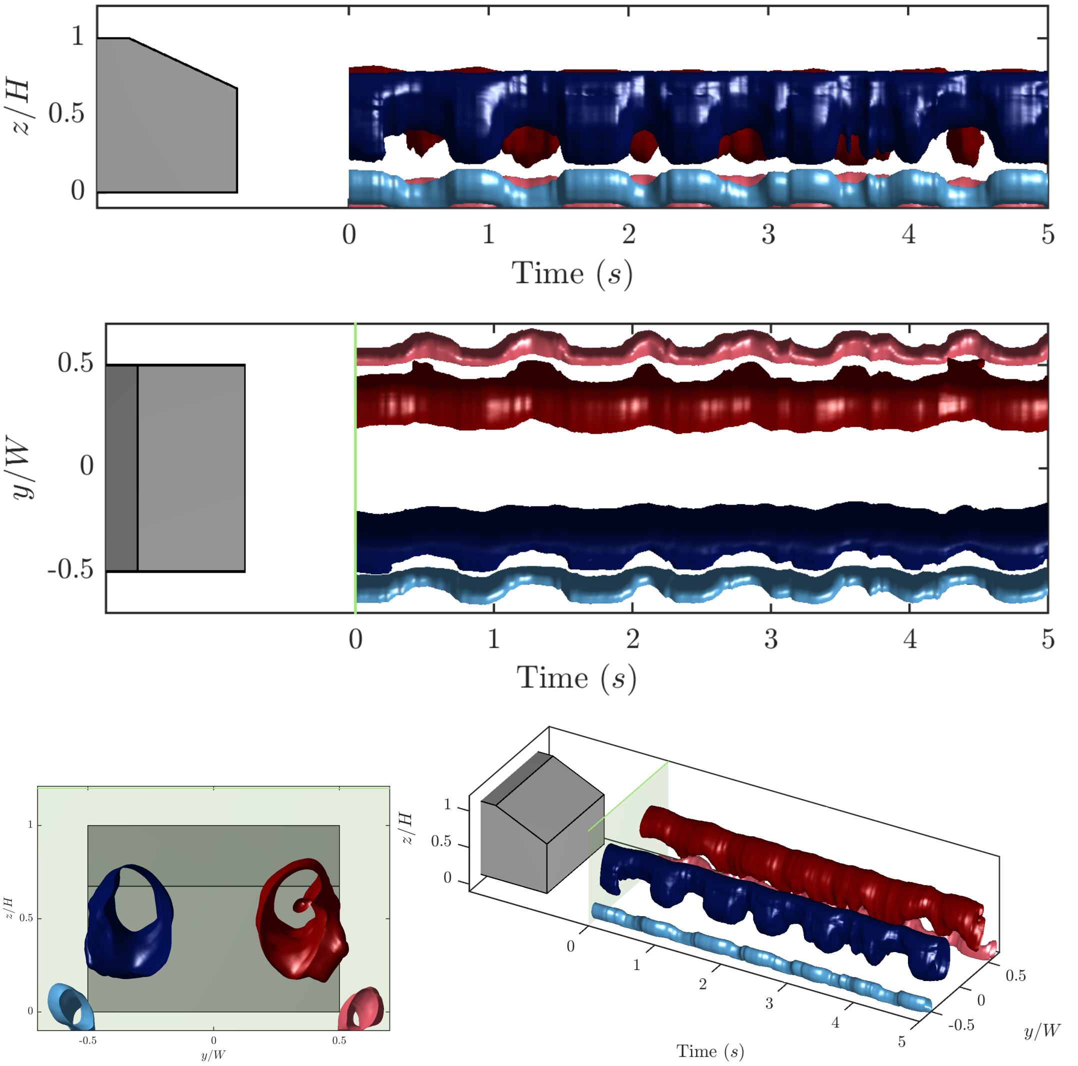

Figure 5.25: Cross-stream dynamics at $x/L = 0.2$ showing motion of the c-pillar and corner vortices over a five second period. Green plane represents relative location of the acquisition plane to the Ahmed body. Positively rotating structures in reds and negatively rotating structures in blues. The c-pillar vortices are the darker structures, the lighter structures being the corner vortices.

The largest (in terms of distance moved) cross-stream motion of all the structures occurs to recirculation region B. The movement of this structure is isolated in figure 5.27. Here we see the motion is switching sides of one leg of the vortex being high and outboard of the c-pillar vortex while the other leg moves downwards, inboard, and weakens. The flapping of this horse-shoe vortex is significant as it explains why the negative circulation of this vortex does not have as large an impact on the downstream structures as might be expected. The vortex location is varying over a large ($\sim$40% of the body's width) portion of the base area, and is fluctuating periodically, meaning over time, the structure is weaker than the A region, which is much more constant and compact. Interestingly, this symmetry and periodicity of trailing streamwise vortices has been observed in other bluff body wakes, from that of a high-speed train (Bell *et al.*, 2014) to a rotating sphere (Stewart *et al.*, 2010).

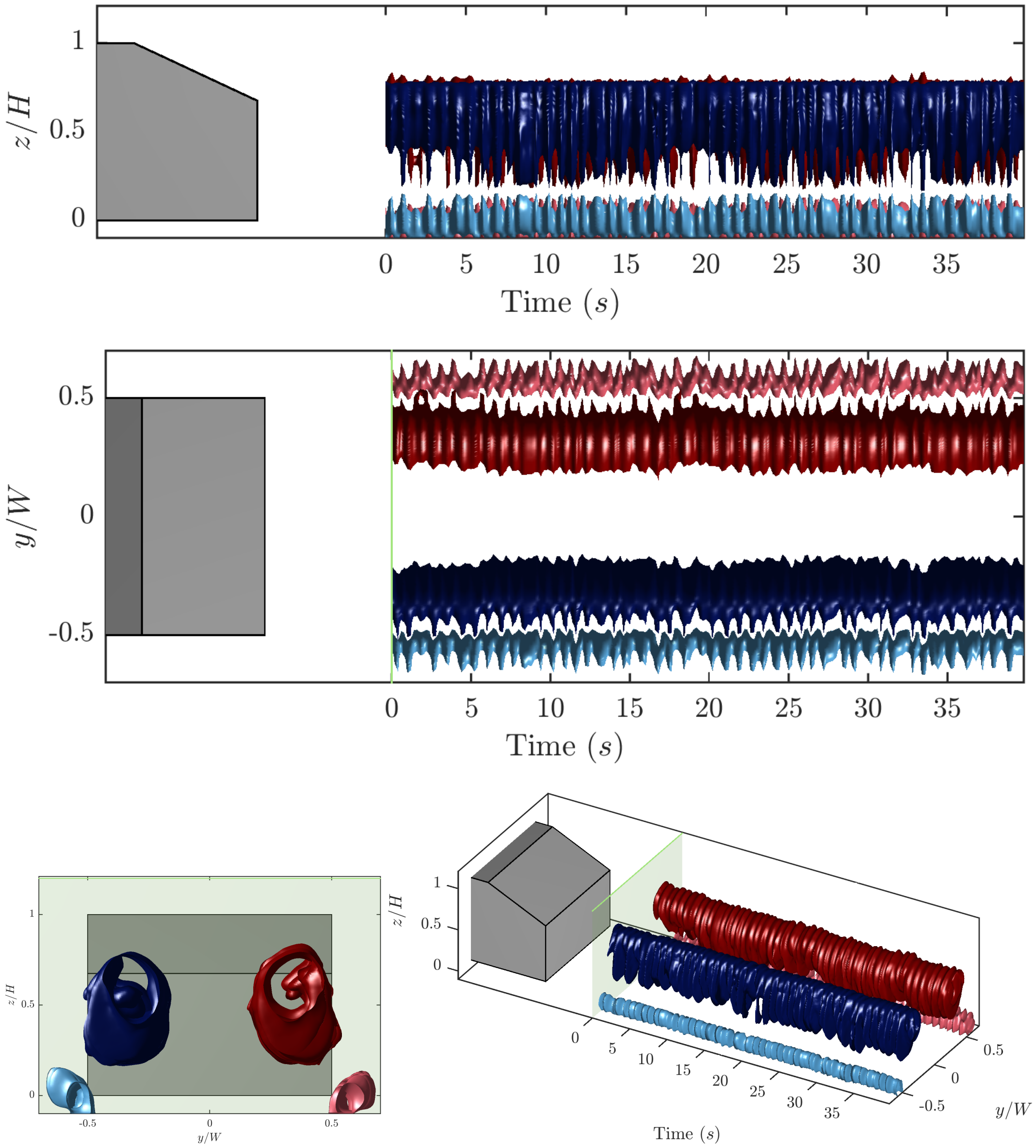

Figure 5.26: Cross-stream dynamics at $x/L = 0.2$ showing motion of the c-pillar and corner vortices over a forty second period, showing that the periodic behaviour is not transient. Green plane represents relative location of the acquisition plane to the Ahmed body.

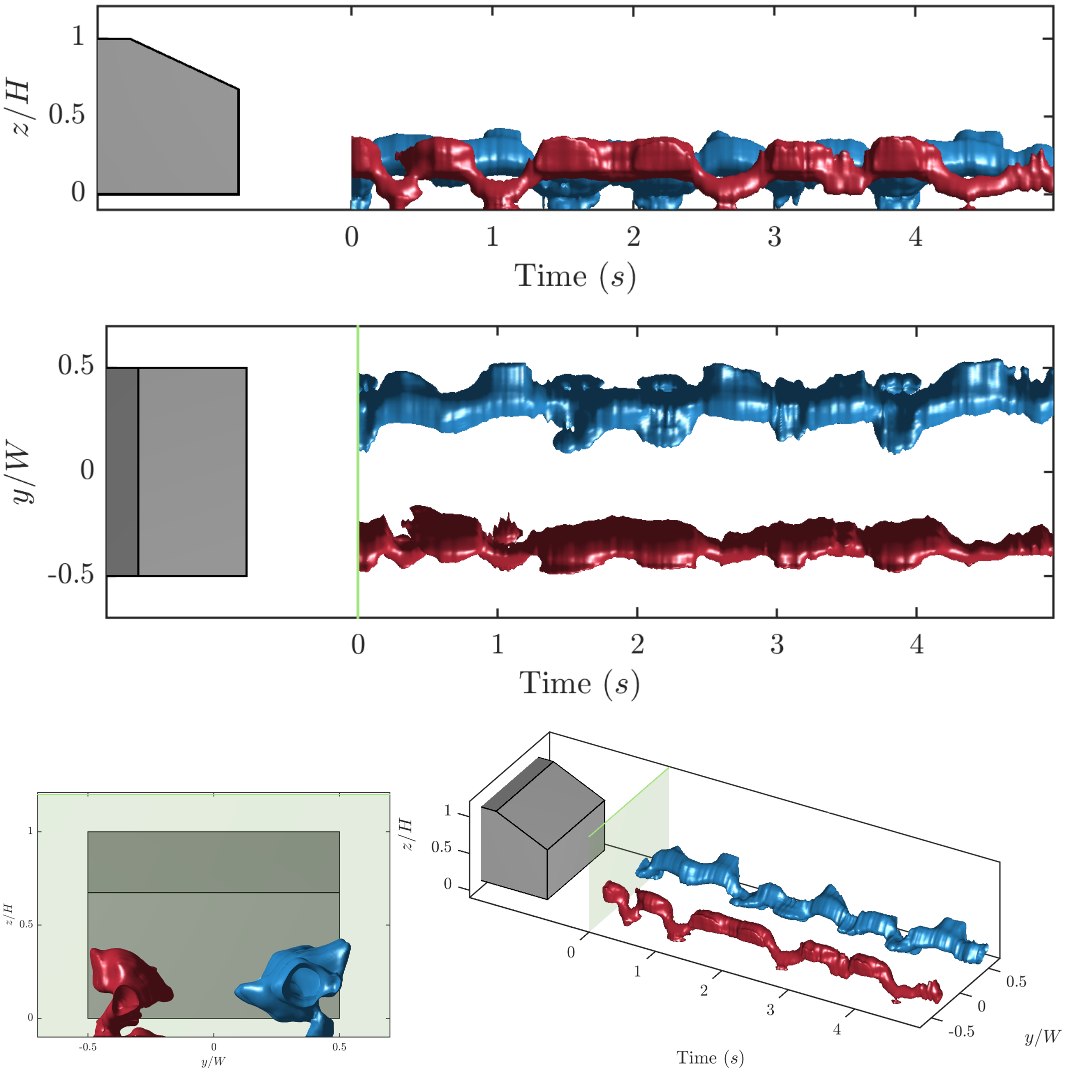

Figure 5.27: Cross-stream dynamics at $x/L = 0.2$ showing motion of the streamwise element of recirculation region B. Green plane represents relative location of the acquisition plane to the Ahmed body.

Figure 5.28, which is closer to the rear of the body ($x/L = 0.05$) shows that initially, the locations of the c-pillar vortices are stable. There is almost no motion at all.

The PIV data was binned based on the $\mathrm{St} = 0.241$ frequency into three bins according to their phase. These are plotted in figure 5.29, showing the two extremities as well as the balanced case. It is clear that the lower part of the each c-pillar vortex alternately moves downwards. At the same time, the corner vortex is pushed outboard and upwards, causing the spanwise velocity fluctuations seen in the lower corners of figure 5.24(a). The top of the vortex is stable, as its location is maintained due to the constancy of the roll-up over the c-pillars.

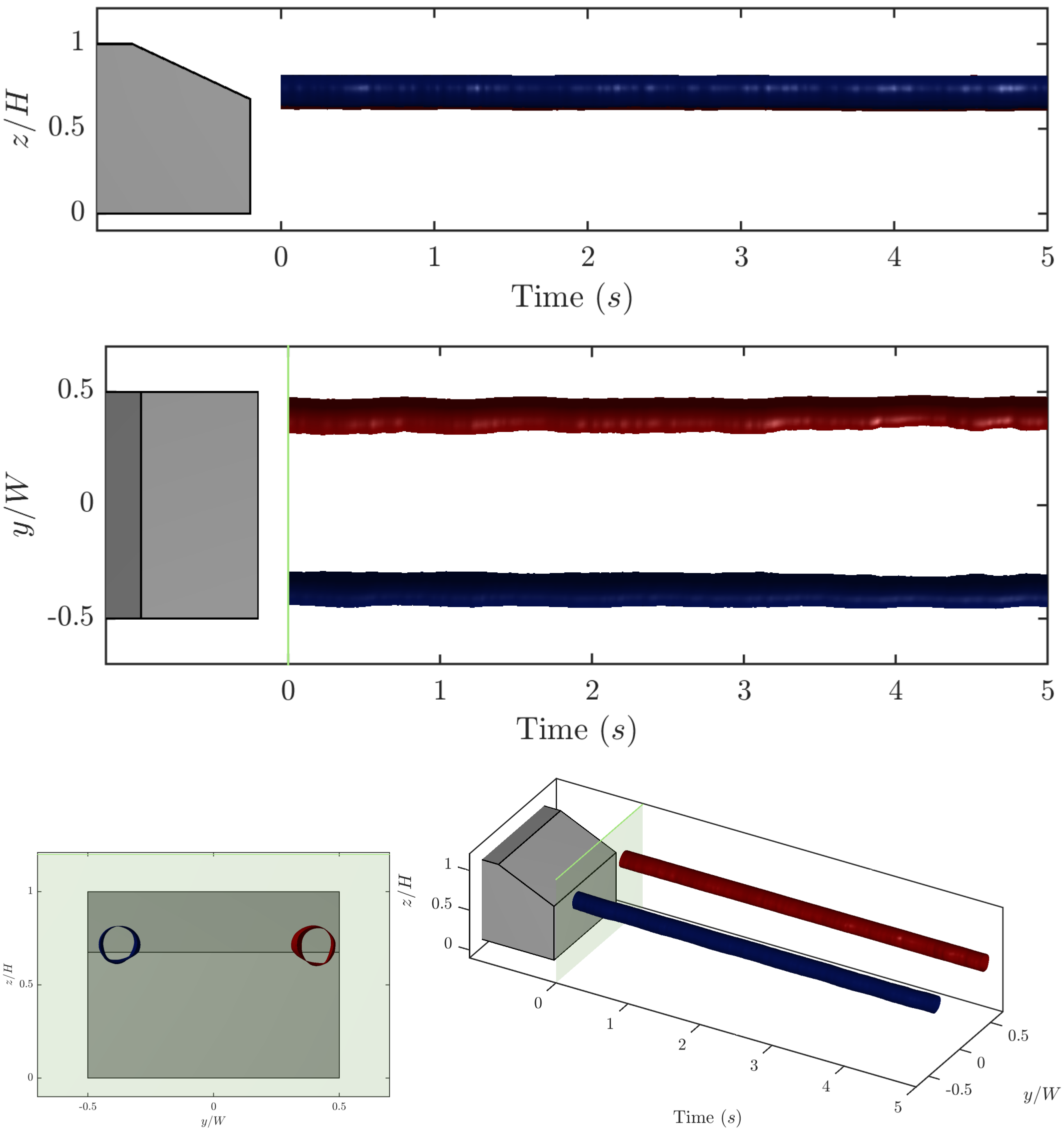

FIGURE 5.28: Cross-stream dynamics at $x/L = 0.05$ showing the stability of the c-pillar vortices over a five second period. Green plane represents relative location of the acquisition plane to the Ahmed body.

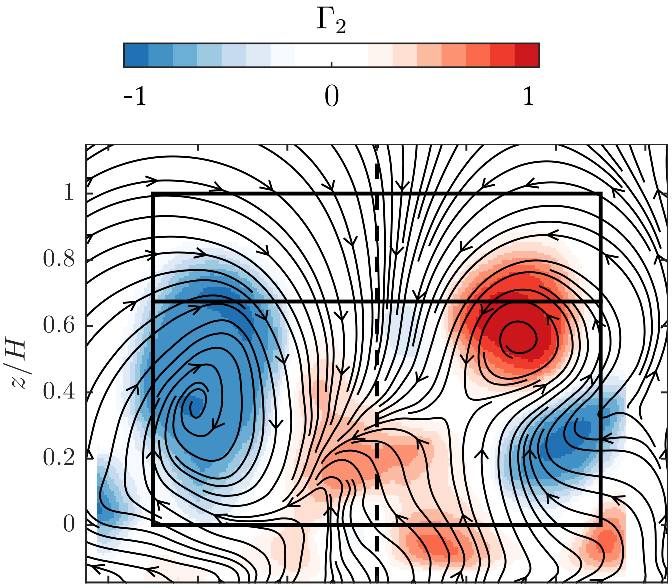

(a) Negative

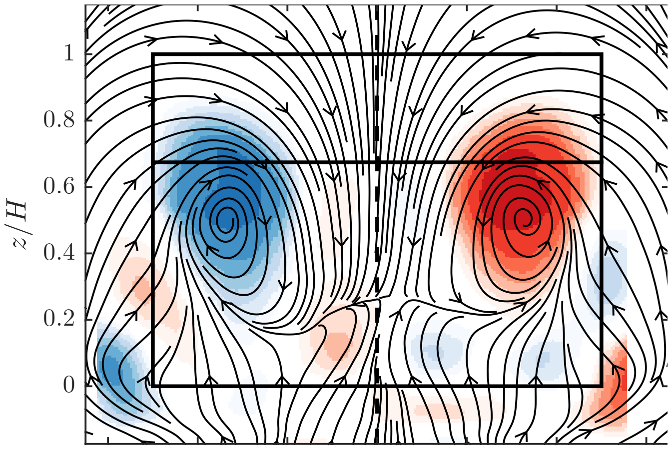

(b) Balanced

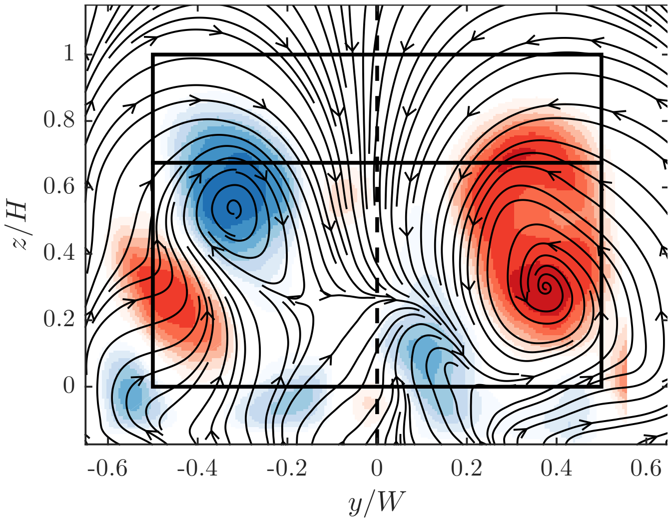

(c) Positive

Figure 5.29: The three states between which the wake oscillates at $x/L = 0.2$. Streamlines and filled contours of Γ_2, levels are ± 1. Streamlines are only used to indicate the local flow direction and should not be interpreted as literal streamlines. Flow is towards the observer.

5.4.2 Streamwise plane

5.4.2.1 Flapping over the back-light

A Proper Orthogonal Decomposition was used to analyse the frequencies in the streamwise planes. A 980 frame subset of the PIV data set was broken down into orthogonal modes, then ranked based on the kinetic energy content in each. The energy of each mode is given in figure 5.30.

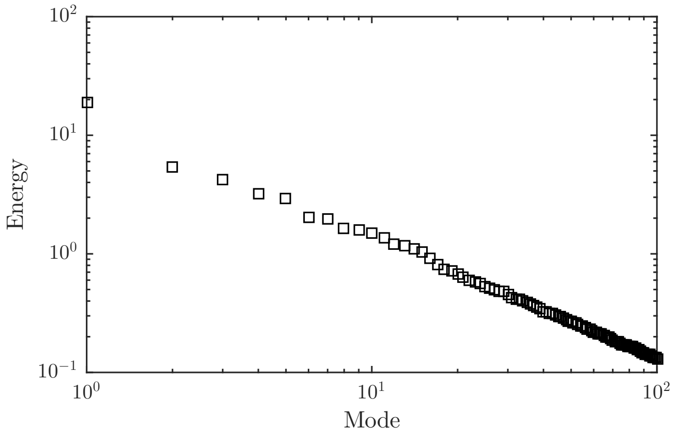

FIGURE 5.30: Percentage energy of each mode from the POD. Only 980 frames are used for the decomposition.

The most energetic mode has no pair, that is, this mode is uncorrelated with any other mode, indicating that this structure is not a vortex shedding mechanism. This mode coefficient indicates whether or not the flow is attached. This can be seen in figure 5.31 showing the correlation between the mode coefficient and the pitch angle of the velocity vector at the end of the slant angle. Figure 5.31(b) gives the PDF of the mode norms. As this distribution is more Gaussian than bimodal, the flapping of the recirculation region is a constantly varying phenomenon, rather than a direct switching between two states.

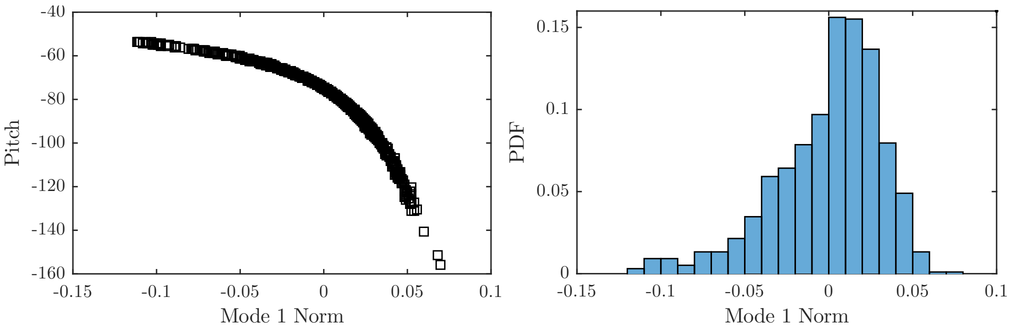

FIGURE 5.31: (a) Correlation between the mode 1 coefficient and vector pitch at the end of the slant from the POD reconstructed frame. (b) Probability density function of the mode norms for the first POD mode.

Extracting a reconstruction of the instantaneous flow structure using the first mode plus the mean gives figure 5.32, which shows the field associated with the two extremities of figure 5.31(a). Here we can see that the time-averaged flow separates and then reattaches at the end of the slant. By looking at the instantaneous frames we see that the flow is in fact sometimes completely separated over the back-light, as in (b), or completely attached, as in (d). The mode norms here correspond to lowest and highest norms from figure 5.31. The instantaneous flow fields corresponding to the instances that are reconstructed in (b) and (d) are given in (c) and (e). This shows that the reattachment is not simply an artifact of the POD methodology, as it is seen in the instantaneous snapshots themselves.

The frequency that the flow is flapping at can be extracted from the frequency of variations in the mode norms. It is evident from figure 5.33 that there is no dominant flapping frequency across time, rather, the frequency varies significantly. This is indicative that the reattachment above the slant is not regular in time, and may be the cause of the wide variation in flapping frequencies reported by the papers in table 2.1.

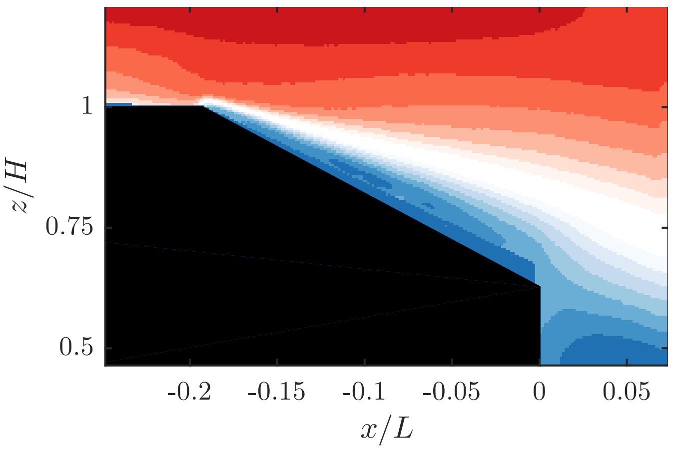

(a) Time-average

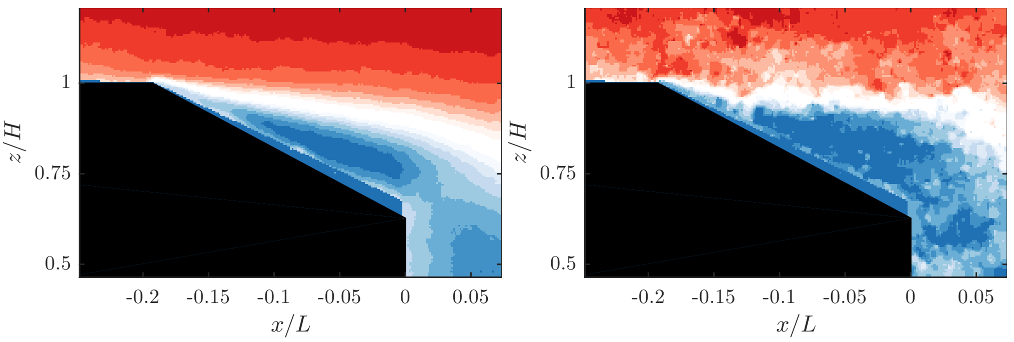

(b) Mode 1 norm = -0.11 Reconstructed (c) Mode 1 norm = -0.11 Instantaneous

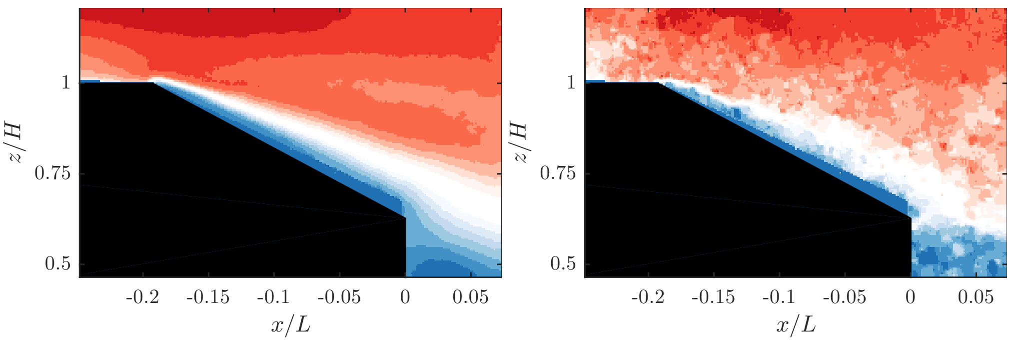

(d) Mode 1 norm = 0.07 Reconstructed (e) Mode 1 norm = 0.07 Instantaneous

Figure 5.32: (a) Ensemble average of u-velocity over the slant of the standard-width Ahmed model. (b-c) Separated flow state. (d-e) Attached flow state. See text for details.

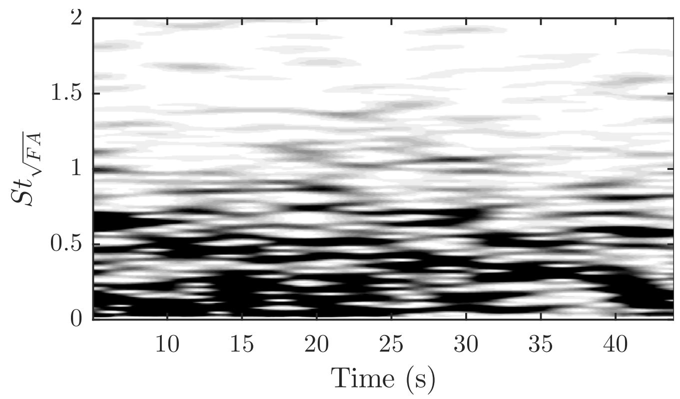

Figure 5.33: Power Spectral Density of the first POD mode norm as it varies with time.

5.5 Summary

PIV data with high spatial resolution and high temporal resolution has been presented. It has been shown that the longitudinal structures are fourfold:

1. The side shear layers roll up over the slant side edges, feeding the c-pillar vortices that advect downstream, forming the main trailing vortex structures.
2. The circulation from the A region feeds into, and strengthens, the c-pillar vortex close to the body, causing an increase in the streamwise circulation up to $x/L = 0.1$.
3. The corner vortices generated from the accelerated underbody flow; and
4. a horseshoe vortex caused by the expansion of the underbody flow away from the groundplane.

In the spanwise sense, the near-wake of the Ahmed body consists of two vortices, A and B. These are generated by the flow separating at the horizontal edges at the back of the body. They are shown to be two horseshoe-shaped vortices with legs pointing downstream, rather than a toroidal vortex. They each induce spanwise flow to the outer edges before tilting into the streamwise direction.

The bulk of the motion in the wake of the Ahmed body comes from the motion of these vortices. The streamwise legs of vortex B are particularly mobile, shifting from side to side and causing the rest of the wake to follow at the same frequency.

CHAPTER 6

THE EFFECT OF ASPECT RATIO ON THE WAKE OF THE AHMED BODY

6.1 Introduction

While chapter 5 furthers our insight into the Ahmed body wake, this chapter investigates the effect of separating the two c-pillar vortices from each other. The Ahmed body geometry is systematically modified by changing the aspect ratio in order to understand and characterise the effects of aspect ratio on the wake. This investigation aims to control the lateral spacing of the c-pillar vortices and thereby understand the influence of their spacing on the strength and nature of these vortices, the topology of other features within the wake, and, by inference, the drag.

The wake is investigated for eight different width Ahmed models as described in section 3.3.2. Similar analysis techniques as were used in chapter 5 are employed. The time-averaged structures are shown to exist in one of two regimes, dependent on whether the c-pillar vortices are close enough to the centre-plane to aid reattachment of the flow onto the slant or not.

The effect of the aspect ratio on the wake dynamics is also investigated. The peak frequency found throughout the wake is invariant to the aspect ratio, showing that the relevant length-scale for that motion should be the height of the body.

Key findings:

There is a critical aspect ratio of $AR = 1.9$, beyond this aspect ratio:

- the flow completely separates over the slant due to the reduced effect of the downwash produced by the two c-pillar vortices
- the flow is much more two-dimensional as the c-pillar vortices are no longer strengthened by the spanwise vorticity from the slant separation region
- this spanwise vorticity is shed downstream directly rather than tilting into and strengthening the c-pillar vortices
- the wake is shifted upwards as evidenced by the core locations of the vortices
- the circulation in the trailing vortices are much weaker
- the ground plane separation horseshoe vortex strength increases with aspect ratio

Additionally, the wake dynamics are investigated, finding:

- the A and B vortical structures are more steady for the reattaching cases, suggesting a pair of standing vortices as opposed to a single standing vortex (B) and a separated shear layer for the wider cases
- the variation of the B vortical structure is still the dominant temporal feature of the wake
- the frequency of this variation is not a function of aspect ratio

This chapter is based on some of the data presented in

Venning, J., Lo Jacono, D., Burton, D., Thompson, M. & Sheridan, J. 2015 The effect of aspect ratio on the wake of the Ahmed body. *Experiments in Fluids* **56** (6).

6.2 Measurement and Data Processing

The eight bodies chosen for this experiment all had slant angle of 25° and varied in width from 60% of the original width to 130%. Each body has two designations in this chapter, firstly, as a percentage of the original width (eg. AM06 is 60%, AM13 is 130%), and secondly as the aspect ratio of the rear slant (i.e. $AR = \frac{W}{L_S}$). Table 6.1 shows the geometries of all the bodies used.

PIV was acquired in the cross-stream (yz) plane behind the models. In order to explore the development of these vortices, the PIV acquisition plane was varied from $x/L = -0.2$ to

Table 6.1: The Ahmed model geometries used in the experiments on the effect of aspect ratio. Bold faced row indicates the scaled geometry matching that of the standard Ahmed body.

Name	Width % standard	Width (mm)	Height (mm)	AR
AM06	60	58.4	72.3	1.05
AM07	70	68.1	72.3	1.23
AM08	80	77.8	72.3	1.40
AM09	90	87.5	72.3	1.58
AM10	**100**	**97.3**	**72.3**	**1.75**
AM11	110	107.0	72.3	1.93
AM12	120	116.7	72.3	2.10
AM13	130	126.4	72.3	2.28

Table 6.2: Time-resolved PIV parameters for the investigation into aspect ratio effects.

	xy	xz	yz
No. of pairs	6250	9796	8266
Framerate	200Hz	200Hz	200Hz
Magnification Factor	$15.7px/mm$	$8.9px/mm$	$13.1px/mm$
Field of View	$0.49L \times 1.31H$	$0.86L \times 1.98W$	$1.56W \times 1.60H$
Vectors	249×249	249×159	249×189
Planes	$z/H = 0.67$	$y/W = 0, 0.2, 0.4$	$x/L = 0.05, 0.1, 0.2, 0.4$
Bodies	AM10	AM06, AM08 AM10, AM12	AM06, AM08 AM10, AM12

$x/L = 0.5$ with increments of $x/L = 0.025$. The experimental parameters are detailed in section 3.4.2.7 and are the same as used for the study into the standard width Ahmed model in table 5.1. Additional streamwise planes were acquired at three positions across the span ($y/W = 0$, $y/W = \frac{1}{6}$, and $y/W = \frac{1}{3}$) for each body. Time-resolved PIV was also recorded using the PCO Dimax camera in all three orientations to investigate the dynamics (table 6.2).

6.3 Effect of the aspect ratio on the time averaged flow

Figure 6.1 gives a cross-stream comparison at the same downstream location in the near wake for all of the bodies. For each aspect ratio, three structures are present: the c-pillar vortex rotating positively (red, upper), the corner vortex (positive) outside the base of the model (red, lower), and the streamwise element of structure B (negative, blue). For the narrower cases, the streamwise leg of vortical structure B is also visible around $z/H = 0.4$. For the wider cases, the c-pillar vortex appears stretched in the vertical direction, possibly indicating that a merger of the A and C vortices has already taken place.

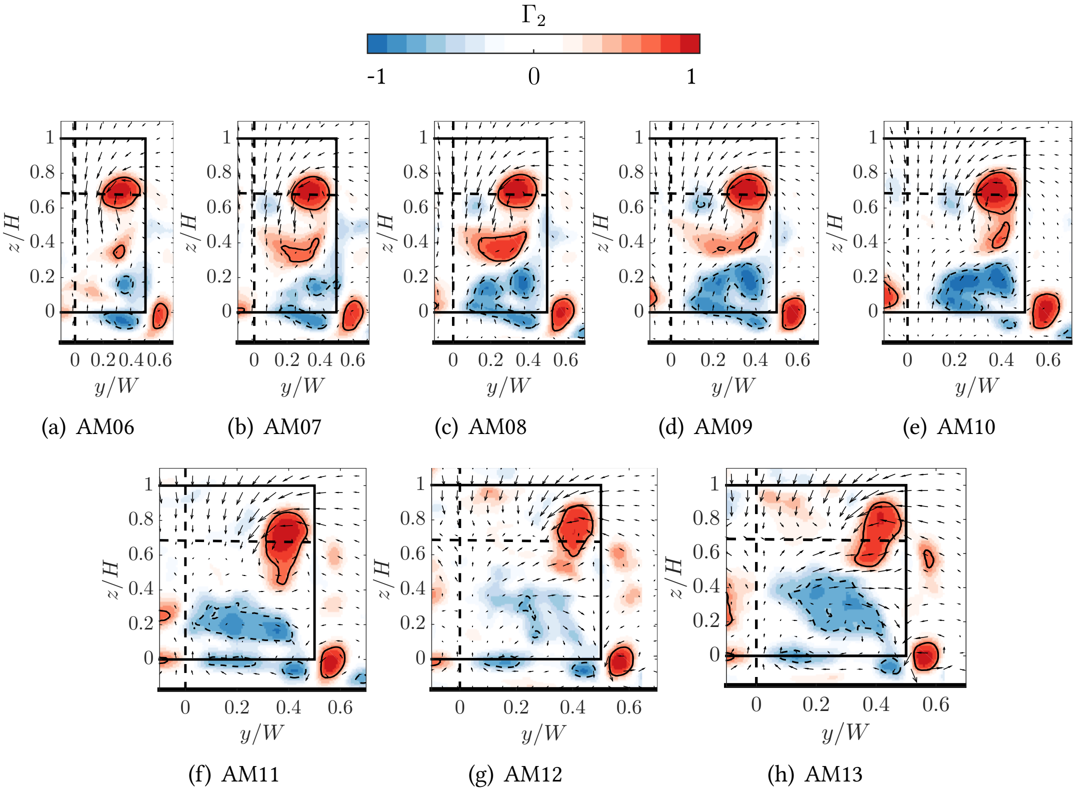

(a) AM06 (b) AM07 (c) AM08 (d) AM09 (e) AM10

(f) AM11 (g) AM12 (h) AM13

Figure 6.1: Velocity field in the near wake ($x/L = 0.075$) overlaid with contours of Γ_2 criterion for various aspect ratio Ahmed bodies. Γ_2 levels are between ±1 and only one in one-hundred vectors are included for clarity. Flow is towards the observer.

Figures 6.2, 6.3 and 6.4 contain the streamlines for the streamwise and vertical velocity components behind each of the Ahmed models for $y/W = 0$, $y/W = \frac{1}{6}$ and $y/W = \frac{1}{3}$ respectively. The flow is broadly the same as the standard-width model (subfigure (e) in each figure), though the aspect ratio changes it in several ways.

The size and location of the A and B vortical structures are dependent on the aspect ratio. There is an increase in the core height of both the A and B spanwise vortices with increasing aspect ratio, since the relative influence of the c-pillar vortices is weaker as they effect less of the width. The streamwise position of the B vortex in particular moves downstream for the wider bodies away from the symmetry plane. For the narrow bodies, the strongest point of the B vortex (in the symmetry plane) are quite close to the edges of the body, so the curvature as the structure is tilted downstream by the edge shear is quite tight. For the wider bodies, there is more spanwise room for the vortex to tilt downstream and hence the core location is moving downstream in figure 6.5(c).

Regarding the tilting of this B structure, the cross-stream coordinates of the core are presented in figure 6.6. Firstly, the persistence downstream of the B vortex is dependent on the flow regime. For the separated cases, the vortices persist much further downstream than for the

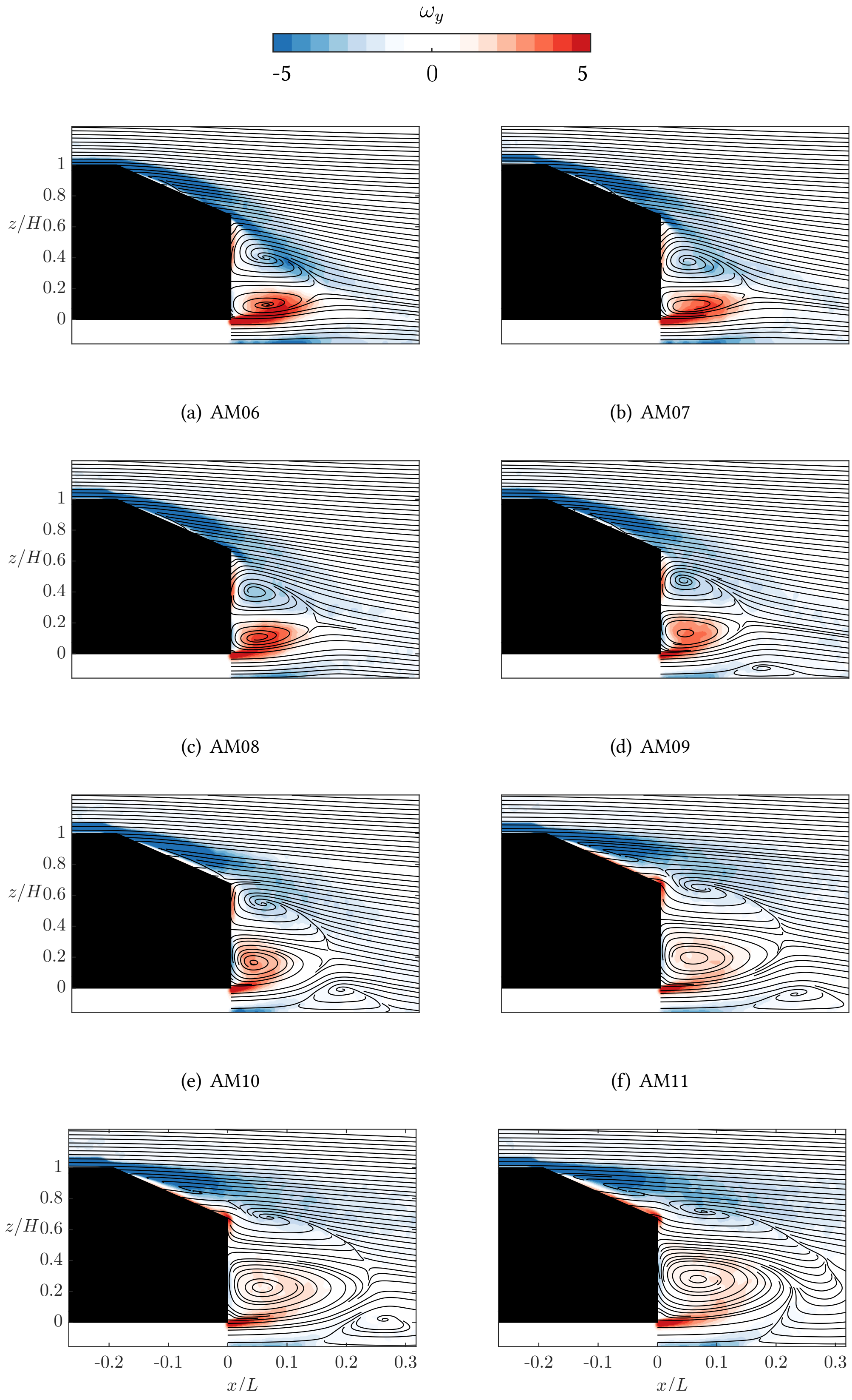

(a) AM06 (b) AM07

(c) AM08 (d) AM09

(e) AM10 (f) AM11

(g) AM12 (h) AM13

Figure 6.2: Time-averaged spanwise vorticity and velocity streamlines in xz planes at $y/W = 0$. Positive vorticity (red) and negative vorticity (blue). Vorticity is non-dimensionalised and levels are between ± 5.

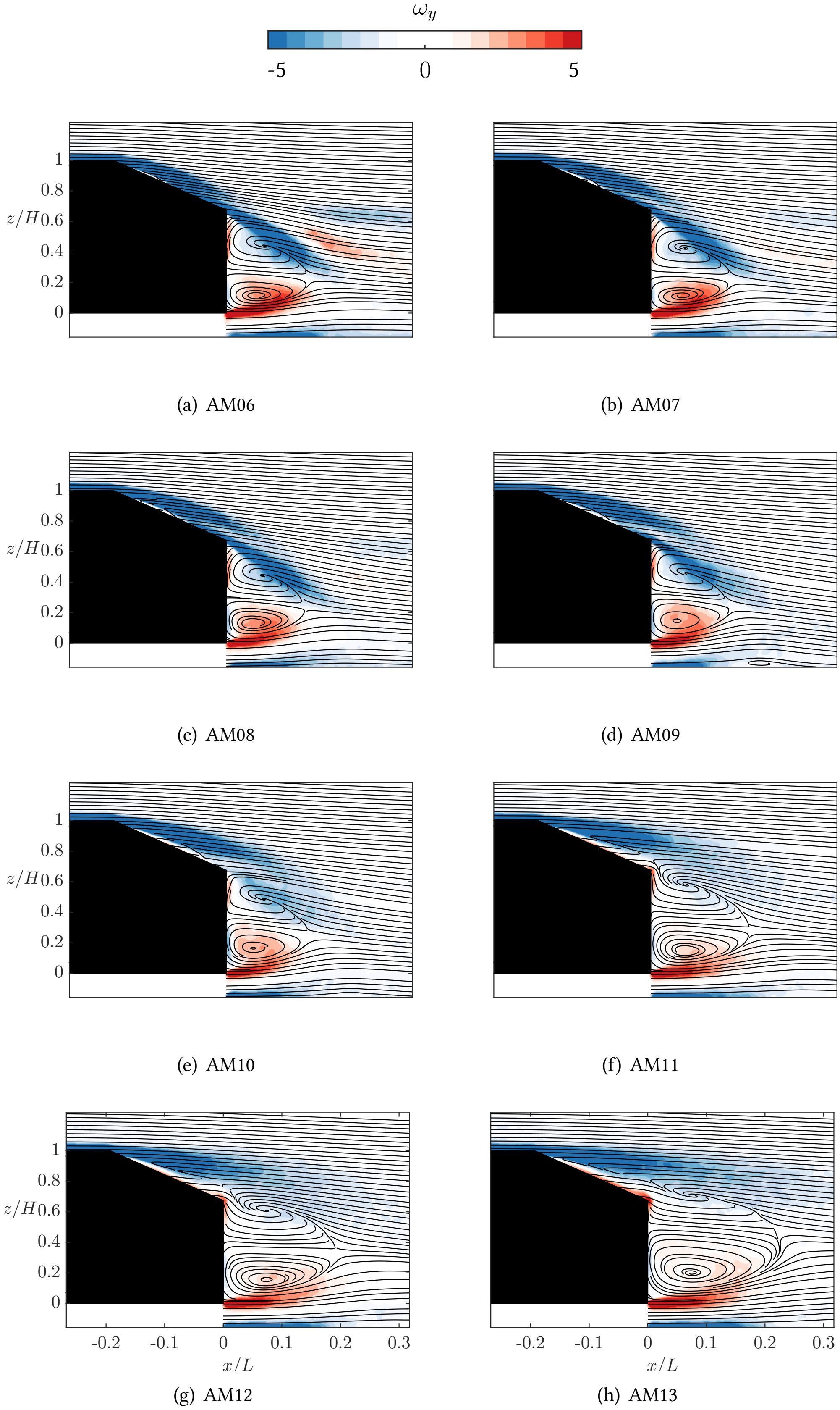

(a) AM06

(b) AM07

(c) AM08

(d) AM09

(e) AM10

(f) AM11

(g) AM12

(h) AM13

FIGURE 6.3: Time-averaged spanwise vorticity and velocity streamlines in xz planes at $y/W = 1/6$. Positive vorticity (red) and negative vorticity (blue). Vorticity is non-dimensionalised and levels are between ± 5.

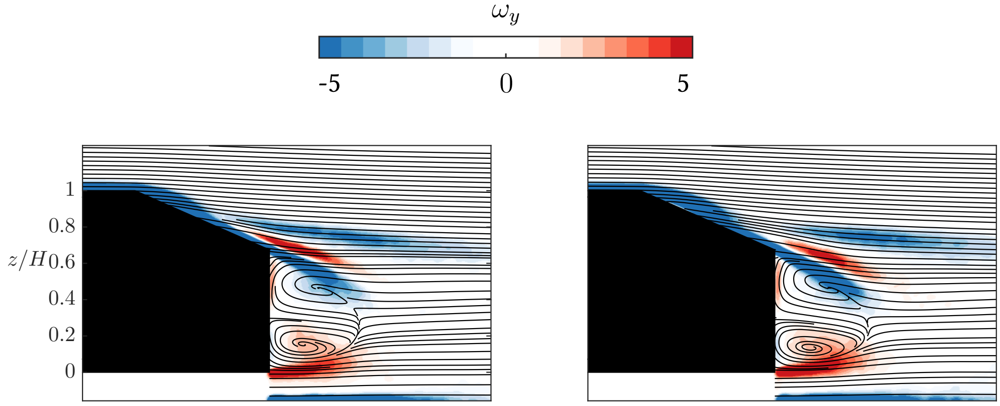

(a) AM06 (b) AM07

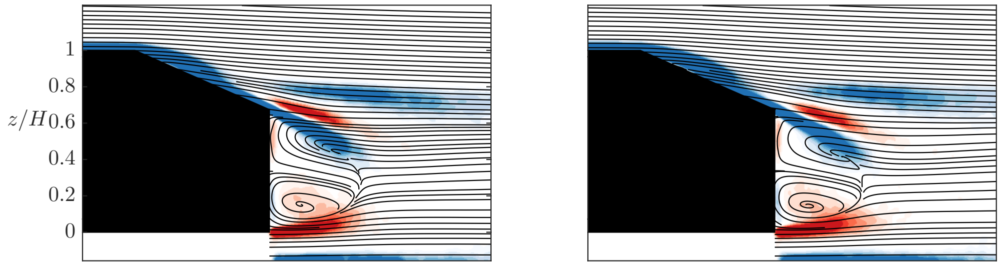

(c) AM08 (d) AM09

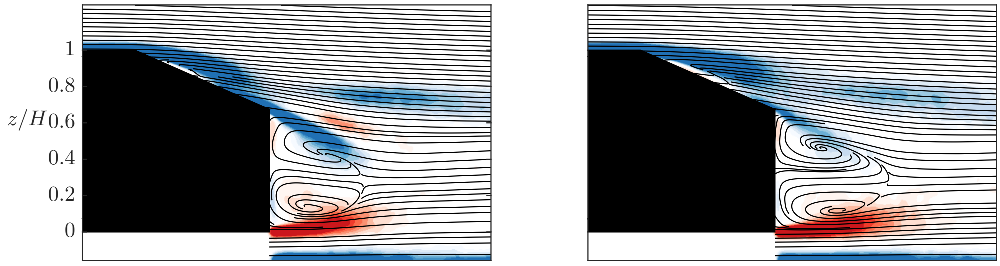

(e) AM10 (f) AM11

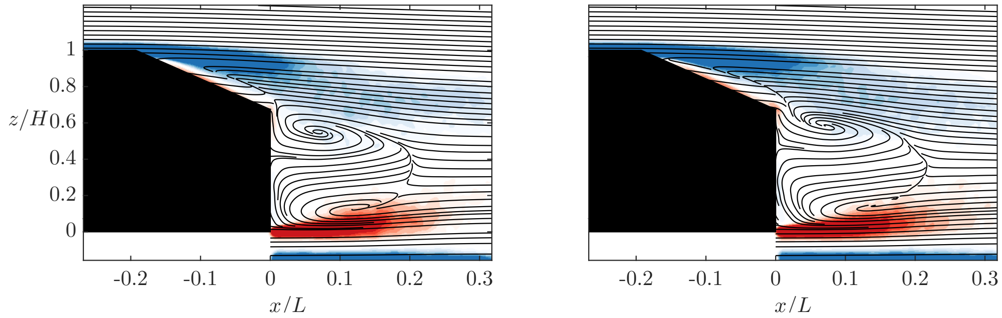

(g) AM12 (h) AM13

FIGURE 6.4: Time-averaged spanwise vorticity and velocity streamlines in xz planes at $y/W = 1/3$. Positive vorticity (red) and negative vorticity (blue). Vorticity is non-dimensionalised and levels are between ± 5.

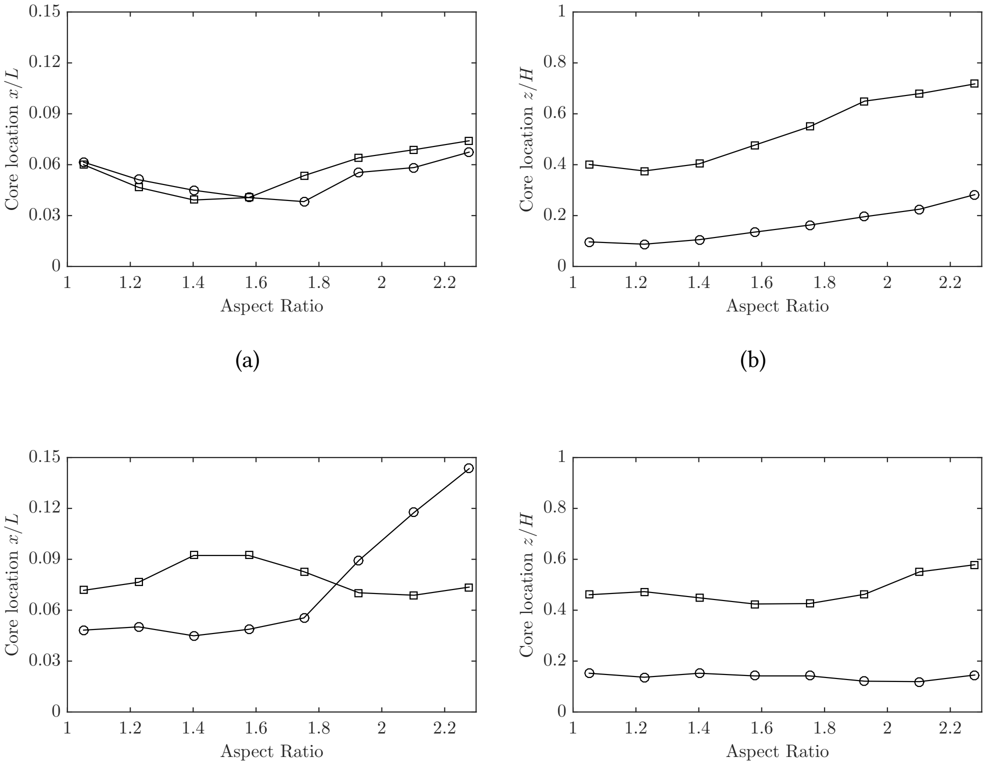

(a) (b)

(c) (d)

FIGURE 6.5: Core location of A (squares) and B (circles) spanwise vortical structures in the symmetry plane (top) and $y/W = \frac{1}{3}$ (bottom) as a function of aspect ratio.

attached cases. They are located more inboard than the c-pillar vortices (compared to the narrower bodies where the B vortices are in-line with the c-pillar vortices) and further from the corner vortices. As such, the vorticity cross-annihilation between these vortices will be delayed. They are also generally higher in vertical position, again due to the weaker c-pillar vortices.

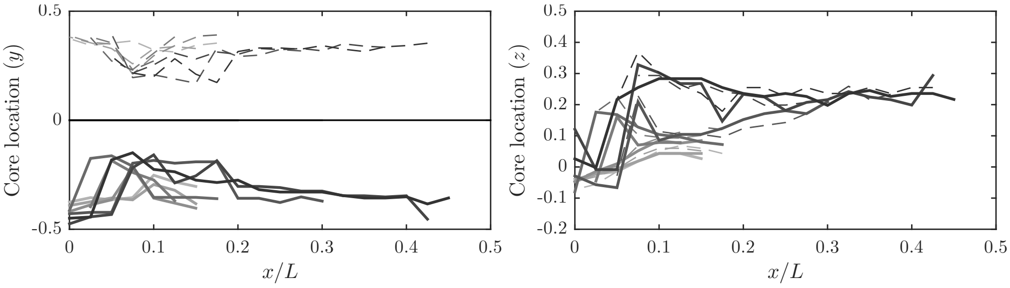

FIGURE 6.6: Core location of B vortex legs as a function of downstream position for various width Ahmed geometries. Darker colours indicate wider bodies (legend in figure 6.9). Lines are dashed for the negatively rotating vortex cores and solid for the positively rotating vortex structures.

The separatrix from the boundary layer separation grows with increasing aspect ratio (indicated by the streamlines in figure 6.2). This is an indication of the base pressure dropping with aspect ratio, a result that might imply an increase in drag with aspect ratio. It is expected from this that the streamwise elements of the horseshoe vortex that forms from the ground plane boundary layer would also be smaller, and even suppressed for the narrower bodies. This is confirmed when the cross-stream planes are investigated for $x/L = 0.3$ (figure 6.7).

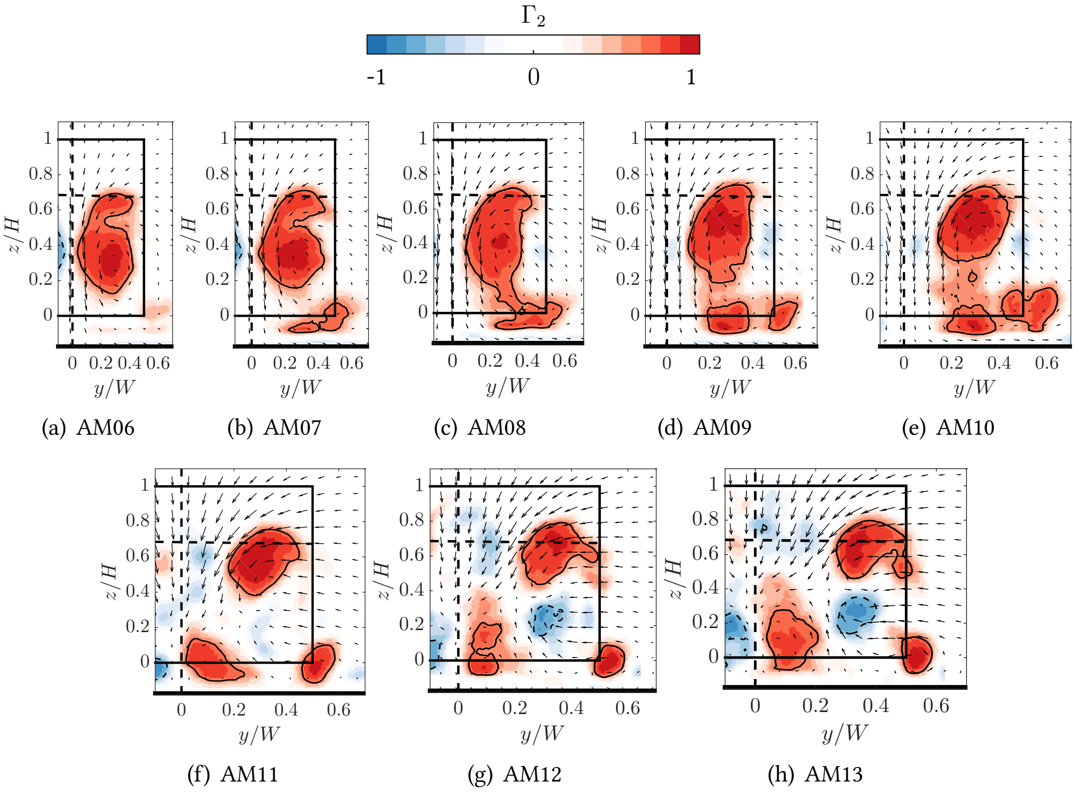

(a) AM06 (b) AM07 (c) AM08 (d) AM09 (e) AM10

(f) AM11 (g) AM12 (h) AM13

Figure 6.7: Velocity vectors and Γ_2 criterion for various width Ahmed models at $x/L = 0.3$. Only one in one-hundred vectors are included for clarity. Flow is towards the observer.

The flow does not reattach over the back slant for bodies wider than the standard-width, whilst for the narrower bodies it does. Figure 6.8 supports this by finding the reattachment length as a function of aspect ratio and spanwise position. The wider the body, the further down the slant the flow reattaches, if it reattaches at all. This behaviour is similar to that seen for a standard width Ahmed geometry as it passes the critical slant angle. At angles lower than the critical, the partially attached flow serves to strengthen the c-pillar vortices, causing a lower core pressure (Morel, 1978*b*) and hence higher drag. Conversely, past the critical angle, the flow separates from the backlight and has lower drag.

Figure 6.9 shows that the wake is both wider and longer for the wider bodies. The increase in wake width stems from whether the flow reattaches over the slant or not. The increase in length would also be dependent on that phenomenon, but there is an additional (besides the abrupt jump between AM10 and AM11) trend increasing the wake length for increasing aspect

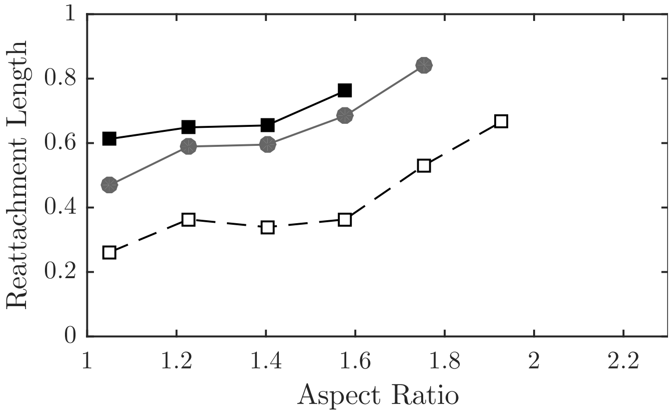

Figure 6.8: Reattachment length of time-averaged flow along the slant. Symmetry plane $y/W = 0$ (-■-), $y/W = 1/6$ (-●-) and $y/W = 1/3$ (-□-).

ratio. This is presumably again caused by the reduced influence of the c-pillar vortices at the centre plane.

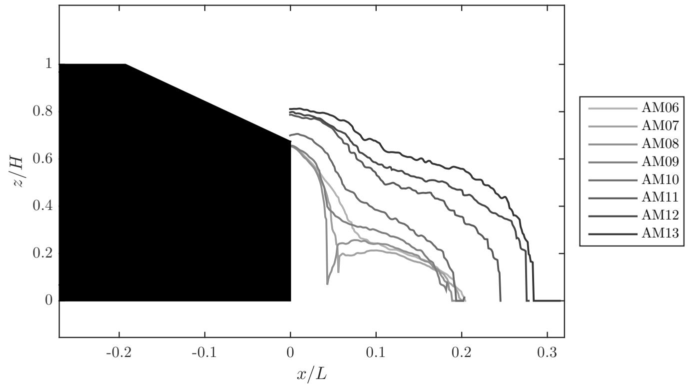

Figure 6.9: Vertical position of the streamwise velocity sign change in the symmetry plane for each downstream position for various width Ahmed geometries.

6.3.1 Circulation in the vortical structures

Following the same procedure as used in section 5.3.2, the circulation was measured in each cross-stream PIV plane (figure 6.10). For all the geometries tested, there is an increase in the circulation in the c-pillar vortex from the start of the slant to $x/L \approx 0.1$. The increase in circulation prior to $x/L = 0$ is due to the roll-up of the c-pillar vortices over the slanted edge. After this point, the increase comes from the merging of the A and C vortical structures (schematised in figure 6.11) as detailed in chapter 5.

The circulation of the narrower five bodies increases between $x/L = 0.1$ and $x/L = 0.4$. This secondary increase in circulation is due to the merging of the c-pillar vortex with the corner

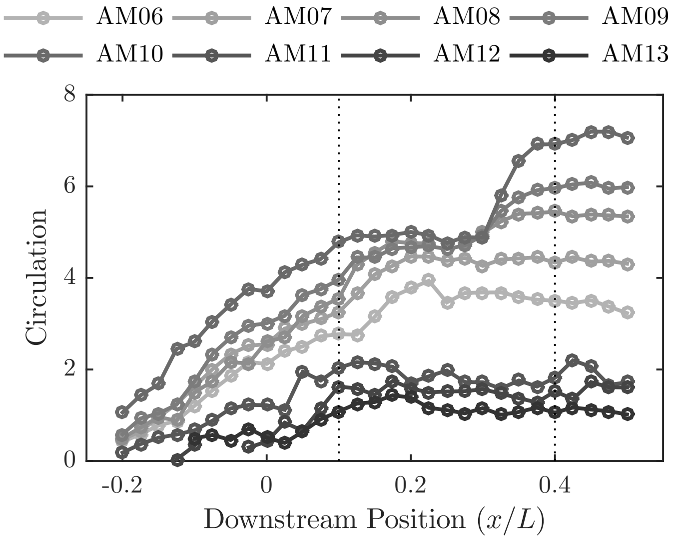

Figure 6.10: Time-averaged circulation (non-dimensionalised) in the c-pillar vortex as it varies with downstream location and aspect ratio. Darker lines represent wider bodies. The vertical dotted lines denote the locations used for figure 6.13.

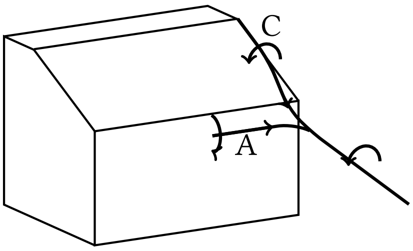

Figure 6.11: Schematic of the A and C vortices merging. Details can be found in figure 5.18.

vortex (figure 6.12). This increase occurs at different points for the different width bodies, but by $x/L = 0.4$ the circulation has again reached a constant level, and the increase is proportional to the circulation, as shown in figure 6.13. The corner vortex is expected to merge with the c-pillar vortex for the wider three cases also, but beyond the measurement volume.

Figures 6.10 and 6.13 highlight the existence of two distinct flow regimes evidenced by the circulation levels in the longitudinal vortical structures. Besides the quantity of circulation, the trend with aspect ratio depends on which regime the body lies in, while the narrower five bodies show an increase in circulation with width, this trend is reversed for the widest three (figure 6.13).

The large difference in circulation in the c-pillar vortices between the bodies with $AR < 1.8$ and those with $AR > 1.9$ stems from the separation over the back slant (figure 6.2). For the narrowest five cases, the stronger induced downwash between the two c-pillar vortices promotes the reattachment of the flow over the slant. In the regimes where the flow reattaches over the slant, the vorticity built up in this recirculation zone must be fed downstream by

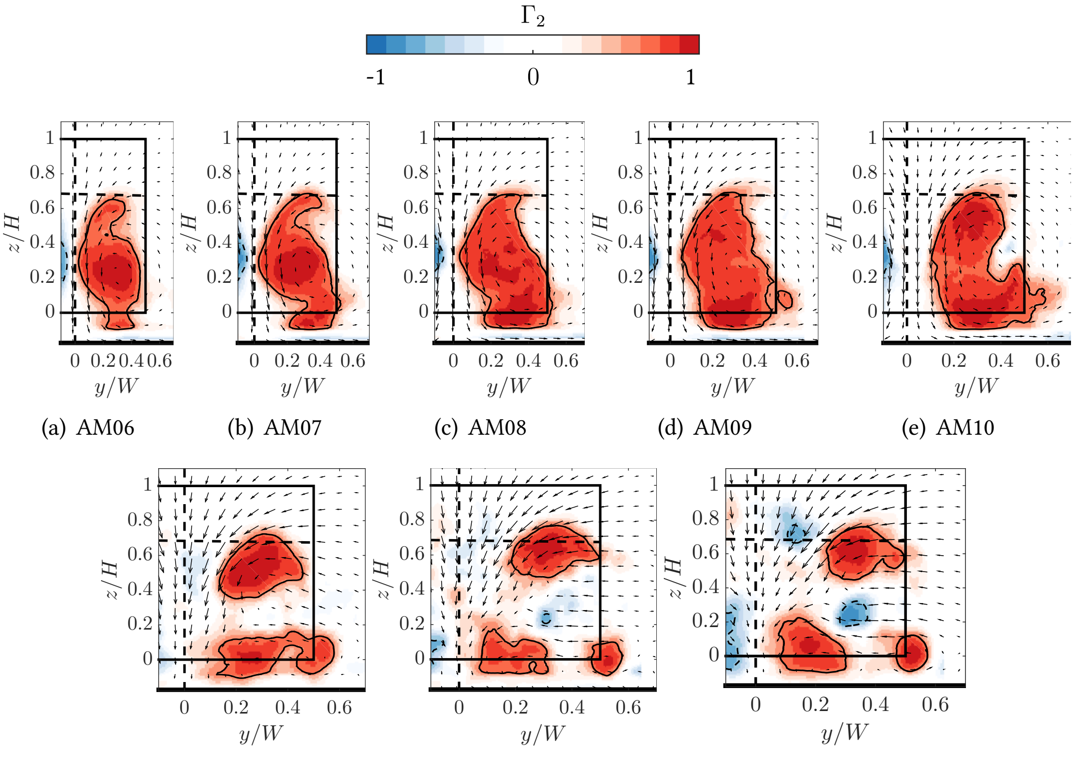

(a) AM06 (b) AM07 (c) AM08 (d) AM09 (e) AM10

(f) AM11 (g) AM12 (h) AM13

Figure 6.12: Velocity vectors (one in one-hundred) and Γ_2 criterion at $x/L = 0.4$. By this downstream position, the corner vortex, c-pillar vortex and ground horseshoe vortex have all merged into one structure for the narrowest five cases. For the widest three they are still separate (except for AM11 which has merging starting to occur between the corner and ground horseshoe structures).

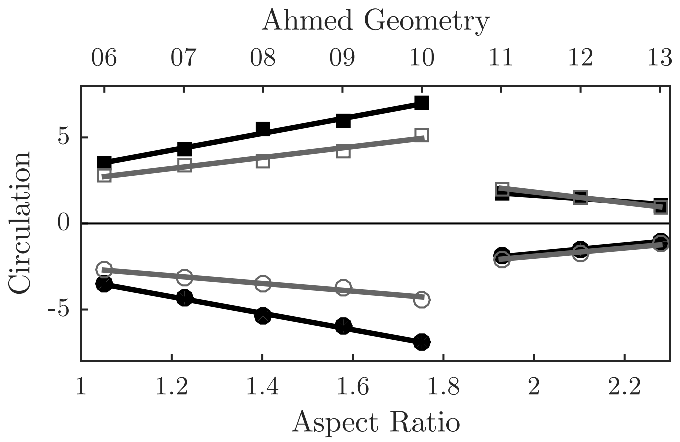

Figure 6.13: Variation of the time-averaged circulation (non-dimensionalised) in the c-pillar vortex at two downstream locations, $x/L = 0.1$ in gray and $x/L = 0.4$ in black. Positive circulation (squares) and negative (circles).

some mechanism; since the flow is attached, the initially spanwise vorticity becomes entrained through the spanwise circulation bubble and is tilted into the c-pillar vortices. This, in turn, strengthens the c-pillar vortices, leading to a recursive effect since these stronger vortices will now aid the reattachment. This leads to an expectation of hysteretic effects in, for example, the drag against Reynolds number curve (see Appendix A for more details).

When the flow remains separated, the vorticity above the slant can be shed downstream directly as spanwise vorticity. When the flow reattaches, the vorticity built up in this recirculation region is shifted outboard towards the edges before tilting downstream and merging with the c-pillar vortices. Figure 6.14 schematises this.

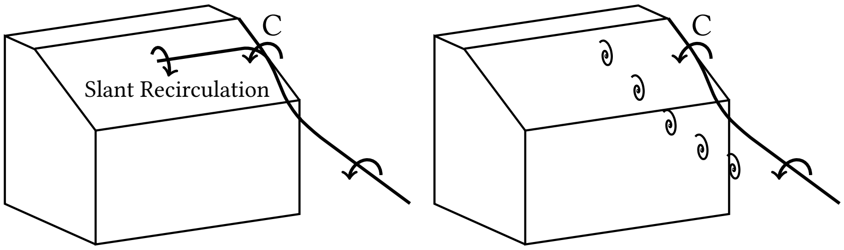

(a) Reattaching Regime (b) Separated Regime

FIGURE 6.14: Proposed mechanisms for downstream transport of spanwise vorticity above the slant. In the reattaching regime, the c-pillars are significantly strengthened by the extra vorticity fed in from the recirculation region. In the separated regime, this vorticity is shed directly downstream.

Figure 6.15 shows the percentage of time the flow remains attached for each aspect ratio. This is calculated by comparing the pitch angle of the velocity vector at each snapshot at the end of the slant. If the pitch angle is aligned with the slant then the flow is defined as attached. It is clear that the narrower bodies have much more attached flow over the rear slant. For all cases the flow was more separated closer to the symmetry plane, further from the c-pillar vortices.

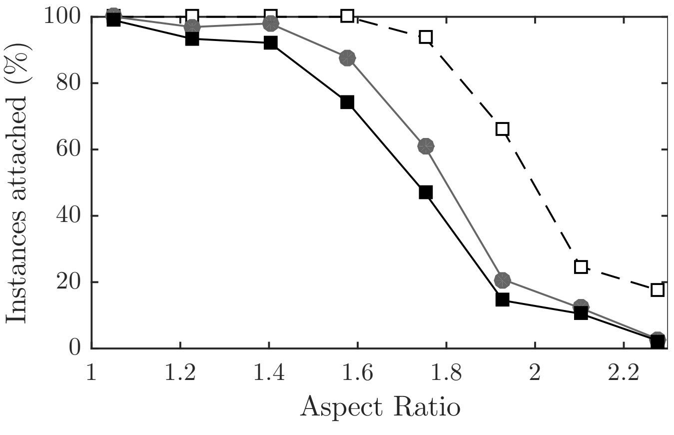

FIGURE 6.15: Ratio of instantaneous frames with the flow attached at the end of the slant to those with the flow separated. Symmetry plane $y/W = 0$ (-■-), $y/W = 1/6$ (-●-) and $y/W = 1/3$ (-□-).

While the flow in the high drag regime for the standard body ($\alpha < 30°$) is recognized as three-dimensional (Gilliéron *et al.*, 1999), for $AR > 1.9$ the flow is in a sense much more two-dimensional. Figure 6.16 shows the vertical velocity as it varies with spanwise position. For the narrowest four bodies, the velocity in the wake shows a high dependency on spanwise position, indicating the three-dimensionality of the flow. However, for the widest three cases, the spanwise position has little effect on the flow velocity.

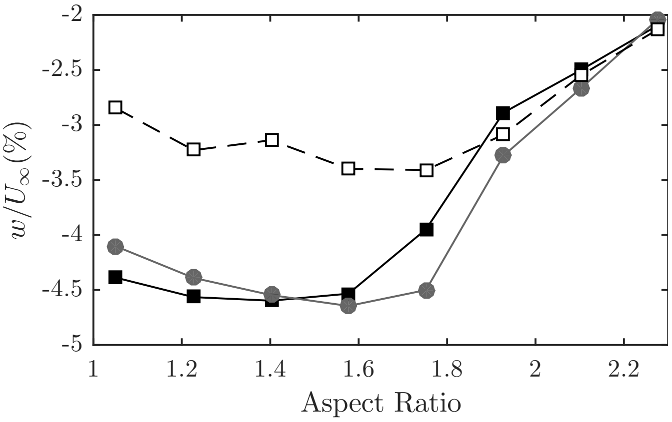

FIGURE 6.16: Time average of vertical velocity at a point $x/L = 0$, $z/H = 1$ showing the increased three-dimensionality of the flow behind the low aspect-ratio models. Symmetry plane $y/W = 0$ (-■-), $y/W = 1/6$ (-●-) and $y/W = 1/3$ (-□-).

The turbulence levels in the wake also increase with aspect ratio (figure 6.17). While there is insufficient data to provide fully converged turbulent statistics, these results already indicate a significant change in the wake topology. There is a clear correlation between figures 6.17 and 6.15 showing that the separation that occurs for the wider bodies causes the increase in turbulence intensity in the wake. This is consistent with our hypothesis that there is increased spanwise vorticity shedding into the wake due to the separation.

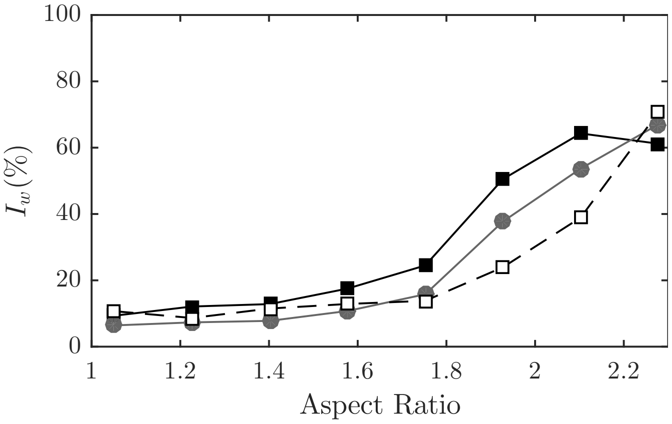

FIGURE 6.17: Vertical turbulence intensity at a point $x/L = 0$, $z/H = 1$. Symmetry plane $y/W = 0$ (-■-), $y/W = 1/6$ (-●-) and $y/W = 1/3$ (-□-).

6.3.2 Summary of time-averaged results

Figure 6.18 shows the wake structure of three geometries: AM08, which has attached flow and no groundplane horseshoe vortex; AM10, which has attached flow over the slant and the groundplane horseshoe vortex; and AM12, which has separated flow and the groundplane vortex. The skin friction lines on the back surface of AM08 and AM10 show a negative bifurcation line near the back slant. This is because when the slant boundary layer separates at the end of the body, there exists both the separation zone A (in red) and a much smaller secondary structure above (not shown). In the wider case (AM12), this negative bifurcation line disappears since there is no secondary structure because the flow has already separated across the slant.

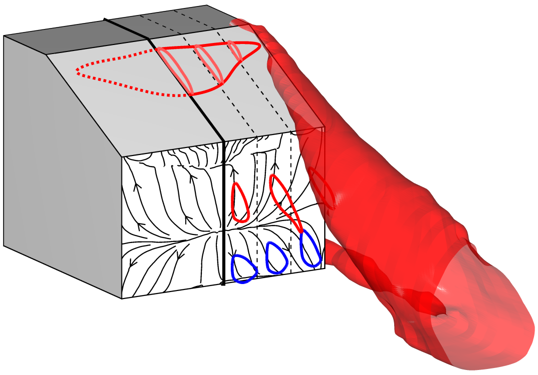

(a) AM08

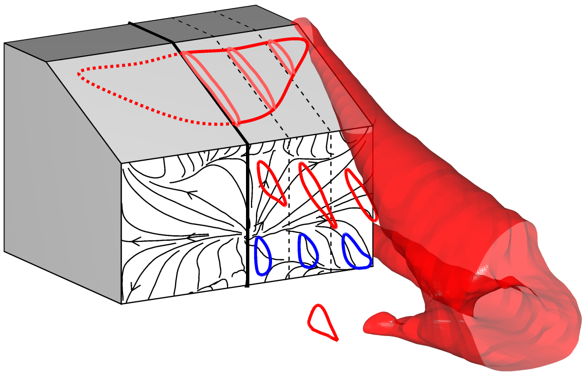

(b) AM10

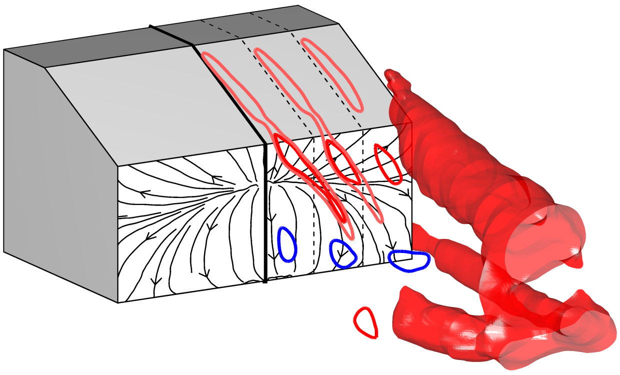

(c) AM12

Figure 6.18: The time-averaged flow topology as it varies with aspect ratio. Skin friction lines on the back surface are calculated from PIV data near the surface.

6.4 Effect of the aspect ratio on the wake dynamics.

One method for investigating the dynamics is to study how the core of a structure varies in time. This technique has been applied to the A and B spanwise vortical structures. For each of the 9000 instantaneous frames, the core location is extracted using the Γ_1 criteria. A two-dimensional histogram of the core location is presented in figures 6.19 to 6.22. For the narrowest body (AM06), the upper (A) vortex is quite stable in time, indicating a steady recirculatory vortex structure. The B vortex location, however, is spread out over a wide downstream position, indicating that this may be more similar to the shedding of shear-layer vortices than a standing vortex. Figure 6.20 shows an instantaneous snapshot of the velocity field supporting this hypothesis.

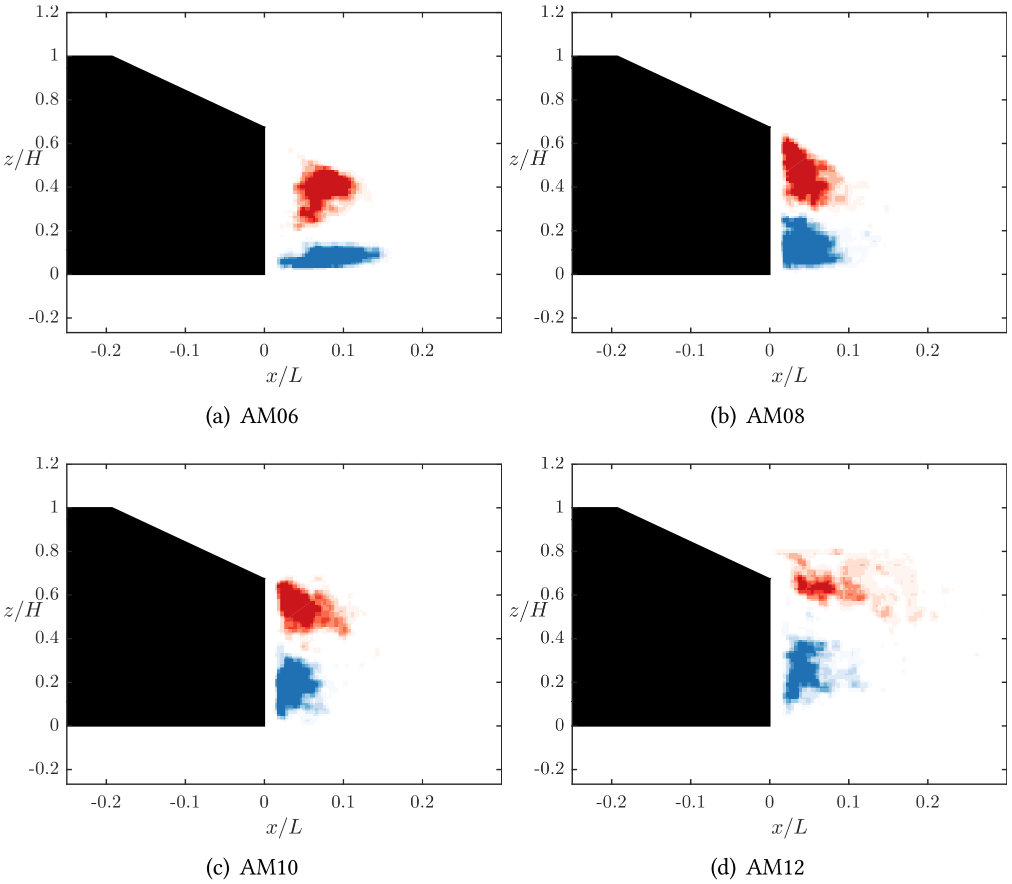

(a) AM06 (b) AM08

(c) AM10 (d) AM12

FIGURE 6.19: Distribution of the maximum (red) and minimum (blue) of the Γ_1 field highlighting the variation of the cores of the A and B vortices respectively, as aspect ratio is varied. Time-resolved data at $y/W = 0$.

For the AM08 and AM10 cases, the two vortices are tighter in spatial variation, and closer to the body. This indicates the presence of two stable recirculation regimes and the proximity to the body could indicate a higher drag (as the low pressure cores will be close to the body). The

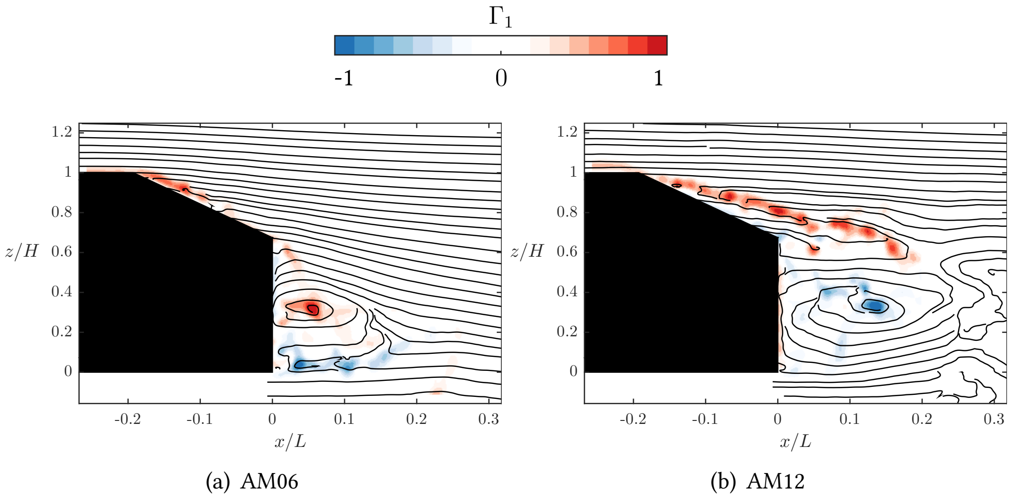

(a) AM06

(b) AM12

FIGURE 6.20: Instantaneous wake of the AM06 (left) and AM12 (right) models corresponding to figure 6.19(a) and (d) respectively. In (a) streamlines and contours of Γ_1 showing a stable A vortex (in red) and a series of shear layer vortices being shed from the lower surface (in blue). In (b) the shear layer is now at the top of the model and the stable vortex is B. The overlaid streamlines are indicative of the local flow direction only.

rear stagnation point between the two vortices has also moved upwards with the increase in aspect ratio.

For the widest case, both vortices show higher scatter in their core location, indicating more significant motion of the structure. The B vortex is in a similar position to the AM08 and AM10 bodies, but the A vortex is now spread along in the manner similar to that of a shear layer. As the body gets wider, the centre-plane flow becomes more like that behind a two-dimensional body, and the separated flow over the slant causes the A vortex to be much weaker.

Away from the symmetry plane (figure 6.21), the B vortex tends to be more shear-layer like in all the bodies, whilst the A vortex is more stable in all but the AM12 case. Far away from the symmetry plane (figure 6.22), the structures are both close to the base of the model except for AM12. The influence of the side shear layer is disrupting these spanwise structures, except in the more two-dimensional flow of AM12, where two shear layers are present.

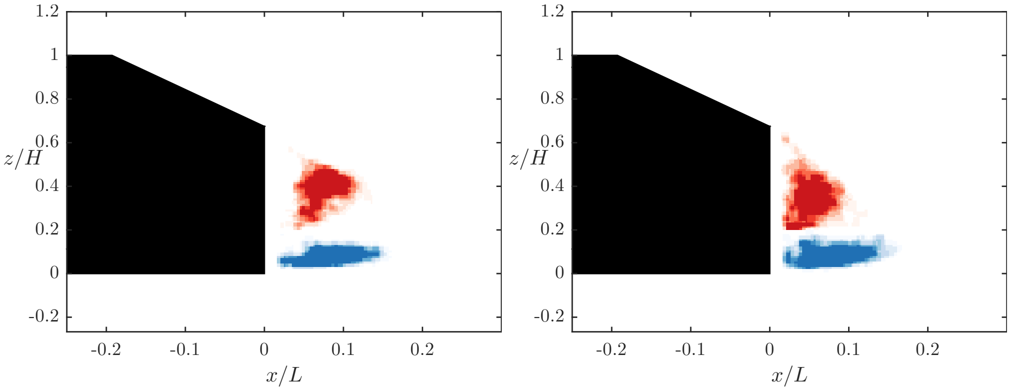

(a) AM06 (b) AM08

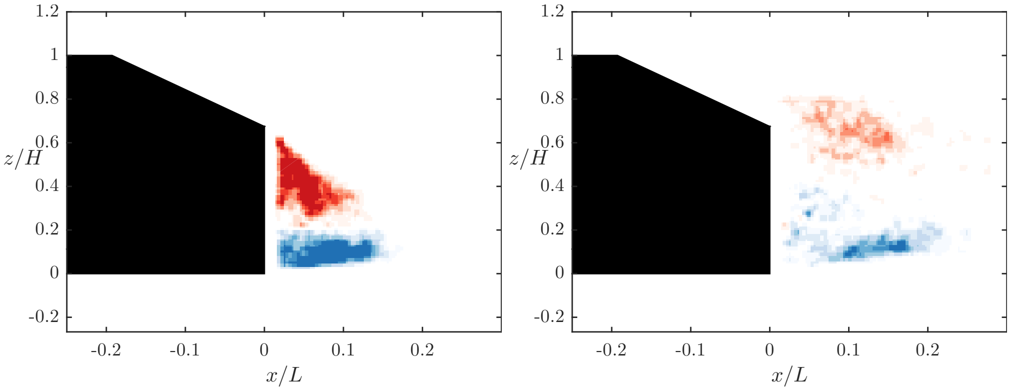

(c) AM10 (d) AM12

FIGURE 6.21: Distribution of the maximum (red) and minimum (blue) of the Γ_1 field, highlighting the variation of the cores of the A and B vortices respectively. Time-resolved data at $y/W = \frac{1}{6}$.

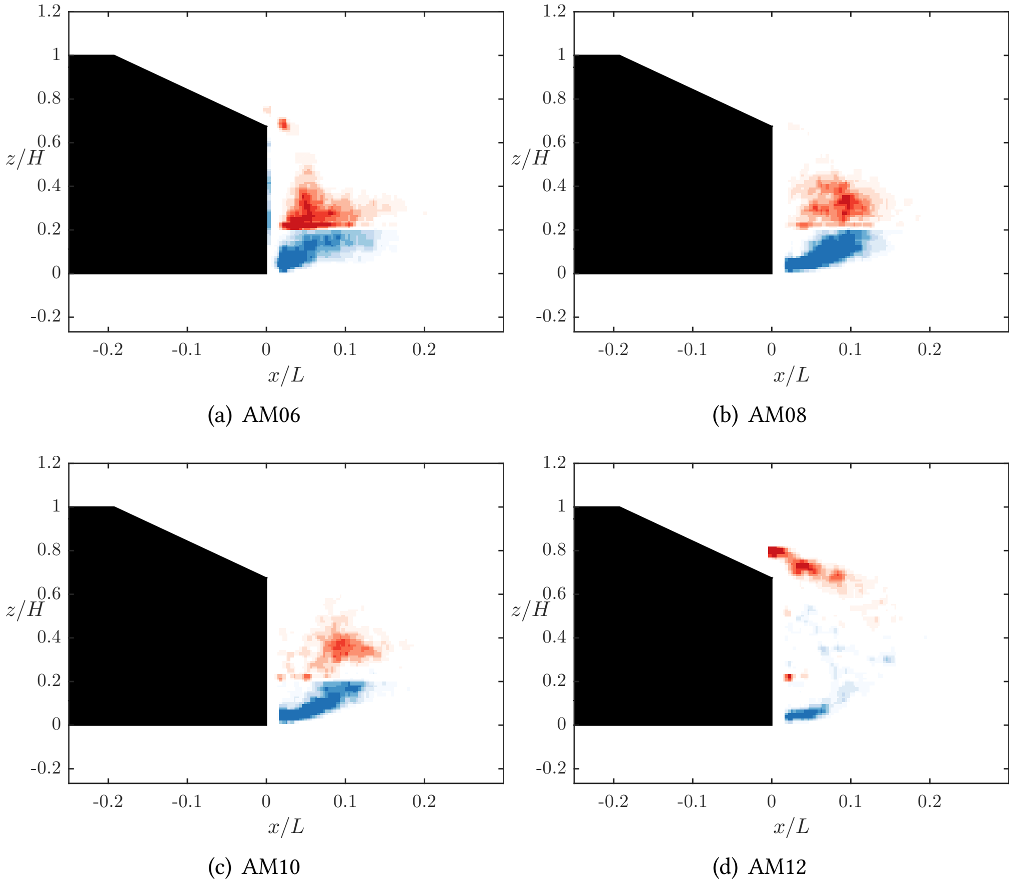

(a) AM06

(b) AM08

(c) AM10

(d) AM12

Figure 6.22: Distribution of the maximum (red) and minimum (blue) of the Γ_1 field, highlighting the variation of the cores of the A and B vortices respectively. Time-resolved data at $y/W = \frac{1}{3}$.

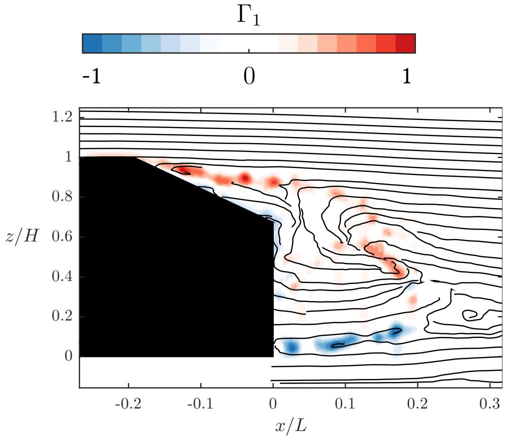

Figure 6.23: The upper and lower shear layers in the wake of the AM12 Ahmed model at a spanwise position of $y/W = \frac{1}{3}$ corresponding to figure 6.22(d). Velocity streamlines and filled contours of Γ_1.

6.4.1 Reynolds stresses

The Reynolds stresses for each body in the symmetry plane for each body are contained in figure 6.24 through figure 6.26. Figure 6.24 shows a significant increase in the symmetry plane $\overline{u'u'}$ Reynolds stress for bodies past the critical aspect ratio. The stresses behind the base of the body are relatively constant with aspect ratio, but behind the slant the increase is quite stark. When considering the $\overline{w'w'}$ component, it seems like there is a decrease in that component with AR at the base of the body. Again, behind the slant there is a gradual increase with AR, indicating the increased flapping of the wake.

For the $\overline{u'w'}$ components there is also a shift in the streamwise position of the positive stress at the base of the body. Past the critical AR, it moves downstream from around $x/L = 0.15$ to $x/L = 0.2$, another indication of the lengthening of the wake.

6.4.2 Standard deviation

The standard deviations of the velocity fields are also reported. Figure 6.27 shows a general decrease in standard deviation of the spanwise velocity field with increasing aspect ratio. The w component is reported in figure 6.28, showing this component is higher behind the slanted area of the Ahmed body for the wider models. This fits with the fact that the flow is separated and turbulently flapping above the slant for the wider bodies, whereas it remains attached and vorticity is fed outboard for the narrower bodies.

Further downstream, we see the opposite trend. Figure 6.29 gives an increase in standard deviation with increasing width. For the narrower bodies, the regions of high standard deviations are generally where there is high rotation in the field (i.e. it matches the regions of Γ_2). For the wider cases, this is not so, with the standard deviation being high across the whole wake, not just where the rotation is. For these cases, the separate vortical structures have not yet merged and the cross-stream motion of these is high.

6.4.3 Space-time diagrams

The space-time plots can be used to visualise this motion. When considering AM08 (figure 6.31), the dynamics are similar to those of the standard width model presented in section 2.2.3. The motions are all consistent, and the shedding frequency does not vary (figure 6.32). This indicates

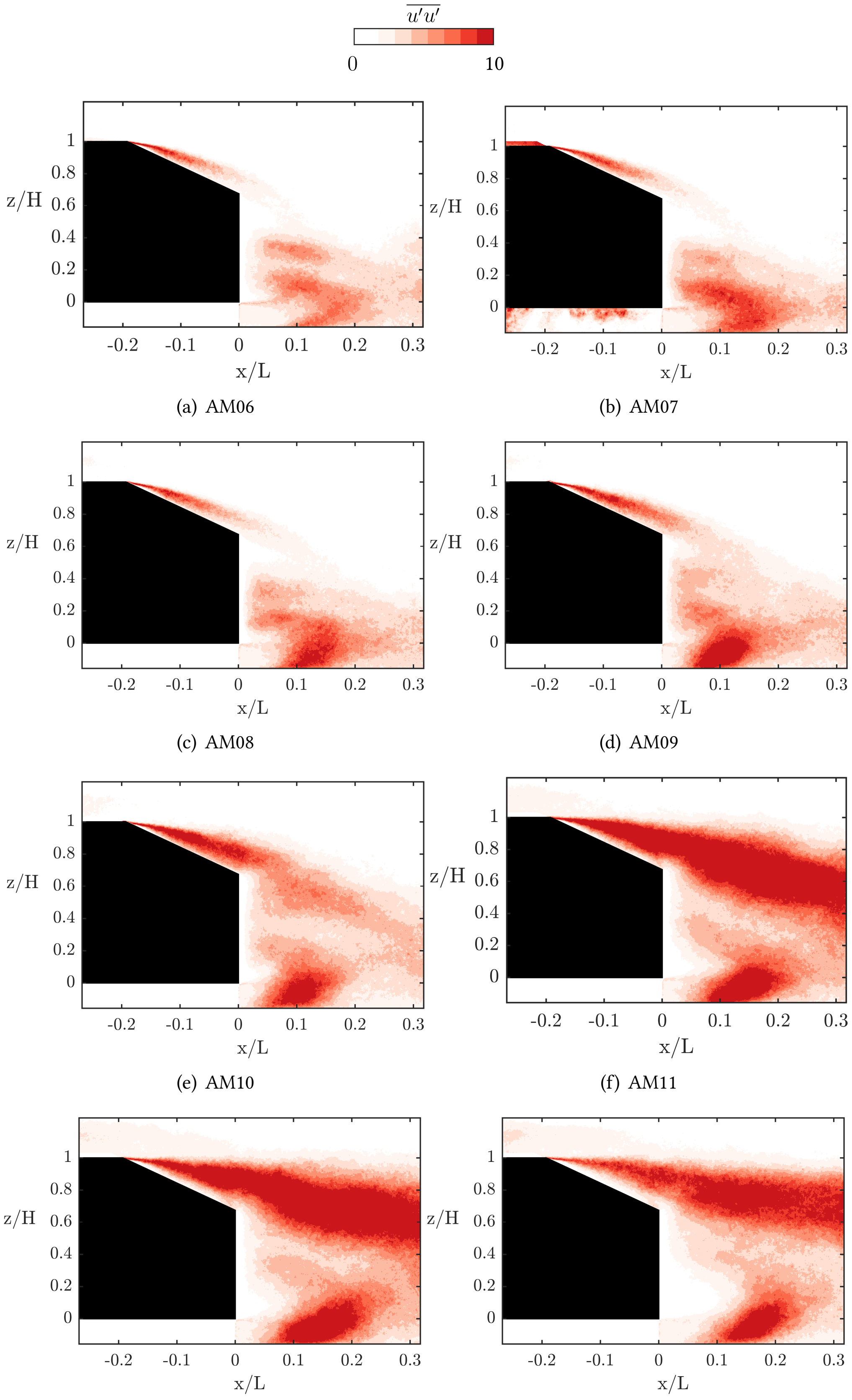

(a) AM06 (b) AM07

(c) AM08 (d) AM09

(e) AM10 (f) AM11

(g) AM12 (h) AM13

FIGURE 6.24: Reynolds stress $\overline{u'u'}$ in xz planes at $y/W = 0$.

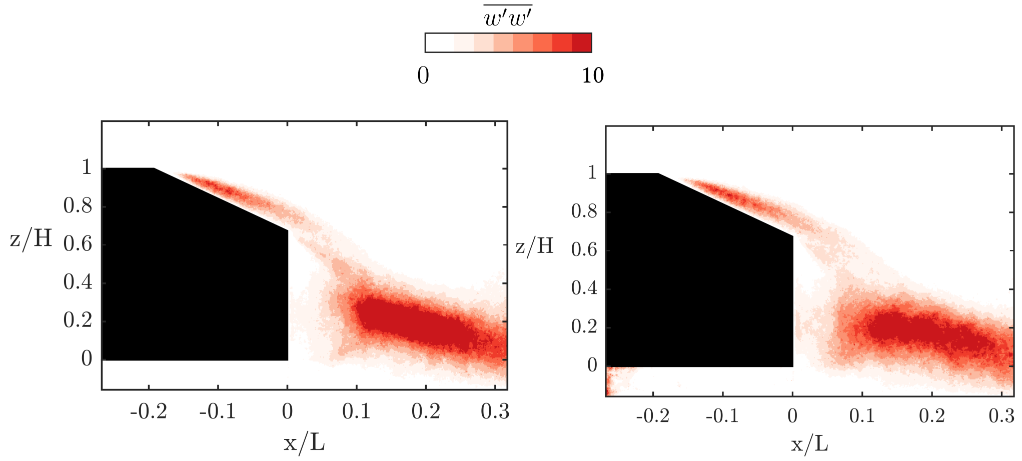

(a) AM06 (b) AM07

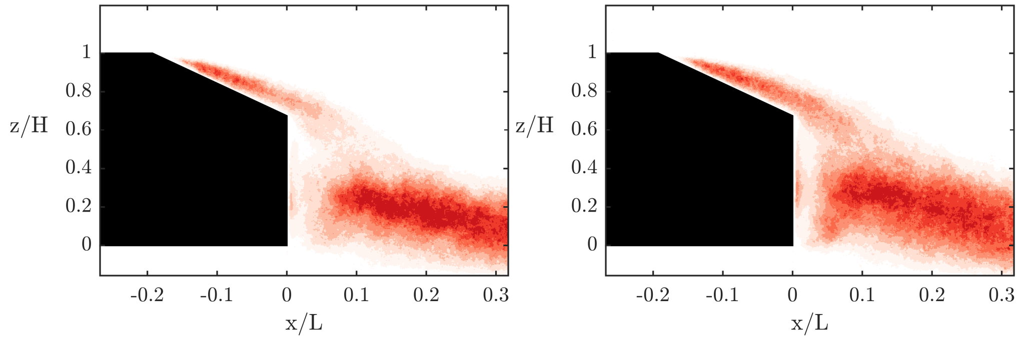

(c) AM08 (d) AM09

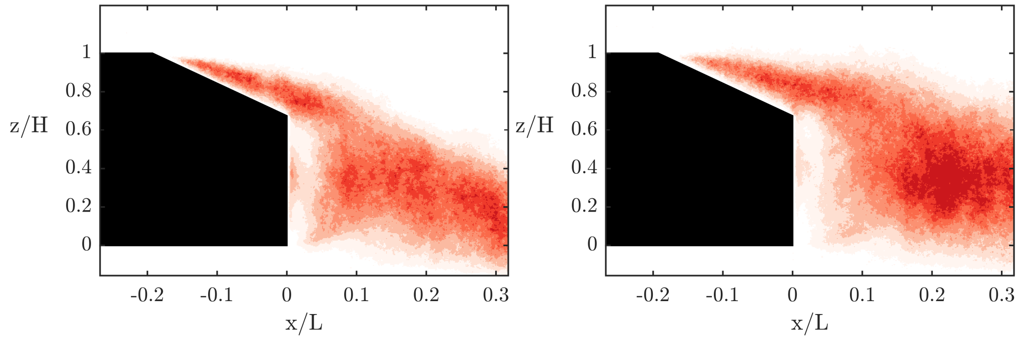

(e) AM10 (f) AM11

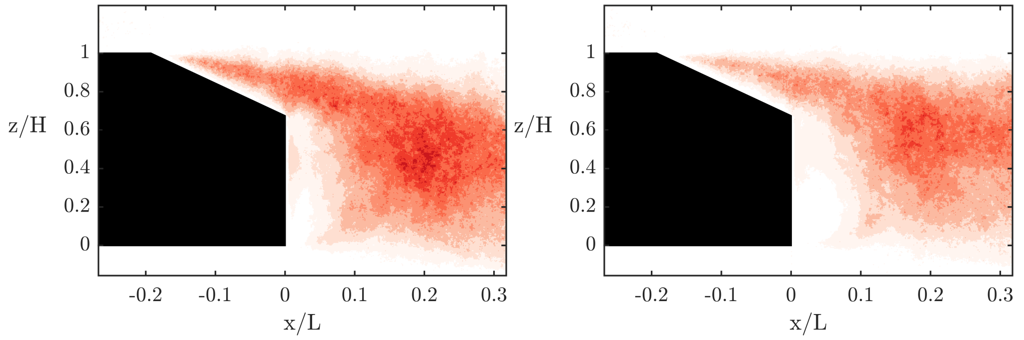

(g) AM12 (h) AM13

FIGURE 6.25: Reynolds stress $\overline{w'w'}$ in xz planes at $y/W = 0$.

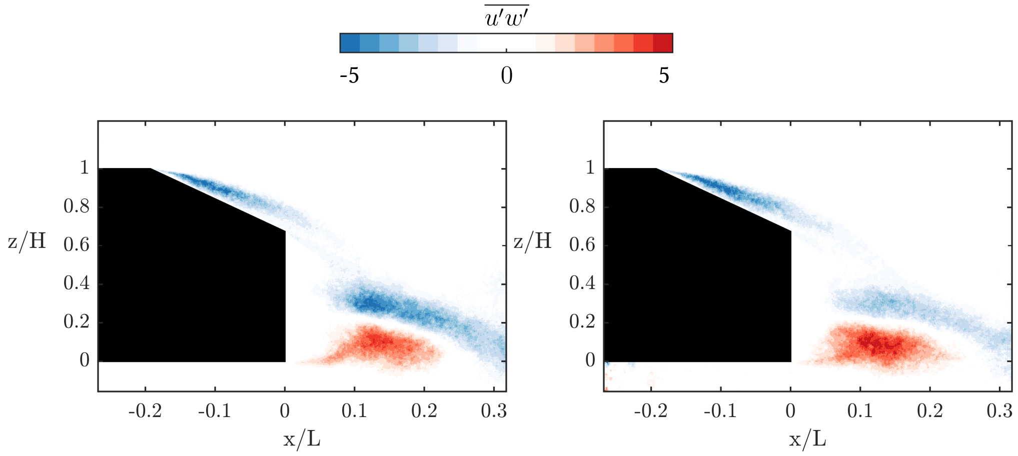

(a) AM06 (b) AM07

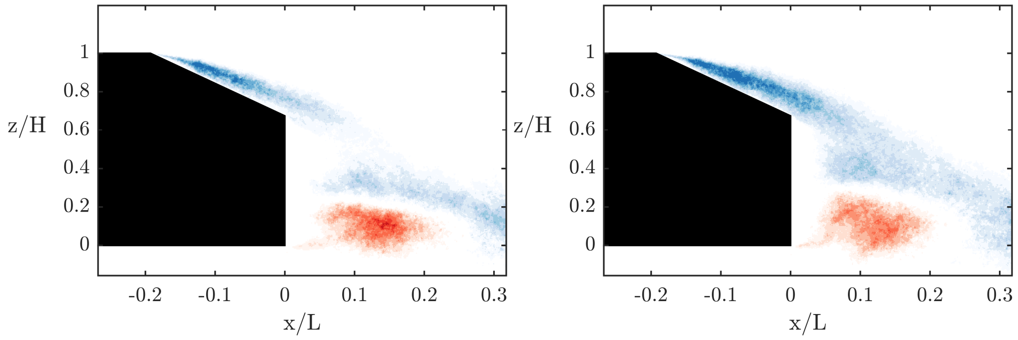

(c) AM08 (d) AM09

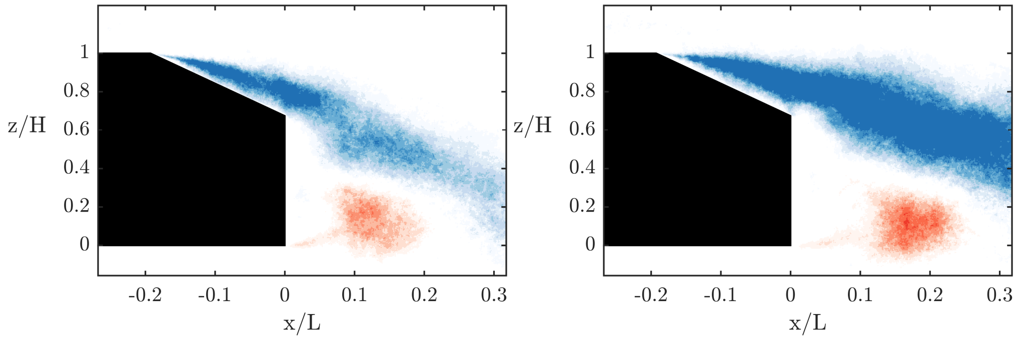

(e) AM10 (f) AM11

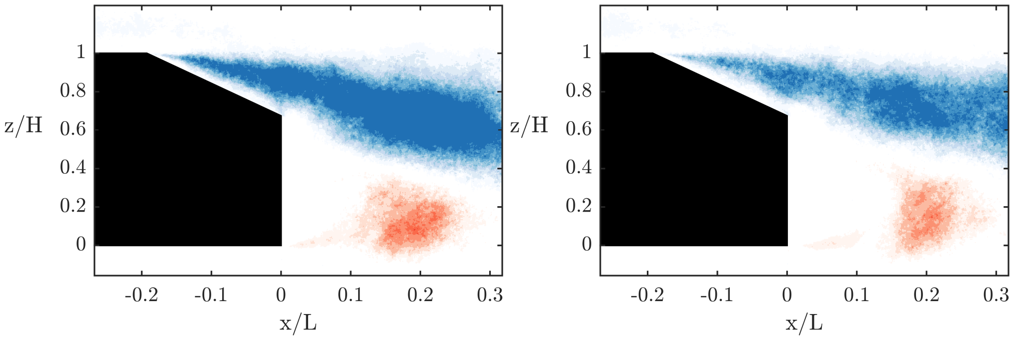

(g) AM12 (h) AM13

FIGURE 6.26: Reynolds stress $\overline{u'w'}$ in xz planes at $y/W = 0$.

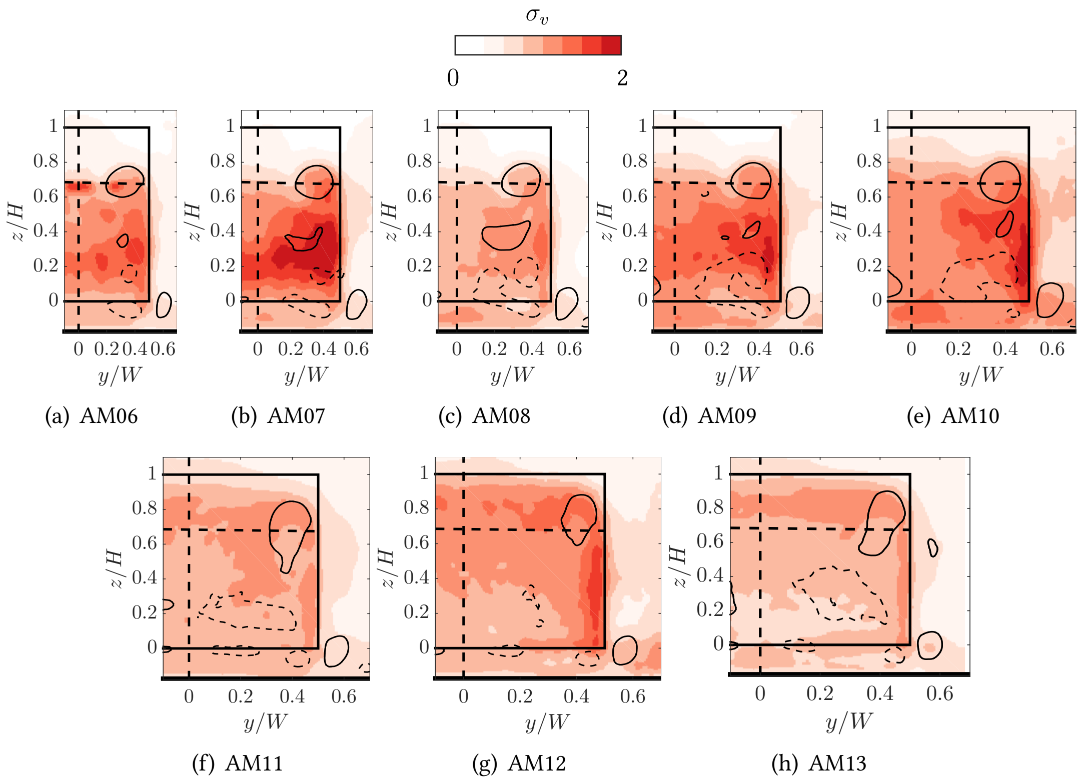

(a) AM06 (b) AM07 (c) AM08 (d) AM09 (e) AM10

(f) AM11 (g) AM12 (h) AM13

FIGURE 6.27: Standard deviation of v velocity component near to the body (at downstream position $x/L = 0.075$). Black contours represent time-averaged vortex bounds with dashes indicating negative rotation.

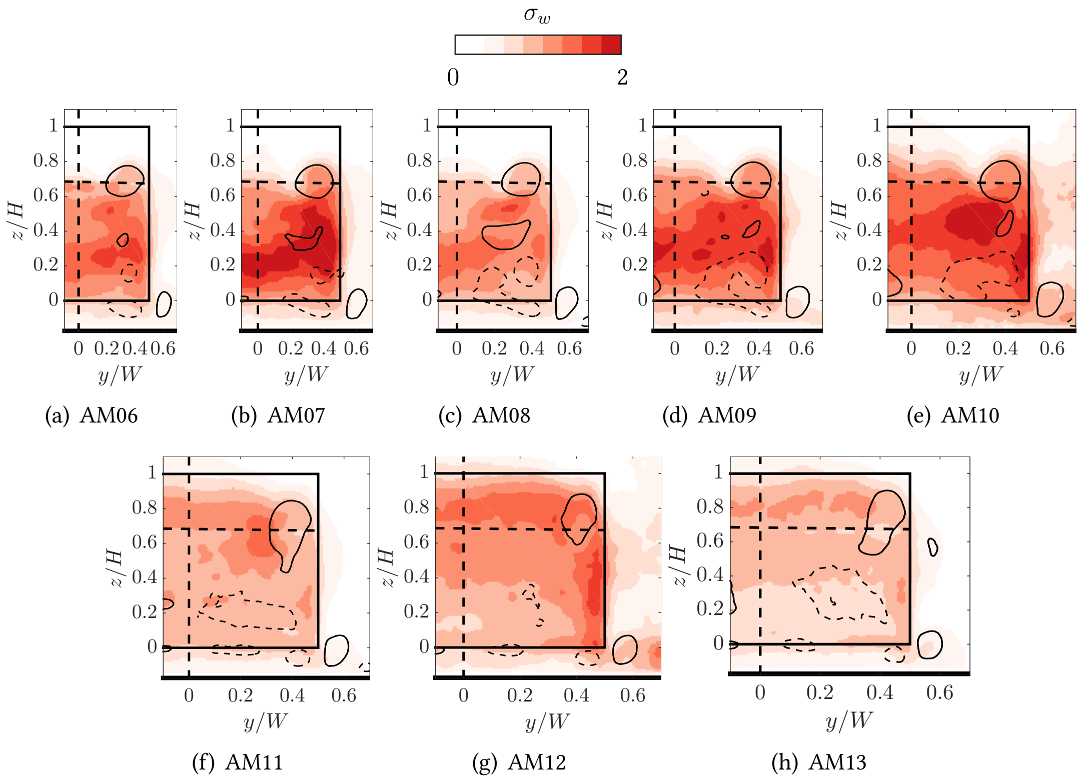

(a) AM06 (b) AM07 (c) AM08 (d) AM09 (e) AM10

(f) AM11 (g) AM12 (h) AM13

FIGURE 6.28: Standard deviation of w velocity component near to the body (at downstream position $x/L = 0.075$). Black contours represent time-averaged vortex bounds with dashes indicating negative rotation.

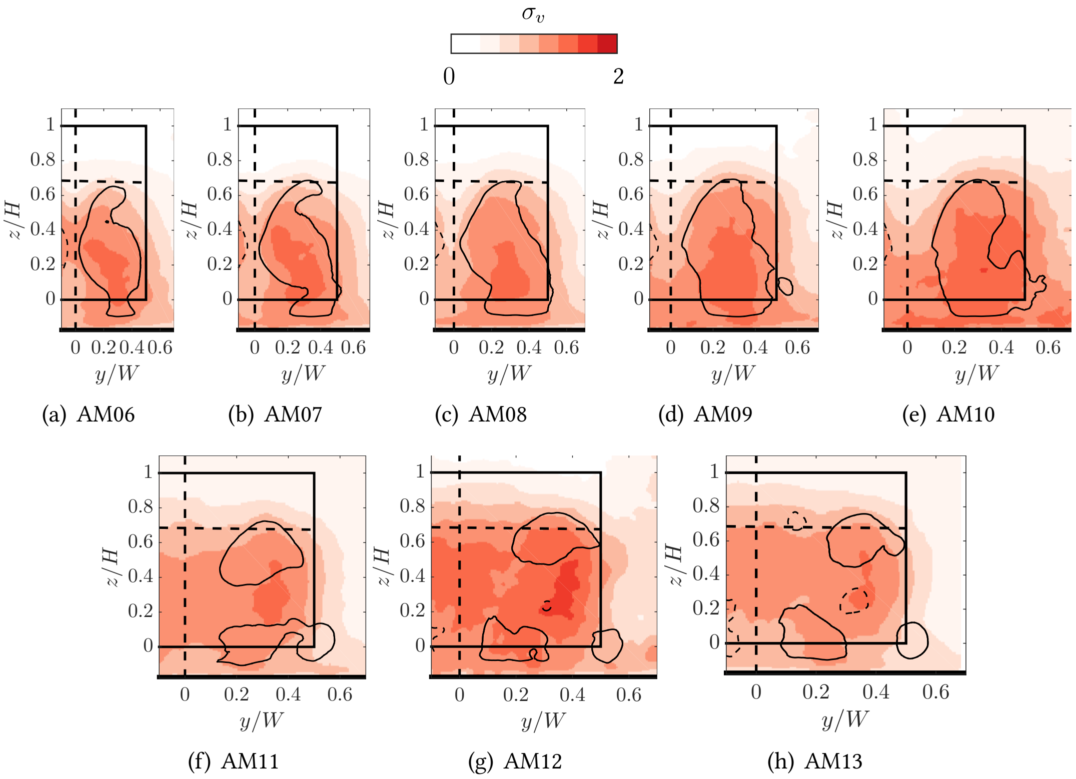

(a) AM06 (b) AM07 (c) AM08 (d) AM09 (e) AM10

(f) AM11 (g) AM12 (h) AM13

Figure 6.29: Standard deviation of v velocity component in the wake at downstream position $x/L = 0.4$. Black contours represent time-averaged vortex bounds with dashes indicating negative rotation.

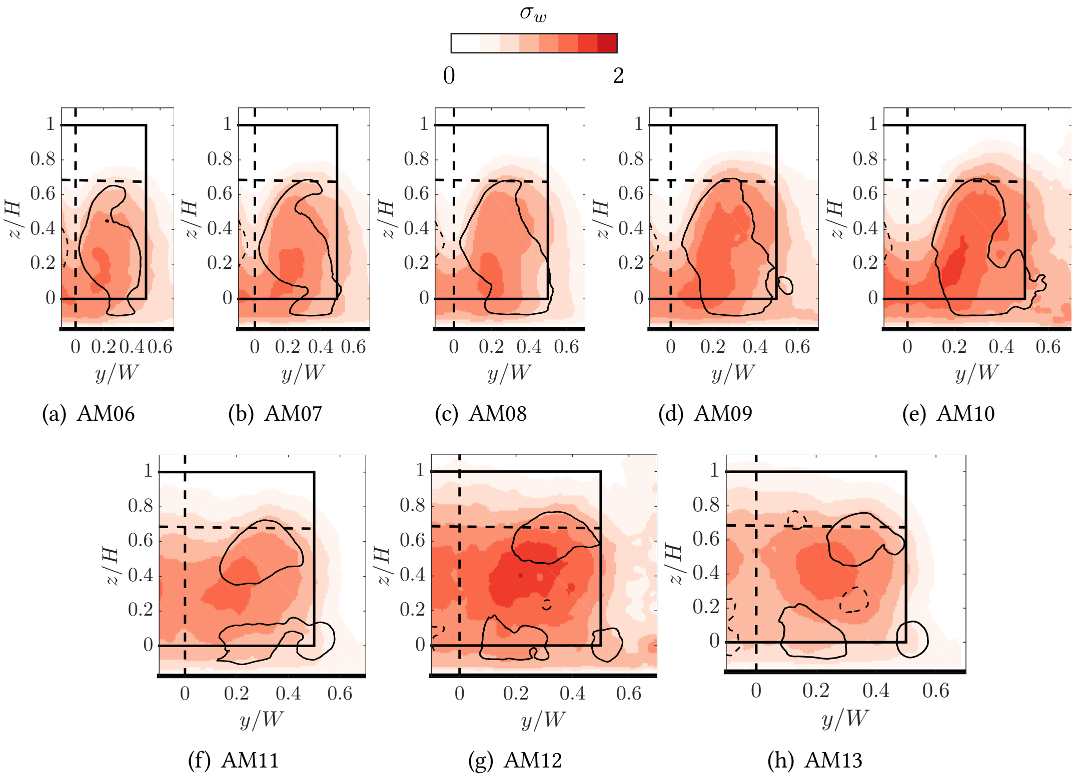

(a) AM06 (b) AM07 (c) AM08 (d) AM09 (e) AM10

(f) AM11 (g) AM12 (h) AM13

Figure 6.30: Standard deviation of w velocity component in the wake at downstream position $x/L = 0.4$. Black contours represent time-averaged vortex bounds with dashes indicating negative rotation.

that the major motion in the wake is not a function of the body's aspect ratio, even though the motion is symmetric about the xz plane.

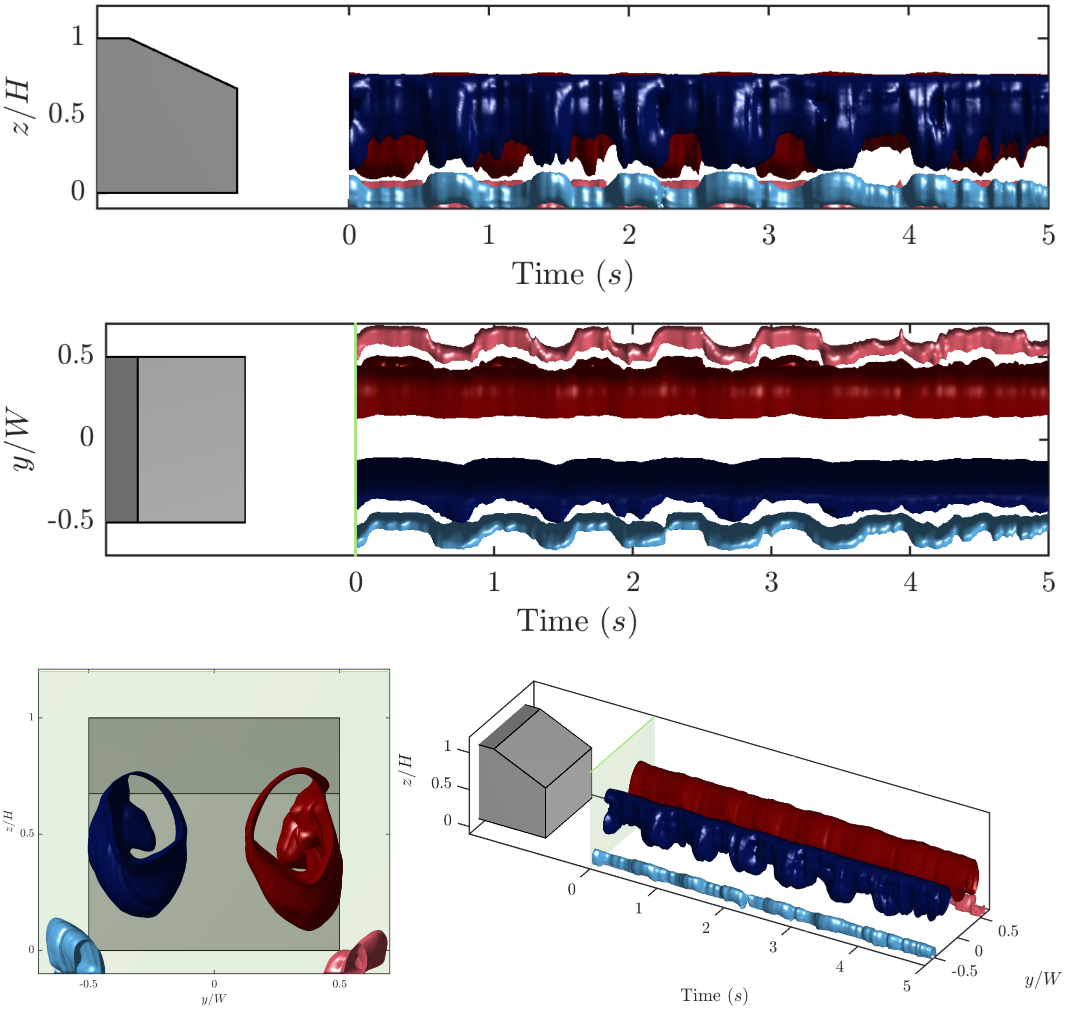

Figure 6.31: Cross-stream dynamics at $x/L = 0.2$ showing the wake motion of the c-pillar and corner vortices over a five second period in the wake of the AM08 model. The green plane represents the location of the acquisition plane relative to the rear surface of the Ahmed body. Positively rotating structures are shown in red and negatively rotating structures in blue. The c-pillar vortices are the darker structures, the lighter structures being the corner vortices.

For the wider body, the wake motions are even more exaggerated, with even the previously stable c-pillar vortex varying at the same frequency.

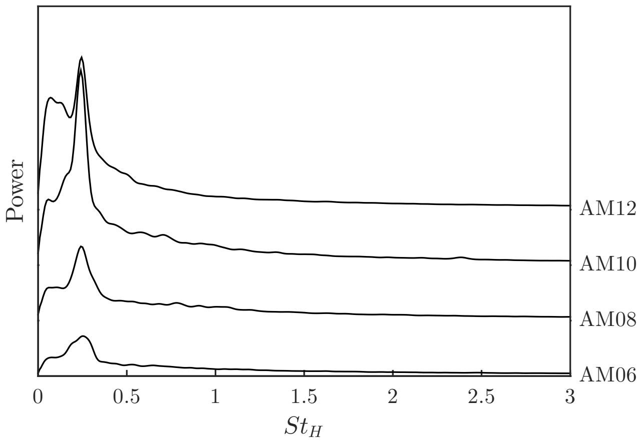

Figure 6.32: Frequency spectra (arbitrary power units) for each of the Ahmed models tested in the cross-stream plane at $x/L = 0.2$. The spectrum for each body has been shifted vertically for clarity. The dominant shedding frequency is not dependent on the body width.

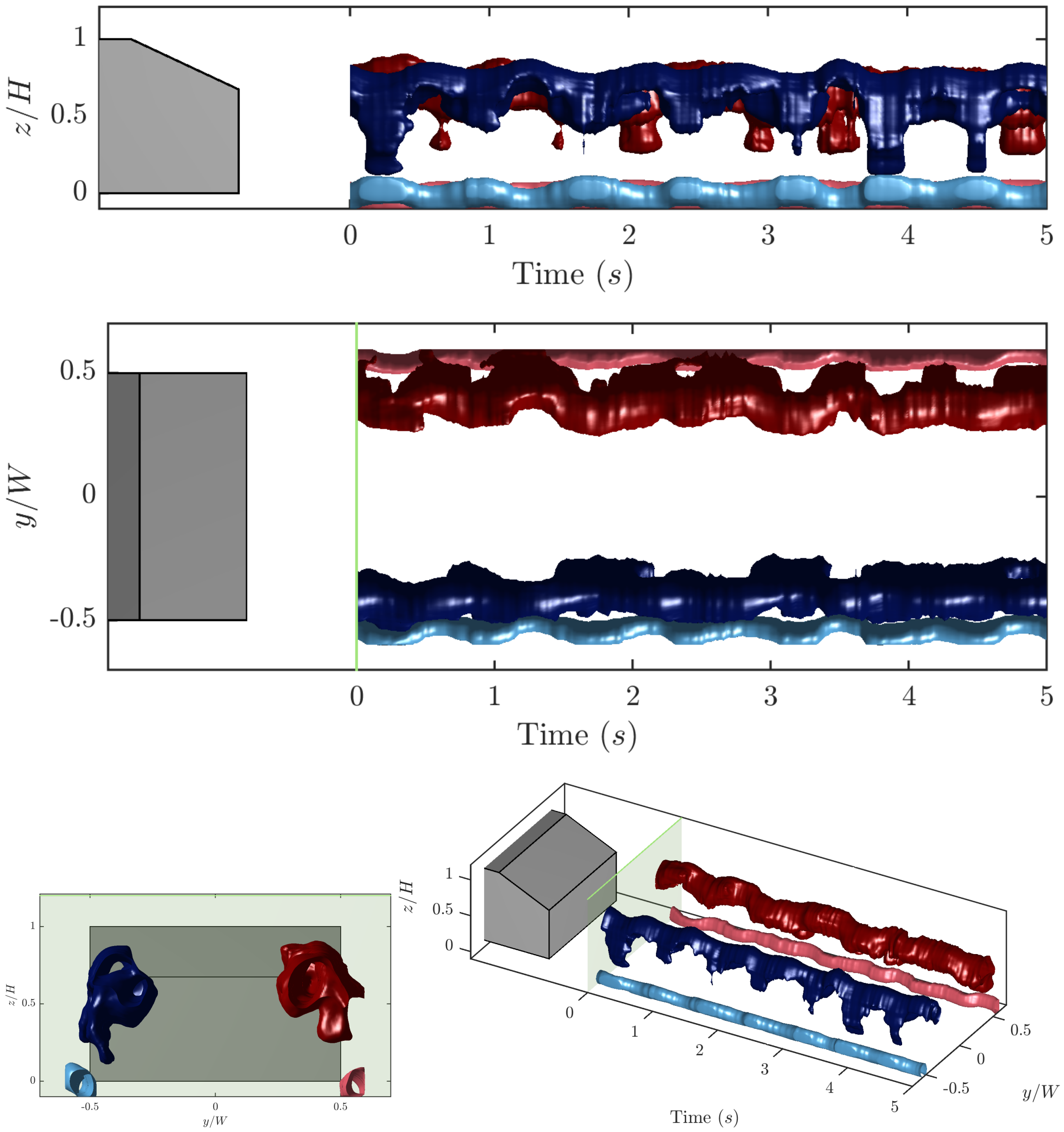

Figure 6.33: Cross-stream dynamics at $x/L = 0.2$ showing the wake motion of the c-pillar and corner vortices over a five second period in the wake of the AM12 body. The green plane represents the location of the acquisition plane relative to the rear surface of the Ahmed body. Positively rotating structures in reds and negatively rotating structures in blues. The c-pillar vortices are the darker structures, the lighter structures being the corner vortices.

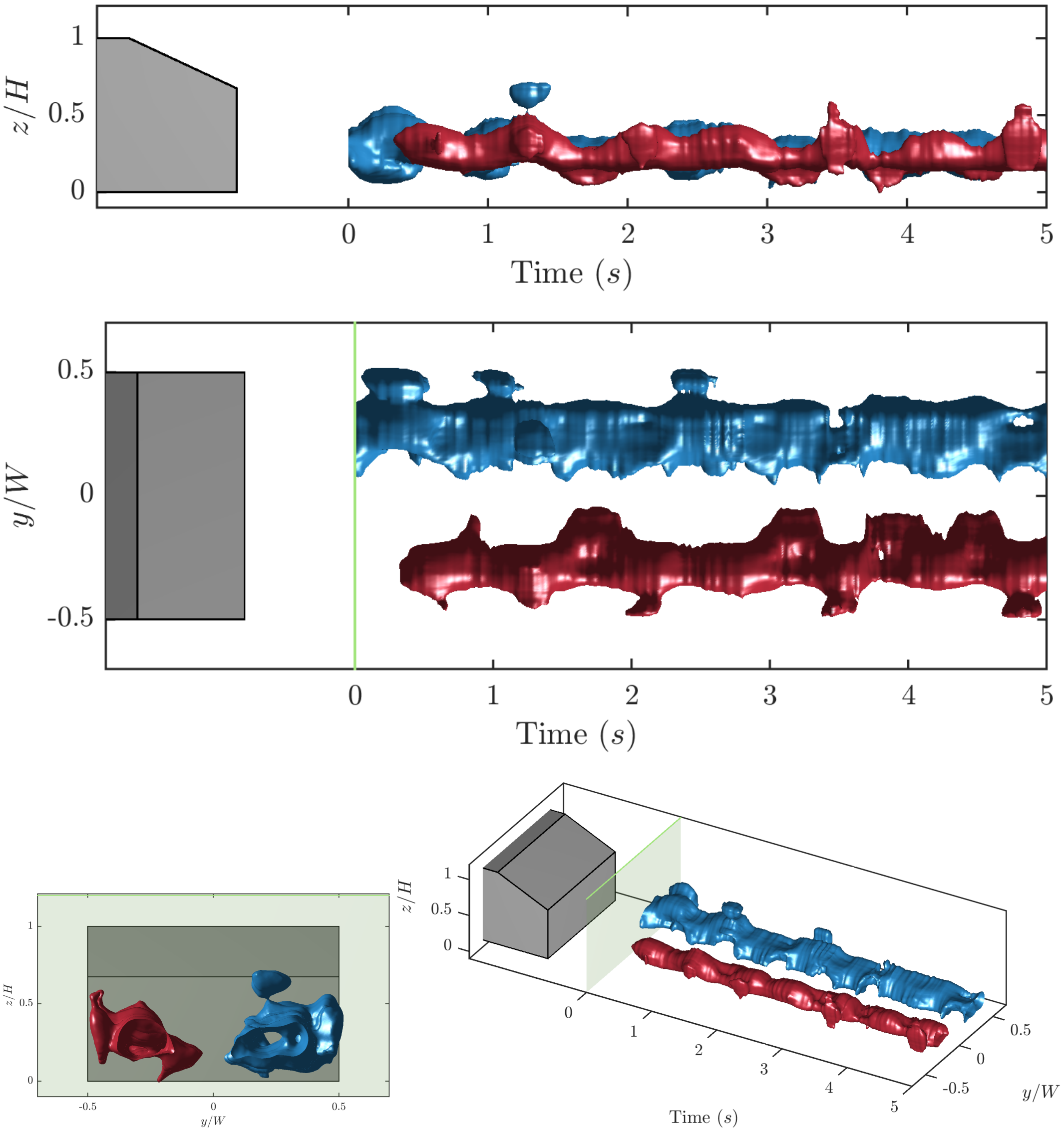

Figure 6.34: Cross-stream dynamics at $x/L = 0.2$ showing the wake motion of the streamwise elements of recirculation region B in the wake of the AM12 body. The positively rotating element is in red and the negatively rotating element is in blue. The green plane represents the location of the acquisition plane relative to the rear surface of the Ahmed body.

6.5 Summary

The detailed wake structure derived from high resolution PIV data has been reported in this chapter for Ahmed bodies with different aspect ratios. The circulation has been quantified for each of the major wake elements, and it has been found that when the flow is attached, spanwise vorticity is fed along the span into the c-pillar vortices above the slant, strengthening them as this vorticity is tilted into the streamwise direction. When the aspect ratio is increased, the flow separates over the slant, and this vorticity is now shed directly downstream. The wake is more turbulent, yet also more two-dimensional in this regime.

The locations of each of the A, B and c-pillar structures were shown to be dependent on the flow regime. Primarily there is an increase in the vertical position for each of these structures in the wake as the body is widened. The ground plane horseshoe vortex is stronger for the wider cases. Above the critical aspect ratio of 1.9, the wake contains a shear layer above the base, but a quasi-stable recirculating vortex at the bottom of the near wake.

The wake dynamics were also analysed with high-speed PIV. The frequency of the motion of the macro structures were seen to be invariant with aspect ratio, although the magnitude of this oscillation increased with aspect ratio, suggesting the frequency scales with vehicle height rather than width.

CHAPTER 7

CONCLUSIONS

Spatially and temporally resolved wake measurements were obtained for flow over a flat plate for a range of Reynolds numbers and angles-of-attack. The formation of the von Kármán vortices from the continuous advection of vorticity through the shear layers was visualised. The trajectory of shear layer vortices during this transition supports the claim by Gerrard (1966) that a kink in the shear-layer caused by the opposite von Kármán vortex results in the formation of a new von Kármán vortex. The non-dimensionalised frequency ratio of this formation was analysed and found to follow a power law.

The time-averaged wake structure of the Ahmed body was also presented, focusing on the development of the c-pillar vortical structures. The circulation of each structure was measured throughout the spatial domain allowing the downstream evolution to be quantified. It was shown that rather than forming a toroidal structure, the A and B vortices are in fact two horseshoe vortices, with the vorticity collecting in A feeding outwards and streamwise, and then merging into and strengthening the c-pillar vortices. The dynamics of the B vortex were shown to be the dominant temporal feature, causing a transverse pulsing of the near wake.

These experiments were extended to quantify the wakes of various width Ahmed bodies, showing the critical aspect ratio for the 25° back slant case was $\mathrm{AR} = 1.9$. The wake changes beyond this aspect ratio, apparently driven by the fully separated flow over the back slant. Counter to expectations, the drag was measured to increase for bodies past this aspect ratio, at least for the current setup. This may be a cause of concern for vehicle aerodynamicists, as the common aspect ratio is the critical aspect ratio at low Reynolds number. Care must be taken to verify that the flow structures from any studies match what is expected in that regime. Also of note is the large change in drag caused by a small change in aspect ratio.

The analysis presented in this thesis motivates several interesting questions for future work. Firstly, the nature of the critical Reynolds number ($Re = 1500$) that was observed for the flat plate should be investigated. It was also noted during the experiments that capturing the dynamics of the shear layer vortices was more difficult when the plate was normal to the flow compared to when it was inclined. The spatio-temporal behaviour of this flow presents many points for future research. The instability forming the initial kink in the leading edge shear layer, the reason for the coefficient change in the shear-layer to von Kármán ratio, and the variation in formation length are all worthwhile studies themselves.

Regarding the Ahmed body work, there are several interesting avenues of enquiry. Firstly, the preliminary drag measurements concerning the effect of body aspect ratio should be investigated. While the hysteresis was expected, it should be confirmed that it is due to the reattachment over the slant. The bodies could be pressure-tapped in order to see how the observed wake changes influence the pressure on the rear and slant surfaces. This could reveal the details of the physics behind the drag increase beyond the critical aspect ratio. Secondly, due to the wide range of underbody supports used in Ahmed body experiments, a study into the underbody configuration and the resultant effect on the wake would be helpful. Finally, the side radii at the front end of the Ahmed body could be scaled with the width, so that the changes in aspect ratio would not also constitute a change in the normal face of the body close to the stagnation point.

APPENDIX A

PRELIMINARY DRAG MEASUREMENTS ON THE AHMED BODY

A.1 Introduction

Force measurements were carried out on the Ahmed bodies using the methodology described in section 3.4.3. For each body, the Reynolds number was varied across the possible range of the water channel. Three key results came out of this experiment. Firstly, there was hysteresis in the drag measurements, which is further indication that the hypothesis presented in section 6.3.1 may be correct. Secondly, the effect of rear slant angle on the drag was as expected from previous literature. Finally, the expectation of lower drag for the wider models was not realised, instead a large increase in drag was measured. Further work is required to investigate the cause of this.

A.2 The drag of the standard width Ahmed model

When measuring the drag of the Ahmed model with varying flow speed, it was noted that a very large hysteresis effect was present. Figure A.1 shows that as the flow speed is increasing, the drag follows the expected quadratic curve (with $C_D = 0.62$) until $Re = 2.9 \times 10^4$. At this Reynolds number, the curve drops suddenly, and from then continues increasing. When the flow speed is decreased, the measured drag again lies on a quadratic curve, though now with a lower $C_D = 0.48$. It continues in this regime until $Re = 1.3 \times 10^4$, where the drag increases suddenly and lies on the original curve.

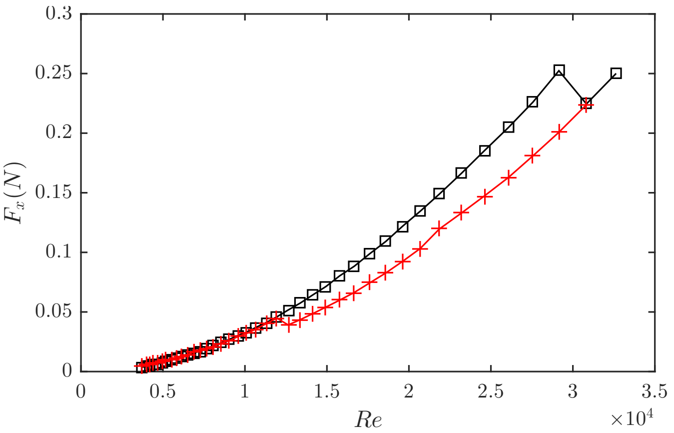

Figure A.1: Variation of drag force (F_x) with Reynolds number for the standard width Ahmed model. Black and red points represent force measurements while the velocity is increasing and decreasing respectively.

Our hypothesis is that the drag is in the high drag regime while the flow is fully separated. It is known that separation is accentuated by low Reynolds numbers, and given the marginal nature of the separation for the standard width model, it is expected that the flow is initially separated. Once the Reynolds number is high enough to force the reattachment, the drag drops significantly. Once the flow is reattaching, the vorticity in the slant region is fed into the c-pillars, strengthening them. As the Reynolds number drops, the downwash from the strengthened c-pillar vortices is enough to keep the flow attached to much lower Reynolds number.

It is interesting to note that the low drag state occurs at the highest Reynolds numbers when the flow is expected to be attached. Previous studies (e.g. Ahmed *et al.*, 1984; Gilliéron *et al.*, 1999; Corallo *et al.*, 2015) all suggest that the fully separated flow when the rear slant angle is higher than 30° causes the observed drag reduction. Yet the present data suggests that there is a significant decrease in the drag when the flow is attached. Furthermore, the difference in drag from previous studies between the attached and separated cases is about 10% (between 25° and 30°), while our data suggests an increase of about 30%.

Given the surprising nature of these results, the experiment was repeated five times, with varying spacing between the speeds, and with several different schemes for zeroing the gauge. All the results were very consistent.

A.3 Effect of aspect ratio and slant angle on the drag

To investigate these results further, the drag of an Ahmed model with 35° slant angle was measured. Previous PIV results reveal that the flow is completely separated (figure A.2). When the drag was measured, no hysteresis was evident, and the drag coefficient reduced to $C_D = 0.44$, roughly 10% lower than the low drag regime measured for the 25° body. This corresponds well to the available data.

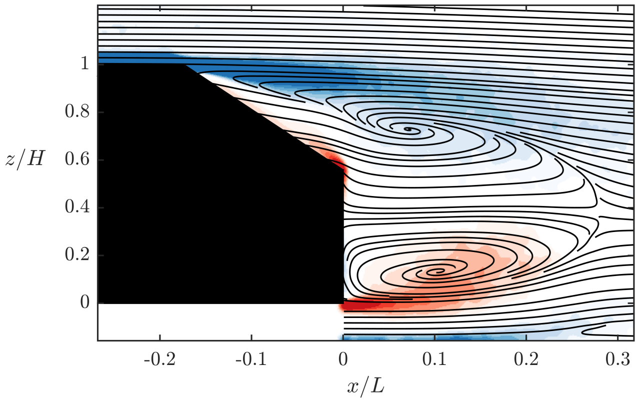

FIGURE A.2: Flow field in the symmetry plane behind the standard width Ahmed model with rear slant angle of 35°. Complete separation is evident at the start of the slant. Streamlines indicate local flow direction only and filled contours are of spanwise vorticity.

When the aspect ratio was reduced, the drag coefficient was relatively constant, as expected given the PIV results indicate a constant (reattaching) flow regime for AR < 1.9 (see figure 6.13 and corresponding text for details). When the aspect ratio was increased, however, there was a large increase in the drag coefficient (figure A.3).

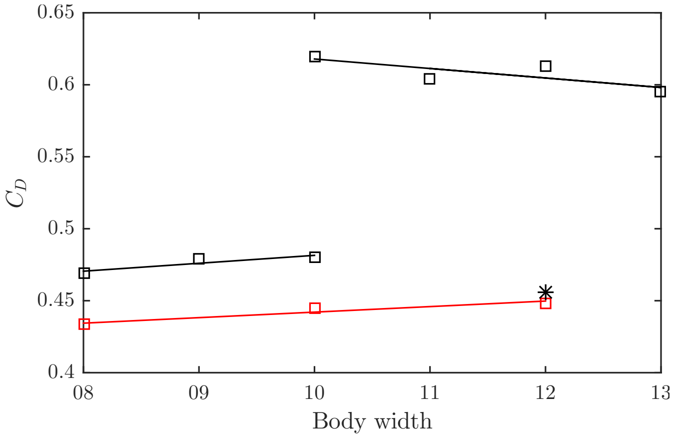

FIGURE A.3: Drag coefficient as it varies with aspect ratio for 25° (black) and 35° (red) Ahmed bodies. Black asterisk corresponds to the 25° body with rear spoiler. Solid lines are linear fits to the corresponding regime.

The critical aspect ratio from the drag measurements is consistent with that found from the PIV results. Two data points are included at this body width (AM10) to represent the two regimes presented in figure A.1.

The reason for the increase in drag is unclear. The two additional cases for the AM12 body of a spoiler (black asterisk in figure A.3 and the 35° slant show that the increase is not due to the changes at the front end as suggested by Corallo *et al.* (2015). As detailed in chapter 6, the PIV measurements point to a flow regime change due to the flow completely separating off the rear slant, the same mechanism that is seen for the 35° case (figure A.2), yet they produce vastly different drag coefficients. The vortex strength, measured by the circulation, is also much lower for the wider bodies (figure 6.13), implying that the vortex drag (equation 2.2) should also be lower, and yet the total drag is higher.

A comparison between the 35° (low drag) and 25° (high drag) slant angles for the AM12 case shows that there are differences within the wake even though both cases are fully separated (figure A.4). Firstly, the ground separation is more extreme in the low drag case (similar to the AM13 case in figure 6.2(h)), even though this would be related to the base pressure. Secondly, the wake is considerably longer in the low drag case, which is understandable, yet the mechanism driving this change is unclear. Thirdly, the top shear layer is spread over a longer downstream range for the 35° body.

These preliminary results have indicated that there are more mechanisms behind the drag coefficient than simply whether the flow is separated or not. Further work is necessary to unravel the physics driving these changes.

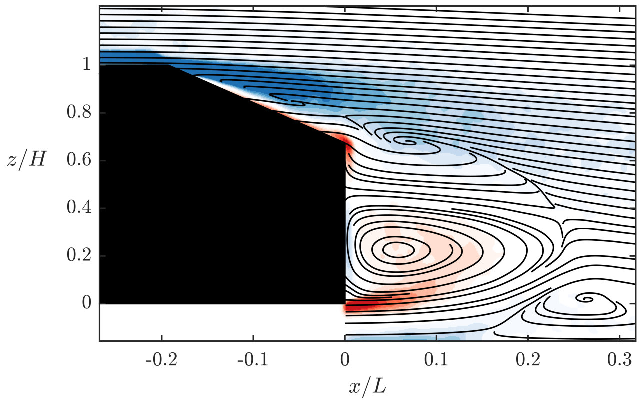

(a) $C_D = 0.61$

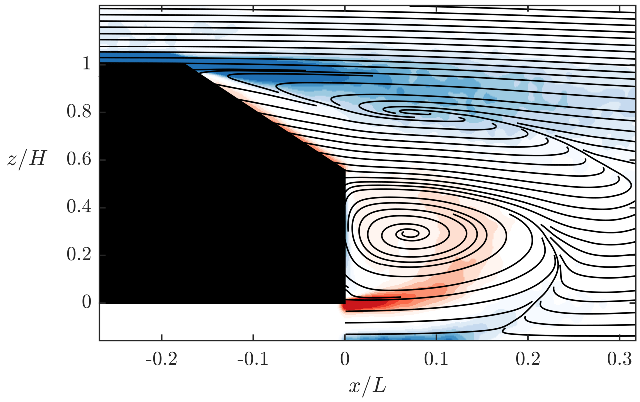

(b) $C_D = 0.45$

FIGURE A.4: Flow field in the symmetry plane behind the AM12 Ahmed model with rear slant angle of 25 ° (top) and 35° (bottom). Streamlines indicate local flow direction only and filled contours are of spanwise vorticity.

REFERENCES

ADRIAN, R J 1991 Particle-image techniques for experimental fluid mechanics. *Annual Review of Fluid Mechanics* **23**, 261–304.

AHMED, SR, RAMM, G. & FAITIN, G. 1984 Some salient features of the time-averaged ground vehicle wake. *Tech. Rep.*. Society of Automotive Engineers, Inc., Warrendale, PA.

ANDERSON, JOHN D. 2007 *Fundamentals of Aerodynamics*, 4th edn. McGraw Hill.

BASLEY, J., PASTUR, L. R., LUSSEYRAN, F., FAURE, T. M. & DELPRAT, N. 2010 Experimental investigation of global structures in an incompressible cavity flow using time-resolved PIV. *Experiments in Fluids* **50** (4), 905–918.

BAYRAKTAR, ILHAN, LANDMAN, DREW & BAYSAL, OKTAY 2001 Experimental and Computational Investigation of Ahmed Body for Ground Vehicle Aerodynamics. *SAE Technical Paper Series* .

BEARMAN, P. W., DE BEER, D. & HARVEY, J. K. 1989 Experimental studies of road vehicle flow fields. In *AIAA 20th Fluid Dynamics, Plasma Dynamics and LAsers Conference*.

BEAUDOIN, JEAN-FRANÇOIS & AIDER, JEAN-LUC 2008 Drag and lift reduction of a 3D bluff body using flaps. *Experiments in Fluids* **44** (4), 491–501.

BEAUDOIN, J. F., CADOT, O., AIDER, J. L., GOSSE, K., PARANTHOEN, P., HAMELIN, B., TISSIER, M., ALLANO, D., MUTABAZI, I., GONZALES, M. & WESFREID, J. E. 2004 Cavitation as a complementary tool for automotive aerodynamics. *Experiments in Fluids* **37** (5), 763–768.

BELL, J.R., BURTON, D., THOMPSON, M., HERBST, A. & SHERIDAN, J. 2014 Wind tunnel analysis of the slipstream and wake of a high-speed train. *Journal of Wind Engineering and Industrial Aerodynamics* **134**, 122–138.

BERGER, E, SCHOLZ, D & SCHUMM, M 1990 Coherent Vortex Structures in the Wake of a Shere and a Circular Disk at Rest and under Forced Vibrations. *Journal of Fluids and Structures* **4**, 231–257.

Bloor, M. Susan 1964 The transition to turbulence in the wake of a circular cylinder. *Journal of Fluid Mechanics* **19** (1949), 290.

Bradbury, L. J. S. 1976 Measurements with a pulsed-wire and a hot-wire anemometer in the highly turbulent wake of a normal flat plate. *Journal of Fluid Mechanics* **77**, 473.

de Brederode, V & Bradshaw, P 1972 Three-dimensional Flow in Nominally Two-dimensional Separation Bubbles: Flow Behind a Rearward-facing Step. I. *Tech. Rep.*. Imperial College, Aeronautical Report.

Chakraborty, Pinaki, Balachandar, S. & Adrian, Ronald J. 2005 On the relationships between local vortex identification schemes. *Journal of Fluid Mechanics* **535**, 189–214.

Chong, M. S., Perry, a. E. & Cantwell, B. J. 1990 A general classification of three-dimensional flow fields. *Physics of Fluids A: Fluid Dynamics* **2** (1990), 765–777.

Coleman, Hugh W. & Steele, W. G. 1995 Engineering application of experimental uncertainty analysis. *AIAA Journal* **33** (10), 1888–1896.

Corallo, M, Sheridan, J & Thompson, M C 2015 Effect of Aspect Ratio on the Near-Wake Flow Structure of an Ahmed Body. *Journal of wind engineering and industrial aerodynamics* .

Dallman, U. & Schewe, G. 1987 On topological changes of separating flow structures at transition reynolds numbers. In *AIAA 19th Fluid Dynamics, Honolulu, USA*.

Delery, J 2011 Separation in three-dimensional steady flow, Part 3.

Delery, Jean M 2001 Toward the Elucidation of Three-Dimensional Separation. *Annual Review of Fluid Mechanics* **33**, 129–168.

Dennis, SCR, Qiang, Wang, Coutanceau, M & Launay, J 1993 Viscous flow normal to a flat plate at moderate Reynolds numbers. *Journal of Fluid* **248**.

Dennis, S. C. R. & Chang, Gau-Zu 1970 Numerical solutions for steady flow past a circular cylinder at Reynolds numbers up to 100. *Journal of Fluid Mechanics* **42**, 471.

Drouin, Vincent, Giovannini, A. & Gilliéron, Patrick 2002 Topology and characterisation of the vortical near-wake flow over a simplified car model. In *Conference on Bluff Body Wakes and Vortex-Induced Vibrations (BBVIV3)*, pp. 1–4.

Duell, Edward G. & George, A. R. 1999 Experimental Study of a Ground Vehicle Body Unsteady Near Wake. *SAE Technical Paper Series* .

Elle, B. J. 1958 On the breakdown at high, incidence of the leading edge vortices on delta wings. *Tech. Rep.*. ARC.

Fage, A *&* Johansen, F. C. 1927 On the flow of air behind an inclined flat plate of infinite span. *Proceedings of the Royal Society of London. Series* **116** (773), 170–197.

Fouras, Andreas, Lo Jacono, David *&* Hourigan, Kerry 2007 Target-free Stereo PIV: a novel technique with inherent error estimation and improved accuracy. *Experiments in Fluids* **44** (2), 317–329.

Fouras, A. *&* Soria, J. 1998 Accuracy of out-of-plane vorticity measurements derived from in-plane velocity field data. *Experiments in Fluids* **25** (5-6), 409–430.

Gant, S. E. 2002 Development and Application of a New Wall Function for Complex Turbulent Flows. PhD thesis, University of Manchester Institute of Science and Technology.

Gerrard, B Y J H 1978 THE WAKES OF CYLINDRICAL BLUFF BODIES ReOs. In *Philosophical transactions. Series A, Mathematical and Physical Sciences*, , vol. 288, pp. 351–382.

Gerrard, J. H. 1966 The mechanics of the formation region of vortices behind bluff bodies. *Journal of Fluid Mechanics* **25** (02), 401.

Gilhome, Brendan R 2002 Unsteady and Time-Averaged Near-Wake Flow over the Rear of Sedan Automobiles. PhD thesis, Monash University.

Gilliéron, Patrick *&* Kourta, Azeddine 2009 Aerodynamic drag reduction by vertical splitter plates. *Experiments in Fluids* **48** (1), 1–16.

Gilliéron, P, Renault, S A, Golf, Avenue *&* Cedex, Guyancourt 1999 Modelling of Stationary Three-Dimensional Separated Air Flows around an Ahmed Reference Model. In *Third International Workshop on Vortex Flows and Related Numerical Methods*, pp. 173–182.

Graftieaux, Laurent 2001 Combining PIV, POD and vortex identification algorithms for the study of unsteady turbulent swirling flows. *Measurement Science and …* **1422**.

Grandemange, M., Gohlke, M. *&* Cadot, O. 2013 Turbulent wake past a three-dimensional blunt body. Part 1. Global modes and bi-stability. *Journal of Fluid Mechanics* **722**, 51–84.

Grant, H L 1958 The large eddies of turbulent motion. *Journal of Fluid Mechanics* **4** (02), 149–190.

Grinstein, Fernando F., Glauser, Mark N. *&* George, William K. 1995 VORTICITY IN JETS. In *Fluid Vortices* (ed. Sheldon I. Green), pp. 65–94. Springer Science & Business Media.

Herry, Benjamin B., Keirsbulck, Laurent, Labraga, Larbi & Paquet, Jean-Bernard 2011 Flow Bistability Downstream of Three-Dimensional Double Backward Facing Steps at Zero-Degree Sideslip. *Journal of Fluids Engineering* **133** (5), 054501.

Ho, Chih-Ming & Huang, Lein-Saing 1982 Subharmonics and vortex merging in mixing layers. *Journal of Fluid Mechanics* **119** (-1), 443.

Huang, L.-S. & Ho, C.-M. 1990 Small-scale transition in a plane mixing layer. *Journal of Fluid Mechanics* **210**, 475–500.

Huang, Yuqi, Venning, James, Thompson, Mark C & Sheridan, John 2015 Vortex separation and interaction in the wake of inclined trapezoidal plates. *Journal of Fluid Mechanics* pp. 1–26.

Hucho, W 1993 Aerodynamics of road vehicles. *Annual review of fluid mechanics* **25**, 485–537.

Hucho, W 1998 *Aerodynamics of Road Vehicles*. Society of Automotive Engineers.

Hunt, J.C.R., Wray, A. A. & Moin, P. 1988 Eddies, Streams, and Convergence Zones in Turbulent Flows. In *Center for Turbulence Research - Proceedings of the Summer Program*, pp. 193–208.

Janssen, LJ & Hucho, W 1974 Aerodynamic Development of the VW Golf (Rabbit) and VW Scirocco. In *Symposium on Road Vehicle Aerodynamics*, pp. 49–70.

Jeong, Jinhee & Hussain, Fazle 1995 On the identification of a vortex. *Journal of Fluid Mechanics* **285** (-1), 69.

Johnson, Shaun A, Hourigan, Kerry & Thompson, Mark C 2004 Effect of aspect ratio on the wake structures of simplified automotive geometries. In *Proceedings of 5 th International Colloquium of Bluff Body Aerodynamics and Application, Ottawa, Canada.*

Joseph, Pierric, Amandolèse, Xavier & Aider, Jean-Luc 2011 Drag reduction on the 25° slant angle Ahmed reference body using pulsed jets. *Experiments in Fluids* pp. 1–17.

Joseph, Pierric, Amandolèse, Xavier & Aider, Jean Luc 2012 Drag reduction on the 25° slant angle Ahmed reference body using pulsed jets. *Experiments in Fluids* **52** (5), 1169–1185.

Joseph, Pierric, Amandolese, Xavier, Edouard, Christophe & Aider, Jean Luc 2013 Flow control using MEMS pulsed micro-jets on the Ahmed body. *Experiments in Fluids* **54** (1).

Joshi, D. S., Vanka, S. P. & Tafti, D. K. 1994 Large eddy simulation of the wake of a normal flat plate. In *ASME-PUBLICATIONS-FED*, p. 231.

VON KARMAN, T & RUBACH, H 1912 Über den mechanismus des flüssigkeits-und luftwiderstandes. *Phys. Z* .

KHALAK, A. & WILLIAMSON, CHK 1996 Dynamics of a hydroelastic cylinder with very low mass and damping. *Journal of Fluids and Structures* **10** (5), 455–472.

KIYA, M. & MATSUMURA, M. 2006 Incoherent turbulence structure in the near wake of a normal plate. *Journal of Fluid Mechanics* **190** (-1), 343–356.

KLEMPERER, W 1922 LUFTWIDERSTANSUNTERSUECHUNGEN AN AUTOMOBILMODELLEN. *ZEITSCHRIFT FUER FLUGTECHNIK UND MOTOR-LUFTSCHIFFAHRT* **13**, 201–206.

KNISELY, C.W. 1990 Strouhal numbers of rectangular cylinders at incidence: A review and new data. *Journal of Fluids and Structures* **4** (4), 371–393.

KOCH, W. 1985 Local instability characteristics and frequency determination of self-excited wake flows. *Journal of Sound and Vibration* **99**, 53–83.

KOURTA, A., BOISSON, H. C., CHASSAING, P. & MINH, H. HA 1987 Nonlinear interaction and the transition to turbulence in the wake of a circular cylinder. *Journal of Fluid Mechanics* **181**, 141–161.

KRAJNOVIĆ, SINIŠA & DAVIDSON, LARS 2005*a* Flow Around a Simplified Car, Part 1: Large Eddy Simulation. *Journal of Fluids Engineering* **127** (5), 907.

KRAJNOVIĆ, SINIŠA & DAVIDSON, LARS 2005*b* Flow Around a Simplified Car, Part 2: Understanding the Flow. *Journal of Fluids Engineering* **127** (5), 919.

KUPFER, K., BERS, A. & RAM, A. K. 1987 The cusp map in the complex-frequency plane for absolute instabilities. *Physics of Fluids* **30** (10), 3075.

LAWFORD, J A 1964 Low-speed wind tunnel experiments on a series of sharp-edged delta wings: Part II. Surface flow patterns and boundary layer transition measurements. *Tech. Rep.*. Royal Aircraft Establishment.

LEDER, A 1991 Dynamics of fluid mixing in separated flows. *Physics of Fluids A* **3** (1991), 1741–1748.

LEONTINI, J. S., THOMPSON, M. C. & HOURIGAN, K. 2010 A numerical study of global frequency selection in the time-mean wake of a circular cylinder. *Journal of Fluid Mechanics* **645**, 435.

LIENHART, HERMANN & BECKER, STEFAN 2003 Flow and Turbulence Structure in the Wake of a Simplified Car Model. *SAE Technical Paper Series* .

LIENHART, HERMANN & PÊGO, JOÃO PEDRO 2012 Spectral Density and Time Scales of Velocity Fluctuations in the Wake of a Simplified Car Model. In *SAE International*.

LIM, K S, PARK, S O & SHIM, H S 1990 A Low Aspect Ratio Backward-Facing Step Flow height duct wid i uct. *Experimental Thermal and Fluid Science* **3**, 508–514.

LISOSKI, DEREK LEE ASHTON 1993 Lisoski_dla_1993.pdf. PhD thesis, California Institute of Technology.

MCNALLY, JONATHAN, FERNANDEZ, ERIK, KUMAR, RAJAN, ALVI, FARRUKH & NUMBER, STROUHAL 2012 Near Wake Dynamics for an Ahmed Body with Active Flow Control. In *6th AIAA Flow Control Conference*, pp. 1–11.

MICHALKE, A. 1965 On Spatially Growing Disturbances in an Inviscid Shear Layer Between Parallel Streams. *1Journal of Fluid Mechanics* **23**, 521–544.

MINGUEZ, M., BRUN, C., PASQUETTI, R. & SERRE, E. 2011 Experimental and high-order LES analysis of the flow in near-wall region of a square cylinder. *International Journal of Heat and Fluid Flow* **32**, 558–566.

MINGUEZ, M., PASQUETTI, R. & SERRE, E. 2008 High-order large-eddy simulation of flow over the "Ahmed body" car model. *Physics of Fluids* **20** (9).

MONKEWITZ, P.A. & NGUYEN, L.N. 1987 Absolute instability in the near-wake of two-dimensional bluff bodies. *Journal of Fluids and Structures* **1**, 165–184.

MOREL, T 1978*a* Aerodynamic drag of bluff body shapes characteristic of hatch-back cars. *SAE* .

MOREL, T 1978*b* The effect of base slant on the flow pattern and drag of three-dimesnional bodies with blunt ends. In *Symposium on Aerodynamic Drag Mechanisms of Bluff Bodies and Road Vehicles*, pp. 216–217.

MUNSON, BR, YOUNG, DF & OKIISHI, TH 1990 *Fundamentals of fluid mechanics*. Wiley.

NAJJAR, F. M. & BALACHANDAR, S. 1998 Low-frequency unsteadiness in the wake of a normal flat plate. *Journal of Fluid Mechanics* **370**, 101–147.

NAJJAR, F. M. & VANKA, S. P. 1995*a* Effects of intrinsic three-dimensionality on the drag characteristics of a normal flat plate. *Physics of Fluids* **7** (10), 2516.

NAJJAR, FADY M; & VANKA, S. P. 1995*b* SIMULATIONS OF THE UNSTEADY SEPARATED FLOW PAST A NORMAL FLAT PLATE. *International Journal for Numerical Methods in Fluids* **21**, 525–547.

Nakamura, Y., Ohya, Y. & Tsuruta, H. 1991 Experiments on vortex shedding from flat plates with square leading and trailing edges. *Journal of Fluid Mechanics* **222**, 437–447.

Narasimhamurthy, Vagesh D. & Andersson, Helge I. 2009 Numerical simulation of the turbulent wake behind a normal flat plate. *International Journal of Heat and Fluid Flow* **30** (6), 1037–1043.

Norberg, C. 1994 An experimental investigation of the flow around a circular cylinder: influence of aspect ratio. *Journal of Fluid Mechanics* **258** (-1), 287.

Okada, Mitsushi, Sheridan, John & Thompson, Mark 2005 Effect of Width-to-Height Ratio on Wake Structures of Simplified Vehicle Geometry. In *Proceedings of the Fourth Conference on Bluff Body Wakes and Vortex-Induced Vibrations - BBVIV4*, pp. 243–246.

Onorato, M & Costelli, AF 1984 Drag measurement through wake analysis. *AIAA Journal* .

Pagliarella, Riccard 2009 On the aerodynamic performance of automotive vehicle platoons featuring pre and post-critical leading forms. PhD thesis, RMIT University.

Peckham, D. H. & Atkinson, S. A. 1957 Preliminary results of low speed wind tunnel tests on a gothic wing of aspect ratio 1.0. *Tech. Rep.*. ARC.

Prasad, Anil & Williamson, Charles H. K. 1997 The instability of the shear layer separating from a bluff body. *Journal of Fluid Mechanics* **333**, 375–402.

Radi, Alexander, Lo Jacono, David & Sheridan, John 2014 A device to achieve low Reynolds numbers in an open surface water channel. *Experiments in Fluids* **55** (5), 1–8.

Raffel, M, Willert, C & Kompenhans, J 2007 *Particle Image Velocimetry*. Springer.

Rajasekaran, J 2011 On the flow characteristics behind a backward-facing step and the design of a new axisymmetric model for their study. PhD thesis, University of Toronto.

Reynolds, Osborne 1883 An experimental investigation of the circumstances which determine whether the motion of water shall be direct or sinuous, and of the law of resistance in parallel channels. In *Proceedings of the Royal Society of London*, pp. 84–99.

Rouméas, M., Gilliéron, P. & Kourta, A. 2009 Analysis and control of the near-wake flow over a square-back geometry. *Computers & Fluids* **38** (1), 60–70.

Saha, Arun K. 2007 Far-wake characteristics of two-dimensional flow past a normal flat plate. *Physics of Fluids* **19** (12), 128110.

Sakamoto, H. & Haniu, H 1990 A Study on Wortex Shedding From Spheres in a Uniform Flow. *Journal of Fluid Engineering* **112** (December), 386–392.

Schlichting, Herrmann 2000 *Boundary-layer theory.*. Springer Science & Business Media.

Schmid, Peter J. & Henningson, Dan S. 2001 *Stability and Transition in Shear Flows*. Springer.

Sims-Williams, D.B, Dominy, R.G. & HOWELL, J 2001 An Investigation into Large Scale Unsteady Structures in the Wake of Real and Idealized Hatchback Car Models. *Society of Automotive Engineers* .

Sims-Williams, D. B. & Dominy, R G 1998 Experimental Investigation into Unsteadiness and Instability in Passenger Car Aerodynamics. *SAE Technical Paper Series* .

Sirovich, L 1987 Turbulence and the dynamics of coherent structures. I - Coherent structures. II - Symmetries and transformations. III - Dynamics and scaling. *Quarterly of Applied Mathematics (ISSN 0033-569X)* **45** (August), 561.

Spohn, A & Gilliéron, P. 2002 Flow separations generated by a simplified geometry of an automotive vehicle. In *IUTAM Symposium: unsteady separated flows*.

Stewart, B. E., Thompson, M. C., Leweke, T. & Hourigan, K. 2010 Numerical and experimental studies of the rolling sphere wake. *Journal of Fluid Mechanics* **643** (October 2015), 137.

Taira, Kunihiko & Colonius, Tim 2009 Three-dimensional flows around low-aspect-ratio flat-plate wings at low Reynolds numbers. *Journal of Fluid Mechanics* **623**, 187.

Taneda, Sadatoshi 1956 Experimental investigation of the wake behind a sphere at low Reynolds numbers.

Thacker, Adrien, Aubrun, Sandrine, Leroy, Annie & Devinant, Philippe 2010 Unsteady analyses of the flow separation on the rear window of a simplified ground vehicle model. In *28th AIAA Applied Aerodynamics Conference, Chicago*, pp. 1–11.

Thacker, a., Aubrun, S., Leroy, a. & Devinant, P. 2013 Experimental characterization of flow unsteadiness in the centerline plane of an Ahmed body rear slant. *Experiments in Fluids* **54** (3).

Thom, A 1933 Royal Society. In *Proceedings of the Royal Society of London. Series A, Containing Papers of a Mathematical and Physical Character*, , vol. 141, pp. 651–669.

Thompson, Mark C. & Hourigan, Kerry 2005 The shear-layer instability of a circular cylinder wake. *Physics of Fluids* **17**, 1–4.

TROPEA, CAMERON, YARIN, ALEXANDER & FOSS, JOHN, ed. 2007 *Springer Handbook of Experimental Fluid Mechanics*. Springer.

TUNAY, TURAL, SAHIN, BESIR & OZBOLAT, VELI 2014 Effects of rear slant angles on the flow characteristics of Ahmed body. *Experimental Thermal and Fluid Science* **57**, 165–176.

VAN DYKE, MILTON 1982 An album of fluid motion.

VENNING, J., LO JACONO, D., BURTON, D., THOMPSON, M. & SHERIDAN, J. 2015 The effect of aspect ratio on the wake of the Ahmed body. *Experiments in Fluids* **56** (6).

VINO, G, WATKINS, S, MOUSLEY, P, WATMUFF, J & PRASAD, S 2005 Flow structures in the near-wake of the Ahmed model. *Journal of Fluids and Structures* **20** (5), 673–695.

VOLPE, R, DEVINANT, P & KOURTA, AZEDDINE 2014 UNSTEADY EXPERIMENTAL CHARACTERIZATION OF THE NATURAL WAKE OF A SQUAREBACK AHMED MODEL. In *Proceedings of the ASME 2014 4th Joint US-European Fluids Engineering Division Summer Meeting, Chicago, USA*, pp. 1–9.

VOLPE, RAFFAELE, DEVINANT, PHILIPPE & KOURTA, AZEDDINE 2015 Experimental characterization of the unsteady natural wake of the full-scale square back Ahmed body: flow bi-stability and spectral analysis. *Experiments in Fluids* **56** (5), 1–22.

WALDMAN, RYE M. & BREUER, KENNETH S. 2012 Accurate measurement of streamwise vortices using dual-plane PIV. *Experiments in Fluids* **53** (5), 1487–1500.

WANG, X. W., ZHOU, Y., PIN, Y. F. & CHAN, T. L. 2013 Turbulent near wake of an Ahmed vehicle model. *Experiments in Fluids* **54** (4).

WEI, T. & SMITH, C. R. 1986 Secondary vortices in the wake of circular cylinders. *Journal of Fluid Mechanics* **169**, 513.

WERLE, H 1973 Hydrodynamic Flow Visualization. *Annual Review of Fluid Mechanics* **5** (1), 361–386.

VON WIESELSBERGER, C 1921 Neuere Feststellungen {ü}ber die Gesetze des Fl{ü}ssigkeits-und Luftwiderstandes. *Phys. z* **22** (11), 321–328.

WILLIAMS, JACK, BARLOW, JEWEL & RANZENBACH, ROBERT 1999 Experimental Study of C D Variation With Aspect Ratio. *SAE Congress* .

WILLIAMSON, CHARLES H. K. 1996 Vortex Dynamics in the Cylinder Wake. *Annua* .

WINANT, C. D. & BROWAND, F. K. 1974 Vortex pairing : the mechanism of turbulent mixing-layer growth at moderate Reynolds number. *Journal of Fluid Mechanics* **63**, 237.

WU, J., SHERIDAN, J., HOURIGAN, K. & SORIA, J. 1996 Shear layer vortices and longitudinal vortices in the near wake of a circular cylinder. *Experimental Thermal and Fluid Science* **12** (95), 169–174.

WU, J, SHERIDAN, J, SORIA, J & WELSH, M C 1994 An Experimental Investigation of Streamwise Vortices in the Wake of a Bluff Body.

ZDRAVKOVICH, M. M. 1997 *Flow around circular cylinders. Vol 1: Fundamentals.* Oxford University Press.

ZHANG, B, TO, S & ZHOU, Y. 2014 Fluid-Structure-Sound Interactions and Control.

ZHANG, B. F., ZHOU, Y. & TO, S. 2015 Unsteady flow structures around a high-drag Ahmed body. *Journal of Fluid Mechanics* **777**, 291—-326.

ZHAO, JISHENG, LEONTINI, JUSTIN S., LO JACONO, DAVID & SHERIDAN, JOHN 2014 Fluid–structure interaction of a square cylinder at different angles of attack. *Journal of Fluid Mechanics* **747**, 688–721.

ZHOU, J., ADRIAN, R. J., BALACHANDAR, S. & KENDALL, T. M. 1999 Mechanisms for generating coherent packets of hairpin vortices in channel flow. *Journal of Fluid Mechanics* **387** (August 2015), 353–396.